University of Southampton

Faculty of Natural and Environmental Sciences

School of Ocean and Earth Science

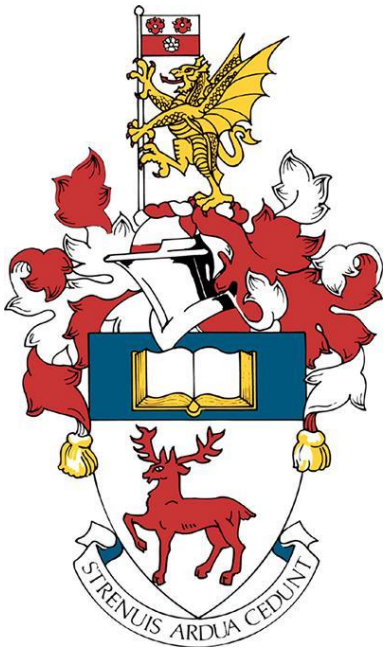

COUPLING MACRO- AND MICRONUTRIENT BIOGEOCHEMISTRY: DISTRIBUTION AND SPECIATION OF IRON AND OTHER BIOACTIVE TRACE METALS REQUIRED FOR PHOSPHORUS ACQUISITION IN THE SUBTROPICAL NORTH ATLANTIC

by

Korinna Gerda Lydia Kunde

ORCID ID 0000-0002-1655-0088

Thesis for the Degree of Doctor of Philosophy

March 2021

University of Southampton

Abstract

Faculty of Natural and Environmental Sciences

School of Ocean and Earth Science

Thesis for the Degree of Doctor of Philosophy

COUPLING MACRO- AND MICRONUTRIENT BIOGEOCHEMISTRY: DISTRIBUTION AND SPECIATION OF IRON AND OTHER BIOACTIVE TRACE METALS REQUIRED FOR PHOSPHORUS ACQUISITION IN THE SUBTROPICAL NORTH ATLANTIC

by

Korinna Gerda Lydia Kunde

To meet cellular phosphorus (P) demands in the phosphate-deplete subtropical North Atlantic, phytoplankton depend on the less readily bioavailable dissolved organic phosphorus (DOP), which is accessible via alkaline phosphatases – metalloenzymes that require co-factors of iron (Fe), zinc (Zn) or cobalt (Co). As the oceanic concentrations of these metals are vanishingly low and as their physicochemical speciation further constrains bioavailability, the coupled biogeochemistry of macronutrient P and metal micronutrients Fe, Zn and Co has the potential to exert a biological control on primary production and hence, impact upon the global carbon cycle.

A summertime longitudinal transect along 22 °N between 60 °W to 30 °W in the subtropical North Atlantic gyre served as a natural laboratory for this thesis, to investigate the distribution, speciation and biological control of Fe (and Zn and Co) for DOP acquisition across strong biogeochemical gradients in metals, macronutrients and phytoplankton community. High-resolution surface sampling and full-depth water column profiling of the Fe distribution were conducted and size-fractionated into soluble (sFe <0.02 µm), colloidal (0.02 µm <cFe <0.2 µm) and total dissolvable (TDFe; unfiltered, acid-leachable) Fe species, which revealed the pervasive role of cFe in driving the distribution of dissolved Fe (dFe <0.2 µm, i.e. dFe = cFe + sFe). While the largest local input across the basin was due to hydrothermal venting from the Mid-Atlantic ridge in the abyss, where dFe reached 27 nM with ~90 % cFe, the surface dFe inventory was strongly controlled by seasonal dust deposition. This resulted in a strong west-to-east decrease in dFe concentrations from 1.53 to 0.26 nM, with the colloidal fraction decreasing concurrently (from 85 to 61 % of dFe). Particle scavenging and biological uptake were the major removal processes of dFe and cFe in the subsurface, drawing

cFe down to 0 to 30 % of dFe in the deep chlorophyll-*a* maximum (DCM). Due the pivotal position of cFe between the particulate and the soluble (i.e. the truly dissolved) phases, it was responsible for setting the dFe inventory at the major sources and sinks across the basin.

Building on these insights, at three representative locations that differed in dust loading and initial Fe concentrations, kinetics bottle experiments were carried out, in which Fe additions enriched in the low abundance isotope ^{57}Fe (as dissolved Fe_2O_3, i.e. inorganic sFe) were made to ambient surface seawater to trace the partitioning into the sFe, cFe and TDFe pools over a 48 h incubation period. Due to the low solubility of Fe in seawater and the absence of excess organic ligands, the ^{57}Fe enriched spike partitioned rapidly (<30 min), almost completely (~90 %), consistently (regardless of initial conditions) and irreversibly (unchanged over 48 h) into the colloidal phase, as nanoparticulate Fe-oxyhydroxides. As these are precursors to larger mineral phases, which remove available dFe and reduce its residence time in surface waters, this result strengthens the argument for the important role of cFe in the oceanic Fe cycle.

The cross-basin gradients in surface Fe concentration and speciation, and less variable dZn and dCo distributions, enabled *in-situ* bioassays with metal amendments to probe the effects of trace metals on DOP acquisition. Calibrated targeted proteomics were applied to quantify the alkaline phosphatases of dominant phytoplankton species, and demonstrated the localised effect of metal availability on alkaline phosphatase abundances at two out of four locations. In the high Fe, low DIP, low DOP western basin, additions of Zn and Co increased the concentration of a Zn/Co-dependent PhoA-type alkaline phosphatase of *Synechococcus* six- and seven-fold, respectively, relative to the unamended Control. In the lower Fe, higher DIP, higher DOP eastern basin, the addition of Fe increased the concentration of the Fe-dependent PhoX of *Prochlorococcus* two-fold relative to the Control. Using cellular metal stoichiometry in *Synechococcus* revealed PhoA to be a potential major sink for cellular Co (1 to 35 %), but not Zn (<1 %), and hence, it may be particularly sensitive to Co availability globally.

Biogeochemical gradients are considered characteristic of latitudinal progression across basins, e.g. from the high Fe North Atlantic into the low Fe South Atlantic. There is, however, a systematic lack of knowledge across longitudinal gradients and therefore, their biogeochemical impact may be underestimated. The key findings of this thesis demonstrate that the biogeochemistry within the subtropical North Atlantic is diverse, as 1) the Fe distribution is subject to large regional variability that is controlled by a dynamic colloidal phase, and 2) metal availability affects P acquisition locally. The combined toolbox of traditional biogeochemical measurements, trace metal measurements, and proteomics was essential to these results, and will prove inevitable in constraining their implications in the future, especially as global change is predicted to alter metal cycles and exacerbate P stress.

Table of Contents

List of Tables

List of Figures

Declaration of Authorship

I, ***Korinna Gerda Lydia Kunde***, declare that this thesis and the work presented in it are my own and have been generated by me, as the result of my own original research.

> ***Coupling Macro- and Micronutrient Biogeochemistry: Distribution and Speciation of Iron and Other Bioactive Trace Metals Required for Phosphorus Acquisition in the Subtropical North Atlantic***

I confirm that –

1. This work was done wholly or mainly while in candidature for a research degree at this University;
2. Where any part of this thesis has previously been submitted for a degree or any other qualification at this University or any other institution, this has been clearly stated;
3. Where I have consulted the published work of others, this is always clearly attributed;
4. Where I have quoted from the work of others, the source is always given. With the exception of such quotations, this thesis is entirely my own work;
5. I have acknowledged all main sources of help;
6. Where the thesis is based on work done by myself jointly with others, I have made clear exactly what was done by others and what I have contributed myself;
7. At the time of submission, parts of this work have been published, have been submitted for publication, or are under review:

   Chapter 3:

   Kunde, K., Wyatt, N. J., González-Santana, D., Tagliabue, A., Mahaffey, C. and Lohan, M. C. (2019). Iron distribution in the subtropical North Atlantic: The pivotal role of colloidal iron. *Global Biogeochemical Cycles*, 33. https://doi.org/10.1029/2019GB006326

_____

Korinna Gerda Lydia Kunde,

Date: _____

Acknowledgements

Thank you to my supervisor Prof Maeve Lohan. Whatever you saw in me in March 2016, I will be forever grateful to you for taking a chance on me then, and for believing in me since. Through your wisdom, patience and personality, the past years have changed my life. I could not have asked for a better supervisor. I would like to extend my gratitude to my co-supervisor Prof Mark Moore, my panel chair Prof Toby Tyrrell, and my mentors Prof Al Tagliabue, Prof Claire Mahaffey and Dr Mak Saito, for making time for me, guiding me, inspiring me, encouraging me and challenging me.

I am grateful for being part of Maeve's trace metal team at NOCS, the lessons of true team spirit I learned, and the knowledge that was passed on to me there. A special thank you goes to Dr Neil Wyatt, without whom I would have given up many times along the way. I would also like to thank the Saito lab at WHOI, and my office mates over there, Dr Noelle Held and Marianne Acker, through whom I found my passion for marine microbiology and who became close friends.

I have met many friends and role models on the journey to and through this PhD. My deepest gratitude is for the friendship and unconditional support given by Dr Tabby Pearman and Hannah Grace McDonald, at any hour in any time zone. Thank you for the valuable lessons on strength and self-worth, and for reminding me that I am more than my thesis. I am grateful for the wonderful PhD community at NOCS, and the lifelong friends I have made through there. Dr David Riley, Elena Cerdan, Ben Chichester, Dr Rach Shuttleworth, Sarah Howarth, Dr Matt Nichols, and Alex Tribolet – you have made the past four years the best ever. I am very fortunate to have Toby Hedges, Laura Nicholas, Dr Fiona Harnischfeger, the dancers at Tracie's Latin Club, and my friends from home in my life – thank you for keeping me sane outside the academic bubble.

Finally, I would like to try to express my thanks to my parents, Elke und Willi Kunde. Mama und Papa – ihr habt mir die Welt eröffnet, mich bei all meinen Hirngespinsten unterstützt und niemals nein gesagt. Ihr habt mich all meine Entscheidungen treffen und all meine Fehler selbst machen lassen. Ihr habt an Erfolgstagen mit mir gefeiert und an schlechten Labortagen mit mir geweint. Ihr habt mich ein Leben in einem anderen Land leben lassen, eine neue Sprache für mich gelernt, und akzeptiert, dass meine Freunde und Partner wahrscheinlich nie eure eigene sprechen würden. Ihr seid in ein Flugzeug gestiegen, wenn ich euch brauchte, und habt mich in eins steigen lassen, wenn ich das brauchte. Und... ihr habt mich das Versprechen brechen lassen, mein nächstes Abenteuer näher am 'Basiscamp' zu finden. Keine Worte, ob Deutsch oder Englisch, können meine Dankbarkeit für all das ausdrücken. Wisst, dass ohne euch das, was dieser Seite folgt, dort nicht stünde!

This work was funded through a stipend by the Graduate School of the National Oceanography Centre Southampton, while field work was also supported through the National Environmental Research Council under grant NE/N001125/1, awarded to Prof Maeve Lohan. Travel grants from the Challenger Society for Marine Science and the Environment, Sustainability and Energy Division of the Royal Society of Chemistry provided financial help towards presenting parts of this work at international conferences.

Definitions and Abbreviations

ABC transporter	ATP-binding cassette transporter
AMBIC	Ammonium bicarbonate
AOU	Apparent oxygen utilisation
APA	Alkaline phosphatase activity
APS	Ammonium persulfate
ATP	Adenosine triphosphate
BATS	Bermuda Atlantic Time-series Study
BCA assay	Bicinchonic acid assay
cFe	Colloidal iron
Chl-*a*	Chlorophyll-*a*
CID	Collision induced dissociation
CM-PEHA	Carboxymethylated pentaethylenehexamine
CTD	Conductivity, temperature, depth
DCM	Deep chlorophyll-*a* maximum
dCo	Dissolved cobalt
dFe	Dissolved iron
DIN	Dissolved inorganic nitrogen
DIP	Dissolved inorganic phosphorus
DNA	Deoxyribonucleic acid
DON	Dissolved organic nitrogen
DOP	Dissolved organic phosphorus
DTT	Dithiothreitol
dZn	Dissolved zinc
EDTA	Ethylenediaminetetraacetic acid
FeL	Ligand-bound iron
FIA-CL	Flow injection analysis with chemiluminescence detection
FCM	Flow cytometry
GEOTRACES IDP17	GEOTRACES Intermediate Data Product 2017
HDPE	High density polyethylene
HNLC	High (macro)nutrient low chlorophyll-*a*
HOTS	Hawaii Ocean Time Series
HPLC-MS/MS	High pressure liquid chromatography-tandem mass spectrometry
HR-ICP-MS	High resolution inductively coupled plasma mass spectrometry
IODA	Iodoacetamide
IPTG	Isopropyl β-d-1-thiogalactopyranoside

ITCZ	Intertropical Convergence Zone
LB	Luria broth
LC-ICPMS-ESIMS	Liquid chromatography inductively coupled plasma mass spectrometry with electrospray ionisation mass spectrometry
LDPE	Low density polyethylene
MLD	Mixed layer depth
MUF-P	4-Methylumbelliferyl phosphate
ODV	Ocean Data View
OMZ	Oxygen minimum zone
OTE	Ocean Test Equipment
PC	Polycarbonate
PE	Polyethylene
pFe_{app}	Apparent particulate iron
PMMA	Polymethylmetacrylate
PMT	Photomultiplier tube
pNPP	4-Nitrophenylphosphate
PISCES	Pelagic Interactions Scheme for Carbon and Ecosystem Studies
PP	Polypropylene
PRM/SRM	Parallel reaction monitoring/Selected reaction monitoring
PTFE	Polytetrafluoroethylene
PVC	Polyvinyl chloride
RNA	Ribonucleic acid
RSD	Relative standard deviation
SAL	Saharan Air Layer
SDS	Sodium dodecyl sulfate
sFe	Soluble iron
SOC	Super optimal broth
SST	Sea surface temperature
SXRF	Synchrotron X-ray fluorescnece
TDFe	Total dissolvable iron
TDN	Total dissolved nitrogen
TDP	Total dissolved phosphorus
TE	Tris-HCl/EDTA
TEMED	N,N,N',N'-Tetramethylethylenediamine
TETA	Triethylenetetramine
UHP water	Ultra-high purity water

Chapter 1 Introduction

1.1 Global Marine Primary Production and Limiting Nutrients

Marine primary production by phytoplankton converts annually ~50 Pg carbon (C) – i.e. roughly half of the Earth's entire primary production – of atmospheric inorganic carbon dioxide (CO_2) to organic forms of C as biomass, of which one third is exported to the deep ocean as sinking dead organic matter, where it is sequestered on geological time scales (Behrenfeld et al., 2006; Falkowski et al., 1998). This transfer of C from the atmosphere to the deep ocean is known as the biological C pump and is relevant for regulating the Earth's climate, as atmospheric CO_2 is a key greenhouse gas. Primary production depends – aside from a source of energy (light) and a space to live (seawater) – on phytoplankton's access to the vital macronutrients nitrogen (N), phosphorus (P), in some instances silicon (Si), and a suite of trace metal micronutrients that include iron (Fe), zinc (Zn) and cobalt (Co). The availability of these macro- and micronutrients is therefore vital, with one or multiple nutrients able to place constraints on, or 'limit' primary production and hence, reducing the efficiency of the biological C pump (e.g. Falkowski et al., 1988). Limitation is defined by Liebig's Law of the Minimum as reaching the upper threshold of biomass accumulation, as the result of the depletion of one of the nutrients beyond viable levels (de Baar, 1994). In other words, the (re-)introduction of this nutrient, the primary limiting nutrient, would result in an increase of biomass. Serial limitation occurs, when the primary limiting nutrient is replenished and the addition of another nutrient, the secondary limiting nutrient, would result in a further increase in biomass. This can be extended to the tertiary limiting nutrient and so on.

To a first order, nutrient distributions drive large-scale limitation patterns of phytoplankton in the global ocean and a broad distinction between two main trends emerges (Figure 1.1) (Moore et al., 2013). In the oligotrophic – i.e. macronutrient-depleted – subtropical gyres of the Atlantic and Pacific Oceans, the primary limiting nutrient is typically N, with P being secondarily limiting in the subtropical North Atlantic. This secondary limitation is the result of large Fe-rich dust deposition in this basin, allowing biological fixation of dinitrogen (N_2) gas, which contributes additional bioavailable N resources and drives P limitation. In contrast, in the high-(macro)nutrient low-chlorophyll (HNLC) regions of the Southern Ocean, equatorial Pacific and subpolar North Pacific, Fe is the primary limiting nutrient, due to the lack of a significant Fe source to the surface like in the North Atlantic. This results in large residual N and P stocks.

While this crude distinction allows global trends in primary production to be reproduced in marine biogeochemical models, mismatches between observational and theoretical data persist that pose

challenges for accurate predictions, especially in the light of global change (e.g. Aumont et al., 2015). Some of these mismatches arise from intricacies of the biogeochemical cycles of N, P and Fe themselves beyond their distribution (e.g. the role of physicochemical metal speciation) and from limitation by other trace metal micronutrients in the global ocean (e.g. Zn and Co), both of which are insufficiently understood, insufficiently resolved in models, and at the core of this dissertation.

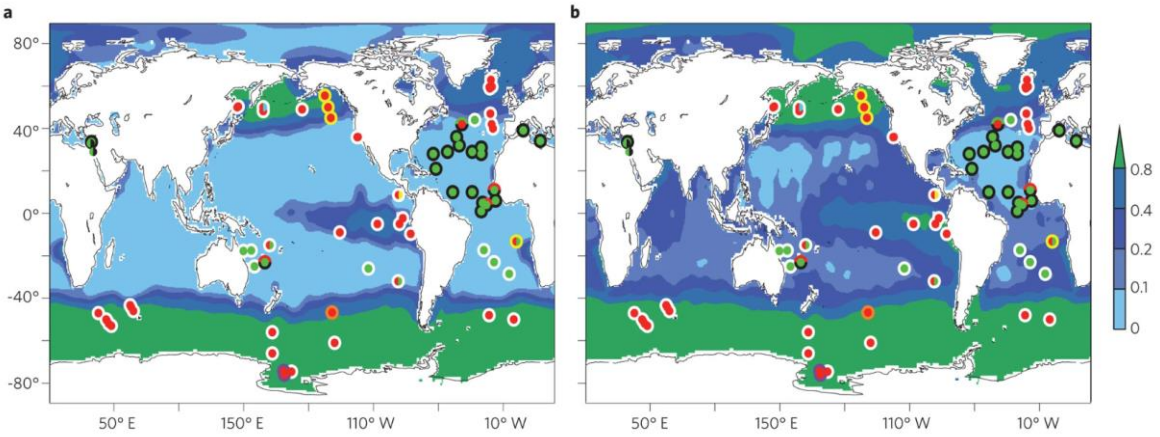

Figure 1.1 Nutrient (co-)limitation of phytoplankton in the global ocean. Central circles and circle rims show primary and secondary limiting nutrients, respectively, inferred from increased chlorophyll-*a* (Chl-*a*) and/or primary production rates in nutrient-amended bioassays: N (green), P (black), Fe (red), Si (orange), Co (yellow), Zn (cyan) and Co-containing vitamin B_{12} (purple). Divided circles indicate potential co-limitation and white circle rims indicate that no secondary limiting nutrient was identified, often due to lack of testing. Background contours show annual average surface concentrations in µmol kg^{-1} of (a) nitrate and (b) phosphate. Nitrate concentrations are scaled by 1:16, the mean N:P ratio of organic matter to aid comparison. Figure taken from Moore et al. (2013).

Firstly, a nutrient's concentration alone does not equate to its bioavailability for primary producers. Instead, its physicochemical speciation, i.e. its physical structure and chemical properties, predicts its reactivity. Trace metal micronutrients, first- and second-row transition metals with rich redox and coordination chemistry, exist as diverse and often ill-defined suites of physicochemical species in seawater (Bruland & Lohan, 2004; Lohan & Tagliabue, 2018). Aside from the regulatory role of metal speciation on bioavailability, the adaptation towards specific physicochemical forms by some organisms has the potential to impact community structure via selective pressure. For example, genes that are involved in the synthesis of high-affinity Fe-chelating compounds ('siderophores') or in the acquisition of siderophore-bound Fe are common in the microbial community of the Fe-deplete oligotrophic gyres (Boiteau et al., 2016; Hopkinson and Barbeau, 2012). Another example is the particle capture and dissolution mechanisms employed by colonies of the diazotroph *Trichodesmium*, which allows efficient utilisation of particle-bound Fe in dust rich environments (Rubin et al., 2011).

Secondly, nutrients cycles can be interlinked, which results in co-limitation, in which only the simultaneous re-introduction of the two (or more) limiting nutrients stimulates growth. Co-limitation can occur under independence of multiple limiting nutrients, under dependence of one nutrient on the access to another, or as biochemical substitution (Saito et al., 2008). In many instances, co-

limitation relates a trace metal to a macronutrient and results from metal co-factor requirements in metalloenzymes that are involved in macronutrient acquisition (Figure 1.2) (Lohan & Tagliabue, 2018). The extent and implication of macro-/micronutrient co-limitation in the ocean is a recently accelerating field of marine biogeochemical research that is facilitated by methodological advances, which include large-scale surveys of trace metals in the ocean (e.g. by the international GEOTRACES program), ultrasensitive macronutrient measurements (e.g. Martiny et al., 2019), and the application of 'omics techniques to the marine environment that offer insight into nutrient stress in the natural environment at the unprecedented cellular scale (Saito et al., 2019). The combination of these tools as applied in this dissertation are indispensable and timely for resolving the coupling of macro- and micronutrient biogeochemistry in the ocean.

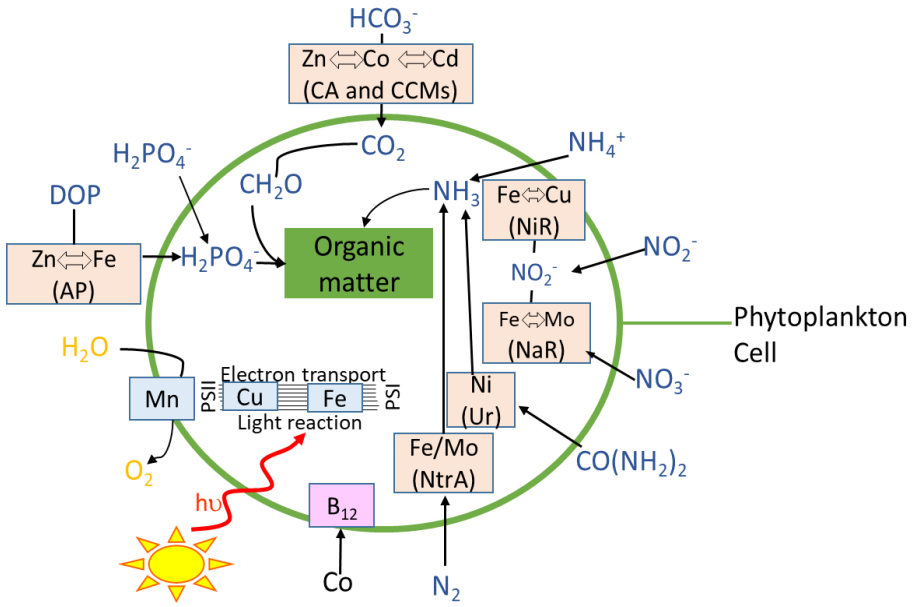

Figure 1.2 Uptake of C, N and P and subsequent conversion into organic matter by a model phytoplankton cell via trace metal-dependent enzymes (yellow). Photosynthesis (blue) and vitamins such as B_{12} (purple) also require trace metals. Abbreviations: AP = alkaline phosphatase, CA = carbonic anhydrase, CCM = carbon concentrating mechanisms, NaR = nitrate reductase, NiR = nitrite reductase, NtrA = nitrogenase, Ur = urease, PSI/II= photosystems I/II. Figure taken from Lohan & Tagliabue (2018).

1.2 Biogeochemistry and Distribution of Macronutrients

Together with fixed C, macronutrients N and P are assimilated into macromolecules that fulfil structural and metabolic roles in phytoplankton cells. The major cellular N sinks are nucleic acids (DNA, RNA) and proteins, while those of P are nucleic acids and phospholipids. Quantitatively minor sinks are chlorophylls for N and adenosine triphosphate for P. Despite variability existing across phytoplankton species, space and time, an average C:N:P ratio of 106:16:1, the 'Redfield ratio', reflects these vital, conserved roles for the cellular machinery in phytoplankton (Geider and La Roche, 2002; Redfield, 1958). Accordingly, it is not attributed to stoichiometry of seawater but

rather to the phytoplankton's effort to achieve sufficient C, N and P cellular inventories regardless of ambient conditions.

1.2.1 Nitrate and Phosphate

Genetic capabilities for N and P assimilation differ between phytoplankton species and even between strains of the same species, but the dissolved inorganic forms of N (i.e. DIN) and P (i.e. DIP) are generally most readily bioavailable, and hence have been the focus of understanding global patterns of nutrient limitation. Nitrate (NO_3^-) and phosphate (PO_4^{3-}) make up the vast majority (~90 %) of DIN and DIP, respectively (Benitez-Nelson, 2000; Gruber, 2008; Paytan & Mclaughlin, 2007), and therefore, nitrate/DIN and phosphate/DIP will be used interchangeably hereafter. As the consequence of biological uptake by phytoplankton, surface ocean concentrations of phosphate and nitrate are low (nanomolar range) and typical oceanic depth profiles exhibit strong depletion signals throughout the entire euphotic zone, where sunlight down to 1 % of surface levels sustains photosynthesis (Figure 1.3a and c). Below this, the degradation of organic matter (dead cells, faecal pellets) by heterotrophic remineralisation becomes dominant and replenishes the nitrate and phosphate pools over time. The switch with depth from biological uptake being dominant to remineralisation being dominant is marked by the 'nutricline', where the largest changes in nutrient concentrations occur over the smallest depth range. With increasing depth and increasing age along the thermohaline circulation higher nitrate and phosphate concentrations accumulate from remineralisation, resulting in higher concentrations in the deep Pacific (phosphate: ~2 to 3 µM, nitrate: ~30 to 40 µM) than Atlantic (phosphate: ~1 to 2 µM, nitrate: ~20 to 30 µM) (Benitez-Nelson, 2000; Gruber, 2008). Where residual macronutrient stocks are preserved due to limitation by trace metals, e.g. in the Southern Ocean or Equatorial Pacific, the surface depletion signal is less pronounced as seen in the background contours of Figure 1.1 for (a) nitrate and (b) phosphate.

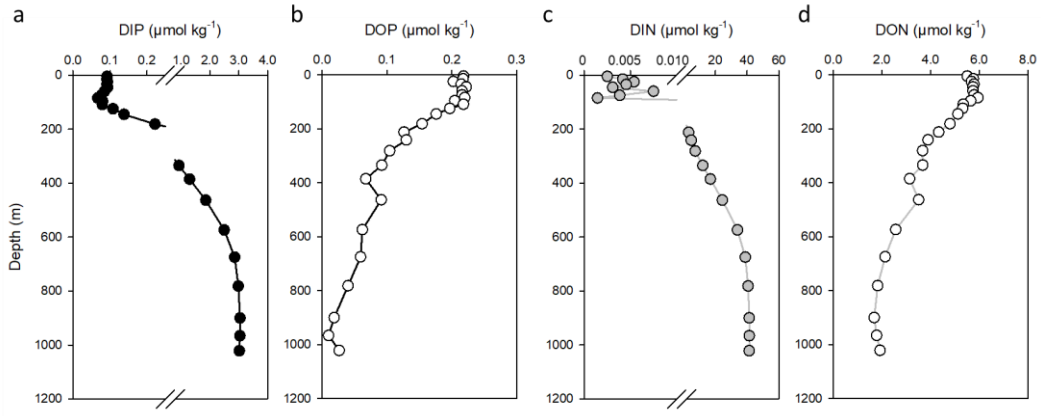

Figure 1.3 Representative upper water column profiles of (a) DIP, (b) DOP, (c) DIN and (d) DON from the North Pacific at HOTS (Hawaii Ocean Time-series). Data extracted from https://hahana.soest.hawaii.edu/hot/hot-dogs/cextraction.html. In the surface, DIN and DIP are depleted due to biological uptake, while DON and DOP are generated in the surface and remineralised to DIN and DIP at depth.

1.2.2 Supply Pathways and Alternative Forms of Nitrogen and Phosphorus

As N is only the 30th most abundant element in Earth's crust, the supply of nitrate relies to ~80 % on upwelling and upward mixing of regenerated nutrient stocks to fuel primary production in the euphotic zone (Bristow et al., 2017; Gruber and Sarmiento, 1997). Phosphorus is more abundant in the Earth's crust (11th) and hence, continental weathering followed by the delivery of phosphate via riverine or atmospheric pathways is more significant than for nitrate. However, riverine run-off is constrained to near-continental regions, so that internal (re-)supply of phosphate is the key source in the open ocean (Paytan & Mclaughlin, 2007). In permanently stratified regions, such as the subtropical gyres, this is not efficient and so, to meet their cellular demands, phytoplankton rely on alternative supply mechanisms or alternative forms of N and P that are less bioavailable than nitrate and phosphate. In addition, nitrate is up to ~100-fold more concentrated than other DIN species like nitrite (NO_2^-) and ammonium (NH_4^+) and assimilated via a reductive uptake mechanisms that form nitrite/ammonium as transient intermediates, which is why these forms are rapidly recycled and not accumulated to large concentrations in the ocean (Gruber, 2008). Some phytoplankton species lack the genes required for nitrate reduction and rely directly on these even smaller pools of ammonium and/or nitrite. This is the case for *Prochlorococcus* with a few exceptions (Berube et al., 2015) and for some strains of *Synechococcus* (Moore et al., 2002). When intracellular ammonium levels drop to levels insufficient to maintain N homeostasis in these cyanobacteria, the ntcA regulon is activated, which increases the expression of genes involved in the utilisation of alternative sources of N including organic N-substrates (Lindell and Post, 2001; Tolonen et al., 2006).

To this end, the dissolved organic analogues to DIN and DIP, i.e. DON and DOP, are less readily available sources of N and P, as these require hydrolysis before assimilation, which is more energetically costly and requires respective genetic capabilities. The DON and DOP pools comprise a whole range of organic molecules that differ in size, molecular weight, recalcitrance and hence in bioavailability. The DON pool is the less well resolved of the two, not least because a majority is too recalcitrant to be captured by current analytical methodology (Aluwihare & Meador, 2008). Amides (–C(=O)N=), as occurring in urea and peptide bonds, make up a fraction of accessible DON via peptidases and ureases. In fact, to *Prochlorococcus* urea is an equally efficient source of N as ammonium (Shilova et al., 2017). Additionally, biological fixation of the abundant atmospheric dinitrogen gas (N_2) into bioavailable NH_4^+ by diazotrophs provides a significant source of new DIN to phytoplankton (Zehr & Capone, 2020). It is estimated that N_2 fixation contributes annually 80 to 110 Tg bioavailable N to the global ocean (for comparison, ~6,800 Tg N yr^{-1} are from regenerated sources in the deep ocean), with 25 % of this fixed in the (sub)tropical regions where it supports the majority of N required for primary production (Bristow et al., 2017; Gruber & Sarmiento, 1997; Montoya et al., 2002). Diazotrophic abilities amongst phytoplankton, e.g. by the cyanobacterium *Trichodesmium*, create a clear ecological niche where DIN levels are limiting for non-diazotrophs,

but they also come at high Fe and P costs. The high Fe requirement is a result of multiple Fe co-factor requirements of the nitrogenase enzymes, so that high ambient Fe availability is a prerequisite for diazotrophy (Held et al., 2020; Moore et al., 2009).

In contrast to biological N_2 fixation acting to replenish the DIN pool, no analogous renewable source exists for DIP. Instead, organisms rely on the more replete, yet less readily available DOP pool for P acquisition. DOP is generally more labile than DON and consists to ~75 % of phosphomonoesters and -diesters (C-O-P bond), as occurring in DNA/RNA/ATP/phospholipid molecules and their degradation products, and to ~25 % of phosphonates (C-P bond), whose origin is in phosphoproteins and membrane phosphonolipids (Kolowith et al., 2001). The more abundant and more labile phosphoesters are relatively easily hydrolysed by 5'nucleotidases, diesterases or alkaline phosphatases. Alkaline phosphatase activity (APA) in the ocean has been measured widely across regions and the microbial realm, including activity by heterotrophic bacteria and eukaryotic and prokaryotic phytoplankton (Duhamel et al., 2010; Hoppe, 2003). Rates are often highest under low DIP, owing to the expression via the *pho* regulon as in *Escherichia coli* (*E. coli*) (Duhamel et al., 2010; Labry et al., 2005; Mahaffey et al., 2014; Vidal et al., 2003), and are concerted with other P-stress biomarkers such as the DIN:DIP ratio and arsenic (As) biogeochemistry (Lomas et al., 2010; Wurl et al., 2013). However, clear gaps in knowledge exists regarding the exact regulation, substrate specificity, co-factor requirements, cambialistic capacities, and subcellular localisation of marine alkaline phosphatases, which makes it difficult to assess the impact for primary production in the ocean. To date, at least three types of alkaline phosphatases are known to be expressed amongst marine bacteria under DIP stress, namely PhoA, PhoX and PhoD. PhoA is a monoesterase that requires four Zn^{2+} and two magnesium^{2+} (Mg) co-factors per dimer (*E. Coli*, Coleman, 1992), although the substitution of Co for Zn can maintain reduced enzyme activity across a wide range of substrates (Lazdunski and Lazdunski, 1969). Approximately half of marine bacterial PhoA are predicted to be active in the cytoplasm, while the other half is split between the periplasm and the extracellular space (Luo et al., 2009). In contrast, the monomeric PhoX hydrolyses both mono- and diesters, requires three calcium^{2+} (Ca) and two Fe^{2+} co-factors (*Pseudomonas fluorescens*, Yong et al., 2014; *Pasteurella multocida*, Wu et al., 2007), and is mapped predominantly to the periplasm and the extracellular space (together ~80 %) for marine bacteria (Luo et al., 2009). Based on searches in marine metagenomics libraries, PhoX was found to be more widespread than PhoA (Sebastian & Ammerman, 2009), while another alkaline phosphatase, PhoD, was even more abundant (Luo et al., 2009). Like PhoX, PhoD is a mono- and diesterase and activated by Ca and Fe (*Bacillus subtilis*; Rodriguez et al., 2014), but only a minority was mapped to the periplasm and the extracellular space (together ~30 %) (Luo et al., 2009).

As the two most important macronutrients, N and P limit primary production in vast oceanic regions, especially the oligotrophic subtropical gyres (Figure 1.1). A plethora of *in-situ* experiments have

shown N to be the typically primary limiting nutrient, while P being the secondary limiting nutrient (references in Table S2 in Moore et al., 2013). This tendency may be explained by the higher availability of DOP over DON and acclimatisation strategies of phytoplankton to P stress (e.g. sulfolipids instead of phospholipids; van Mooy et al., 2009). As N_2 fixation by diazotrophs can alleviate partially the N limitation but an equivalent mechanism for P is missing, Tyrrell (1999) proposed that over geological timescales P will be the ultimate limiting nutrient that sets the upper threshold of primary production. This simplistic framework is continuously being challenged by evidence for N-P co-limitation or primary P limitation (Browning et al., 2017; Dixon, 2008; Mills et al., 2008; Moore et al., 2008; Sohm & Capone, 2006; Thingstad et al., 2006; Turner & Rabalais, 2013), and by wider recognition of the role of DOP in supporting primary production (e.g. Lomas et al., 2010). Biogeochemical cycles of N and P are subject to global change. Anthropogenic influences on nutrient budgets (e.g. combustion products, fertilisers), changes in nutrient-delivering water mass circulation (e.g. Gulf Stream, Atlantic Meridional Overturning Circulation, winter convective mixing), unclear feedbacks on N_2 fixation (suppression by anthropogenic N inputs versus stimulation due to reduced natural inputs) are only a few examples of the potential drivers, while shifts in nutrient biogeochemistry have already been documented across the North Atlantic (Macovei et al., 2019). Henceforth, to understand present and future nutrient limitation and its impacts on the biological C pump, studies must look beyond nitrate and phosphate, and determine the role of DON and DOP resources and the dependency on trace metals for their acquisition.

1.3 Biogeochemistry and Distribution of Trace Metal Micronutrients

Trace metal micronutrients include the first and second row transition metals vanadium (V), chromium (Cr), manganese (Mn), Fe, Co, nickel (Ni), copper (Cu), Zn, molybdenum (Mo) and cadmium (Cd), with the quest for the biological role of others ongoing (e.g. R. Rickaby, https://cordis.europa.eu/project/id/681746). In comparison to macronutrients, the role of trace metal micronutrients for phytoplankton growth is not only less by absolute abundance (only <5 % of cellular elemental composition), but also more diverse across a range of phytoplankton taxa. This is illustrated by the stoichiometric plasticity of cellular trace metal quotas (Figure 1.4). The idea of a metal-inclusive 'extended' Redfield ratio has been put forward, for example by Ho et al. (2003) who suggested a ratio of $(C_{124}N_{16}P_{1.0}S_{1.3}K_{1.7}Mg_{0.56}Ca_{0.5})_{1000}Sr_{5.0}Fe_{7.5}Zn_{0.80}Cu_{0.38}Co_{0.19}Cd_{0.21}Mo_{0.03}$ (S = sulphur, K = potassium, Sr = strontium) across a range of cultured eukaryotic phytoplankton. However, this is strongly debated and others have determined it to be $(C_{147}P_{1.0}S_{0.75})_{1000}$ $Mn_{0.39}Fe_{5.0}Zn_{1.5}Cu_{0.50}Co_{0.15}Ni_{0.40}$ across field populations of some cyanobacteria and autotrophic flagellates (Twining et al., 2015). In fact, the stoichiometric plasticity is suggestive of the fine-tuned responses and adaptations to environmental controls (e.g. luxury storage, metal-free enzyme isoforms, substitution, toxicity responses) and as such, these may be key to resolving the ecological

success of certain phytoplankton species and their interaction with trace metal cycles in the global ocean.

The multiple order-of-magnitude lower cellular quotas of trace metals relative to N and P is generally in tune with their lower, nano- (10^{-9}) to picomolar (10^{-12}), dissolved concentrations (i.e. <0.2 µm) in the open ocean compared to micro- (10^{-6}) to nanomolar concentrations of DIN and DIP (Figure 1.4). However, while the trace metals shown in Figure 1.2 and Figure 1.4 are all involved in biological processes, not all of them are considered limiting nutrients for phytoplankton growth, as their availability greatly exceeds biological requirements (see those metals to the left of the grey shading in Figure 1.4). In capturing sources, sinks and internal cycling processes, a micronutrient's dissolved depth profile can provide clues about their potentially limiting roles. Four types of (idealised) distributions are distinguished: conservative, nutrient-type, scavenged, and hybrid (Bruland & Lohan, 2004; for basin-scale context see Anderson, 2020).

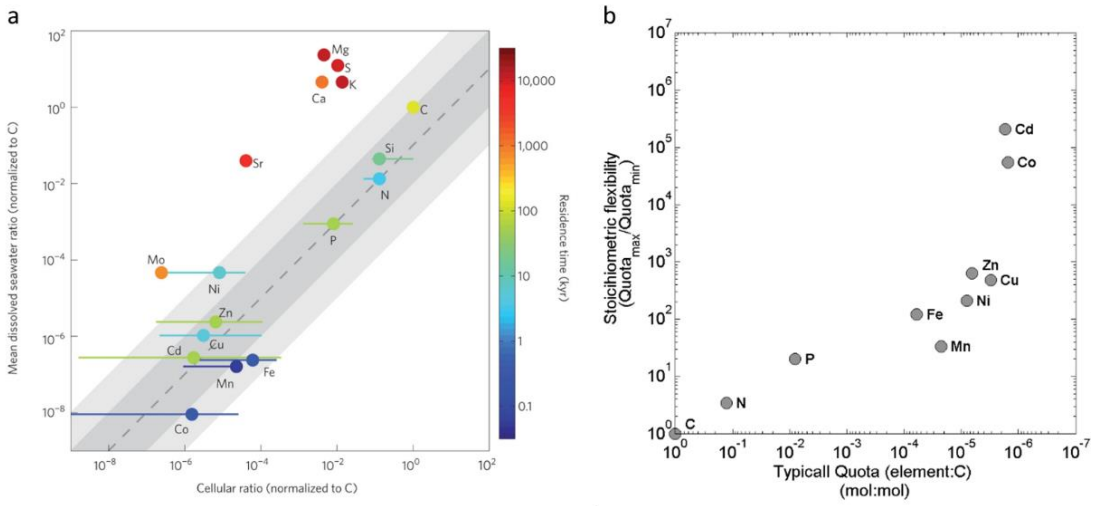

Figure 1.4 (a) Carbon-normalised trace metal quota in oceanic phytoplankton cells plotted against that of the dissolved metal and C concentrations in seawater. Dots indicate representative quotas that are averaged across many taxa and growth conditions, with the horizontal bars showing the observed range. Colour-coding refers to oceanic residence time. Grey shading indicates <10-fold (dark) and <100-fold (light) excess and deficiency relative to N, which is the limiting nutrient in much of the ocean. Thus, trace metals far to the left of the shading are in great excess, whereas some of the trace metals within the shading have potential to become limiting. (b) Typical quotas from (a) plotted against their respective stoichiometric flexibility, i.e. the maximum observed quota divided by the minimum observed quota. Figure combined from figures in Moore et al. (2013).

Conservative. Conservative trace metals exhibit an almost uniform distribution with depth, devoid of depletion signals from biological uptake in the surface and from scavenging processes with depth (Figure 1.5a). Their biological requirements are negligible compared with their concentration in seawater and they are have low particle reactivity, which results in long residence times (~10^5 yr) that exceed the mixing time of the ocean. An important example of a bioactive, conservative trace metal is Mo, which is required in the MoFe-subunit of nitrogenase required for N_2 fixation (Figure 1.2).

Nutrient-type. As the name suggests, nutrient-type trace metals follow distributions typically associated with those of macronutrients (Figure 1.5b), in which biological uptake is reflected in the strong depletion signal at the surface followed by the gradual replenishment via remineralisation over time/depth along the thermohaline circulation. Nutrient-type trace metals, like conservative ones, are not particle reactive but highly soluble under contemporary ocean conditions (including Eh, pH, temperature), so that remineralised concentrations can accumulate. Nutrient-type metals have intermediate oceanic residence times of ~10^3 to 10^5 yr. Examples include Zn, which is required in carbonic anhydrase for C fixation and in alkaline phosphatase for DOP hydrolysis. Nickel is another example, which is required in ureases involved in DON acquisition or as a substitute co-factor in superoxide dismutases. The nutrient-type metal Cd plays a role in substitution for Zn and Co (Figure 1.2).

Scavenged. Scavenged trace metals follow depth distributions that exhibit highest concentrations near sources that decrease gradually with distance from the source. In the case of a strong source at the surface, their distribution is almost a mirror image of nutrient-type metals, with highest concentrations at the surface that are attenuated with depth (Figure 1.5c). Scavenged trace metals have high particle reactivity. As a result, accumulation along the thermohaline circulation is absent and residence times are short with ~10^2 to 10^3 yr. Local source and sink processes (horizontal and lateral) are much more relevant for this type of metal, which results in a level of patchiness in their large scale distribution (Anderson, 2020). A classic example for a scavenged metal is aluminium (Al). However, Al has no known biological function, whereas similarly particle reactive metals that *do* play a role for biology fall into a separate fourth category, the hybrid metals, due their biological utilization in the surface (see below).

Hybrid. Trace metals that combine properties of both nutrient-type and scavenged distributions are hybrids. They have maximal concentrations near sources that are attenuated with distance due to scavenging processes, but they are also subject to biological uptake and remineralisation (Figure 1.5d). The most prominent of example of a hybrid-type trace metal is Fe, which forms co-factors in a range of proteins involved in photosynthesis, N_2 fixation (nitrogenases, nitrate reductases, nitrite reductases) and DOP acquisition (alkaline phosphatases) (Figure 1.2). Characteristically, Fe concentrations are enriched in the surface due to atmospheric Fe-rich dust deposition and removed by biological uptake in the euphotic zone. Below, the competition between scavenging and remineralisation processes exerts a tight control on Fe's concentration. Gradual accumulation as observed for nutrient-type metals like Zn is therefore absent. Another important hybrid-type example is Co, which is required (either absolutely or in substitution for Zn) in carbonic anhydrases and potentially in alkaline phosphatases. Due to the competing processes acting on hybrid metals across horizontal and lateral scales, their residence times are most difficult to constrain, with current

estimates varying over more than order of magnitude for both Fe (~5 to 500 yr) and Co (~7 to 250 yr) (Tagliabue et al., 2019; 2018; 2016).

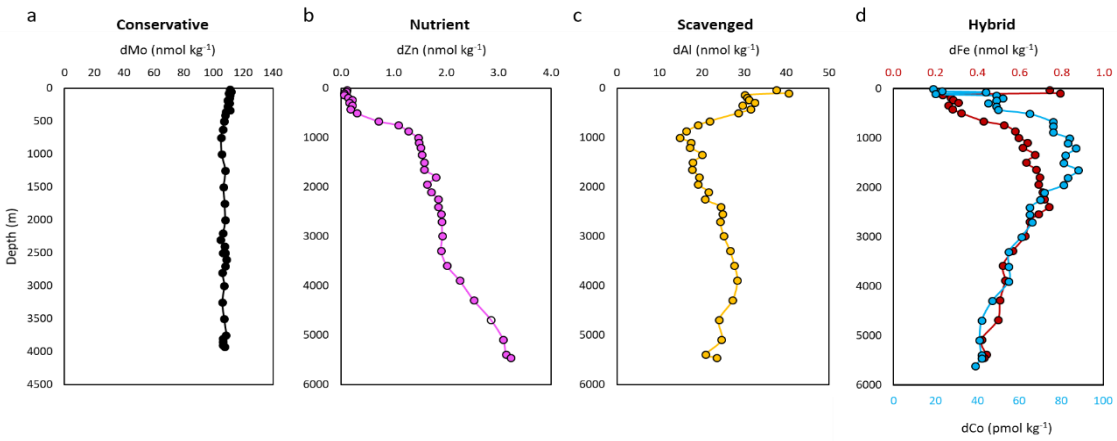

Figure 1.5 Example water column profiles representing the four types of oceanic trace metal distributions: (a) Conservative-type represented by dMo, (b) Nutrient-type by dZn, (c) scavenged-type by dAl and (d) hybrid-type represented by dFe and dCo. Data extracted from the GEOTRACES Intermediate Data Product 2017 (IDP17) (Schlitzer et al., 2018) for dAl, dFe and dZn, and Noble et al. (2017) for dCo, using Station USGT11-12 of transect GA03. Data for dMo was extracted from the GEOTRACES IDP17, using Station 15 of transect GP16.

From these distributions, it appears a paradox that Fe is the quantitatively most important trace metal for phytoplankton and the biochemical 'choice' for co-factors, when simultaneously it is highly susceptible to scavenging and hence easily removed from the dissolved phase in seawater. By the same logic, Zn is quantitatively less important despite being highly soluble and accumulating in the dissolved phase. The evolutionary origin of cyanobacteria, major contributors to photosynthetic marine primary production, was in the ancient anoxic (and later euxinic, i.e. anoxic and sulfidic) ocean about 2.5 Gyr ago. Under those environmental characteristics, Fe (and some other metals including Co but not Zn) were more soluble and more readily available than today, which likely influenced the evolution of cyanobacterial metal requirements (Dupont et al., 2006, 2010; Rickaby, 2015; Saito et al., 2003). The current paradigm is that it was energetically more favourable to adapt strategies to thrive under low Fe availability (e.g. via high affinity uptake systems such as siderophores; Hopkinson & Barbeau, 2012) than to re-design enzymes with metal co-factors other than Fe. In support of this, the metalloproteomes of more recently evolved eukaryotic phytoplankton have higher Zn contents (Dupont et al., 2010). Much of this Zn is involved in structural functions, such as in Zn fingers that are widespread eukaryotic protein subunits in eukaryotes folded around a central Zn ion and employed in DNA binding for gene regulation. In addition, some diatoms and haptophyte species were found to have Zn requirements that can partially be met by Co, but cyanobacteria have absolute Co requirements that cannot be met by Zn (Sunda and Huntsman, 1995). These hypothesised evolutionary trends also highlight the impact of microbes on metal cycles as the evolution of cyanobacteria triggered the oxygenation of the oceans, which in turn caused lower availability of Fe and Co (Saito et al., 2003).

In the following, the discussion is focussed on the biogeochemical cycling of those trace metals that are involved in the acquisition of P via requirements in the metalloenzyme alkaline phosphatase, namely Fe, Zn and Co.

1.4 Biogeochemistry and Distribution of Iron, Zinc and Cobalt

1.4.1 Iron

The involvement of Fe in many major cellular processes including photosynthesis, respiration, the N cycle and – as more recently suggested – DOP acquisition have initiated whole 'Iron Age' in the field of oceanography, initiated by John Martin's half-joking statement 'Give me half a tank of Fe and I give you the next Ice Age', based on the hypothesis that residual N and P in the Southern Ocean would be removed if the limiting nutrient Fe was added. This would lead to enhanced CO_2 fixation by phytoplankton, the removal of this greenhouse gas from the atmosphere and ultimately a drop in the Earth's temperature (formally in Martin, 1990). A range of large-scale Fe fertilisation experiments were conducted in the Southern Ocean (and equatorial Pacific) between 1980 and the early 2000s, which did stimulate the growth of phytoplankton and did evidence the global impact of Fe on marine primary production, although the hypothesised stimulated C sequestration to the deep ocean remained difficult to assess and subtle at best (de Baar et al., 2005; Bowie et al., 2001). The expansion of observational data and modelling efforts, has since revealed a more complex picture of the oceanic Fe cycle, especially with regards to different sources and physicochemical species.

1.4.1.1 Sources and Sinks

As the fourth most abundant element in the Earth's crust (Wedepohl, 1995), it is unsurprising that lithogenic sources exert a large control on the oceanic Fe inventory via atmospheric, sedimentary, riverine, hydrothermal or glacial pathways, with relative contributions differing strongly with depth, locale and time. Figure 1.6 provides an overview of the major external Fe sources to the ocean on global scale.

Atmospheric deposition of Fe-rich terrestrial material is the major source to the surface ocean, especially in the North Atlantic, which receives >40 % of the global dust flux and where strong dust-derived spatial and seasonal trends are imprinted in the surface ocean Fe concentrations (Jickells et al., 2005). The majority of this dust originates from the Saharan Desert and despite the low fractional Fe solubility of desert dust (~1 to 5 %) (Aguilar-Islas et al., 2010 and references therein; Baker et al., 2013), deposition events can result in dFe surface concentrations >1.0 nM, which are markedly higher than less dusty regions like the South Atlantic, Pacific or Southern Ocean (typically <0.25 nM

dFe) (e.g. Buck et al., 2018; Chever et al., 2010; Nishioka et al., 2001; Ussher et al., 2013). Although these basins receive some lithogenic dust from the surrounding continents, e.g. from Australia to the Southwest Pacific and from Patagonia to the Southern Ocean, the magnitude is low compared to the North Atlantic (Jickells et al., 2005). Anthropogenic dust, derived from the combustion of fossil fuels or biomass burning, is associated with lower deposition rates but an order-of-magnitude higher Fe solubility (~19 %) (Baker et al., 2013; Sedwick et al., 2007). Consequently, anthropogenic emissions may play an important role in setting the surface Fe inventory and fuelling primary production even in the North Atlantic (Conway et al., 2019), and do so certainly in the North(west) Pacific via emissions from East Asia, in the South Atlantic via emissions from South America, and in the Indian Ocean via emissions from India and South Africa, which are likely to increase with ongoing industrialisation in these regions (Ito & Shi, 2016; Luo et al., 2008)

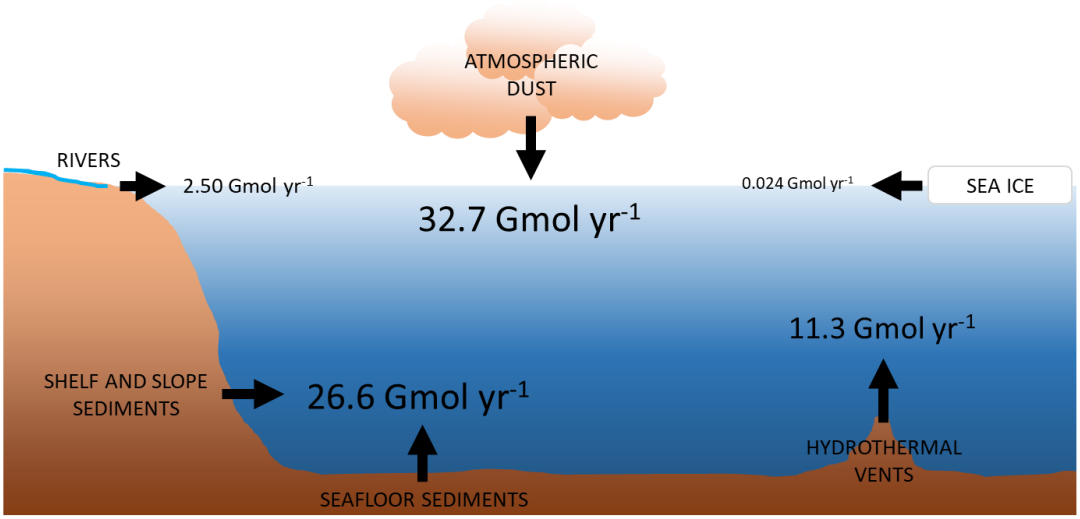

Figure 1.6 The major external Fe sources to the global ocean. Font size is roughly scaled to the magnitude of each source. The total external Fe flux is approximately 73 Gmol yr^{-1}. Values are those used in the PISCESv2 biogeochemical model (Aumont et al., 2015; and augmented as in Tagliabue et al., 2016). Note that all estimates currently carry large uncertainties.

While atmospheric dust deposition at the surface influences the entire water column inventory of dFe in the North Atlantic (Conway & John, 2014), the most important dFe sources on a global full-depth scale are seafloor- or shelf-derived sedimentary inputs and hydrothermal venting, which dominate the dFe inventory in ~74 % and ~23 % of the global ocean, respectively (Tagliabue et al., 2014). As dFe from these sources is not immediately accessible to phytoplankton in the sunlit ocean, it may be less relevant from the perspective of fuelling primary production and driving C export (Figure 1.7).

However, recent investigations showed that hydrothermally-derived Fe is stabilised in the dissolved phase and transported over large distances (>1,000 km) (Resing et al., 2015; Tagliabue & Resing, 2016), and can potentially be upwelled to support primary production in the sunlit ocean, especially where surface Fe concentrations are low such as in the Southern Ocean (Ardyna et al., 2019). Off-shelf transport of Fe-bearing sediments to the open ocean can occur via benthic nepheloid layers, but

its extent may be restricted by physical constraints, i.e. along-shelf currents (Birchill et al., 2019). Nevertheless, the impact of shelf-derived Fe on primary production on global scale is high as shelf seas contribute disproportionally to global marine primary production (Birchill, 2017).

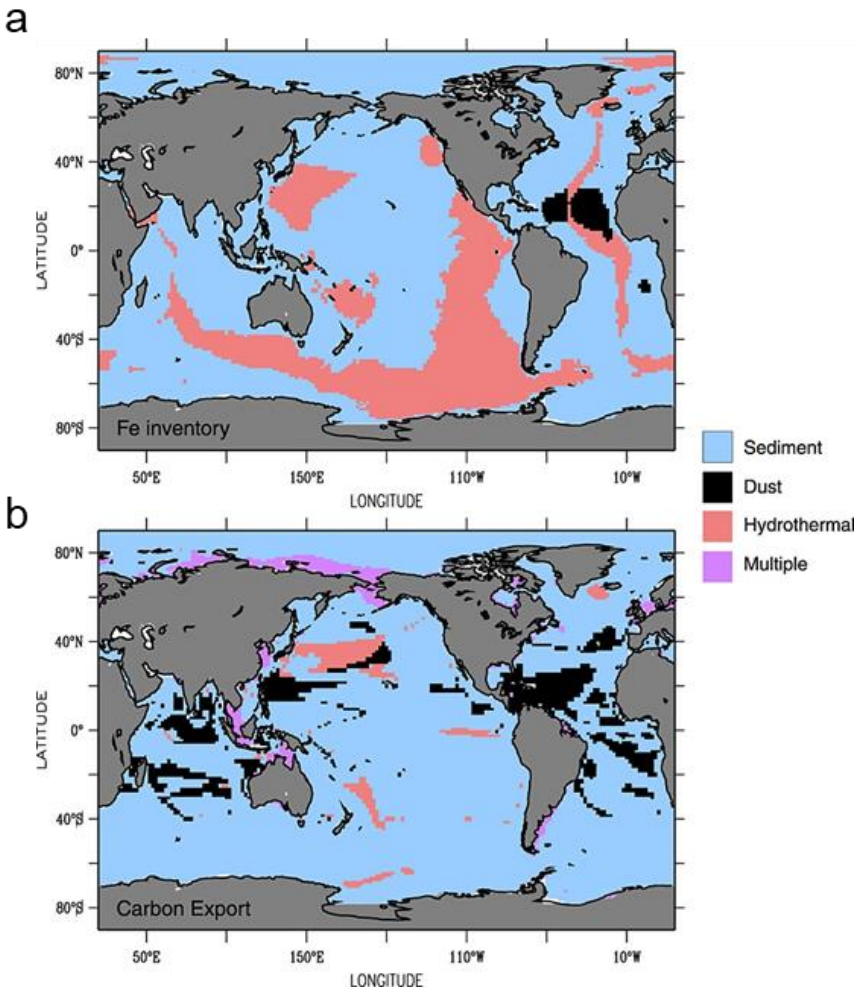

Figure 1.7 Maps of the global ocean showing which source of Fe dominates the anomalies in (a) the integrated water column dFe inventory and (b) the C export. Figure taken from Tagliabue et al. (2014).

The riverine influx of dFe to the ocean is comparably small (Figure 1.6), as a consequence of non-conservative behaviour of dFe during mixing of river and sea water. Its high particle reactivity leads to large flocculation losses (~90 % of the river endmember) before reaching the open ocean (Boyle et al., 1977; Sholkovitz, 1978). Nevertheless, the influence of the Amazon/Orinoco river plume in the (sub)tropical western Atlantic can lead to high dFe concentrations of >1.4 nM at salinities <36 (Kunde et al., 2019; Rijkenberg et al., 2014; Subramaniam et al., 2008), with local effects on biological activity and N_2 fixation (Subramaniam et al., 2008). In the shelf-surrounded, high-latitude Arctic Ocean, river discharge is a major source of dFe and is complemented by cryogenic sources such as melting sea ice (Klunder et al., 2012). The contribution of cryogenic sources of Fe at the high latitudes is strongly seasonal and arguably least studied, but Lannuzel et al. (2007; 2016) showed

that sea ice-derived Fe can contribute up to 70 % of the Fe flux to Antarctic surface waters during the melt season. Since the high latitudes are subjected to the most severe changes under global warming, they may alter the oceanic Fe inventory significantly in the future, for example as the result of increased melting (Dinniman et al., 2020; Hopwood et al., 2019).

All of the above sources are external supply mechanisms, on which internal sources are superimposed that are particularly important in the remote open ocean and the ocean interior. Internal sources derive from regeneration processes of Fe-bearing biogenic particulate matter that replenish dFe stocks via heterotrophic remineralisation, viral lysis or grazing activities (Boyd et al., 2017). As these processes dominate at depths below the euphotic zone, regenerated dFe depends on upward, cross-isopycnal mixing to fuel primary production through the 'ferrous wheel' (Kirchman, 1996). The *f*e ratio quantifies the contribution of externally supplied 'new' Fe over the sum of new plus internally supplied 'regenerated' Fe that sustains biological activity. Low *f*e ratios of <0.2 demonstrate the importance of internal replenishment in sub-Antarctic waters, whereas high *f*e ratios of >0.6 demonstrate the lesser role of such pathways in the subtropical North Atlantic, because the external, atmospherically-derived Fe supply is high here (Boyd et al., 2017)

In competition with any dFe input, be it new or regenerated, is the removal by scavenging, the major sink of dFe in the water column, aside from biological uptake in the surface. Scavenging results from the high particle reactivity of dFe and covers the adsorption of dFe onto surfaces of biogenic (e.g. dead cells) or lithogenic (e.g. dust) sinking particles as well as colloidal aggregation and removal by authigenic Fe-oxyhydroxide particle formation (more details in Section 1.4.1.2).

1.4.1.2 Physicochemical Speciation

The framework for studying trace metals was adapted from the study of macronutrients, in that the 'dissolved' phase (dFe <0.2 or <0.45 µm), which is separated from the particulate phase (pFe >0.2 or <0.45 µm), was of interest because it is presumably most bioavailable to phytoplankton growth and hence carries the highest biogeochemical relevance. However, the underlying mechanisms that drive the oceanic Fe cycle could not be reconciled from dFe as one bulk parameter, because it exists as a continuum of exchangeable physicochemical species, which behave differently in the oceanic environment (Figure 1.8). The chemical and biological reactivity of dFe in the ocean is a function of its speciation, which influences scavenging rates (i.e. residence times) and bioavailability directly. Current estimates for the oceanic residence time of dFe vary between ~5 and 500 years (Tagliabue et al., 2016) and its relative bioavailability ranges over three order of magnitude depending on the Fe-substrate (Lis et al., 2015a, 2015b). Additional differences in bioavailability result from processing and uptake capabilities, rooted in the physiology and genome of phytoplankton species. While a few physicochemical species of Fe (and other metals) are distinctly characterised in terms

of their chemical nature, operational definitions are applied to distinguish different fractions of the Fe continuum – in the physical dimension by filtration size and in the chemical dimension by organic complexation. Although Fe is most extensively studied, these distinctions equally apply to other trace metals in the ocean (see Sections 1.4.2 and 1.4.3).

Physical speciation. Only a small fraction (<1 %) of dFe is 'truly' dissolved and present as free Fe', due to the low solubility ferric Fe(III) (~0.1 nM at 25 °C, pH = 8, salinity = 35), which is the thermodynamically stable redox state and tends to form Fe(III) hydroxide pairs ($Fe(OH)_2^+$, $Fe(OH)_3$, $Fe(OH)_4^-$) in seawater (Millero et al., 1995). The majority of dFe does not pass through a filter of 0.02 µm pore size, hence separating the soluble (sFe <0.02 µm) and colloidal (0.02 µm <cFe <0.2 µm) sub-fractions of dFe. Strictly speaking, colloids are dispersed nanoparticles in solution that are clearly distinguished from the surrounding solution (i.e. the soluble phase) through a surficial interface, but they are of the same density as the solution and hence not subject to gravitational settling like actual particles (Wells, 2002). The high relative surface area of colloids goes hand in hand with their high adsorption potential and susceptibility to aggregation via 'Brownian Pumping'. This mechanism leads to particle formation and removal from the dissolved phase (Honeyman and Santschi, 1989). As such, Fe colloids – originating as nanoparticulate fragments of larger particles or as authigenic Fe-hydroxide particles – are the pivot between dissolved and particulate Fe, and so they have important implications for the residence time and bioavailability of dFe. It is important to re-iterate that under typical ocean conditions, Fe exists predominantly as ferric Fe(III), with a minor transient ferrous Fe(II) pool (Sedwick et al., 2015). Oxidation half-lives of Fe(II) to Fe(III) are a function of pH, salinity and temperature but are typically on the scales of minutes, which inhibits substantial accumulation of Fe(II) in the ocean (Millero et al., 1987). However, exceptions are found near hydrothermal sources, at reducing sediment interfaces and in oxygen minimum zones (OMZs), where depleted O_2 concentrations slow oxidation kinetics and/or the presence of H_2S stabilises Fe in its reduced form (Bennett et al., 2008; Lohan & Bruland, 2008; Moffett et al., 2007; Schlosser et al., 2018; Sedwick et al., 2015). In addition, the photochemical and biological reduction in the immediate surface ocean and the passive release of Fe(II) from organic matter through remineralisation, viral lysis or grazing can contribute to measurable Fe(II) concentrations (Sarthou et al., 2011; Sedwick et al., 2015). Although less thermodynamically stable, Fe(II) is highly soluble as free Fe^{2+} and hence, it is a component of the sFe fraction that is readily available for biological uptake (Lis et al., 2015b).

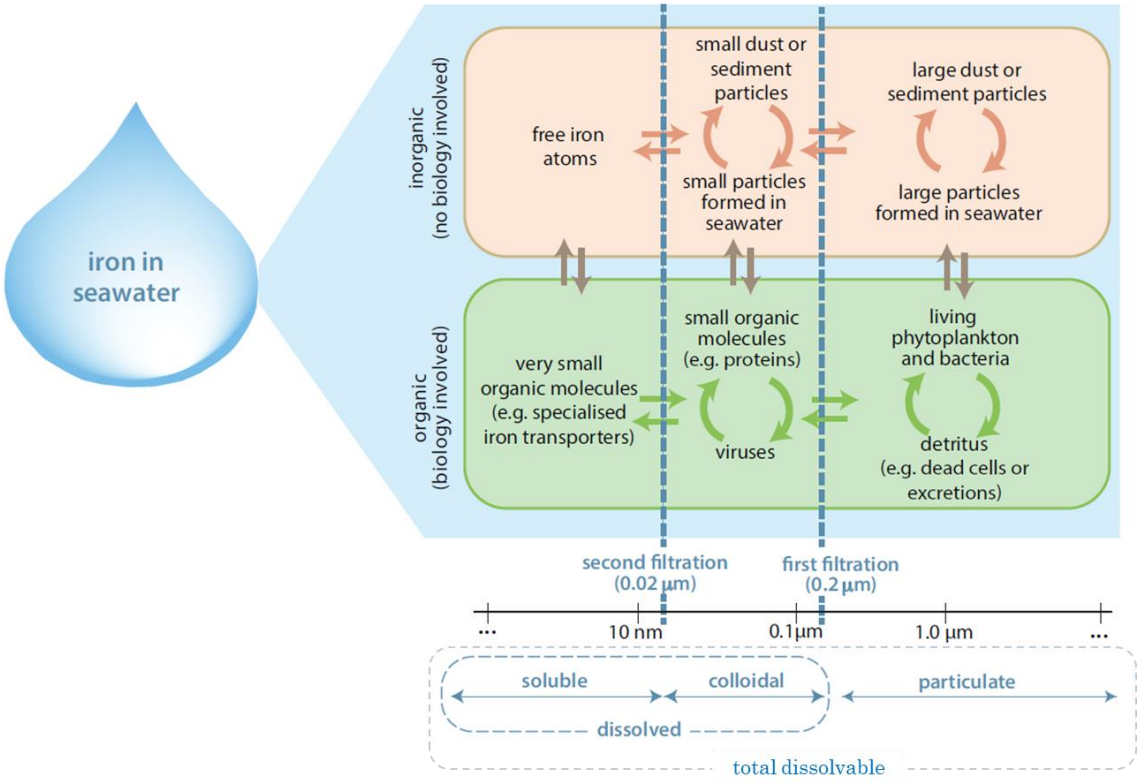

Figure 1.8 Schematic of the different species that Fe can take in seawater. Soluble (<0.02 µm), colloidal (0.02 to 0.2 µm) and particulate (>0.2 µm) pools are defined operationally by means of filtration. Iron species cycle across and within the different boundaries of this exchangeable continuum. The figure is adapted from Tagliabue et al. (2017).

Chemical speciation. The physical distinction between Fe colloids and truly dissolved (i.e. soluble) Fe stems from considerations of the *inorganic* composition of the sFe and cFe fractions, when in fact 99 % of dFe is thought to be complexed by *organic* compounds (Gledhill & Buck, 2012). Therefore, organic Fe-ligand complexes are important contributors to both cFe and sFe pools and explain how dFe concentrations in the ocean can exceed the solubility limit. Analogous to the operational distinction between physical dFe species by means of filtration, the distinction between different chemical dFe species is made operationally. It is based on the conditional stability constant ($K_{FeL,Felabile}$) of the Fe-binding ligand, where FeL is the organic Fe-ligand complex and Fe_{labile} denotes the inorganic labile Fe complexes that readily exchange with FeL. The values for $K_{FeL,Felabile}$ are obtained by voltammetric equilibrium experiments that are calibrated against a competitive well-characterised Fe-binding ligand and typically grouped into a strong ('L_1') ligand class with $\log K_{FeL,Felabile}$ >12) and a weaker ('L_2') ligand class with $\log K_{FeL,Felabile}$ <12). A drawback is the likely presence of inert inorganic complexes within the dFe continuum, such as refractory lithogenic nanoparticles that are not captured by this approach, so that concentrations and binding strengths of FeL in natural samples are potentially overestimated (Cullen et al., 2006; Gledhill & Buck, 2012). The weaker organic Fe-binding ligands, L_2, are diffuse and ubiquitous. They are typically derived externally from organic matter transported to the ocean from riverine, atmospheric, hydrothermal, sedimentary sources or internally from passive release through remineralisation, grazing and viral

lysis. They occur concomitant with dFe input and are typically in excess to dFe concentrations. Humic substances and exopolymeric saccharides are thought to be a major component of this weaker ligand pool. In contrast, the stronger ligand class, L_1, is most abundant in the surface ocean and the putative product of active excretion by heterotrophic bacteria and some phytoplankton to retain an accessible Fe stock. Amongst these are siderophores such as ferrioxamines and amphibactins that are low molecular weight ligands with very high Fe-affiinty ($\log K_{FeL,Felabile}$ ~12 to 15) (e.g. Boiteau et al., 2016; Bundy et al., 2018; Mawji et al., 2008). While providing a highly competitive uptake strategy for those organisms that are capable of utilising siderophore-bound Fe, weaker FeL complexes are more bioavailable across the entire phytoplankton community (Lis et al., 2015b). However, organic ligands are under constant competition amongst each other and with the inorganic counterparts for binding Fe. Furthermore, they undergo biologically or photochemically mediated degradation processes that can increase their bioavailability (Barbeau et al., 2001; Barbeau et al., 1996).

In summary, the speciation of dFe in seawater is described either from the physical perspective as the sum of dFe = sFe + cFe or from the chemical perspective as the sum of $dFe = Fe_{labile} + Fe_L + Fe_{inert}$. The exact mass balance of dFe that reconciles these two sums and characterises individual physicochemical species within each summand is an ongoing challenge that is complicated further by the constant exchange between the different species.

1.4.2 Zinc

As a nutrient-type element, the concentration range of dZn in the ocean is much larger than that of dFe. Surface concentrations are commonly depleted to <0.20 nM and increase to 2 to 3 nM in the deep Atlantic and up to 10 nM in the deep Pacific, as the result of regeneration from organic matter over time (Bruland et al., 1978). However, the simplistic concept of biological uptake and remineralisation that applies to macronutrients is insufficient to explain global dZn distributions in detail. The remineralisation length scale of dZn is decoupled from those of DIN and DIP. Instead, it aligns remarkably with silicate (SiO_4^{4-}) along the thermohaline circulation (Bruland et al., 1978). This correlation was initially hypothesised to be due to the uptake of Zn into the opal frustules of diatoms that are more refractory to remineralisation than the soft tissue that N and P largely reside in (Bruland, 1980). In fact, the Zn demand by diatoms in the Southern Ocean is with a Zn:P ratio of ~12 mmol mol^{-1} about one order of magnitude higher than for other phytoplankton groups and hence, diatoms do exert a major control on global Zn uptake (Twining et al., 2015; Twining & Baines, 2013). However, Ellwood & Hunter (2000) showed that <3 % Zn was associated with the opal frustules and that Zn is more tightly associated with the soft tissue and hence, with phosphate rather than silicate. The high Zn:P uptake ratios arise from the proportional Zn uptake relative to free Zn' concentrations (e.g. Sunda & Huntsman, 1992), which are high in the Southern Ocean due to upwelling of circumpolar deep water, in which dZn is not organically complexed (Vance et al., 2017).

This mechanism was proposed to reconcile the similar distribution of Zn with Si through the global ocean, as the extraordinarily high Zn uptake rates decouple Zn from P and link it to Si instead, which is rapidly stripped from the diatom-dominated surface waters of the Southern Ocean (Vance et al., 2017). Water masses that form in the Southern Ocean ventilate much of global ocean and so, the Zn:P and Si:P signatures are exported by circulation (Vance et al., 2017). However, others argue that reversible scavenging following the regeneration of Zn from organic matter along the thermohaline circulation is necessary to explain global Zn (and Zn isotope) profiles fully, despite only ≤0.5 % of total Zn being adsorbed to particle surfaces (John & Conway, 2014; Weber et al., 2018). It is also becoming more recognised that hydrothermalism can supply significant amounts of Zn to the global inventory (Roshan et al., 2016; Wyatt et al. in preparation).

No solubility constraints exist for the free and presumably bioavailable Zn^{2+} in seawater, but nevertheless >95 % of dZn is complexed by organic ligands, reducing the free Zn' pool to picomolar concentrations (Bruland, 1989; Ellwood & van den Berg, 2000). An advantage for active excretion of specific Zn-binding ligands to retain a bioavailable Zn resource is therefore not obvious, but ligand production *was* observed, both in response to artificial Zn enrichments and in response to Zn starvation, potentially as detoxification or retention mechanisms, respectively (Lohan et al., 2005b). In the natural water column, Zn-binding ligands are weaker (logK ~10 to 11) than those of Fe and more uniformly distributed, which hint at passively produced degradation products during remineralisation of organic matter (Ellwood & van den Berg, 2000).

The cellular Zn content of marine phytoplankton is lower than that of Fe (Figure 1.4) (Twining & Baines, 2013), but more Zn- (>300) than Fe-containing proteins have been identified to date that are involved in a range of cellular functions (Vallee & Auld, 1990). Two key Zn-containing enzymes are carbonic anhydrase, which is involved in C fixation as it facilitates the conversion of bicarbonate (HCO_3^-) to CO_2, and alkaline phosphatase, which is involved in DOP acquisition as it facilitates the cleavage of phosphate from the ester moieties of phosphoesters (Figure 1.2). At the expense of reduced growth rates, Co can substitute for cellular Zn requirements, such as at the active site of carbonic anhydrase in a range of diatom species (e.g. Kellogg et al., 2020; Yee & Morel, 1996). In the coccolithophore *Emiliana huxleyi*, Zn and Co were shown to be equally efficient, with substitution by Cd sustaining yet lowering growth rates (Sunda & Huntsman, 1995; Xu et al., 2007). Theoretical extrapolation of minimum requirements (~1 pM) in these cultures to Zn availability in the global surface ocean suggests Zn limitation of phytoplankton growth to occur, where free Zn' concentrations are strongly depleted, such as in the subarctic North Pacific (~2 pM; Lohan et al., 2005b) or subantarctic South Pacific (~0.3 pM; Ellwood, 2004). However, Zn limitation during field-based incubations in these regions was absent (Ellwood, 2004) or subtle at most (Crawford et al., 2003; Lohan et al., 2005b). This was explained by potential Co/Cd substitution mechanisms, lower Zn requirements than those expected from culture work and the bioavailability of organic Zn-

complexes in addition to free Zn' that counteracts Zn to become limiting. Nevertheless, Zn was shown to have an indirect effect on phytoplankton success in the field, by which Zn enrichments stimulated alkaline phosphatase activity (APA) in the North Atlantic (Mahaffey et al., 2014). Therefore, it is difficult to constrain Zn limitation for global primary production. In addition, cyanobacteria, who have smaller or no absolute Zn requirements, are in fact susceptible to Zn toxicity via competitive Zn-binding at metal binding sites in enzymes (Hawco & Saito, 2018).

1.4.3 Cobalt

The oceanic dCo inventory is the smallest of all trace metal micronutrients with concentrations ranging from <5 pM in the surface to maximum values of >100 pM in OMZs. Its redox chemistry is the driving factor behind this scarcity, as the soluble Co^{2+} is rapidly oxidised to Co^{3+} by Mn-oxidising bacteria and co-precipitated with Mn-oxides (Moffett & Ho, 1996), resulting in heavily scavenged depth profiles and a lack of accumulation along the thermohaline circulation (Figure 1.5). The cellular demand of Co in phytoplankton is one to two orders of magnitude lower than those of Fe and Zn, but it is simultaneously one of the most variable ones (Figure 1.4). In fact, some more recently evolved eukaryotic phytoplankton species do not have the absolute Co requirement that cyanobacteria have, and instead, Co functions solely as a substitute in carbonic anhydrase under Zn scarcity (Sunda & Huntsman, 1995). In addition, Co-independent isoforms of methionine synthase have evolved and eukaryotes often lack the pathway for *de novo* cobalamin synthesis, an abundant major Co-containing co-factor (Helliwell et al., 2016). In contrast, cyanobacteria, which evolved under lower O_2 and higher soluble Co^{2+} concentrations, do rely on Co for use in methionine synthase, ribonucleotide reductase and do synthesise cobalamin (vitamin B_{12}) *de novo*. In fact, the inhibition of Co assimilation by *Prochlorococcus* occurs under high ambient Zn, as the result of competition at enzymatic binding sites (Hawco and Saito, 2018). Evidence for an efficient Co-containing alkaline phosphatase is hitherto only indirect (Jakuba et al., 2008; Saito et al., 2017; Shelley et al., 2012).

Similar to dZn, dFe and dissolved transition metals in general, dCo is complexed to ~90% by organic ligands in seawater, the majority of which (up to 100 % in surface waters) are extraordinarily strong and specific Co^{3+}-chelators with logK >16.8 that are not readily exchangeable with competitive complexing agents (Saito et al., 2002; 2005). This ligand-bound Co probably comprises cobalamin complexes and its derivatives, although the potential for the production of 'cobalophore'-type ligands by cyanobacteria has been invoked, in analogue to siderophores that facilitate Fe acquisition under Fe scarcity (Morel, 2003; Saito et al., 2005).

Lowest concentrations of dCo occur at the surface and throughout the euphotic zone with typical values <5pM. Although solubilisation of Co from dust particles is higher (~9 % solubility) than that of Fe (4%), its lower crustal concentrations and biological uptake result in low dCo signals from dust

deposition at the surface (Shelley et al., 2018). In the high-dust North Atlantic, where a discernible dust signature would be expected, its absence highlights the strong biological control on surface dCo, which is attributed to its utilisation in alkaline phosphatases and in N_2 fixation by *Trichodesmium* populations that are abundant in the North Atlantic (Shelley et al., 2012; Shelley et al., 2017). Below the euphotic zone, dCo concentrations reach maxima in OMZs around the world. This is the result of advection of shelf-derived Co^{2+} (either from reductive dissolution of sediments or from the remineralisation of organic matter) that is stabilised under lower O_2 concentrations, as these slow Co^{3+} oxidation kinetics and associated scavenging (Hawco et al., 2016; Tagliabue et al., 2018). This mechanism is the major source of Co to the ocean globally and hence, O_2 exerts a key control of dCo distributions. Under global change, OMZs are predicted to expand, with the potential for larger stabilised dCo budgets to be sustained in the ocean. This is important because other external sources that are relevant to Fe (compare Figure 1.6) are weak for Co. Hydrothermally-derived Co is comparably inefficient and long-range transport is absent, as Co is readily scavenged onto Fe- and Mn-oxides close to the vent sites (Hawco et al., 2016; Noble et al., 2017). Similarly, riverine input is the weakest Co source on global scale, because only small fractions of Co overcome scavenging in the early river plume (Tagliabue et al., 2018).

All of the three trace metal micronutrients Fe, Zn and Co have been hypothesised to play a role in DOP acquisition as co-factors of alkaline phosphatases in marine phytoplankton. Despite this common biological role, the above sections highlight the strong differences in their biogeochemistry with regards to their sources, sinks and internal cycling and how these have changed over geological time scales. Under global change scenarios, the biogeochemistry of Fe, Zn and Co (and of other bio-relevant trace metals) will be impacted in different ways (e.g. OMZ expansion may aid dCo stabilisation, while ocean acidification may increase to Fe solubility), which will impact metal-microbe interactions in the ocean.

1.5 The Subtropical North Atlantic

As evident in the distribution of chlorophyll-*a* (Chl-*a*), as the phytoplankton biomass proxy in Figure 1.9a, the subtropical permanently stratified, warm, oligotrophic gyres of the Atlantic, Pacific and Indian Oceans count towards some of the least productive regions in the global ocean and are often referred to as the ‘ocean deserts’. However, their sheer spatial extent amounts to 30 % of the global marine primary production (Longhurst et al., 1995) and hence, they are key to the global C cycle. The phytoplankton community of the subtropical oligotrophic gyres is dominated by cyanobacteria, especially *Prochlorococcus* (~10^4 to 10^5 cells ml^{-1}) and *Synechococcus* (~10^4 cells ml^{-1}). Cyanobacteria are very small prokaryotic phytoplankton (<2 µm in diameter), compared to protists like diatoms, dinoflagellates and haptophytes that dominate in the macronutrient-rich upwelling

regimes and higher latitudes (Flombaum et al., 2013; Pierella Karlusich et al., 2020). Their small size results in high surface area-to-volume ratios, which allow the efficient nutrient assimilation under nutrient scarcity by populating the cell surface with comparably large amounts of nutrient transporters. Together with their streamlined genome and targeted nutrient uptake strategies, it explains some of the competitiveness and hence the ecological success of cyanobacterial species in these nutrient deplete environments (Partensky and Garczarek, 2010).

Generally, primary production by phytoplankton in the subtropical gyres is primarily limited by N (see Section 1.1; Moore et al., 2013). This is the case too for the subtropical North Atlantic, but with the important distinction being that large Fe-rich dust deposition creates a niche for biological N_2 fixation, which utilises large resources of Fe and phosphate to provide a bioavailable source of DIN. Therefore, the subtropical North Atlantic exhibits ultraoligotrophic DIP levels (i.e. <10 nM) (Figure 1.9) and phytoplankton are more readily P stressed and secondarily P limited compared to other subtropical gyres (Martiny et al., 2019; Moore et al., 2013). An important enzyme that can act on a dominant alternative P source (phosphoesters) is alkaline phosphatase, which is highly active in the North Atlantic (Mahaffey et al., 2014) and demonstrates a physiological P stress response, namely DOP acquisition, against the background of the prevailing N limitation. Alkaline phosphatase has a variety of forms with different trace metal requirements for Fe, Zn or Co. Of these, Co and then Zn are most deplete, while Fe is comparably higher in the subtropical North Atlantic than in any other subtropical gyre, but it is subject to strong gradients in its physicochemical speciation that affect its bioavailability. The stress that is exerted on phytoplankton growth by the trace metal requirements of alkaline phosphatase is not well understood, but the subtropical North Atlantic forms an ideal study site, because of its unique biogeochemical setting related to the high Fe inputs and ultraoligotrophic DIP levels.

To add more detail, compared with other oligotrophic gyres, the subtropical North Atlantic receives a large amount of Fe-rich dust, namely >40 % of the total global dust flux to the ocean, which originates predominantly from the Bodélé depression in the Saharan desert (Jickells et al., 2005) (Figure 1.9b). Evidence for Saharan influence has been determined as far as the American continent, where it can fertilise even the Amazonian rainforest (Yu et al., 2015). Strong spatial and seasonal gradients of dust-derived Fe are imprinted in the surface ocean across the basin, which are related to shifts in wind patterns between winter and summer and to the differential gravitational settling of larger versus smaller dust particles (Schepanski et al., 2009; Tsamalis et al., 2013). The latter results in larger particles being deposited closer to the continent, while smaller particles are transported further and therefore, are also subjected to more cloud processing, which affects the solubility of Fe.

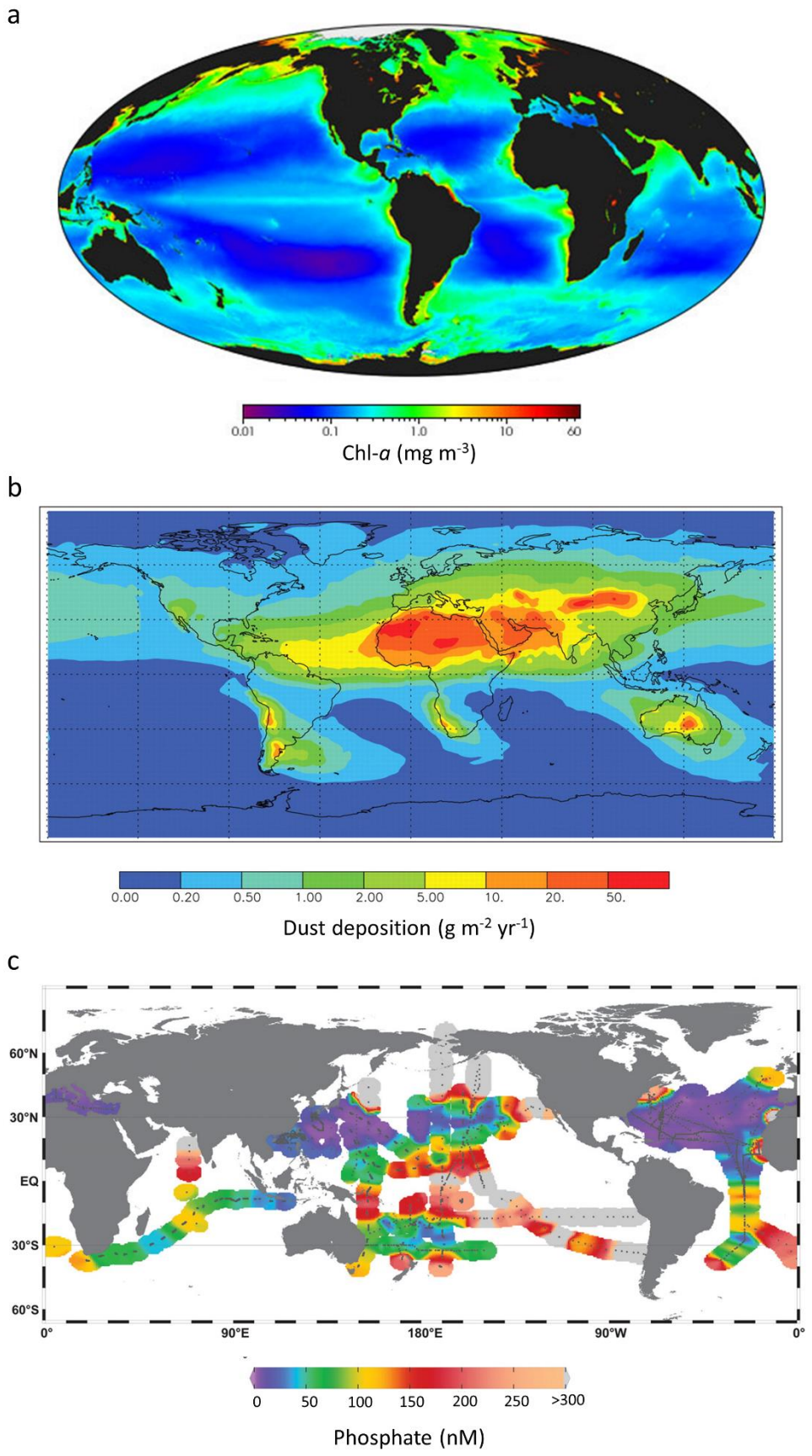

Figure 1.9 Global distributions of (a) Chl-*a*, (b) annual dust deposition and (c) phosphate in the ocean. The figure was combined from figures from https://oceancolor.gsfc.nasa.gov/, Jickells et al. (2005) and Martiny et al. (2019), respectively, with colour bars relabelled for consistent layout.

Furthermore, the seasonal shift of the Intertropical Convergence Zone (ITCZ), an atmospheric low pressure belt that results in heavy precipitation, controls regions of wet and dry dust deposition, with wet deposition being efficient in delivering Fe. This is primarily due to the low pH of rainwater, which readily solubilises Fe from dust particles (Schlosser et al., 2014). The Bermuda Atlantic Time-series Study (BATS) at 31.7 °N, 64.2 °W resolved the strong seasonality of dust-derived surface dFe concentrations in the western subtropical North Atlantic, with peak Fe delivery in the summer months that results in strong dFe enrichments of >1.0 nM (Fishwick et al., 2014; Sedwick et al., 2020), which are in stark contrast to low-dust regions such as the subtropical South Pacific gyre where Fe is <0.2 nM (Ellwood et al., 2018). Aside from the Fe concentrations, its physicochemical speciation exhibits marked changes across dust deposition regimes. This is most prominent in that cFe, the larger size fraction of the dFe pool, is primarily introduced (up to ~90 % of dFe) from aerosols (Fishwick et al., 2014). Colloidal Fe is considered less bioavailable than sFe (Chen and Wang, 2001). As the rates (probably on the scale of days; Fishwick et al., 2014; Hurst and Bruland, 2007) and mechanisms (e.g. ligand-mediated versus nanoparticle dissolution/aggregation; Fitzsimmons et al., 2015a) of exchange between cFe to sFe are not well resolved and cFe is rapidly attenuated between the surface and the deep chlorophyll-*a* maximum (DCM), the (size-fractionated) speciation of Fe is complementary to its concentration in dictating the overall bioavailability of dFe.

Nevertheless, the extraordinary atmospheric Fe source to the North Atlantic creates a niche for biological N_2 fixation by diazotrophs that provide bioavailable form of DIN (as NH_4^+) to the otherwise DIN-depleted gyre (Figure 1.9c). Enzymes involved in biological N_2 fixation have large Fe demands (tens of Fe atoms per enzyme) (Kustka et al., 2003), and hence diazotrophy is unfavourable in other, less-Fe rich gyres that are low in DIN. Indeed, the large-scale patterns of N_2 fixation track dust-derived Fe distributions with a marked decrease of N_2 fixation from the high-Fe North Atlantic into the low-Fe South Atlantic (Moore et al., 2009). In addition, *Trichodesmium* – an abundant and well-characterised diazotroph – possesses the ability to utilise particle-bound Fe directly by selectively capturing, concentrating and solubilising pFe within its colonies (Basu et al., 2019; Rubin et al., 2011). This widens the ecological niche even further, as other organisms rely on the smaller dFe (or even sFe) pool for assimilation. As atmospheric N_2 is converted by diazotrophs into bioavailable NH_4^+, the prevailing N stress in the North Atlantic can partially be alleviated and can subsequently drive the system into P stress (Moore et al., 2008; Wu et al., 2000). While non-diazotrophic phytoplankton are serially limited by N and P, *Trichodesmium* experiences P and Fe co-limitation as the norm in the North Atlantic (Held et al., 2020).

Since an analogous mechanism to N_2 fixation does not exist for the replenishment of DIP stocks (see Section 1.2.2), there exists an important role for DOP utilisation by phytoplankton in the subtropical North Atlantic to meet cellular P demands. As a major labile fraction of the abundant DOP pool (~80 % of total dissolved P; e.g. Reynolds et al., 2014), phosphoesters are hydrolysed via alkaline

phosphatases, whose activity in the subtropical North Atlantic is very high with rates of 20 to 60 nM P d^{-1} (at DIP <30 nM), compared to the Pacific with typically <20 nM P d^{-1} (Mahaffey et al., 2014 and references therein). However, based on the well-studied enzyme homologues of *E. Coli* alkaline phosphatases (Coleman, 1992), indirect field evidence (Browning et al., 2017; Mahaffey et al., 2014; Noble et al., 2017; Saito et al., 2017), metal-culture work (Shaked et al., 2006), and 'omics studies (Barnett et al., 2014; Cox and Saito, 2013; Frischkorn et al., 2019), phytoplankton alkaline phosphatases are metalloenzymes hypothesised to require Ca and Fe co-factors in the PhoX-type enzyme (Yong et al., 2014) and Zn or substitute Co in the PhoA-type enzyme (Coleman, 1992; Gong et al., 2005). The exact determination of metal co-factors in marine alkaline phosphatases, cambialistic capabilities, regulation and preferences amongst species for the different types is still pending.

The biogeochemistry of the subtropical North Atlantic is often compared and contrasted to that of the subtropical South Atlantic, with its markedly lower Fe-rich dust influx (Jickells et al., 2005; Ussher et al., 2013) and slightly higher DIP inventories (Mather et al., 2008). As outlined above, however, gradients along longitudinal transects are key to understanding the role and requirements of alkaline phosphatases, due to the strong east-to-west dust-driven gradients in Fe concentrations, ranging from <0.2 nM to >1.5 nM dFe that are of a similar range as the gradients between the North and South Atlantic subtropical gyres (Kunde et al., 2019; Sedwick et al., 2020; Sedwick et al., 2005). Similarly, DIP concentrations differ markedly between the ultraoligotrophic Sargasso Sea in the west with <10 nM DIP and the higher, yet oligotrophic eastern basin with ~10 to 60 nM DIP, concurrent with trends in DOP concentrations (Sargasso Sea: <100 nM; eastern gyre: 100 to 300 nM) (Lomas et al., 2010; Martiny et al., 2019; Reynolds et al., 2014). The systematic lack of knowledge on longitudinal biogeochemical gradients may underestimate their global biogeochemical implications. This is particularly critical with regards to the role of alkaline phosphatases to primary production: future alterations of biogeochemical cycles in the ocean are currently being debated that arise both from the increased stratification by warming, which reduces upward mixing of nutrients and potentially extends the diazotrophic niche, and from the increased influx of anthropogenic N relative to P from agricultural fertilisers and industrial combustion (Duce et al., 2008; Jickells et al., 2017; Wrightson & Tagliabue, 2020). Both pathways would further disproportionate the skewed N:P budget of the subtropical North Atlantic, exacerbate P stress and therefore, may increase the importance for DOP acquisition via alkaline phosphatases in the future.

1.6 Thesis Aims and Objectives

As evidenced in this chapter, the biogeochemical cycling of macronutrients and trace metal micronutrients in the ocean – more specifically their distribution and speciation – play a major role

for primary production and ultimately for the efficiency of the biological carbon pump on climate-relevant scales. The interplay between macronutrients and trace metals, rooted in the requirement of the latter in metalloproteins involved in vital cellular functions is a rapidly accelerating theme in marine biogeochemical research that is aided by advances in metallomics methodology. However, the extent of macro- and micronutrient coupling and its implications are yet to be resolved. The subtropical North Atlantic with its severe P stress and gradients of metal availability presents itself as a natural laboratory to probe one aspect of coupled macro-/micronutrient dynamics; namely the limitation of DOP acquisition by Fe, Zn and/or Co via the metalloenzyme alkaline phosphatase. Therefore, a suite of geochemical trace metal measurements were conducted in this region, built upon by experimental bioassays, and finally complemented by cellular-level proteomics. The overarching aim of this dissertation is to elucidate on the biogeochemical coupling of macronutrient P and micronutrients Fe, Zn and Co across strong gradients in their distributions across the subtropical North Atlantic gyre. To achieve this, the following objectives were addressed:

Objective 1: To determine the natural distribution of Fe in high resolution full-depth water column profiles in the subtropical North Atlantic gyre along a west-to-east gradient and to resolve its physical speciation into sFe, dFe and TDFe to gain insight into the biogeochemical cycling of Fe (Chapter 3).

Objective 2: To track experimentally, the kinetics (minutes-to-days) exchange of Fe between different size fractions in subtropical North Atlantic surface waters across gradients of ambient Fe concentrations (Chapter 4).

Objective 3: To determine experimentally using quantitative proteomics from bioassays, the impact of Fe, Zn and Co additions on alkaline phosphatase production in subtropical North Atlantic waters across strong gradients in ambient metal availability, P stocks and phytoplankton community (Chapter 5).

Chapter 2 Methodology

2.1 Study Area and Field Work

Trace metal-clean field work at sea formed the basis of addressing the aims and objectives of this thesis. All samples originated from a single research cruise, JC150, onboard the *RRS James Cook* that crossed the subtropical North Atlantic gyre between Guadeloupe and Tenerife in summer 2017 (June 26th to August 12th). Research activities were carried out underway along the transect and at seven occupied stations (Figure 2.1). The following subsections provide details on sampling the natural environment, i.e. by high-resolution surface sampling and water column profiling (Section 2.1.2), and on the experimental work (Section 2.1.3). In line with the unique biogeochemistry of the subtropical North Atlantic as outlined above (Section 1.5), strong longitudinal gradients in the distributions of trace metals, macronutrients and other relevant biogeochemical parameters were expected. Many of the sample measurements were made near real-time at sea and were key to the experimental design at each station. Therefore, a brief overview of the biogeochemical gradients observed during JC150 is provided as part of the methodology in Section 2.1.5, ahead of their in-depth analysis in the subsequent chapters. Analysis of auxiliary samples that was key to the results presented in this thesis, but that was *not* conducted by the author are briefly described in Section 2.1.4, while the main sample analyses, i.e. those conducted by the thesis author, are described in detail in Sections 2.2 and 2.3.

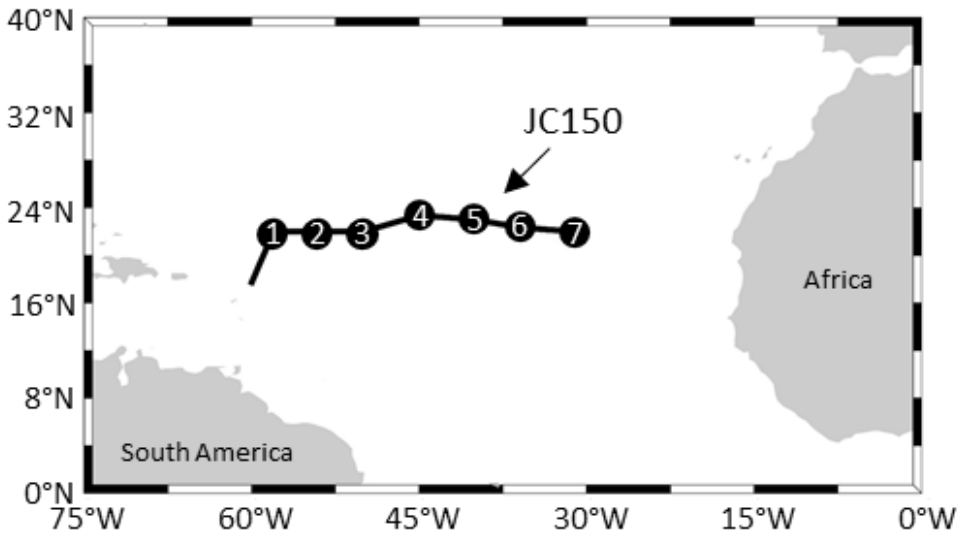

Figure 2.1 Map of the North Atlantic showing the track (black line) and occupied stations (black dots with numbers) of research cruise JC150.

Table 2.1 provides an overview of the research activities during JC150 and their relevance to the chapters of this thesis. At all Stations 1 to 7, full-depth water column profiles and high-resolution surface sampling enabled analysis of the basin-wide distribution of Fe and its physical speciation (TDFe, dFe, sFe). This formed the core of Chapter 3. At a subset of stations, namely Stations 3, 4 and 7, low abundance Fe isotope tracing experiments were conducted, in which seawater from 40 m depth was incubated with a spike enriched in ^{57}Fe to track the short-term exchange between Fe size fractions. These experiments were complemented by small volume (2 L) Fe bioassays, in which multiple incremental additions of Fe probed for Fe limitation of phytoplankton growth at all seven stations. Chapter 4 deals with the low abundance isotope experiments and small volume Fe bioassays. Lastly, large volume (24 L) bioassays carried out at Stations 2, 3, 4 and 7 – conducted in a similar fashion to the small volume bioassays but with fewer nutrient amendments per station – probed for the effects of metal additions (Fe, Zn, Co) on phytoplankton alkaline phosphatase expression by means of quantitative proteomics. This is subject of Chapter 5.

Table 2.1 Research activities at each station during JC150, indicating the sample origin and main sample types that are relevant to the chapters of this thesis.

	Sample origin (and key sample type)	**Station 1**	**Station 2**	**Station 3**	**Station 4**	**Station 5**	**Station 6**	**Station 7**	**Relevant chapter**
Ambient	Surface (TDFe, dFe)	×	×	×	×	×	×	×	3
	Water column (TDFe, dFe, sFe)	×	×	×	×	×	×	×	3
Experimental	Low abundance fe isotope experiments (TDFe, dFe, sFe)	-	-	×	×	-	-	×	4
	Small-volume Fe bioassays (Chl-*a*)	×	×	×	×	×	×	×	4
	Large-volume bioassays (Proteins)	-	×	×	×	-	-	×	5

2.1.1 Pre-Cruise Trace Metal Clean Procedures

While research into oceanic trace metal cycles contributes significantly to the understanding of global marine biogeochemistry, the challenges associated with the sampling and analysis of trace metals are equally as significant and well beyond those of major elements. This is due to the vanishingly low, typically nano- to picomolar concentrations of trace metals in seawater, hence the name. Superimposed on this are ubiquitous contamination risks, originating from sampling onboard a vessel, where various metals are present. To minimise these risks and preserve the naturally low concentrations, ultra-clean protocols have been developed since the earliest studies of trace metals

in the ocean (e.g. Bruland et al., 1979), and have been standardised across the community, especially through more recent efforts by large international programs like GEOTRACES (https://www.geotraces.org/methods-cookbook/). Key to collecting clean trace metal samples are thorough cleaning procedures of the used materials prior to any sample collection.

Trace metal seawater samples were collected into 60 or 120 ml low-density polyethylene (LDPE) bottles (Nalgene), while incubation containers for experimental work were 2 L or 24 L polycarbonate (PC) bottles (Nalgene), which are translucent. Any additional bottles involved in sample analysis (Section 2.2) were made of LDPE (typically 1 or 2 L; Nalgene). All of these bottles were prepared in a three-step cleaning procedure as detailed in Table 2.2. An amended procedure (Table 2.3) was applied for polypropylene (PP) collection vials (Wheaton), which were involved in the trace metal extraction and pre-concentration procedure of Section 2.2.2. During the cleaning process (and later on during the sample collection, handling and analysis), polyethylene (PE) gloves (QRP QualaSheerXC) and PE overalls (DuPont Tyvek), designated polyurethane shoes (Birkenstock) and polypropylene (PP) bouffant caps (Pal International) were worn.

2.1.2 Surface and Water Column Sampling

Surface sampling. Seawater samples were collected from the surface ocean at a resolution of approximately ~0.23 °, using a towed 'Fish' sampler that was deployed off the starboard side of the vessel at <5 m depth (approximately 2 to 3 m). The towed Fish was connected to pre-cleaned (as in Table 2.2) PVC hosing, through which seawater was pumped into a class-100 clean air van onboard using a Teflon diaphragm pump (A-15, Almatec). The seawater was pumped continuously during steaming, with a T-piece inside the clean van allowing the sampling of seawater or discarding it back into the ocean. When turned into sampling mode, the T-piece and attached tubing were flushed for a few minutes prior to sample collection.

Water column sampling. Seawater samples from the water column were collected using a titanium (Ti)-rosette that was fitted with 24 × 10 L trace metal-clean Teflon-coated Ocean Test Equipment (OTE) bottles with external springs, and a conductivity, temperature and depth (CTD) profiler (Seabird Scientific), deployed to full-depth on a conducting Kevlar-coated wire. The OTE bottles were stored prior to and in between CTD casts inside a class-100 clean air van. For protection against contamination, their taps were covered PE gloves (QRP QualaSheerXC), except just before and after deployment. Upon recovery, the OTE bottles were transported back into the class-100 clean air van, their outside rinsed with UHP water and wiped dry. The bottles were pressurized (0.7 bar) with compressed air filtered in-line through a 0.2 µm PTFE filter capsule (Millex-FG 50, Millipore).

Table 2.2 Cleaning procedure for LDPE and PC plastic ware, identical to that used in Birchill (2017) and Wyatt (2014).

Step	Procedure
Stage 1 – In general laboratory	• Rinse (inside and outside) three times with distilled water • Immerse and cap in 3 M HCl (Fisher, reagent grade) for one week • Rinse three times with distilled water • Rinse three times with UHP water
Stage 2 – In class-100 laboratory	• Immerse and cap in 0.5 M HCl (Fisher, trace metal grade) for one week • Rinse three times with UHP water
Stage 3 – Storage	• Fill with UHP water, cap and acidify to 0.024 M HCl (Romil, SpA) • Double bag (PE bags) and store in clean plastic container

Table 2.3 Cleaning procedure for PP vials involved in off-line metal extraction and pre-concentration (see Section 2.2.2).

Step	Procedure
Stage 1 – In class-100 laboratory	• Rinse (inside and outside) three times with distilled water • Immerse vials and lids (separately) in 3 % Decon-90 solution for one week • Rinse three times with UHP water
Stage 2 – In class-100 laboratory	• Immerse as before in 20 % (2.4 M) HCl (Fisher, trace metal grade) • Rinse three times with UHP water
Stage 3 – In class-100 laboratory	• Immerse as before in 20 % (3.2 M) HNO_3 (Fisher, trace metal grade) • Rinse three times with UHP water
Stage 4 – Storage	• Place vials and lids separately under laminar flow hood until completely dry (~48 h) • Cap vials, double bag (PE bags) and store in class-100 laboratory

The subsampling process (into 60 or 125 ml LDPE; Nalgene) for trace metal seawater samples, involved removing the 0.024 M HCl content and pre-conditioning the bottles three times with ambient unfiltered (for TDFe samples) or filtered (for dFe samples) seawater. This included thorough rinsing of the lid and screw necks. Subsamples for dFe were collected after in-line filtration through 0.2 µm acetate membrane cartridge filters or 0.8/0.2 µm polyethersulfone membrane cartridge filters (both Sartobran 300, Sartorius) from OTE or the towed Fish, respectively. The filter units were stored double-bagged at 4 °C between sampling sessions and re-used for ~48 h. Subsamples for sFe were collected from a separate dFe subsample that went through an additional filtration step inside a laminar flow hood through 0.02 µm syringe filters (Anotop, Whatman) at 1 ml min^{-1}. The filtration manifold consisted of polytetrafluoroethylene (PTFE) manifold tubing and polyvinyl chloride (PVC) peristaltic pump tubing, cleaned daily with weak 1 M HCl (SpA, Romil) and conditioned prior to use with low Fe seawater (Ussher et al., 2010; Wu et al., 2001). A new filter was used for each sFe sample. Samples for TDFe were collected unfiltered. All trace metal seawater samples were acidified to pH 1.7 (0.024 M) by addition of 12 M HCl (Romil, UpA) under a laminar flow hood inside the clean van on the same day as collection (Lohan et al., 2006).

2.1.3 Experimental Set-up and Sampling

At all or a subset of stations, three sets of trace metal clean bioassays were conducted (Figure 2.1), 1) the 'low abundance Fe isotope experiments' that aimed to trace the partitioning of an initially sFe addition into different Fe size fractions at high temporal resolution using the low abundance ^{57}Fe as tracer, 2) the 'small volume Fe bioassays' that aimed to assess the nutritional Fe status of the resident phytoplankton community from a number of incremental Fe additions, and 3) the 'large volume bioassays' that aimed to probe for Fe, Zn or Co effects on alkaline phosphatase expression. For all experiments, incubation seawater was collected into pre-cleaned 2 L PC bottles or 24 L PC carboys (both Nalgene) that served as incubation containers. The large 24 L carboys were shipped while containing a small amount (~1 L) of UHP water, instead of filling them to the top with 0.024 M HCl, as it is done typically, including for the 2 L incubation bottles (see Table 2.2). Incubation containers were re-cycled at each station, following three rinses with 0.5 M HCl (Romil, SpA) and three rinses with UHP water to remove any wall-adsorbed metal impurities.

Unfiltered incubation seawater was collected strictly before dawn from 40 m depth in either of two modes. At Stations 1 and 2, a Ti-rosette fitted with 24 × 10 L trace metal-clean Teflon-coated OTE bottles and a CTD profiler (Seabird Scientific) was deployed on a conducting Kevlar wire. Upon recovery, the OTE bottles were transported into a class-100 clean air van and pressurized (0.7 bar) with compressed air filtered in-line through a 0.2 µm PTFE filter capsule (Millex-FG 50, Millipore). Each incubation container received water from a minimum of three different OTE bottles during the

filling process to avoid bias, and was filled to a third from the first Ti-CTD deployment. Two subsequent deployments were made to collect enough seawater. This process was amended for Stations 3 to 7, where braided PVC hosing cable-tied to a conducting Kevlar wire was lowered aided by an epoxy-coated weight, so that seawater was pumped directly into a class-100 clean air-van using a Teflon diaphragm pump (Almatec). The tubing was flushed with ambient seawater for 15 min prior to seawater collection. Incubation containers were conditioned with ambient, unfiltered seawater and then filled in random order to a third of their volume, which was then repeated for the second and last thirds to remove bias. Still in the dark, but aided by red light head lamp, incubation seawater was spiked with metals and/or nutrients (see below paragraphs for details). Where space inside the sampling van allowed, i.e. for the 2 L incubation bottles only, spikes were added inside a laminar flow hood. Finally, containers were screw-capped, sealed with Parafilm, gently shaken and incubated for 48 h in a custom-built van, which was fitted with LED light panels on a 12 h on/off cycle (Part no: LED-PANEL-300-1200-DW and LED-PANEL-200-6-DW, Daylight White, supplier Power Pax UK Limited). The incubation temperature was set to match that of 40 m at each station, which ranged from 25 to 27 °C.

Low abundance Fe isotope experiments. Filled incubation bottles were perturbed with concentrations of between 0.5 to 1.0 nM of an ^{57}Fe enriched working stock solution (details in Chapter 4). The initial stock was prepared from isotopically enriched (96.64 %) $^{57}Fe_2O_3$ (Cambridge Isotope Laboratories) that was dissolved in 6 M HCl (Romil, SpA). The working stock was made up in 0.024 M HCl. At the western most Stations 3 and 4, additions of nitrate and ammonium were made with 1.0 µM each, hereafter referred to as the DIN spike. Nitrate and ammonium stock solutions were prepared from $NaNO_3$ and NH_4Cl salts (both Sigma-Aldrich) dissolved in UHP water and passed through a prepared cation exchange resin (Chelex-100, BioRad) to remove metal impurities. At six time points over the 48 h incubation period (t_1 = 30 min, t_2 = 90 min, t_3 = 6 h, t_4 = 12 h, t_5 = 24 h, t_6 = 48 h), three of the 2 L incubation bottles were removed at random. Bottles were sacrificed for each time point to minimise the risk of contamination that may have incurred upon repeated time point sampling (Lohan et al., 2005a). Sacrificed bottles were brought to a class-100 clean van onboard and their outsides were rinsed with UHP water. One of three replicates was subsampled for Chl-*a* and inorganic macronutrients (DIP and DIN). All three replicate bottles were subsampled for multiple Fe size fractions into acid-cleaned 60 ml or 120 ml LDPE bottles (Nalgene) after pre-conditioning once with ~20 ml of incubation seawater. The small rinse volume was the result of volume restrictions for samples. Specifically, TDFe samples were taken unfiltered by pouring directly from the incubation bottles, dFe samples were taken using a vacuum-filtration tower with 0.45 µm track-etched PC membrane filters (Nucleopore, Whatman), and sFe samples were taken from dFe subsamples after syringe filtration with 0.02 µm pore size (Anotop, Whatman). The filter tower and syringes were acid-cleaned between time points, while Nucleopore and Anotop filters were also conditioned with

1 M HCl (Romil, SpA), UHP water and ambient seawater immediately before use, as in the sFe ultrafiltration procedure applied water column sampling (Section 2.1.2). Additional samples for initial (t_0) concentrations of TDFe, dFe, sFe and auxiliary parameter Chl-*a* were taken during the initial filling process from a t_0-designated 2 L incubation bottle that was filled and processed immediately. All Fe subsamples were acidified to pH 1.7 (0.024 M) by addition of 12 M HCl (Romil, UpA) (Lohan et al., 2005a) and stored double-bagged for at >12 months prior to analysis at the University of Southampton (UK).

Small-volume Fe bioassays. Filled incubation bottles were spiked in duplicate or triplicate with Fe additions between 0.2 to 2.0 nM with and without additions of DIN between 1.0 to 4.0 µM (details in Chapter 4) and complemented by at least two unspiked Control bottles. The Fe working stock was dissolved $FeCl_3$ (Sigma; natural isotopic abundance) in 0.024 M HCl (Romil, SpA), while the DIN stocks were the same as for the low abundance Fe isotope experiments above. In contrast to the low abundance Fe isotope experiments, all bottles were removed from the incubator at a single time point at 48 h. All replicates of all treatments were subsampled for Chl-*a* and measured onboard. During the initial filling process, samples for initial (t_0) Chl-*a* and dFe concentrations were collected directly from the OTE bottles (Stations 1 and 2) or pumped through the PVC hosing (Stations 3 to 7). The dFe t_0 samples were filtered in-line using 0.2 µm membrane cartridge filters (Sartobran 300, Sartorius), acidified to pH 1.7 as described before, and measured onboard by flow injection analysis with chemiluminescence (FIA-CL) detection (Section 2.2.1).

Large-volume bioassays. Filled incubation carboys were spiked in duplicate or triplicate with single-metal additions of Fe (1.0 nM), Zn (0.5 or 1.0 nM) or Co (20 to 50 pM) (details in Chapter 5) and complemented by at least two unspiked Control carboys. Following the 48 h incubation period, one replicate of each treatment was transferred to a class-100 clean air van onboard, where the outside was rinsed with UHP water and a pre-cleaned (Table 2.2) spigot was attached to the carboy. For protein subsamples, unfiltered incubation seawater was collected into pre-cleaned 10 L PC carboys (Nalgene) and immediately filtered, collecting the >0.22 µm fraction on a polyethersulfone membrane filter cartridge (Millipore, Sterivex). Any remaining water was pressed out with an air-filled syringe and the filtration unit was sealed with clay. This procedure was repeated for the second (and third where applicable) replicate carboy of each treatment. Protein samples were stored for ~18 months at -80 °C prior to further processing and analysis at the Woods Hole Oceanographic Institution (USA). During the initial filling process, samples for initial (t_0) dFe concentrations and auxiliary parameters were collected directly from the OTE bottles (Station 2) or pumped through the PVC hosing (Stations 3, 4 and 7). The dFe t_0 samples were filtered in-line using 0.2 µm membrane cartridge filters (Sartobran 300, Sartorius), acidified to pH 1.7, and measured onboard by FIA-CL (Section 2.2.1).

2.1.4 Auxiliary Sample Types and Analysis

Auxiliary samples that are relevant to the results presented in this thesis were collected and analysed as follows by members of the JC150 scientific party. Analytical procedures were the same regardless of the sample origin, i.e. ambient environment or experimental work, unless stated otherwise.

Standard sensor data. Salinity, temperature, O_2 and turbidity were measured by sensors during CTD casts, with temperature and salinity also monitored by the ship's underway system. Salinity sensors (Seabird Electronics 4C) were calibrated against distinct samples using an Autosal 8400B salinometer (Guildline). Dissolved O_2 sensors (Seabird Electronics 43) were calibrated onboard using a photometric-automated Winkler titration system (Carritt & Carpenter, 1966). Data from turbidity sensors (WETLabs BBRTD) were used uncalibrated. Analysis of the O_2 calibration samples was conducted at sea by C. Mahaffey (University of Liverpool, UK).

Chlorophyll-a. Samples for Chl-*a* analysis were collected on glass microfiber filters with pore sizes of 0.7 µm (Whatman GF/F, 25 mm) (for high-throughput samples from surface, water column, ^{57}Fe experiments and small-volume bioassay) or on PC filters with pore sizes of 0.2 µm (Whatman Nucleopore, 25 mm) (for samples from large-volume bioassays). Samples were extracted in glass test tubes filled with 90 % acetone at 4°C overnight (Holm-Hansen et al., 1965). Concentrations of Chl-*a* were determined in the acetone solution on a precalibrated (Spinach Chl-*a* Standard, Sigma) Turner Design Trilogy fluorometer (Welschmeyer, 1994) and further used to calibrate fluorescence sensors (Seabird Electronics 911+) daily. Sample analysis was conducted at sea by L. Johnson and C. Davis (University of Liverpool, UK).

Phytoplankton community. Samples for cell abundances of *Synechococcus* and *Prochlorococcus* were fixed at sea with 20 µl of a 50 % glutaraldehyde solution to 1.8 ml unfiltered seawater and stored at -80 °C in cryovials. Sample analysis was conducted by flow cytometry by Glen Tarran at the Plymouth Marine Laboratory (UK), according to Tarran et al. (2006).

Inorganic macronutrients. Micromolar concentrations of DIP (here specifically phosphate) and DIN (here specifically nitrate + nitrite) were measured from unfiltered samples, collected into aged 60 ml high-density polyethylene (HDPE) bottles, using segmented flow techniques on a Bran and Luebbe AAIII autoanalyser with spectrophotometric detection no more than 12 h after sample collection (Brewer and Riley, 1965; Woodward & Rees, 2001). Additional nanomolar measurements of DIP and DIN were made using colorimetric methods with segmented flow analysis coupled to a 2 m liquid waveguide as the analytical flow cell to improve detection limits (Patey et al., 2008). Certified

reference materials from KANSO Technos (Japan) were measured for quality control. Sample analysis was conducted at sea by E.M.S. Woodward and P. Shelley (Plymouth Marine Laboratory, UK).

Dissolved organic phosphorus. Concentrations of DOP were calculated from the difference between total dissolved phosphorus (TDP) and DIP concentrations, i.e. DOP = TDP – DIP, where DIP concentrations were taken from the inorganic macronutrient measurements described above. Samples for TDP were collected as unfiltered seawater into 125 ml HDPE bottles and stored at -20 °C until analysis in the home laboratory. Concentrations of TDP were determined as DIP by the molybdenum blue method (Murphy and Riley, 1962), using a Bran and Leubbe QuAAtro 5-channel autoanalyser, after persulfate oxidation as in Lomas et al. (2010). As a calculated variable, the DOP concentrations are only accurate to the propagated combined uncertainty from the TDP and DIP measurements, with relative standard deviations (RSD) from analytical replication of <10 % and <5 %, respectively. Sample analysis was conducted by C. Davis at the University of Liverpool (UK).

Alkaline phosphatase activity. Rates of APA were determined from unfiltered seawater samples incubated in triplicate in 250 ml PC bottles at ambient temperature and light conditions in an incubator van with final concentrations of 500 nM of the synthetic fluorogenic substrate 4-methylumbelliferyl-phosphate (MUF-P, Sigma Aldrich; Ammerman, 1993). Hydrolysis of MUF-P yields the fluorescent product 4-methylumbelliferone (MUF) that was monitored over 8 to 12 h on a Turner 10AU field fluorometer (365 nm excitation; 455 nm emission), as applied in Davis et al. (2019). Sample analysis was conducted at sea by C. Davis (University of Liverpool, UK).

Nitrogen fixation. Rates of biological N_2 fixation were measured from unfiltered seawater, collected into overfilled 4.5 L PC bottles, screwed tight with a septum cap and spiked with 8 ml of ^{15}N isotope enriched N_2 gas. After mixing, a 12 ml were subsampled into a vacutainer and analysed using a Hiden Analytical membrane inlet mass spectrometer (MIMS) to determine the isotopic composition of N_2 gas present in each sample. The 4.5 L bottle was topped up with seawater, incubated for 24 h, then filtered onto 0.7 µm glass microfiber filters (Whatman GF/F, 25 mm) and stored at -80 °C in Al foil-lined petri dishes, until analysis by isotope ratio mass spectrometry on a Carlo Erba elemental analyser coupled to a Thermo mass spectrometer. Sample analysis was conducted by C. Mahaffey at the University of Liverpool (UK).

Dissolved trace metals (excluding Fe). Samples for dissolved trace metal concentrations (dZn and dCo) were filtered in-line through 0.2 µm acetate membrane cartridge filters (Sartobran-300, Sartorius). Concentrations for dZn were measured by flow injection analysis (FIA) with spectrophotometric detection on a Shimadzu RF-10Axl fluorometer, which included a pre-concentration step onto a cation exchange resin (Toyopearl AF-Chelate 650 M). This analysis was

conducted at sea by N. Wyatt (University of Southampton, UK), following Wyatt et al. (2014). Concentrations for dCo were measured by high resolution inductively coupled mass spectrometry (HR-ICP-MS) on a Thermo Element 2XR, preceded by UV-digestion and off-line pre-concentration onto a chelating resin (WAKO). This analysis was conducted at the University of Southampton (UK) by A. Lough, following Lough et al. (2019).

2.1.5 Overview Ambient Biogeochemistry

An overview of the ambient surface biogeochemistry of the subtropical North Atlantic as observed during JC150 is provided in Figure 2.2. For the majority of the transect, temperature and salinity were characteristically high for the warm, stratified subtropical ocean. Temperature decreased from a maximum of 28.5 °C in the Sargasso Sea in the west to a minimum of 25.3 °C in the eastern subtropical gyre. Salinity averaged 37.2 ± 0.3 between 58.4 °W and 30.5 °W. The influence of the Amazon/Orinoco River plume resulted in lower salinities of 33.9 to 36.2 west of 58.4 °W. Concentrations of Chl-*a*, as a phytoplankton biomass proxy, ranged between 0.050 to 0.190 µg L^{-1} in a gradually increasing trend from west to east. *Prochlorococcus* cell abundance correlated with this gradient, ranging from minimum concentrations of <15,000 cells ml^{-1} in the Sargasso Sea to >230,000 cells ml^{-1} in the east. Contrastingly, *Synechococcus* cell abundance decreased eastwards from >8,000 cells ml^{-1} to <700 cells ml^{-1}. Standing stocks of DIP ranged from ultraoligotrophic concentrations of <10 nM DIP in the Sargasso Sea, excluding the riverine influence west of 58 °W, to higher but still oligotrophic concentrations of 15 to 20 nM east of 35 °W. Concentrations of DOP exhibited a similar increase from west to east as DIP, but were generally one to two orders of magnitude higher than DIP (range between 44 nM to 158 nM) and hence, accounted for the majority of TDP. Concentrations of DIN were more variable than DIP across the basin, but were generally <60 nM with the majority <30 nM. Rates of APA generally followed a decreasing trend from west to east with rates between 0.62 to 3.41 nM h^{-1}, although with large variability. Rates of biological N_2 fixation averaged 0.15 ± 0.05 nM h^{-1} across the basin, excluding the data point at 41.7 °W, where the rate reached 0.66 nM h^{-1}. Lastly, gradients in trace metals were strongest in dFe, with >1.50 nM at the western end of the transect to <0.25 nM at the eastern end, while concentrations of dZn were <0.40 nM for most of the transect but decreased to <0.10 nM between 54.4 °W to 58.2 °W and between 34.9 °W and 35.9 °W, and peaked to ≥0.7 nM at the most western and eastern extremities. Concentrations of dCo averaged 12.3 ± 1.4 pM, although further variability may be obfuscated by the limited resolution. In summary, the ambient biogeochemistry of the study area marks a progression from the ultraoligotrophic Sargasso Sea, where high Fe, low Chl-*a* and high relative *Synechococcus* abundance prevailed, to the oligotrophic eastern subtropical gyre, where low Fe, higher Chl-*a* and maximal *Prochlorococcus* abundance prevailed. These strong gradients made the JC150 transect an ideal natural laboratory to for the aims of this thesis (Section 1.6).

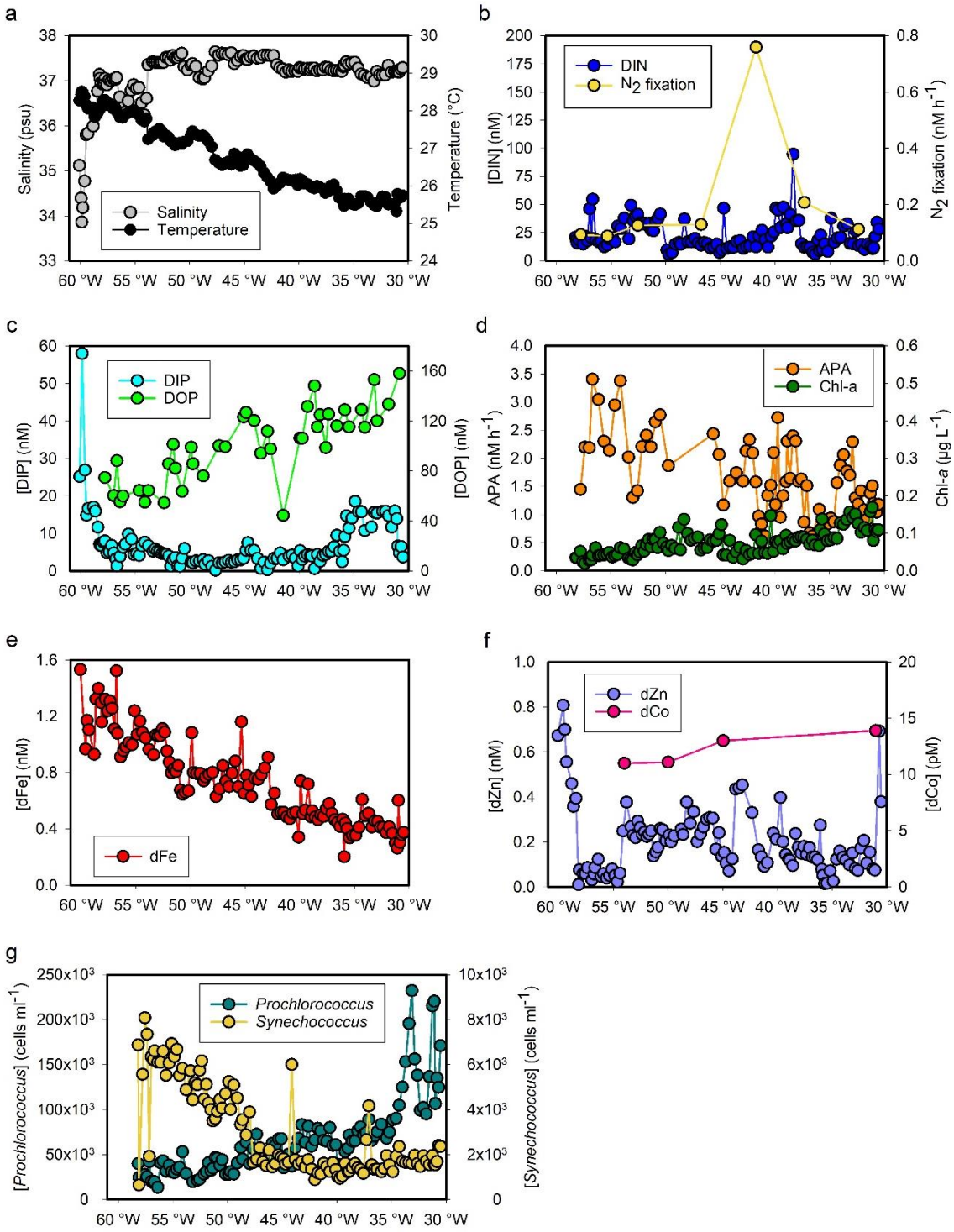

Figure 2.2 Overview of surface distributions during JC150 in (a) salinity and temperature, (b) DIN concentration and N_2 fixation rate, (c) DIP and DOP concentrations, (d) APA rate and Chl-a concentration, (e) *Prochlorococcus* and *Synechococcus* cell abundances, (f) dFe concentration, (g) dZn and dCo concentrations. Note that dCo data does not originate from the underway sampling, but from the 40 m depth water column sample from CTD casts at a subset of stations. It is included here for completeness of relevant biogeochemical parameters.

2.2 Trace Metal Analysis

The development of sufficiently sensitive methods, inter-calibration across techniques and laboratories, and the supply of reference materials by the SAFe (Johnson et al., 2007) and GEOTRACES (www.geotraces.org/) programs were critical milestones to the advancement of oceanic trace metal research. A range of accurate and reliable techniques is available, of which HR-ICP-MS, FIA and voltammetric methods are most commonly applied (Bowie & Lohan, 2009). The choice for either of these depends on a variety of factors including the metal(s) and/or their isotopes of interest and the location of analysis (i.e. shipboard or based in home laboratory). For this dissertation, measurements of size-fractionated Fe concentrations (sFe, dFe, TDFe) from surface and depth profile samples that are at the core of Chapter 3 were made by FIA (shipboard and at the University of Southampton), while measurements of Fe isotope concentrations (^{56}Fe, ^{57}Fe) from *in-situ* incubation samples that are at the core of Chapter 4 were made by HR-ICP-MS on an Thermo Element 2XR at the Facility for Inorganic Elemental and Isotopic Analysis at the University of Southampton. In both cases, the concentrations of cFe and pFe_{app} were not measured directly, but calculated as cFe = dFe – sFe and pFe_{app} = TDFe – dFe, respectively. Consequently, the concentrations of cFe and pFe_{app} are only accurate to the combined propagated uncertainty (from analytical replication) of the respective dFe and sFe concentrations, as detailed in Sections 2.2.1.4 and 2.2.2.3 for FIA-CL and ICP-MS, respectively.

2.2.1 Flow Injection Analysis by Chemiluminescence Detection for the Determination of Iron Concentrations

In FIA, a seawater sample is pre-concentrated onto a chelating resin and then injected into a continuous reagent stream triggering a chemical reaction that is then measured to quantify the metal concentration present in the sample. Its advantages over ICP-MS include high sample throughput, portability (e.g. use onboard ship), and the low consumption of sample and reagent volumes. Flow injection analysis techniques are optimised for a single metal in question, and near-real-time measurements are possible (Bowie & Lohan, 2009). The latter is especially useful for informing the set-up of *in-situ* bioassays that often depend on the ambient Fe concentrations. Furthermore, FIA forms a closed sample analysis system, so that contamination risks are minimised (Bowie & Lohan, 2009). Two detection modes can be coupled to FIA, namely spectrophotometry or chemiluminescence (CL). Here, FIA-CL was used with the chemiluminescent reaction of Fe with luminol (5-amino-2,3-dihydro-1,4-phtalazinedione) after Obata et al. (1993).

2.2.1.1 Luminol Chemiluminescent Reaction

At the heart of FIA-CL is the chemiluminescent reaction of Fe with luminol, resulting in the measurable and scalable emission of light at 425 nm. Although the exact mechanism of this reaction remains poorly understood (Barni et al., 2007; Rose & Waite, 2001), it is likely a three-step process that is dependent on temperature, pH, reaction medium, oxidants and catalysts (Merényi et al. 1990). A schematic of the reaction mechanism is depicted in Figure 2.3.

1. In aqueous alkaline solutions, i.e. pH > 7, luminol exists in two deprotonated forms, specifically as the monoanion (LH^-) and dianion (L^{2-}), of which the latter dominates at pH 8 to 14 (Figure 2.4) (Barni et al., 2007). Under the presence of an oxidant (here H_2O_2) and a suitable metal ion (here Fe(III)) both forms can oxidize to form luminol radicals ($LH^{\cdot}$, L^{-}) (Merényi et al., 1990).

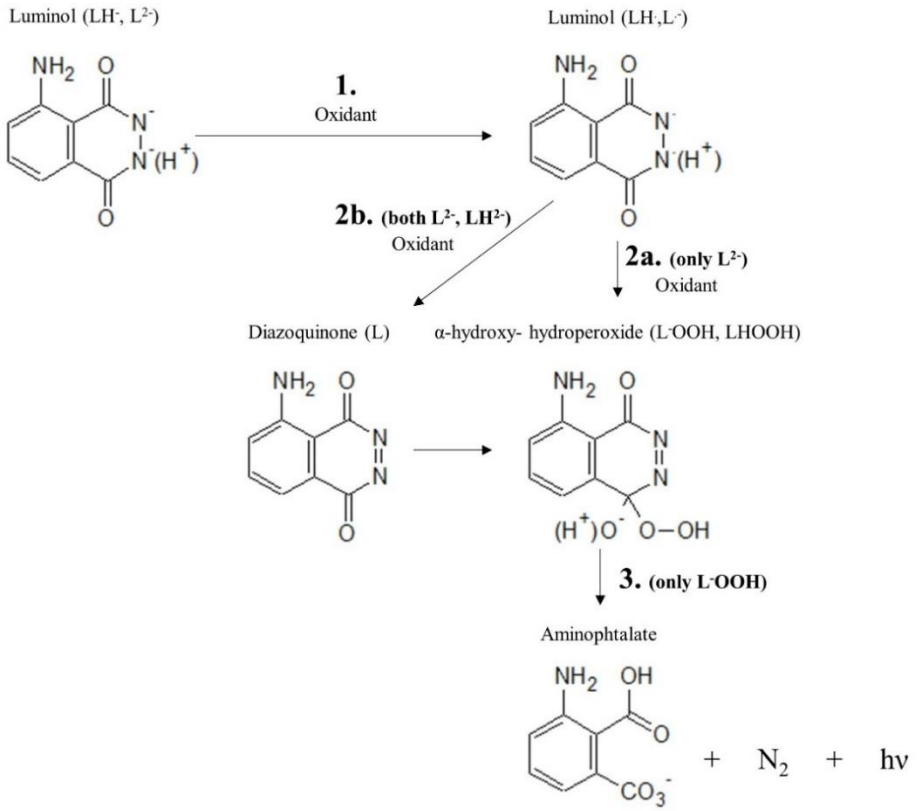

The catalyst-like action of Fe(III) is not entirely understood but probably promotes the dissociation of H_2O_2 and hence the rate at which its oxidizing radicals are formed, because H_2O_2 alone does not suffice to initiate the oxidation (Barni et al., 2007; Obata et al., 1993; Rose and Waite, 2001). As Fe(III) does not return to its initial state, its notation as 'catalyst' would be incorrect (Rose & Waite, 2001).

Figure 2.3 The three major reaction steps of luminol chemiluminescence. Redrawn from Merényi et al. (1990) and Rose & Waite (2001).

2. In the next step, the luminol radicals are oxidised to form α-hydroxy-hydroperoxide (α-HHP) via either of two possible pathways depending on the type of radical (Merényi et al., 1990).

    a. In the direct pathway which is exclusive to the monoanionic $L^{\cdot -}$, the luminol radical is oxidised to α-HHP by superoxide, a derivative of the initial oxidant H_2O_2 (Merényi et al., 1990; Rose and Waite, 2001).
    b. Alternatively, diazoquinone (L) is formed in an intermediate step and then oxidised to α-HHP (Merényi et al., 1990; Rose & Waite, 2001). Both luminol radicals $LH^{\cdot}$, $L^{\cdot -}$ can follow this pathway (Merényi et al., 1990; Rose & Waite, 2001).

3. Due to the deprotonation of α-HHP in aqueous media, it can be present in a non-dissociated form (LHOOH) or as the monoanion (L^-OOH), both of which decompose to 3-aminophtalate (Merényi et al., 1990). Only the monoanionic form of α-HHP, whose formation is pH dependent, lead to the electronically excited state 3-aminophtalate* (Rose & Waite, 2001). Upon relaxation, 3-aminophtalate* emits light at 425 nm (blue), matching that of luminol perfectly (Rose & Waite, 2001). Hence, it is the light-emitting intermediate in the luminol chemiluminescent reaction (White & Bursey, 1964).

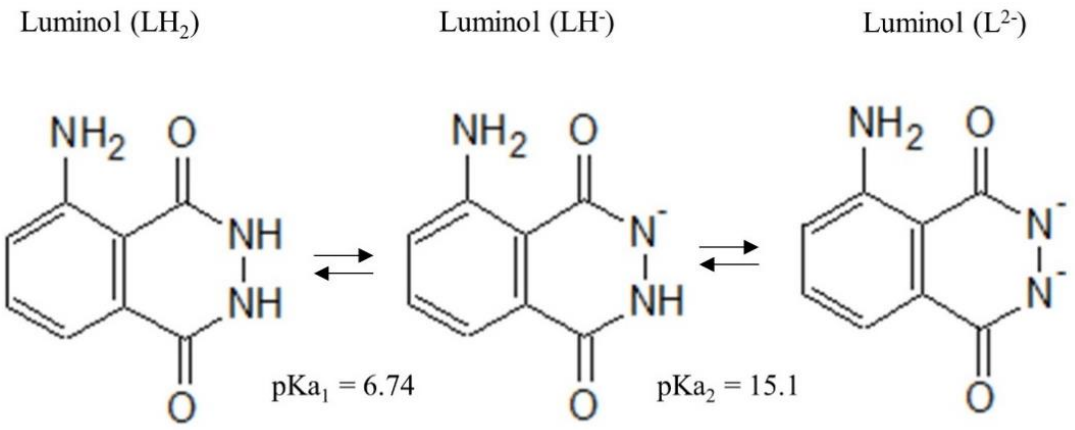

Figure 2.4 Luminol protonation. LH_2, LH^- and L^{2-} represent the diprotic, monoanionic and dianionic forms of luminol. Redrawn from Barni et al. (2007).

2.2.1.2 Reagents

All reagents were prepared inside a class-100 laminar flow hood using ultra-high purity (UHP) water (Milli-Q, Merck-Millipore).

Luminol – An initial 50 mM stock was prepared from 177 mg luminol (≥ 97 %, for HPLC, Sigma-Aldrich) and 250 mg Na_2CO_3 (Sigma-Aldrich) dissolved in 20 ml UHP water. The solution was shaken thoroughly for dissolution of luminol and Na_2CO_3, and left for equilibration in a light-proof

container for several days. A 0.15 mM luminol solution was prepared from 9.2 ml stock to 2 L UHP water. The original luminol chemical is not available in a high purity grade and the 'dirty' reagent interferes with the sensitivity of the system (data not shown), therefore the working solution was pre-cleaned by an iminodiacetate group resin (Chelex-100, Sigma-Aldrich) to extract metal impurities. The resin cleaning and resin activation were achieved with a peristaltic pump, with 100 ml 1 M HCl (Romil, SpA), followed by 200 ml of 0.1 M $NH_{3(aq)}$ (Romil, SpA), until the outflow was pH > 10. After column drainage, 4 L of the luminol reagent were passed over the column in reverse flow (from bottom to top), with the first 150 ml discarded. The cleaning and re-activation steps were carried out after every 4 L of luminol reagent. For 1 L of cleaned luminol reagent 70 µl of concentrated triethylenetetramine (TETA, Sigma-Aldrich) was added (after the cleaning process) , which increases the chemiluminescent sensitivity by chelation of Fe(III) and catalysis of H_2O_2 decomposition (Wang, 1955).

Hydrochloric acid – A 0.24 M hydrochloric acid (HCl) was prepared by diluting 20 ml of concentrated HCl (Romil, SpA) in 1 L UHP water and served as elution acid. A 0.013 M HCl rinse solution was prepared by diluting 550 µl of concentrated HCl in 500 ml UHP water. Finally, a 0.5 M cleaning acid was prepared from 40 ml concentrated HCl in 1 L UHP water.

Ammonia solution – To obtain a 1 M ammonia solution, 66 ml concentrated ammonia solution ($NH_{3(aq)}$, Romil, SpA) was diluted with UHP water to 1 L.

Ammonium acetate buffer – A buffer stock was prepared from 100 ml concentrated acetic acid (CH_3COOH, Romil, SpA), 50 ml $NH_{3(aq)}$ (Romil, SpA) and 100 ml UHP water. For the working reagent, 50 ml of the buffer stock was diluted with 950 ml UHP. The buffer (pH >4.6) and the acidified sample (pH = 1.7) are mixed in-line resulting in a pH of 3.5 to 4.0.

Hydrogen peroxide – Concentrated H_2O_2 solution (30 % w/w in H_2O, Sigma-Aldrich, Trace Analysis Grade) was kept refrigerated until use. To 970 ml UHP water, 30 ml concentrated H_2O_2 was added to obtain a 0.4 M working solution. One ml of this reagent was further diluted with 30 ml UHP water to a 0.013 M solution and used to spike the seawater samples at least 1 h prior to analysis, to allow for the oxidation of any present Fe(II) to Fe(III).

Iron standards – For calibration purposes, various amounts of Fe was added to 100 ml of low Fe seawater. An original Fe standard of 17.9 M (1000 ± 4 mg/l, for AAS, Fluka Analytical) was diluted in 0.024 M HCl (Romil, SpA) to an intermediate stock, which was further diluted to a working stock of 500 nM. Small amounts (40 to 400 µl) of Fe stock were added to acidified calibration seawater (pH 1.7 with 12 M HCl; UpA, Romil), so that the volume of the added standard did not exceed 1 % of the seawater volume.

2.2.1.3 Instrumentation and Procedure

A schematic of the FIA-CL manifold is presented in Figure 2.5. It consisted of three peristaltic pumps (Gilson MiniPuls3) with two-stop accu-rated™ PVC pump tubing (Elkay), PTFE manifold tubing (Elkay), a ten-port autosampler, a six-port injection valve (both VICI Valco Instruments), a solenoid valve (Cole-Parmer), a photomultiplier tube (PMT) (Hamamatsu, Model H82259) and two columns containing a resin with iminodiacetate groups (Toyopearl® AF-Chelate-650M, Sigma-Aldrich). To acquire data and control the instrumentation a Samsung laptop equipped with the LABVIEW™ V7.1 (National Instruments) software was used.

Every seventh measurement day, the pump tubing was exchanged to prevent wear-out effects on the flow, and columns were reversed to avoid channel formation, which could otherwise have impacted on the metal retention efficiency. Additionally, all tubing was cleaned by passing the cleaning HCl followed by UHP through the system for 0.5 h each, prior to every measurement day and for 2 h each after every seventh measurement day. All tubing and containers were kept inside a class-100 laminar flow. After the daily cleaning process, the system was conditioned with acidified seawater with Fe concentrations <0.5 nM for 5 to 10 cycles.

At least 1 h prior to any measurement, samples (as well as calibrants, blanks and reference materials) were spiked with weak H_2O_2 to oxidize all present Fe(II) to Fe(III), as Lohan et al. (2005) demonstrated that Fe(II) can form a substantial fraction of Fe in acidified seawater. Accurate measurements relied on the chemiluminescent reaction facilitated by Fe(III), so that any present Fe(II) would have resulted in a lower chemiluminescent signal.

A typical measurement cycle consisted of the following four steps:

1. Pre-start (0 to 90 s): Sampling (sample, buffer) and reagent (elution acid, luminol, $NH_{3(aq)}$, H_2O_2) pumps in elute mode.
2. Load (60 to 130 s): Sampling and reagent pumps in load mode.
3. Rinse (220 to 250 s): Rinse and reagent pumps in load mode.
4. Elute (250 to 330 s): Reagent pump in elute mode.

During pre-start, the sample-buffer mixture flowed to the six-port valve and then to waste, which ensured that the buffered sample was close to the pre-concentration column before the next step. The buffer passed over a clean-up column filled with the Toyopearl®-resin prior to mixing with the sample for removal of any metal impurities. During the load step, the buffered sample was loaded onto the column. The Fe concentration measured during this study were typically low with <2 nM

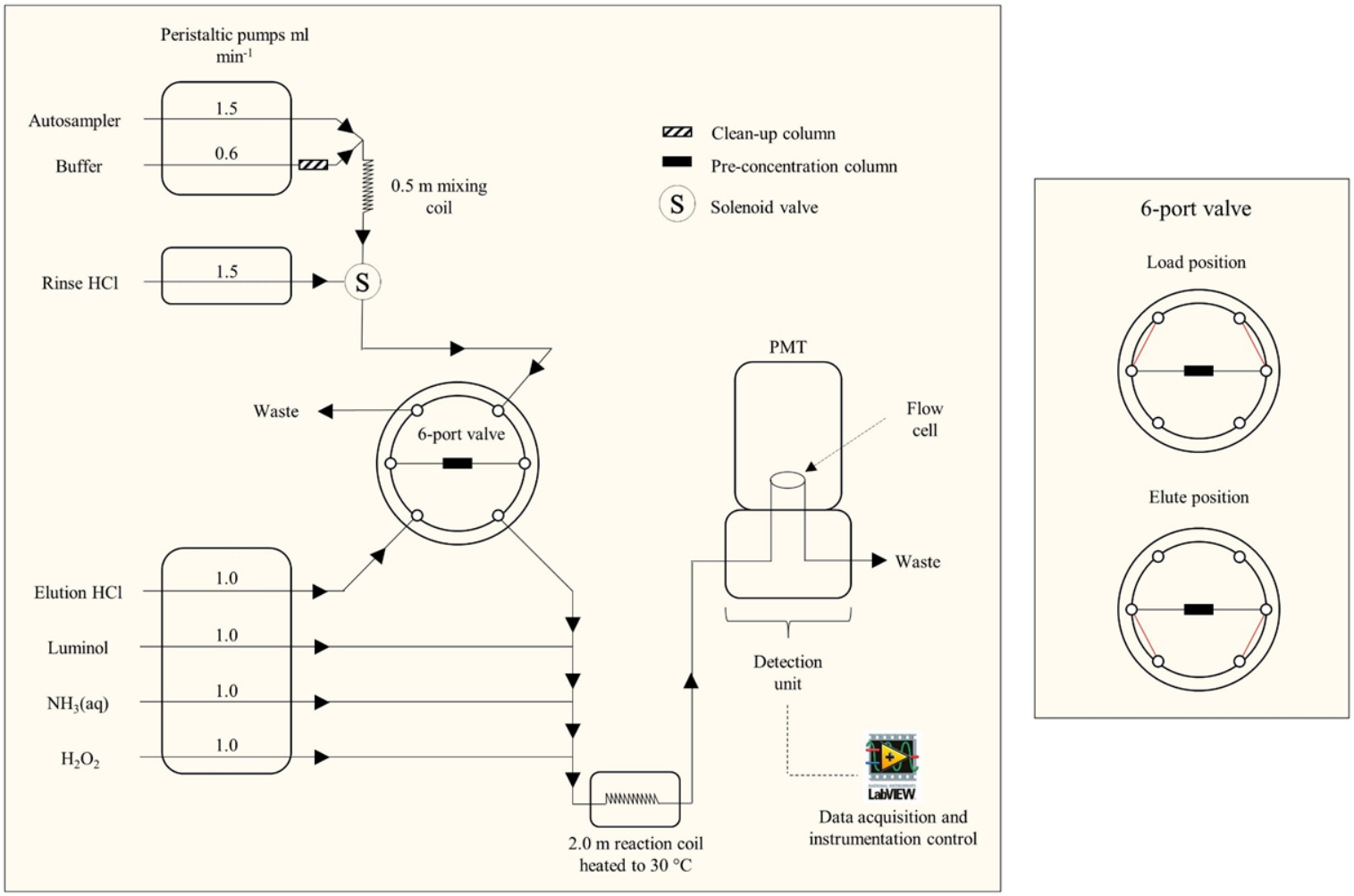

Figure 2.5 Instrumentation manifold for the Fe(III) measurements by FIA-CL.

and hence, this pre-concentration step was necessary to produce sufficiently strong chemiluminescent signals for detection. Maximum retention of Fe(III) on the resin is achieved at a pH of 3.5 to 5.0 (Clough et al., 2015; Obata et al., 1993). In the subsequent step, rinse solution passed over the column to remove any major seawater ions that otherwise interfere with the chemiluminescence signal (Bowie et al., 1998; Shelley et al., 2010). Lastly, the six-port valve switched to the elute mode, so that elution acid passed over the column, thereby liberating the retained Fe(III) and subsequently mixing it with the remaining reagents (reaction pH = 9.4 to 9.6) in a heated reaction coil (kept at 30 ^{o}C with thermocouple device or water bath). The stream then passed through the PMT, where the light emission was amplified and converted to an electric signal recorded by the laptop.

All analyses were carried out in triplicate and therefore steps 2 to 4 were repeated twice per sample. Additionally, during the last 10 s of the elution step, the sample pump was turned on in order to position the sample-buffer mixture before the six-port valve. If this step were omitted, remnant rinse from the previous cycle would have loaded onto the column for the first few seconds of the subsequent load step. The required volumes for triplicate analyses were approximately 18 ml sample, 9 ml buffer, 2 ml rinse and 26 ml of each remaining reagent.

2.2.1.4 Data Acquisition, Calibration and Drift Correction

In order to quantify the Fe concentration from the chemiluminescent signal, calibration was conducted with five to six standard additions to acidified low dFe (<0.2 nM) seawater and a zero addition, in line with recommendations by Floor et al. (2015). The blank contribution of the instrumentation was accessed by loading an acidified (0.024 M HCl, pH 1.7) UHP water sample in the same way as the samples. The blank concentration averaged 0.05 ± 0.03 nM over a total of 69 measurement days.

The concentration range of the seawater samples was small, so one set of calibrants (typically 0 to 2 nM) and settings (i.e. load and elution timings) was used for the majority of sFe, dFe and TDFe analyses. An example of the peaks generated during a typical calibration is shown in Figure 2.6. Peak heights and standards addition were consistently linearly correlated (R^2 = 0.99, Figure 2.7). The absolute concentration of each calibrant was calculated by adding the concentration of the calibration seawater, i.e. the zero addition, to the known addition. The concentration of the calibration seawater was calculated by extrapolating to 0 nM, i.e. the x-axis intercept of the standard addition curve. The linear function relating peak height to absolute concentration was calculated and forced through the origin as shown in Figure 2.7.

The limit of detection was calculated from three times the standard deviation of the lowest standard addition and was on average 0.03 ± 0.02 nM (n = 69), while the precision of three analytical peaks was 2.78 ± 2.02% (n = 1764). Accuracy was confirmed by measuring repeatedly the dFe content in SAFe reference samples (Johnson et al., 2007) yielding 0.11 ± 0.02 nM (n = 6) and 0.94 ± 0.04 nM (n = 17) for SAFe S and SAFe D2, respectively, which agree with the reported consensus values (S = 0.095 ± 0.008 nM; D2 = 0.96 ± 0.02 nM).

Instrumental drift was observed over long measurement days. This 'within sequence (in-)stability' (Floor et al., 2015) was monitored by measuring a low (<0.5 nM) and a high (>1 nM) internal standard after every 8 samples and running an additional 4-point calibration including the zero, lowest, highest and one intermediate Fe calibrant at the end of each day. Peak signals were corrected for instrumental drift if either peak heights differed by ≥5 % between the start and end calibrations, or if obvious jumps occurred in the peak heights of internal standards throughout the day.

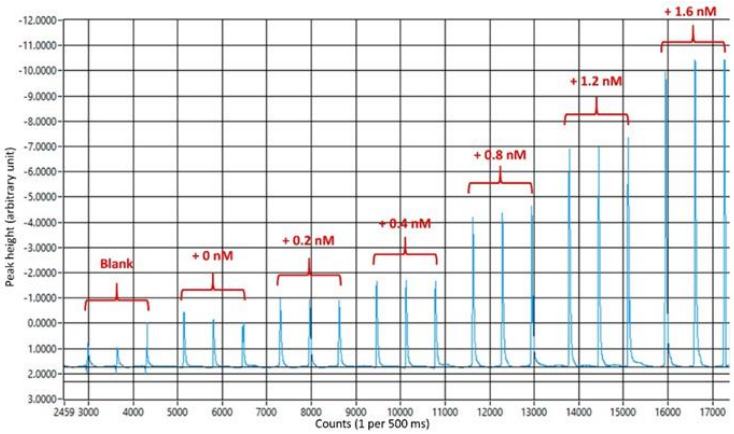

Figure 2.6 Peak signals generated during a typical six-point calibration curve with standard additions of 0 to 2 nM.

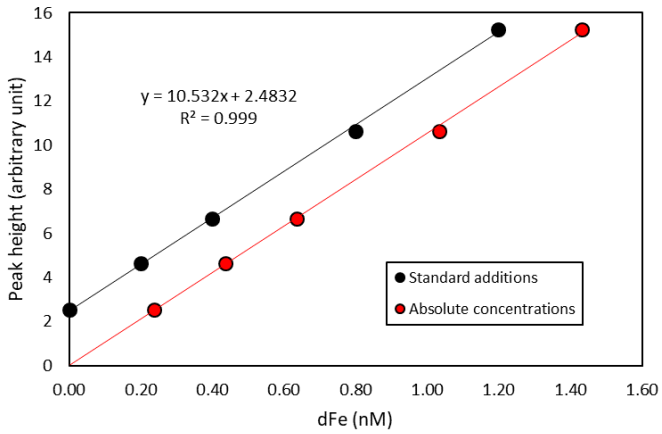

Figure 2.7 The standard additions of Fe versus peak height (blue) and the final calibration curve with absolute Fe concentrations versus peak height (orange), as part of a typical calibration procedure.

2.2.2 High Resolution Inductively Coupled Plasma Mass Spectrometry for the Determination of Iron Isotope Concentrations

Measurement by HR-ICP-MS enables the simultaneous determination of the concentrations of multiple metals and their isotopes in seawater samples, which FIA cannot cater for (Bowie & Lohan, 2009; Milne et al., 2010). High resolution ICP-MS is rooted in the separation of the unique mass-to-charge (m/z) ratios of elements or isotopes following ionisation of the analyte by partially ionised argon (Ar) gas. The detected signal intensity of each m/z is proportional to the concentration in the sample. Similar to FIA, low concentrations in seawater require metal extraction from the salt matrix and pre-concentration onto a chelating resin prior to analysis. Here, a custom-built off-line extraction and pre-concentration system was used (Figure 2.8), drawing on the manifold design by Milne et al. (2010) and the extraction chemistry by Rapp et al. (2017). Subsequent measurements of ^{56}Fe and ^{57}Fe concentrations were made by HR-ICP-MS (e.g. Biller & Bruland, 2012; Lough et al., 2019; Milne et al., 2010). The high mass resolution improves accuracy by removing spectral interferences that occur from overlapping m/z of interfering ions with analyte ions (e.g. $^{40}Ar^{16}O$ = 55.956 interference with ^{56}Fe = 55.934), which is the primary limitation of analysis by ICP-MS. It is important to note that the seawater samples in question were artificially enriched in the low abundance isotope ^{57}Fe (see Chapter 4). For natural isotopic ratios, even more sensitive methodology including the use of multi-collector ICP-MS would be required (e.g. Lacan et al., 2008).

2.2.2.1 Reagents

All reagents were prepared inside a class-100 laminar flow hood using UHP water.

Ammonium acetate buffer – A buffer stock was prepared from 56 ml concentrated CH_3COOH (Romil, UpA), 91 ml concentrated $NH_{3(aq)}$ (Romil, UpA) with UHP water to a total of 500 ml (final pH = 8.4). For the working buffer (2 M), 210 ml of the buffer stock was diluted to 1000 ml in UHP. Concentrated CH_3COOH or $NH_{3(aq)}$ was added at 1 ml at a time to adjust the pH to 8.45 ± 0.05 if necessary.

Ammonium acetate rinse – A 0.05 M rinse was prepared with 30 ml of the 2 M working buffer diluted to 2000 ml with UHP water (final pH = 8.2).

Nitric acid – Trace Grade nitric acid (HNO_3) (14 M; FisherScientific) was purified by sub-boiling (s.b.) quartz distillation. A 1 M HNO_3 solution was prepared by diluting 160 ml s.b. HNO_3 to 2000 ml with UHP water, following the addition of 1 ml of a 500 ppb Indium (In) stock (prepared from single element standard, Inorganic Ventures) as internal standard. The 1 M HNO_3 was used as the

elution acid. An additional 2 M cleaning acid was prepared from 160 ml concentrated HNO_3 diluted to 1000 ml in UHP water.

Multi-metal standards – For calibration purposes, various amounts (25 to 500 µl) of a multi-metal stock solution including Fe, V, Mn, Co, Ni, Cu, Zn, Cd and Pb (Fe concentration was 239 nM) in 0.045 M HNO_3 were added to 60 ml of acidified (pH 1.7) low Fe (<0.2 nM) calibration seawater, so that the volume of the added standard did not exceed 1 % of the seawater volume at any point. The stock was prepared from single element standards for ICP-MS (Inorganic Ventures).

^{57}Fe standards – For a second set of calibrants specific to ^{57}Fe isotope, various amounts (15 to 150 µl) of a ^{57}Fe enriched stock were added to 60 ml of the same calibration seawater as above. An initial stock solution (395 µM) was prepared by dissolving 10.68 mg of isotopically enriched (96.64 %) $^{57}Fe_2O_3$ (MW = 161.87 g mol^{-1}) (Cambridge Isotope Laboratories) in 125.82 mg 6 M HCl (Romil, SpA), which was diluted into a ^{57}Fe enriched working stock of 1 µM with 0.024 M HCl (Romil, SpA).

2.2.2.2 Off-Line Metal Extraction and Pre-Concentration

A schematic of the off-line extraction and pre-concentration manifold is presented in Figure 2.8. It consisted of three peristaltic pumps (Gilson MiniPuls3) with two-stop accu-rated™ PVC pump tubing (Elkay), PTFE manifold tubing (Elkay), two ten-port autosamplers, two six-port injection valve (all VICI Valco Instruments), a solenoid valve (Cole-Parmer) and two columns with an internal volume of 27 µl (Global FIA), which contained pre-cleaned (see Biller & Bruland, 2012) resin with immobilised carboxymethylated pentaethylenehexamine (CM-PEHA) functional groups (WAKO; Kagaya et al., 2009). To control the instrumentation a Samsung laptop equipped with the LABVIEW™ V7.1 (National Instruments) software was used.

Every third day of use the pump tubing was exchanged to prevent wear-out effects on the flow and columns were reversed to avoid channel formation, which could otherwise have impacted on the metal retention efficiency. Additionally, all tubing was cleaned by passing the cleaning HNO_3 followed by UHP through the system for 0.5 h each at the start of each day. All sample and reagent tubing and containers were kept inside a class-100 laminar flow. After the daily cleaning process, the system was conditioned with acidified seawater with dFe concentrations <0.2 nM for 3 cycles.

The blank contribution of the instrumentation was accessed using acidified UHP water (pH 1.7) treated in the same way as the seawater samples.

An extraction and pre-concentration cycle consisted of the following five steps:

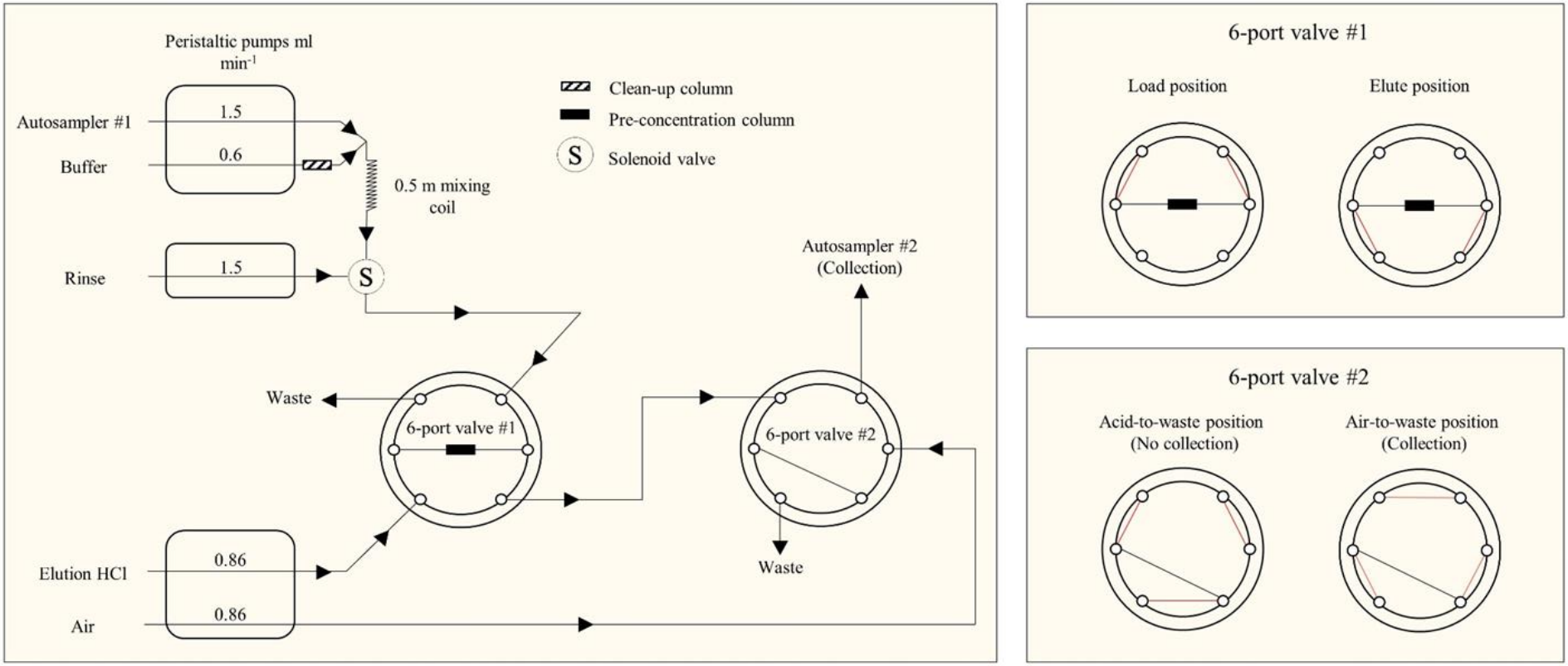

Figure 2.8 Manifold for off-line extraction and pre-concentration of trace metals for subsequent HR-ICP-MS analysis.

1. Pre-load (0 to 65 s): Sampling (sample, buffer) pump on, rinse pump off. Valve #1 in elute position, valve #2 in no-collection position.
2. Column conditioning (65 to 95 s): Sampling pump off, rinse pump on. Valve #1 in load position, valve #2 in no-collection position
3. Load (95 to 695 s): Sampling pump on, rinse pump off. Valve #1 in load position, valve #2 in no-collection position.
4. Rinse (695 to 725 s): Sampling pump off, rinse pump on. Valve #1 in load position, valve #2 in no-collection position.
5. Elute (725 to 900 s): Sampling pump off, rinse pump off. Valve #1 in elute position, valve #2 in no-collection position from 725 to 736 s and from 801 to 900 s, and in collection position 736 to 801 s.

The elution acid/air pump ran continuously and was not controlled by the software. It was set to 4.00 rpm, while the sample/buffer and rinse pumps run at 7.00 rpm, resulting in the flow rates indicated in Figure 2.8. During pre-load, the sample-buffer mixture flowed to the six-port valve and then to waste ensuring that the buffered sample was positioned just before to the pre-concentration column for the subsequent loading step. The buffer passed over a clean-up column filled with the WAKO resin prior to mixing with the sample to remove any metal impurities. The column conditioning step ensured that the column was at the correct pH for the sample loading to maximise the metal retention efficiency. During the loading step, the metal content of the sample was retained on the column. Maximum retention of Fe is achieved at a pH of 5.4 to 7.4 (Rapp et al., 2017). In the current study, a pH of 6.4±0.2 was used. In the rinse step, the rinse passed over the column to remove any major seawater ions that would interfere with the HR-ICP-MS analysis. In the last step, the elution acid was passed over the column. The resulting drop in pH liberated the trace metals off the column and the metal-acid mixture was collected into a 4 ml PP scintillation vial (Omni-Vial, Wheaton) via the 10-port autosampler at the end. Complete clearance of individual autosampler lines and prevention of cross-contamination between subsequent samples was achieved by air flow trailing the elution acid. The required volumes per extraction were approximately 17 ml seawater sample (includes brief pre-load step plus loading volume of 15 ml), 10 ml buffer, 1.5 ml rinse and 13 ml elution acid (flowing continuously). The final pre-concentrated sample had volume of 0.93 ml, and hence the achieved pre-concentration factor (from 15 ml loaded volume) was ~16.

2.2.2.3 Data Acquisition, Calibration and Drift Correction

High resolution ICP-MS measurements were made on a Thermo Element 2XR Magnetic Sector Mass Spectrometer (ThermoFisher). Following established protocols (e.g. Biller & Bruland, 2012; Lough et al., 2019; Milne et al., 2010), Ni sample and skimmer cones were used and an ESI-PC3 Peltier

cooled spray chamber at 4 °C was implemented to reduce plasma loading and production of interfering oxides. Sample gas flow was set to 0.75 ml min^{-1}, with additional gas flow subjected to daily tuning. Tuning also included torch and lens positioning to achieve maximum performance with regards to peak shape and background levels. Mass offsets were adjusted daily.

Signal intensities in counts per second (cps) for ^{56}Fe and ^{57}Fe were recorded in medium resolution mode. Medium resolution ^{115}In cps were used to account for sensitivity changes over long measurement days. For this, ^{115}In cps were first corrected for ^{115}Sn interference (Corrected ^{115}In = ^{115}In – 0.0149 * ^{118}Sn) and then correction factors were calculated from ^{115}In cps in each sample relative to the start of the day. This was made possible by the ^{115}In spike in the elution acid used during sample extraction. Correction factors were then applied to ^{56}Fe and ^{57}Fe cps. Instrumental acid-only blanks (i.e. 2 M HNO_3) and a drift monitor (multi-metal spike to 2 M HNO_3) were measured every 10 samples to monitor precision and blank associated with instrument.

In order to convert signal intensities from the HR-ICP-MS to concentrations of ^{56}Fe and ^{57}Fe in the seawater samples, two separate external calibration curves were applied, each consisting of six additions of multi-metal (i.e. natural Fe isotope composition) or ^{57}Fe enriched standards, respectively, to acidified, low dFe (<0.2 nM) seawater, alongside a zero addition. Calibrants were extracted via the off-line manifold in the same manner as seawater samples. Manifold blanks were assessed from acidified UHP water samples (0.024 M HCl, pH 1.7; Romil, UpA). Their signal intensities include combined blanks from extraction and ICP-MS measurement and were deducted from samples and calibrants. The blank concentration averaged 0.09 ± 0.02 nM and 0.003 ± 0.004 nM over all extraction days (n = 16) for ^{56}Fe and ^{57}Fe, respectively. Signal intensities in counts per second (cps) and standard additions were consistently linearly correlated (R^2 = 0.99). The absolute concentration of each calibrant was calculated in the same way as for FIA-CL analyses (refer to Section 2.2.1.4). The limit of detection was assessed from three times the standard deviation of the mean concentration of the zero seawater calibrant over multiple measurements throughout the extraction day. It was 0.15 ± 0.06 nM and 0.034 ± 0.031 nM for ^{56}Fe and ^{57}Fe, respectively. Precision from triplicate injection into the ICP-MS was at <5 % RSD, while accuracy was established by repeated extraction and subsequent measurement of dFe concentrations in the GEOTRACES (https://www.geotraces.org/standards-and-reference-materials/) and SAFe (Johnson et al., 2007) reference materials GSP (0.19 ± 0.10 nM, n = 9) and SAFe D1 (0.81 ± 0.08 nM, n = 7). The GSP material was in good agreement with the published consensus value (0.16 ± 0.05 nM), while the SAFe D1 was higher than the reported consensus of 0.69 ± 0.04 nM. However, the SAFe D1 reference material suffers from inter-bottle variability, with linearly decreasing concentrations from ~0.9 to 0.7 nM with increasing bottle number (Johnson et al., 2007). The bottle used here was #290 out of ~600 bottles and therefore, the measured Fe concentrations are believed to be accurate.

2.3 High Pressure Liquid Chromatography with Tandem Mass Spectrometry for the Determination of Selected Protein Concentrations

While distributions of macro- and trace metal micronutrient concentrations form a cornerstone to the understanding of marine biogeochemistry, more recently 'omics tools (e.g. genomics, transcriptomics, proteomics and metabolomics) that originate in biomedical research have been developed for the marine environment. These allow for cellular level-insights into the biogeochemical environment that microbes are experiencing in the ocean. For this dissertation, a targeted calibrated proteomic technique was applied to a suite of cyanobacterial proteins extracted from *in-situ* bioassay samples that formed the core of Chapter 5. Measurements were made by parallel reaction monitoring (PRM) on a tandem mass spectrometer coupled to a high pressure liquid chromatography step (HPLC-MS/MS) and yielded absolute concentrations of selected proteins in seawater. This is an emerging data type in field-based oceanography. This work was carried out at the Woods Hole Oceanographic Institution (USA) under the supervision of Dr Mak Saito.

2.3.1 Reagents

Reagent recipes listed below cover the use in sample preparation, labelled standard preparation and HPLC-MS/MS measurements. Organic solvents and water were LC-MS grade.

SDS extraction buffer – A 1 % sodium dodecyl sulfate (SDS) extraction buffer was made from 5 g SDS (Fisher), 50 ml 1 M Tris-HCl (pH 7.5; Fisher) and 10 ml 0.5 M EDTA (pH 8.0; Fisher) with 390 ml water to a final volume of 500 ml.

Precipitation mixture – A 50:50 solvent mixture was prepared from 250 ml methanol (Fisher) and 250 ml acetone (Fisher) at 21 µl concentrated HCl (Sigma, ACS 37 %).

TE buffer – A Tris-HCl/ EDTA (TE) buffer was prepared from 250 µl 1 M Tris-HCl (pH 7.5; Fisher) and 0.5 ml 0.5 M EDTA (pH 8.0; Fisher) with 249.25 ml water to a final volume of 250 ml.

Gel premix – A gel premix was prepared from 252 µl 1M Tris-HCl (pH 7.5; Fisher) and 736.5 µl Bis-acrylamide L (40 %, 29:1; Bio-Rad).

Gel fix solution – Fifty ml ethanol (Woods Hole Oceanographic Institution Supplies) and 10 ml concentrated CH_3COOH (Fisher) were added to 40 ml water to a final volume of 100 ml.

Destain solution – Fifty ml methanol (Fisher) and 10 ml concentrated acetic acid (Fisher) were added to 40 ml water to a final volume of 100 ml

APS – A 1 % ammonium sulfate solution was prepared from 10 mg ammonium persulfate (Arcos Organics) in 1 ml water.

AMBIC – A 25 mM ammonium bicarbonate (AMBIC) solution was prepared by dissolving 2 g ammonium bicarbonate (Sigma) in 1000 ml water.

Wash solution – A wash solution was prepared from 100 ml acetonitrile (Fisher) and 100 ml AMBIC.

Peptide extraction buffer – One hundred ml acetonitrile (Fisher) and 10 ml concentrated formic acid (Fisher) were added to 90 ml water for a final volume of 200 ml.

DTT solution – A 10 mM dithiothreitol (DTT) solution was prepared from 15.5 mg DTT (Sigma) in 10 ml AMBIC.

IODA solution – A 55 mM iodoacetamide (IODA) solution was prepared from 93 mg IODA (Sigma) in 10 ml AMBIC.

Agar plates – Agar plates were poured from a solution containing 5 g of Luria broth (LB) powder (Fisher) and 5 g agar powder (Thermo) in 1 L water with a kanamycin spike of 50 µl ml^{-1} (Fisher).

Urea solution – A 6 M urea solution was prepared from 1.80 g (Sigma) in 5 ml AMBIC.

HPLC buffers – Buffer A was prepared from 0.5 ml concentrated formic acid (Fisher) to 495 ml water (i.e. buffer A = 0.1 % formic acid), while buffer B was prepared from 0.5 ml concentrated formic acid to 495 ml acetonitrile (Fisher) (i.e. buffer B = 0.1 % formic acid in acetonitrile).

2.3.2 Sample Preparation

Samples for proteomic analysis were in the form of filtered biomass (>0.22 µm), collected on a polyethersulfone membrane filtration unit (Sterivex, Millipore) that was sealed with clay and stored at -80 °C before processing. All materials in the following procedure (e.g. razor blades, microfuge tubes) were washed with ethanol and dried before usage.

Extraction. Frozen filtration units were transported to the laboratory on ice and cut open with a tube cutter. Filters were cut out from its holder with razor blades and placed into 2 ml microfuge tubes

(Eppendorf). Following protocols of Held et al. (2020), 2 ml SDS extraction buffer was added and samples incubated for 15 min at room temperature, followed by 10 min at 95 °C to denature proteins. Samples were then shaken at 350 rpm at 20 °C for 1 h. Afterwards, filters were removed from tubes and protein extract was centrifuged at 13.5 rpm for 20 min, with the supernatant collected in order to remove particulate impurities. Next, samples were spin-concentrated for 1 h in 5 kD membrane filters (Vivaspin columns, GE Healthcare), reducing the volume to 90 to 160 µl, and transferred into a fresh microfuge tube. Total protein concentrations were measured via a standard bicinchoninic assay (BCA) (Pierce) on a Nanodrop ND-1000 spectrophotometer (ThermoScientific). The ice-cold precipitation mixture was added in a 1:4 ratio to sample volume, and samples were left to precipitate for 5 days at 4 °C. At the end of the precipitation period, samples were centrifuged at 13.5 rpm at 4 °C, supernatants were removed and remaining protein pellets were vacuum-dried (DNA110 Savan SpeedVac, ThermoFisher) for 10 min or until dry. Pellets were redissolved in 50 µl SDS extraction buffer, and post-precipitation total protein concentrations were measured via a second BCA assay (for recovery assessment).

Digestion. Samples were digested as tube gels after Lu & Zhu (2005), with amendments after Saito et al. (2014). Resuspended pellets were placed into 0.5 ml microfuge tubes (Eppendorf) and combined with 37 µl TE buffer, 103 µl gel premix, 3 µl TEMED (N,N,N',N'-Tetramethylethylenediamine, Acros Organics) and 7 µl APS to yield a final volume of 200 µl. Gels were left to polymerise for 1 h at 20 °C. After the addition of 200 µl of gel fix solution, they were incubated for 20 min at 20 °C. Any liquid was removed, and gels were carefully detached from tube walls with small pipette tips, transferred into larger 2 ml tubes, and incubated for 1 h with 1 ml gel fix solution at 350 rpm at 20 °C. Afterwards, gel fix solution was replaced with 1 ml destain solution, followed by incubation for 1.5 h at 350 rpm at 20 °C. Destain solution was removed and gels decanted onto a bench surface, where they were cut into ~1 mm^3 pieces using scalpels. This step simultaneously increased the gel's surface area and decreased the required reagent volumes in the subsequent steps. Gel pieces were returned to the tubes together with 1 ml wash solution and left overnight at 350 rpm and 20 °C. The wash step was repeated with fresh solution for 1 h on the following morning. Wash solution was removed and gel pieces were dehydrated three times with acetonitrile (Fisher) for 10 min at 350 rpm until hard and white, and then vacuum-dried for 5 min. Next, gels were incubated with 600 µl DTT solution for 1 h at 350 rpm at 56 °C to break any disulphide bonds between cystines. Absorbed volumes were recorded to calculate hydrated gel volumes. Gel pieces were then rinsed with 600 µl AMBIC, and finally incubated with 600 µl 55 mM IODA solution for 1 h at 350 rpm at 20 °C to alkylate the thiol moieties on the cysteines irreversibly. Breakage and subsequent alkylation of cysteine's thiol groups were necessary to avoid interference during protein digestion. Remaining liquid was removed and rinsed with 1 ml AMBIC for 10 min at 350 rpm at 20 °C, followed by triple dehydration with acetonitrile and vacuum-drying as above. One

hundred µg of the proteolytic enzyme Trypsin (Promega #V5280) was resuspended in 1 ml AMBIC on ice and it was added to the gels at 1 µg per 20 µg protein. AMBIC was added at appropriate volume (see DTT step) to rehydrate and submerse gels. Gels were checked for pH ~8 and left to digest overnight at 350 rpm at 37 °C. At the end of the digestion period (17 to 19 h), gels were briefly spun down at 13.5 rpm and supernatants collected in a fresh 2 ml microfuge tube. Fifty µl peptide extraction buffer was added, followed by incubation for 20 min at room temperature. Gels were spun down and supernatants were combined with the previous supernatants. This step was repeated once more. Combined supernatants were centrifuged for 20 min and transferred to fresh microfuge tubes to remove any remaining debris. Finally, samples were concentrated by vacuum drying and stored at -20 °C until analysis by HPLC-MS/MS. Sample volumes were recorded to calculate protein concentration, typically 1 µg μl^{-1}.

2.3.3 Heavy-Labelled Standard Peptides

Absolute concentration measurements of individual proteins were achieved using isotope labelled (^{15}N) standards of tryptic peptides occurring in the amino acid sequence of the proteins of interest. Following protocols by Saito et al. (2020) and Held et al. (2020), labelled standards were obtained and calibrated by heterologous expression of a custom-designed kanamycin-resistant plasmid (Novagen; obtained through PriorityGENE, Genewiz) in competent *E. coli* cells (Tuner(DE3)pLysS cells, Novagen), grown in ^{15}N-enriched medium. The plasmid vector contained an *E. coli* K12-optimised reverse-translated, spacer-separated (amino acid sequence: TPELFR) sequence of selected peptides and of multiple, commercially available standard peptides. The commercially available peptides served calibration purposes and included multiple peptides of a retention time calibration mixture (Product No. 88320, Pierce) and equine apomyoglobin peptides (Sigma). The compiled gene sequence was inserted into the plasmid vector pET30a(+) using the BamHI 5' and XhoI 3' restriction sites. Different nucleotide sequences were used to encode for the spacer to avoid repetition.

As per manufacturer instructions, the plasmid was suspended in TE buffer to 10 ng μl^{-1}, and of this 1 µl was added to 20 µl *E. coli* cells on ice. After 5 min on ice, cells were heated to 42 °C for 30 sec to initiate transformation, followed by 2 min on ice. At room temperature, 80 µl ^{15}N-labelled, kanamycin-containing (50 µl ml^{-1}) SOC medium was added and cells were incubated for 30 min at 37 °C at 300 rpm. Subsequently, 25 µl were transferred to pre-heated (37 °C) 50 µg ml^{-1} agar plates and incubated overnight. One colony was added to 500 µl ^{15}N-enriched SOC medium containing 50 µl ml^{-1} kanamycin as a starter culture, and incubated for 3 h at 37 °C at 350 rpm. Next, 200 µl starter culture were transferred into 50 ml flat incubation flasks (Fisher) with 10 ml SOC medium and incubated for approximately 3 h at 37 °C and 350 rpm until optical density (OD_{600}) 0.6 was reached. Protein expression was induced with 100 µl 100 mM IPTG (Isopropyl β-D-1-thiogalactopyranoside), and cells were incubated overnight at 25 °C at 350 rpm and harvested by centrifugation.

Cells were lysed using BugBuster detergent with added benzonase nuclease (Millipore). For this, cell pellets were suspended in 5 ml BugBugster reagent per 1 g of wet cell paste with 1 µl benzonase nuclease per 1 ml BugBuster reagent and incubated at room temperature for 20 min at 350 rpm. Afterwards, they were centrifuged at 4,000 rpm for 20 min at 4 °C and the supernatant was removed. The remaining pellet contained insoluble inclusion bodies of nearly pure protein, which were solubilised in 400 µl urea solution at 4 °C overnight, then reduced, alkylated, and trypsin-digested to obtain the standard peptide mixture. For this, 10 µl DTT solution was added to a 200 µl aliquot, followed by incubation at 56 °C for 1 h, addition of 40 µl IODA solution and a second incubation step at 20 °C for 1 h. Trypsin was resuspended to 0.5 µg μl^{-1} in 25 mM AMBIC, and added at a ratio of 1:50 to total protein mass as determined by BCA. Protein was left to digest at 350 rpm at 37 °C overnight.

The resulting peptide standard mixture, containing the heavy-labelled peptides of interest and of the commercial standards (Pierce and apomyglobin; see above) to stoichiometric (1:1) concentrations, was calibrated by adding a known amount (10 fmol μl^{-1}) of the commercially available standard peptides (i.e. not heavy-labelled). The ratio of Pierce (isotopically labelled according to JPT standards) or apomyoglobin (light) peptides to their heavy counterparts was calculated from the MS2 peak areas from the HPLC-MS/MS measurements (see Section 2.3.4 for details) to establish the peptide concentrations of the standard mixture. The resulting concentration was averaged across results from multiple Pierce and apomyoglobin peptides with a RSD of 11.7 %. Six-point dilution curves of the standard mixture between 0 and 10 fmol μl^{-1} were measured to determine the linear range of peak area to concentration of each peptide in injected samples. The injection volume was 10 µl, consistent with sample injection volumes (see Section 2.3.4).

2.3.4 Data Acquisition and Processing

Targeted proteomic measurements of absolute peptide concentrations were made by PRM on an Orbitrap Fusion Tribrid Mass Spectrometer equipped with a Thermo Flex ion source (ThermoFisher) coupled to a one-dimensional HPLC step (Dionex Ultimate3000 RSLC-nanospary). Samples were prepared with 2 µg sample protein that was diluted to 10 µl in buffer B and spiked with 10 fmol μl^{-1} of the heavy-labelled peptide mixture. Samples were injected into onto a trap column (100 µm × 150 mm, 3-µm particle size, 120-Å pore size, C18 Reprosil Gold, Dr. Maisch, packed in-house in a New Objective PicoFrit column) at a flow rate of 0.17 µl min^{-1} and eluted into the mass spectrometer over a 120-min continuous gradient of 5 to 95 % of buffer B and A. Precursor (MS1) ions were scanned for the m/z ratio in the of the heavy peptide standards and their natural light counterparts with a targeted mass list at 240,000 Orbitrap resolution at 380 to 1,580 m/z with isolation window at 1.6m/z. Only peptides included in the precursor inclusion list were isolated and sent for MS2 analysis. After collision-induced dissociation (CID) for fragmentation of the precursor ion into product ions, MS2

scans were performed in the Orbitrap with a maximum injection time of 50 ms and no dynamic exclusion. PRM produces full MS/MS spectra (i.e. including all precursor/product transitions) that allow for higher resolution and confidence in peptide identification and quantification compared with selected reaction monitoring (SRM), in which a refined set of transitions is filtered and detected.

Absolute peptide concentrations as fmol L^{-1} seawater were calculated from the ratio of the peak areas of the product ions (MS2) of natural (light) peptides to the heavy-labelled peptides (known concentration) (extracted using Skyline software; MacLean et al., 2010) multiplied by the spike concentration (i.e. 10 fmol μL^{-1}), with manual validation of peak shapes for each peptide and sample. Corrections were applied with regards to seawater filtration volume (7 ± 3 L), total protein mass (69 ± 34 µg; as per first BCA assay) relative to injected protein (always 0.2 µg μl^{-1}) and recovery (87 ± 18 %; calculated as per second BCA assay) to arrive at the final concentration, as shown for a hypothetical peptide 'A' in the below equation. Final peptide concentrations are reported representatively of corresponding protein concentrations.

$$\text{Concentration in seawater}_{\text{A,light}} = \frac{\text{Peak area}_{\text{A,light}}}{\text{Peak area}_{\text{A,heavy}}} \cdot 10 \text{ fmol } \mu l^{-1} \cdot \frac{\text{Total protein mass}}{0.2 \text{ µg } \mu l^{-1}} \cdot \frac{1}{\text{Filtration volume}} \cdot \frac{100}{\text{Recovery}}$$

Chapter 3 Iron Distribution in the Subtropical North Atlantic: The Pivotal Role of Colloidal Iron

Preface

The research presented in this chapter has been published in *Global Biogeochemical Cycles* (Kunde et al., 2019) and is reprinted here with some additional text and figures to meet the requirements for the thesis examination. I participated in the associated research cruise, collected all Fe samples, conducted the Fe measurements, and lead the interpretation of the results. With contributions from all co-authors, I wrote the manuscript and designed all figures, except Figure 3.4 (courtesy of A. Tagliabue). A copy of the publication is included in Appendix A.1, with associated data publicly from the British Oceanographic Data Centre under https://doi.org/doi:10/c63f.

Kunde, K., Wyatt, N. J., González-Santana, D., Tagliabue, A., Mahaffey, C. and Lohan, M. C. (2019). Iron distribution in the subtropical North Atlantic: The pivotal role of colloidal iron. *Global Biogeochemical Cycles*, 33. https://doi.org/10.1029/2019GB006326

3.1 Abstract

The low availability of the essential micronutrient Fe in the ocean impacts the efficiency of the biological carbon pump, and hence, it is vital to elucidate its sources, sinks, and internal cycling. We present size-fractionated dFe (<0.2 μm) measurements from 130 surface samples and 7 full-depth profiles from the subtropical North Atlantic during summer 2017 and demonstrate the pivotal role of cFe (0.02 to 0.2 μm) over sFe (<0.02 μm) Fe in controlling the dFe distribution. In the surface (<5 m), a strong west-to-east decrease in dFe (1.53 to 0.26 nM) was driven by a dust gradient, which retained dFe predominantly as cFe (61 % to 85 % of dFe), while sFe remained largely constant at 0.19 ± 0.05 nM. In the euphotic zone, the attenuation of dFe resulted from the depletion of cFe (0 % to 30 % of dFe), with scavenging as an important driver. In the mesopelagic, cFe was released from sinking biogenic and lithogenic particles, creating a zone of elevated dFe (0.7 to 1.0 nM) between 400 to 1100 m depth. While the ocean interior, below the mesopelagic and above the seafloor boundary, exhibited a narrow range of cFe (40 % to 60 % of dFe), the abyssal cFe fraction varied in range from 26 % to 76 % due to interactions with seafloor sediments and a hydrothermal source with almost 100 % cFe. Overall, our results produced an hourglass shape for the vertical cFe-to-dFe fraction and highlight the primary control of cFe on the dFe distribution.

3.2 Introduction

Iron is an essential micronutrient for marine primary production due to its enzymatic requirement in key metabolic functions such as photosynthesis, respiration, and the acquisition of macronutrients (Falkowski, 1997; Morel, 2003). For example, diazotrophs require Fe to fix N_2 into more bioavailable forms, where surface nitrate concentrations are sufficiently low to limit biological activity (<10 nM), such as in the oligotrophic North Atlantic gyre (Mahaffey et al., 2003; Moore et al., 2009). However, due to the low solubility of Fe(III), the thermodynamically stable Fe species in seawater (Kuma et al., 1996; Liu and Millero, 1999), chronically low surface water dFe concentrations prevail (<0.1 nM) that limit phytoplankton growth in large regions and result in a less efficient biological carbon pump (Moore et al., 2013). Concentrations exceeding the solubility limit can be maintained by organic ligands (Gledhill & Buck, 2012), which form a crucial component in the regulation of Fe bioavailability in the oceans (Tagliabue et al., 2014).

Superimposed on its low concentration is the 'hybrid' nature of Fe, where it displays a combined nutrient-type and scavenged-type vertical distribution (Bruland & Lohan, 2004). Scavenging, an umbrella term for adsorption, absorption, aggregation processes, and the eventual transfer to the particulate phase (Honeyman & Santschi, 1989; Wells & Goldberg, 1992), reduces the residence time of Fe and exacerbates the potential of Fe limitation.

Of the total Fe pool, only dFe, a continuum of exchangeable physicochemical species, is considered bioavailable (Tagliabue et al., 2017). Despite great progress in our understanding of the oceanic dFe cycle, thanks to GEOTRACES (http://www.geotraces.org/) and similar studies, major unknowns persist. These include its residence time with estimates ranging between 5 and 500 years (Tagliabue et al., 2016) and its bioavailability with variations over three orders of magnitude depending on the Fe substrate (Lis et al., 2015b). To determine the complex mechanisms controlling the particle reactivity and bioavailability of Fe, total Fe can be separated into different size classes using operationally defined filter sizes (Table 3.1). Size fractions of Fe can be defined as sFe (<0.02 µm), cFe (0.02 µm to 0.2 µm), dFe (<0.2 µm), apparent particulate (pFe_{app} >0.2 µm), and total dissolvable Fe (TDFe, unfiltered).

Table 3.1 The different size-fractionated Fe species used in this study.

Iron Species	Abbreviation	Filtration Size	Measurements
Soluble Fe	sFe	<0.02 µm	Direct measurement by FIA-CL
Colloidal Fe	cFe	0.02 µm <cFe <0.2 µm	Calculated using cFe = dFe - sFe
Dissolved Fe	dFe	<0.2 µm	Direct measurement by FIA-CL
Apparent particulate Fe	pFe_{app}	>0.2 µm	Calculated using pFe_{app} = TDFe - dFe
Total dissolvable Fe	TDFe	Unfiltered	Direct measurement by FIA-CL

Soluble Fe represents the 'truly dissolved' Fe fraction, although only a small portion is present as free Fe, while the majority is complexed by organic ligands such as high-affinity siderophores (Gledhill & Buck, 2012). Soluble Fe is highly bioavailable in both free and complexed forms and arguably the favourable species for biological uptake (Lis et al., 2015b; Shaked et al., 2005). In contrast, cFe, present in suspended nanoparticles or bound to colloidal-sized organic ligands, is rarely or less readily bioavailable (Chen & Wang, 2001; Wang & Dei, 2003) but can constitute almost 100 % of dFe (Fitzsimmons et al., 2015b).

Colloids serve as conduit for transferring Fe between the soluble and particulate phases in a two-step scavenging process termed 'Brownian pumping', which involves the sorption of sFe onto the colloidal intermediate followed by the aggregation of colloids to larger particles (Honeyman & Santschi, 1989; Wells & Goldberg, 1992). While scavenging and biological uptake result in the transfer from the dissolved to the particulate phase, particles simultaneously replenish the dFe inventory via dissolution or remineralisation (Milne et al., 2017).

Published data on size-fractionated Fe revealed two opposing hypotheses concerning the role of sFe and cFe in driving the Atlantic dFe distribution in particular. Largely invariable concentrations of sFe and variable cFe concentrations led Bergquist et al. (2007) to conclude that a dynamic colloidal

phase controls the dFe distribution. In contrast, Fitzsimmons et al. (2015b) and Fitzsimmons & Boyle (2014) measured variability in both cFe and sFe, and hence, attributed a joint control on dFe by both size fractions.

The North Atlantic is heavily impacted by Fe-rich dust deposition from the Sahara and to lesser extent from Europe and North America, receiving >40 % of the global dust flux to the ocean (Jickells et al., 2005). Prevailing wind patterns further introduce seasonality to the dust deposition, with highest dust-derived Fe fluxes in the summer (Sedwick et al., 2005), while the seasonal migration of the ITCZ controls wet deposition, which is efficient for delivering Fe to the ocean (Schlosser et al., 2014). Atmospheric deposition imprints elevated dFe concentrations in the surface waters (~0.5 to 1.0 nM) of the North Atlantic that are in excess of those observed in the less dusty South Atlantic (<0.5 nM) (Ussher et al., 2013). This strong external Fe source to the otherwise oligotrophic subtropical gyre creates a unique biogeochemical setting with a hotspot for N_2 fixation (Moore et al., 2009). Hence, the North Atlantic is a key region for the understanding of the oceanic Fe cycle.

Using the physical speciation of Fe from a 3,000 km-long surface transect and 7 full-depth profiles (Figure 3.1), the present study addresses the questions: 1) What external and internal factors drive the distribution of Fe in the subtropical North Atlantic? 2) How do sFe and cFe fractionally contribute to the dFe budget? 3) And which fraction exerts the greater regulatory control?

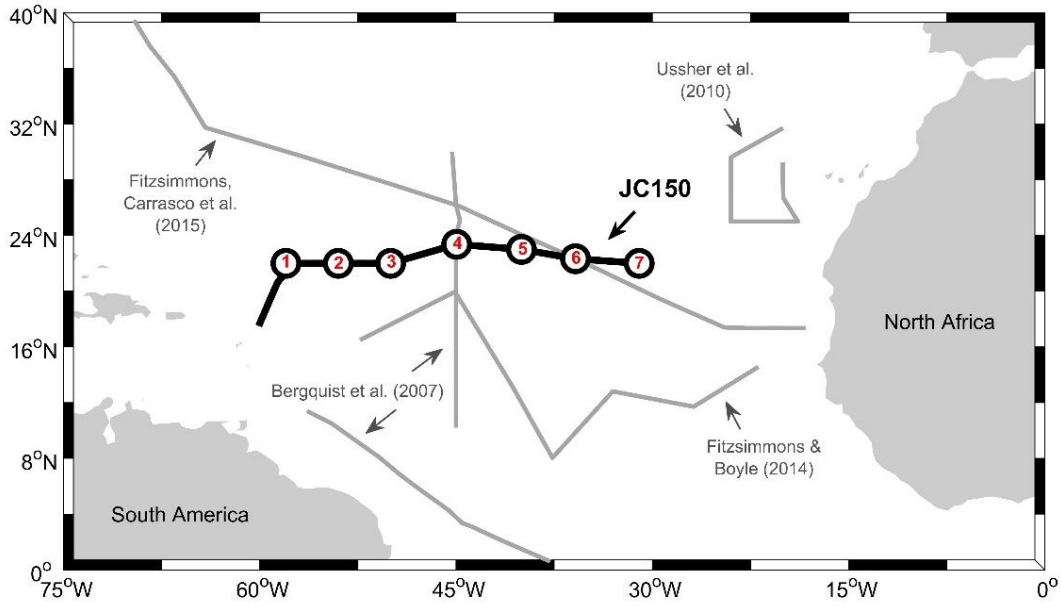

Figure 3.1 Map of the North Atlantic Ocean. Indicated are the stations of full-depth sampling (black dots, red numbers) and the cruise track along which surface samples were taken (black line). Cruise tracks of previous studies on size-fractionated Fe in this region are also shown (grey lines, arrows pointing to associated publication).

3.3 Methods

3.3.1 Sample Collection

Seawater samples were collected during cruise JC150 (Figure 3.1) in the subtropical North Atlantic in summer (26 June to 12 August 2017), sampling between Guadeloupe and Tenerife onboard the *RRS James Cook*. Seven stations were occupied for vertical profiling, while underway surface sampling (<5 m) was conducted along the transect at a resolution of ~0.23 ° longitude (~27 km). Seawater samples were collected using a Ti-rosette fitted with 24 × 10 L trace metal-clean Teflon-coated OTE bottles and a CTD profiler (Sea-Bird Scientific) deployed on a conducting Kevlar wire. Upon recovery, the OTE bottles were transported into a class-100 clean air van and pressurized (0.7 bar) with compressed air filtered in-line through a 0.2 μm PTFE filter capsule (Millex-FG 50, Millipore). Subsamples for dFe were filtered through 0.2 μm membrane cartridge filters (Sartobran 300, Sartorius) into trace metal-clean 125 ml low-density polyethylene bottles and acidified to pH 1.7 (0.024 M) by addition of 12 M ultrapure hydrochloric acid (HCl, Romil, UpA) under a class-100 laminar flow hood (Lohan et al., 2006). Samples for sFe went through an additional in-line filtration step inside a laminar flow hood through 0.02 μm syringe filters (Anotop, Whatman) before acidification. The filtration manifold consisted of PTFE manifold tubing and PVC peristaltic pump tubing, cleaned daily with weak 1 M HCl (SpA, Romil) and conditioned prior to use with low Fe seawater (Ussher et al., 2010; Wu et al., 2001). A new filter was used for each sFe sample. Samples for TDFe were collected unfiltered and then acidified. For the underway samples, seawater was pumped into the trace metal-clean van using a Teflon diaphragm pump (A-15, Almatec) connected by acid-washed PVC tubing to a towed 'Fish' sampler. These samples were filtered in-line (<0.2 μm), and acidified, while the filtration step was omitted for TDFe, and no underway sFe samples were taken.

3.3.2 Iron Measurements

All sFe, dFe, and TDFe samples were analysed in triplicate (three analytical peaks) using flow injection analysis with chemiluminescence detection (Floor et al., 2015; Obata et al., 1997) inside a class-100 clean air laboratory either onboard or at the National Oceanography Centre Southampton, UK. Briefly, each sample was spiked 1 hr prior to analysis with 0.013 M ultrapure H_2O_2 (Sigma-Aldrich) to ensure the complete oxidation of Fe (II) to Fe (III) (Lohan et al., 2006). Each sample was buffered in-line to pH 3.5 to 4.0 using a 0.15 M ammonium acetate buffer (Romil, SpA) before Fe(III) was preconcentrated onto the cation exchange resin Toyopearl-AF-Chelate 650 M (Tosohaas), typically for 60 s at a flow rate of 1.5 ml min^{-1}. Following a rinse step of a weak 0.013 M HCl (Romil, SpA), Fe was liberated from the resin using 0.24 M HCl (Romil, SpA) and entered

the reaction stream where it mixed with a pre-cleaned 0.015 mM luminol solution containing 70 µl L^{-1} TETA (Sigma-Aldrich), buffered to pH 9.4 to 9.6 using a 1 M ammonia solution (Romil, SpA). Chemiluminescence occurred following the addition of 0.4 M H_2O_2, with the light signal detected (425 nm) by a PMT (H82259, Hamamatsu). Iron concentrations were quantified using standard additions (TraceCERT, Fluka Analytical) to low Fe seawater. The limit of detection (three times the standard deviation of the lowest addition) was 0.03 ± 0.02 nM (n = 59), while the precision of three analytical peaks was 2.78 ± 2.02 % (n = 1764). The procedural blank was assessed at the beginning of each analytical run using UHP water, treated in the same way as the samples, and averaged 0.05 ± 0.03 nM (n = 69). Accuracy was established by repeat quantification of dFe in the SAFe reference samples yielding 0.11 ± 0.02 nM (n = 6) and 0.94 ± 0.04 nM (n = 17) for SAFe S and SAFe D2, respectively, which agree with the reported consensus values (S = 0.095 ± 0.008 nM; D2 = 0.96 ± 0.02 nM).

3.3.3 Auxiliary Parameters

Samples for Chl-*a* analysis from both the OTE bottles and the underway system were filtered through 0.7 µm glass microfiber filters (Whatman GF/F) and extracted in 90 % acetone overnight (Holm-Hansen et al., 1965). The Chl-*a* extract was measured on a pre-calibrated (Spinach Chl-*a* Standard, Sigma) fluorimeter (Turner Designs Trilogy) and used to calibrate the fluorescence sensor on the CTD (Seabird 911+) daily. Salinity was calibrated onboard using an Autosal 8400B salinometer (Guildline). Dissolved O_2 was measured by a Seabird SBE43 sensor, calibrated onboard using a photometric-automated Winkler titration system (Carritt and Carpenter, 1966). Turbidity was monitored using a WETLabs BBRTD light scattering sensor.

3.3.4 Calculations and Definitions

Mixed layers were calculated using a density change of 0.03 kg m^{-3} (de Boyer Montégut et al., 2004). To integrate Fe budgets across the upper ocean (Section 3.4.2.2), the 1026.5 kg m^{-3} isopycnal was chosen as lower boundary. We did not try to capture a specific water mass, instead the intention was to compare the total Fe inventory in this layer across stations. This resulted in integration depths between 350 m at Station 1 and 220 m at Station 7. Shallower isopycnals would not have captured the full DCM at Station 7 (Figure 3.6). Similarly, for remineralisation effects on dFe budgets in the mesopelagic (Section 3.4.2.3), we chose the isopycnals 1026.30 and 1027.50 kg m^{-3} as boundaries. This choice was made to cover the core of the low O_2 layer and its slopes from ~180 to 130 µmol kg^{-1} between 220 to 1100 m depth (details found in the Section 3.4.2.3 and in Figure 3.8). Here the biological remineralisation of organic matter was at maximum (by apparent oxygen utilisation proxy), so that its effect on dFe concentration and speciation could best be assessed between these isopycnals. This is different from Fitzsimmons et al. (2015b), who selected a distinct water mass,

namely the Central Water Layer between 1025.8 to 1027.1 µmol kg^{-1} (~100 to 600 m), in a similar exercise, but this would not have captured the full O_2 gradients in our data set. Apparent oxygen utilisation was used to calculate dFe:C ratios (AOU:C = 1.6, Martin et al., 1989). For a global comparison of size-fractionated dFe distributions in the mesopelagic (Section 3.4.2.3), we included all cFe measurements from the referenced data sets that lie within 10 % of the maximum AOU at each station. For consistency, we used the AOU from the global annual 1 ° grid of the World Ocean Atlas 2018 (Garcia et al., 2013). Extracted AOU values were in excellent agreement with those calculated from measured O_2 concentrations during JC150. Stations reportedly influenced by sedimentary or hydrothermal input were excluded. Annual dust fluxes were extracted from Albani et al. (2016). Colloidal Fe data was binned by annual dust flux in 1 g m^{-2} yr^{-1} increments.

3.4 Results and Discussion

3.4.1 Large-scale Distribution of Dissolved Iron

Figure 3.2 displays the full water column distribution of dFe across the transect with four main features of note: 1) an enrichment in the immediate surface layer, 2) a subsurface minimum between 50 to 200 m, 3) an increase in dFe in the mesopelagic between 400 to 1100 m, and 4) a large point source in the deep ocean at 45 °W (Figure 3.2). The most eye catching of these features was the midsection hotspot with up to 27 nM at 3300 m at Station 4, attributed to hydrothermal input from the Snakepit vent field on the Mid-Atlantic Ridge. The surface enrichment was most pronounced west of 54 °W with ≥1 nM dFe at Stations 1 and 2 (Figure 3.3), likely as a result of Fe-rich dust deposition from North Africa. In contrast, distinct dFe minima were present in the subsurface at all stations across the gyre with concentrations as low as 0.09 nM at 60 m in the east (Station 7). Concurrent with the location of the DCM, these dFe minima probably resulted from the combination of scavenging and biological uptake. Below the DCM to a depth of ~1100 m, dFe gradually increased to maxima of 0.7 to 1.0 nM, with highest concentrations in the east. Mesopelagic dFe enrichments correlated with AOU (R^2 = 0.58, n = 100) and probably derived from the continued dissolution of sinking dust particles and from the remineralisation of organic matter. Away from external sources and from the influence of biological processes, the concentration of dFe in the ocean interior below the low O_2 waters and above the seafloor water-sediment interface was 0.67 ± 0.14 nM, excluding the hydrothermal influence observed at Station 4.

In the following, we are going to show that dust acted as the main driver of the surface Fe distribution with far-reaching effects on the underlying water column, while sediment resuspension and hydrothermalism were important in the abyss. Scavenging was the major sink. Our main finding is that the cFe distribution results in an ‘hourglass’ pattern with depth. This is due to the decoupling of

cFe and sFe, where the major sources and sinks of dFe result in increases or decreases of the cFe budget, with large ranges in both the surface ocean and close to the seafloor.

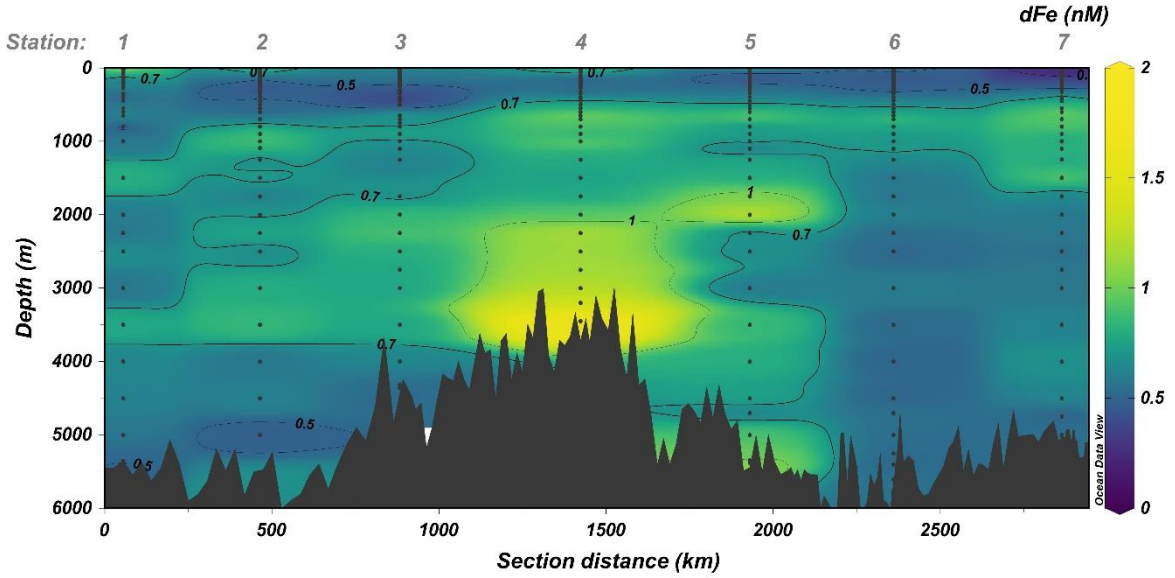

Figure 3.2 Section plot of dFe concentrations against distance from west to east. The very high concentrations measured over the Mid-Atlantic Ridge at Station 4 reached up to 27 nM, but are excluded from the colour bar. The plot was produced with Ocean Data View (ODV) (Schlitzer, 2016), using weighted-average gridding for interpolation with maximum scale lengths of 35 and 33 ‰ for the x- and y-axes, respectively.

The current understanding of the partitioning between cFe and sFe for regulating the dFe distribution stems from the pioneering work done by (Bergquist et al., 2007) and more recently by Fitzsimmons et al. (2015b), the latter of which indicated an equal control between cFe and sFe, given the evidence for a more dynamic soluble phase compared to Bergquist et al.'s (2007) conclusions that colloids alone accounted for the observed partitioning. Based on our cFe data, we argue it is a balance of both of these mechanisms depending on the presence or absence of external drivers at different depths. Where dFe is supplied or removed, the colloidal and soluble phases were strongly decoupled with cFe taking on a greater regulatory control for the dFe distribution and shaping the wide top and bottom sections of the hourglass. In the interior ocean away from external sources or sinks, the dFe partitioning was balanced between cFe and sFe in a steady-state equilibrium, which formed the neck of the hourglass.

3.4.2 Distribution of Soluble and Colloidal Iron

3.4.2.1 The Dusty Surface Ocean

The JC150 transect underlies the northern extent of the Saharan dust plume that provides approximately 200 Tg yr^{-1} of dust to the North Atlantic (Jickells et al., 2005). Dust deposition from Sahara-influenced air masses regulates the Fe budget in the surface North Atlantic via aerosol

solubilisation (Sedwick et al., 2005; Ussher et al., 2013) and is overwhelmingly the largest flux of Fe to this region (Ussher et al., 2013).

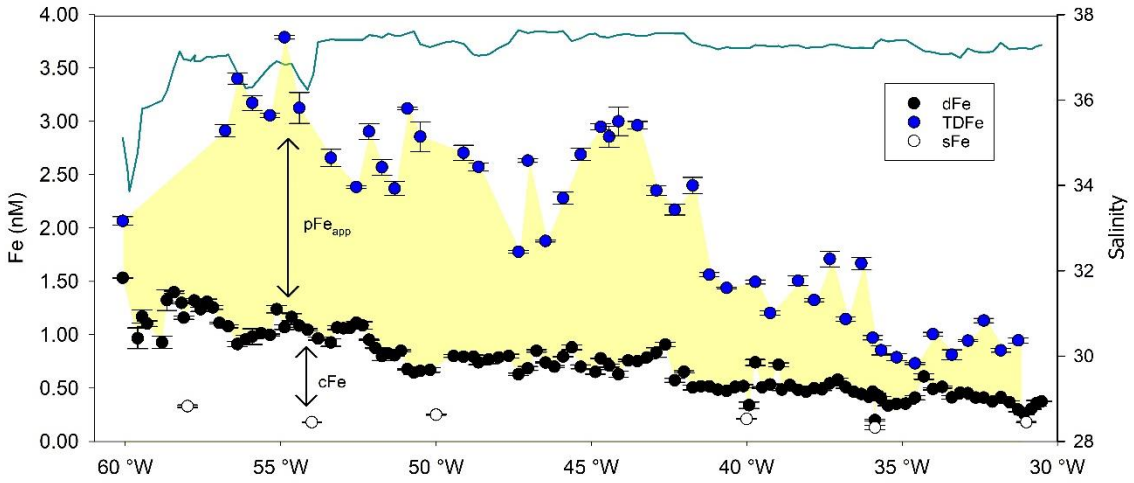

Figure 3.3 Surface concentrations of dFe (black), sFe (white), TDFe (blue), and salinity (cyan line) against longitude along the cruise track. The calculated concentrations of cFe and pFe_{app} are indicated with arrows. The dFe and TDFe concentrations are from the underway samples (<5 m); the sFe concentrations are from the shallowest water column samples (between 15 and 25 m) at each station. Error bars show one standard deviation of the mean concentration of three analytical replicates.

Our surface sampling revealed a longitudinal decrease of surface dFe concentrations from west to east, with a maximum of 1.53 nM at 60 °W and a minimum of 0.26 nM at 31 °W (Figure 3.3). Concentrations >0.5 nM are typical for the dust-dominated North Atlantic (Fitzsimmons et al., 2015b; Hatta et al., 2015; Measures et al., 2008; Sedwick et al., 2005), which contrast with concentrations of <0.25 nM for the dust-limited South Atlantic, Pacific, and Southern Ocean (Buck et al., 2018; Chever et al., 2010; Fitzsimmons et al., 2015c; Nishioka et al., 2001). The west-east gradient we observed appeared counterintuitive with regard to the location of the Saharan source. However, it was consistent with a compilation of upper ocean dFe data from the North Atlantic (Figure 3.4), where Fe profiles appeared more influenced by dust in the west compared to the east. This is because large amounts of dust are entrained into the warm Saharan Air Layer (SAL), which is trapped at altitudes above the dust-free northeasterly trade wind inversion and exported westward with the strong circulation of the Azores-Bermuda High during summer (Schepanski et al., 2009; Tsamalis et al., 2013). As the SAL descends westward, the dust increasingly mixes into the marine boundary layer, from where it seeds the surface ocean (Tsamalis et al., 2013), thereby imprinting the longitudinal gradient of dust-derived Fe that we observed. Previous investigations into atmospherically derived Fe at BATS confirm a large Saharan dust source during summer (Fishwick et al., 2014; Sedwick et al., 2005). Furthermore, dissolved aluminium (dAl), which has no biological role for phytoplankton growth but a large lithogenic source (2nd most abundant element in continental crust; Wedepohl, 1995), strongly correlates with dFe across the surface transect (R^2 = 0.70) (Artigue et al., in preparation). Hence, it serves as an independent proxy for dust being the dominant driver of

dFe during our sampling campaign, despite the strong gradient in phytoplankton biomass across the basin (Figure 2.2d).

Accompanying measurements of TDFe displayed a similar trend to dFe, decreasing from >3 nM in the west to <1 nM in the east, but with larger variability than dFe (Figure 3.3). The dFe:pFe_{app} ratio was 0.57 ± 0.25 for the entire transect except for the most western sample at 60 °W. Here, the pFe_{app} concentration was only 0.53 nM, and the dFe concentration was 1.53 nM, resulting in a dFe:pFe_{app} ratio of 2.87 in stark contrast to the remaining transect, and suggesting a lower influence of dust deposition at this location. The surface samples west of 58 °W (Station 1) were collected at lower latitudes (17.5 to 21.6 °N) than the remaining transect (≥22 °N) (Figure 3.1), where the lower salinities (34 to 36) (Figure 3.3) indicate the northern boundary of the seasonal Amazon and Orinoco River plumes (Fournier et al., 2015). Rijkenberg et al. (2014) showed a strong linear inverse correlation between dFe and salinity during summer 2013. Hence, the elevated dFe concentrations in the surface samples approaching Station 1 possibly originated from the river plume, which may have lost pFe_{app} relative to dFe during the seaward transport and mixing with seawater.

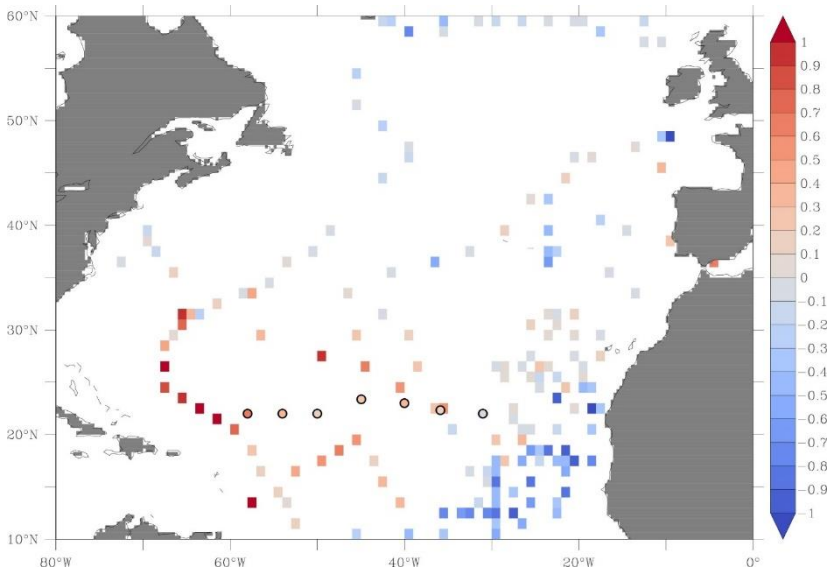

Figure 3.4 Surface plot of the North Atlantic showing the difference of dFe concentration averaged over 0 to 50 m depth minus the concentration averaged over 100 to 150 m depth in a 1° x 1° grid. Red values show higher concentrations in the surface than at depth, a typical dust-driven behaviour. Blue values show lower concentrations in the surface than at depth, a typical nutrient-like behaviour. Circles indicate JC150 stations. Data is from Tagliabue et al. (2012) and augmented with data from the GEOTRACES IDP17 (Schlitzer et al., 2018).

The concentrations of sFe from the shallowest depth from the CTD averaged 0.19 ± 0.05 nM across the transect. Importantly, they displayed no west-to-east gradient, in contrast to the basin-scale distributions of the other Fe size fractions, and appeared to be independent of the magnitude of dFe and pFe_{app} inputs. The average excludes the slightly elevated sFe concentration of 0.33 nM at 58 °W (Station 1), which was possibly an artefact of the Amazon and Orinoco River plumes.

What processes might be responsible for such small variation in the surface sFe concentrations? Potential biogeochemical controls include Fe-binding ligand distributions, a threshold for dust-derived Fe dissolution into the soluble phase or a dilution threshold, beyond which sFe is unreactive. The two size-fractionated ligand studies available concluded that ligand distributions cannot account for size-fractionated Fe distributions alone (Cullen et al., 2006; Fitzsimmons et al., 2015a). Moreover, surface sFe concentrations higher (Ussher et al., 2013) or lower (Chever et al., 2010) than our ~0.2 nM have been observed previously and render the threshold arguments unlikely. Alternatively, the resolution of our surface sFe data alongside the small variations in the concentrations may prevent the identification of a potential gradient for sFe and its biogeochemical controls.

Regardless, the subtlety of the changes in the surface sFe concentrations implies that cFe was the driver of the gradient in dFe concentrations in surface waters across the subtropical North Atlantic. The colloidal contributions to the dFe pool were highest where dFe and TDFe concentrations were elevated as a result of dust input (and riverine input at Station 1), with values of 61 % to 85 % cFe for dFe concentrations of 0.53 to 1.25 nM between Stations 1 and 6. The maximum colloidal contribution of 85 % cFe for a dFe concentration of 0.77 nM was observed at Station 3. In contrast, only 32 % of dFe was in the colloidal form at Station 7 where the dFe concentration was lowest (0.27 nM). While the high surface cFe fractions of >60 % were consistent with previous studies in the dust-dominated North Atlantic (Fitzsimmons et al., 2015b; Fitzsimmons and Boyle, 2014; Sedwick et al., 2005; Ussher et al., 2010), the absence of a surface colloidal maximum at Station 7 is rather atypical of observations from the North Atlantic and resembled the dust-limited surface waters of the Pacific (Fitzsimmons et al., 2015c; Nishioka et al., 2001). The tight coupling of TDFe, dFe, and cFe trends across the basin suggests that higher Fe in the particulate phase results in more dFe via cFe, and hence particles have an important influence on the dFe size partitioning. These links were similarly evident in the size-fractionated Fe data sets, when plotting the top 50 m of the US-GEOTRACES GA03 section, just north of our transect (Fitzsimmons et al., 2015b; Lam, 2018; Twining, 2014).

Seawater leaches of aerosol particles showed that dust-derived dFe is predominantly retained as cFe in the ocean, either as eroded fragments or due to the authigenic formation of colloidal-sized Fe-oxyhydroxides or organic complexes (Fishwick et al., 2014), which explains the observed colloidal maxima in the high dFe-surface waters. Dust deposition is at its minimum in the eastern subtropical North Atlantic during summer because of the high-altitude transport of the SAL and the resulting deposition in the west. Hence, the unusually low colloidal fraction at Station 7 likely resulted from sampling this seasonal extreme. This is an important insight because the North Atlantic is often characterised in bulk as a high dust and high Fe region (Moore et al., 2009), but our results demonstrate the sensitivity of the Fe inventory to strong regional and seasonal variability within the subtropical North Atlantic. This sensitivity resulted in two endmembers along our section: A high

dust endmember with a high colloidal contribution to dFe and a low dust endmember with a low colloidal contribution to dFe.

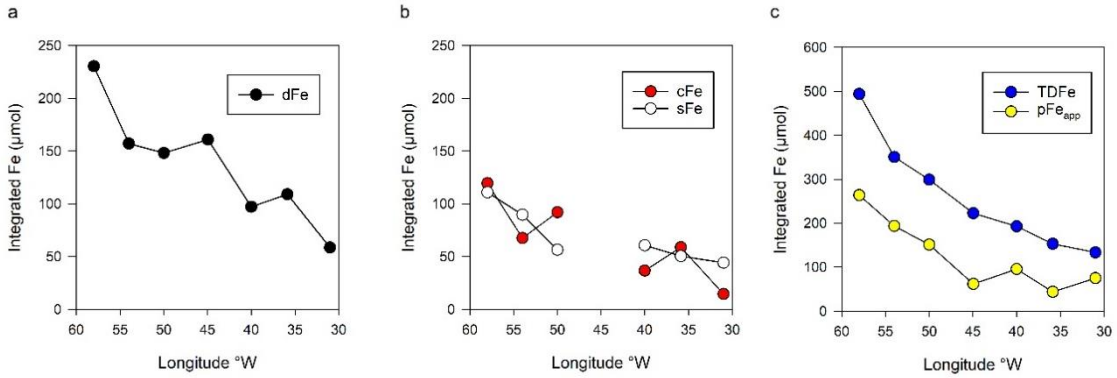

Figure 3.5 The integrated upper ocean Fe inventories of (a) dFe (black), (b) sFe (white) and cFe (red), and (c) TDFe (blue) and pFe_{app} (yellow). Station 4 at 45 °W has been excluded for sFe and cFe due to the lack of data points.

While the instantaneous effect of dust deposition in the immediate surface is on cFe, a dust-driven effect for sFe is apparent when considering the entire upper water column (using integrated Fe inventories). Increasing the sampling resolution enables us to detect impacts on the surface water column after the dust-derived Fe had the chance to undergo internal cycling. Dissolved Fe, cFe, and pFe_{app} inventories were higher in the west than in the east, following a similar gradual longitudinal decrease as in the immediate surface (Figure 3.5), confirming that dust affects the underlying layers too. Surprisingly, the sFe budget also decreased clearly from west to east, a trend not apparent in the immediate surface (Figure 3.3). An important caveat is that the shoaling of the isopycnals toward the west lowers the integrated budgets. However, depth-normalised integrated Fe budgets portray the same overall longitudinal trends for all size fractions. A possible mechanism driving the higher sFe in the upper ocean in the west versus the east is the indirect source from dust, by which Fe is partially mobilised from the colloidal into the soluble phase via ligands as suggested by aerosol-leaching experiments (Fishwick et al., 2014). This transformation could increase the bioavailable portion of dFe.

3.4.2.2 Iron Depletion through the Euphotic Zone

Deep chlorophyll-*a* maxima are a widespread phenomenon in the subsurface of the (sub)tropical oceans and positioned across the nutriclines, where macronutrient supply from deeper waters sustains low light-adapted primary production (Cullen, 2015). The upper water column distributions of macronutrients and Fe are decoupled due to greater remineralisation length scales of Fe (Boyd et al., 2017). Consequently, the DCM can become Fe limited (Sunda & Huntsman, 1997). At most of our stations, the dFe concentration gradually decreased through the euphotic zone toward the DCM, often reaching minima between 60 and 200 m, where Chl-*a* peaked (Figure 3.6a-g). Moreover, there was

a gradual transition from the strongly dust-driven dFe profiles at Stations 1 and 2, where the difference between surface maxima and DCM minima was largest, to the more nutrient-like profile at Station 7 (Figure 3.6a-g). These two endmembers resulted from the dust-driven surface dFe distribution (Figure 3.3) and appear to be characteristic of the western and eastern North Atlantic, respectively (Figure 3.4).

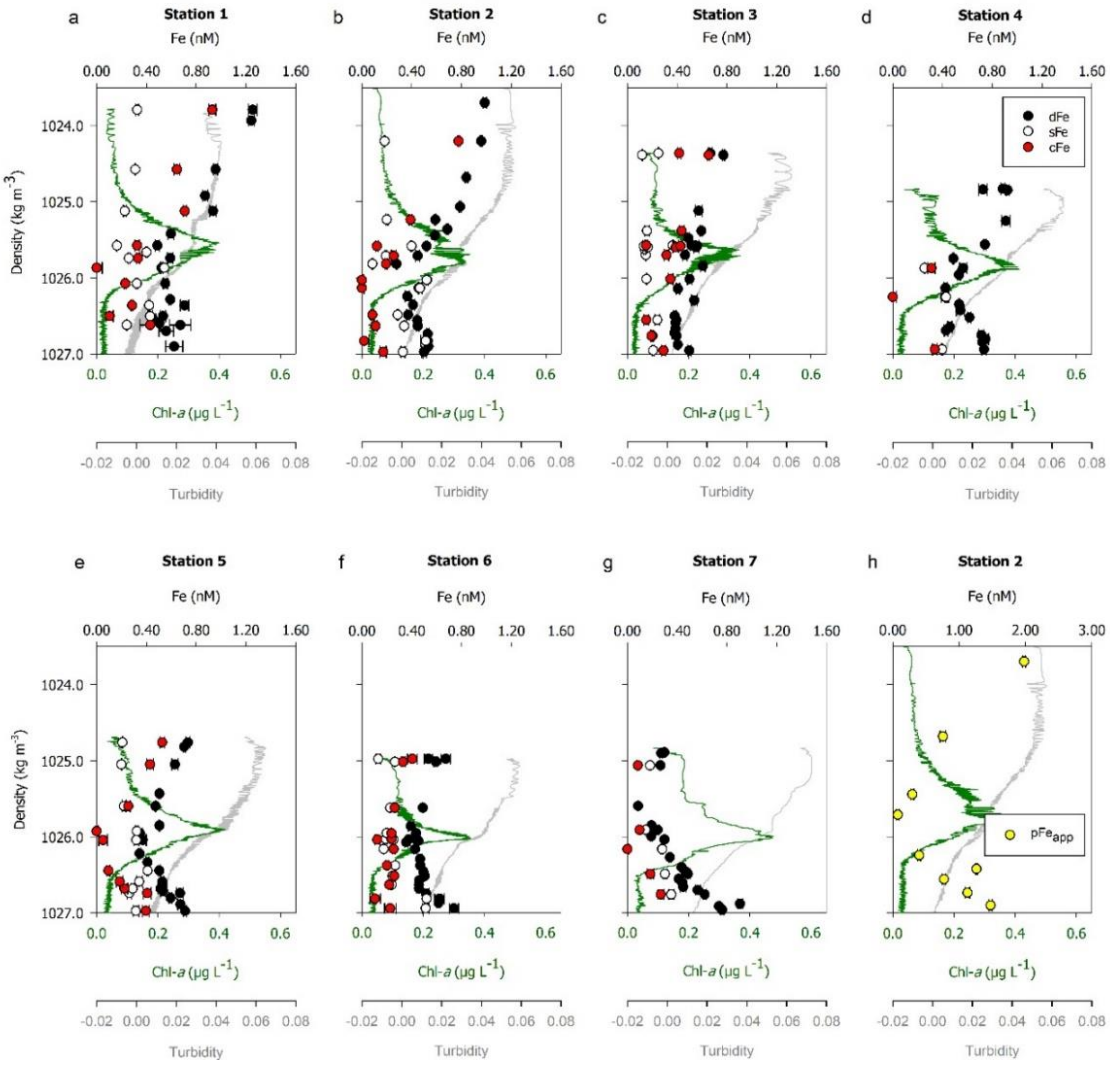

Figure 3.6 (a–g) Profiles of dFe (black), sFe (white), and cFe (red) against density in the upper water column at each station. (h) Representative profile of pFe_{app} (yellow) against density at Station 2. Error bars show one standard deviation of the mean concentration of three analytical replicates. For the calculated cFe and pFe_{app} concentrations, associated measurement errors were propagated. Traces of Chl-*a* (green lines) and turbidity (grey lines, arbitrary units) are included.

The attenuation of the dFe signal between the surface and the DCM was clearly controlled by the attenuation of cFe, which typically decreased to <30 % of dFe in the DCM (Figure 3.6a-g) or even disappeared completely, which was most pronounced at Station 5. Concentrations of sFe were less variable between surface and DCM with slight increases observed in the centre (Station 5) or on the slopes (Stations 2 and 4) of the DCM, where it accounted for up to 100 % of dFe. These characteristics are in line with previous observations from the DCM of the Atlantic (Fitzsimmons et

al., 2015b) and Pacific (Fitzsimmons et al., 2015c). In other words, cFe was removed over sFe in the euphotic zone despite the widespread understanding that sFe is more bioavailable (Birchill et al., 2017). This leads to the question: Does the gradual depletion of dFe via cFe through the euphotic zone mark a biological preference for cFe over sFe, or does scavenging control the observed Fe distribution?

It is possible that the elevated Fe demands of the DCM community (Hogle et al., 2018; Sunda & Huntsman, 1997) force the utilisation of the cFe pool, for example, via a ligand-mediated transfer into the soluble phase prior to uptake (Chen & Wang, 2001; Wang & Dei, 2003). If the uptake is time lagged from the transfer between phases, cFe would be depleted, and (ligand-bound) sFe would accumulate, which matches the observations in many of our depth profiles. However, the few size-fractionated ligand studies concluded that ligand distributions alone cannot account for the observed Fe distributions (Cullen et al., 2006; Fitzsimmons et al., 2015a), while Fitzsimmons et al. (2015a) found no increase in soluble-sized ligand production in the DCM. In addition, cFe and Chl-*a* were not strongly negatively correlated (R^2 = −0.27, surface to 1026.5 kg m^{-3}), which would reflect biological uptake, and we did not observe an enrichment in pFe_{app}, which would capture the cellular Fe pool.

Instead, we observed simultaneous minima of pFe_{app} and cFe in the DCM (Figure 3.6h and Figure 3.7) and a stronger positive correlation of cFe with turbidity as an indicator of particle abundance (R^2 = 0.48). This strengthens the argument that cFe is not simply transferred from the dissolved to the particulate phase, but both phases are removed together, leading us (and others: Ohnemus & Lam, 2015) to conclude that dFe (in form of cFe) is shuttled out of euphotic zone via sinking particles and that this scavenging is a principal mechanism driving the distributions of cFe, dFe, and pFe_{app} here. In support of this is also the change in Chl-*a* between the mixed layer and the DCM (for example 0.288 µg L^{-1} Chl-*a* at Station 2), which can account for a change of ~0.05 nM dFe, when converted to biomass C (using Chl-*a*:C = 0.02 g g^{-1}; Arteaga et al., 2016) and Fe (using Fe:C = 45 µmol mol^{-1}; Twining et al., 2015). This is more than an order of magnitude below the measured difference of 0.71 nM dFe between the mixed layer and DCM. Therefore, biological uptake by phytoplankton appears to be a minor contributor to the removal of dFe (cFe), but it may be important in maintaining sFe levels via the replenishment from other Fe fractions.

Despite the likely co-occurrence of these different processes, our size-fractionated measurements identified the preferential removal of cFe, not sFe, alongside pFe_{app} and, hence, the potential importance of particle scavenging over biological uptake for the removal of Fe. The increasing resolution of size-fractionated Fe measurements repeatedly confirm the cFe minima in the DCM as an intriguing phenomenon of the subtropical ocean which warrants further investigations, as highlighted in a recent review by Anderson (2020), because the central implication of these minima

is that despite large Fe-rich dust depositions, the efficient removal of dFe leads to a potential Fe limitation in the DCM.

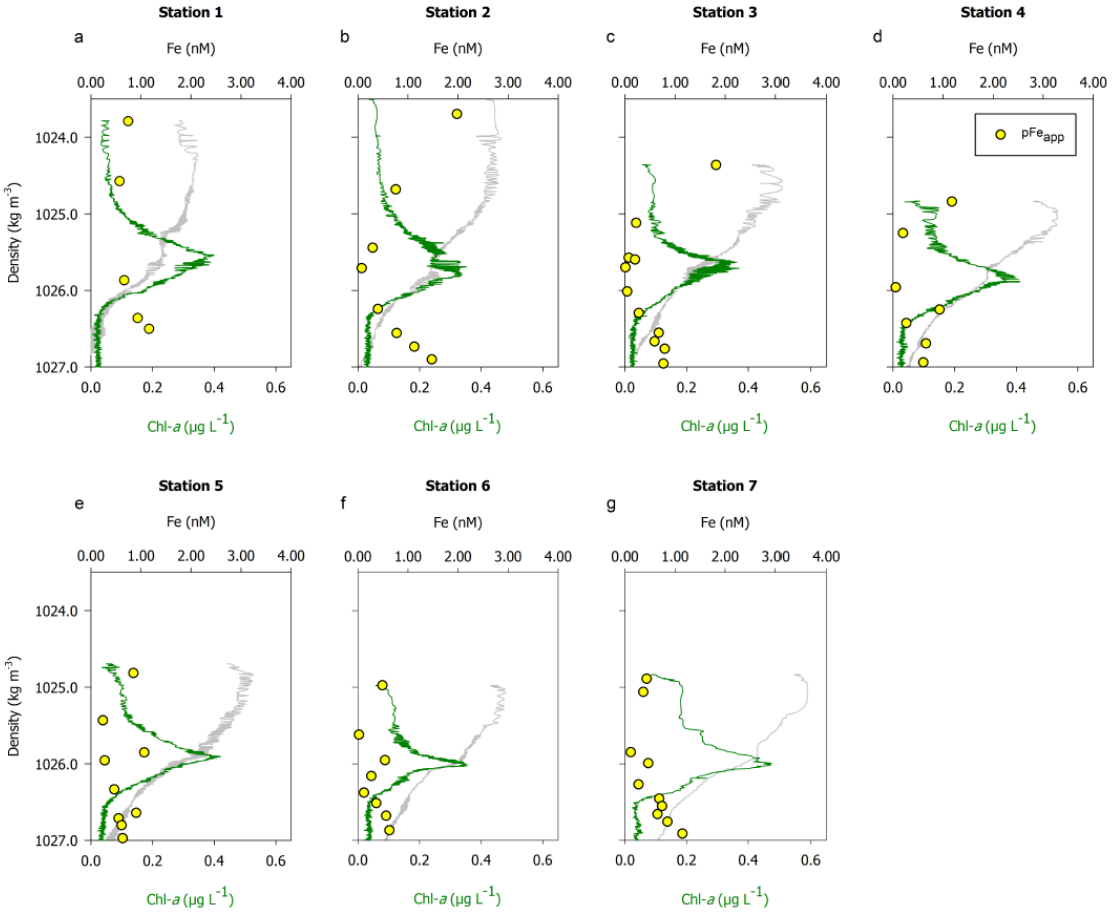

Figure 3.7 Profiles of pFe_{app} against density in the upper water column (~0 to 500 m) at Stations 1 to 7 (a-g).

3.4.2.3 The Mesopelagic: Mirroring the Surface Ocean

It is a long-standing paradigm that the distributions of major nutrients below the euphotic zone are shaped by the balance between a preformed and a regenerated component, which are the result of physical transport and the microbial degradation of organic matter (remineralisation), respectively. Nutrients released by remineralisation can sustain a major fraction of primary production when resupplied into the surface. Unlike the macronutrients, Fe is subjected to additional processes, such as scavenging, that affect its subsurface inventory (Hatta et al., 2015; Tagliabue et al., 2014b; Twining et al., 2015). Apparent oxygen utilisation provides a measure of remineralisation at depth, which is the result of local remineralisation that acts on sinking biogenic particles and of the transport of aging water masses. We observed a zone of lower O_2 concentrations (120 to 150 µM) and elevated dFe concentrations (0.7 to 1.0 nM) between 400 to 1100 m depth (Figure 3.2 and Figure 3.8). The dFe:C ratio along the oxycline was 5.8 ± 0.50 µmol mol^{-1} (R^2 = 0.58, n = 100), which was within the range of ratios previously reported for the North Atlantic (Fitzsimmons et al., 2015b; Hatta et al.,

2015; Milne et al., 2017), but lower than cellular ratios in phytoplankton of 33 to 57 µmol mol^{-1} (Twining et al., 2015), which demonstrates the impact of scavenging as a post-remineralisation sink. Microbial recycling also occurs throughout the upper ocean, but O_2 concentrations are in equilibrium with the atmosphere, and hence AOU cannot function as a measure of remineralisation.

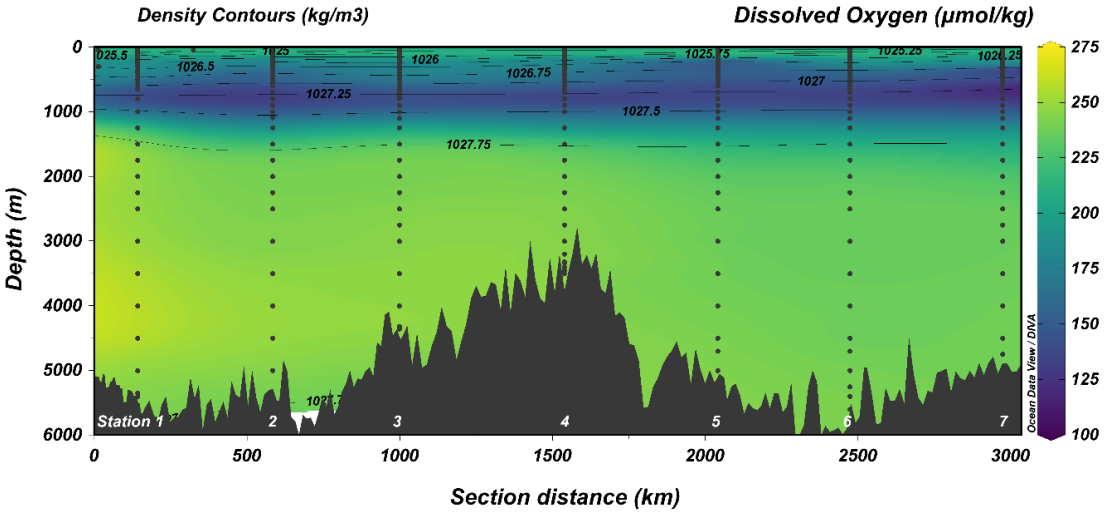

Figure 3.8 Section plot of dissolved O_2 against distance from west to east overlain with contours of the isopycnals between 1025 and 1027 kg m^{-3} in 0.25 kg m^{-3} increments. The plot was produced with ODV (Schlitzer, 2016).

In contrast to the biogenic-dominated macronutrients, the majority of Fe-bearing particles in our study region is lithogenic. Boyd et al. (2010) showed that the dissolution of Fe from lithogenic particles dominates over the release from biogenic material in the North Atlantic. Furthermore, Fe isotope measurements revealed that the entire water column may be impacted by dust (Conway & John, 2014). If the mesopelagic dFe inventory is driven by the release from lithogenic particles, it leads to the hypothesis that the dominance of cFe over sFe may be observed at depth because dust-derived Fe occurs predominantly as cFe. Within our sample subset around the AOU maximum, the dFe size partitioning was 37 ± 16 % cFe, but a global comparison of published size-fractionated dFe data from the mesopelagic enables us to probe this theory (Figure 3.9). Regions of high annual dust flux (6.2 to 22.6 g m^{-2} yr^{-1}) display higher mean cFe contributions of 60 % to 48 % of dFe, respectively. In contrast, regions of lower dust flux (1.0 to 5.1 g m^{-2} yr^{-1}) exhibit lower mean cFe contributions of 39 % to 42 % of dFe. At dust fluxes of <0.3 g m^{-2} yr^{-1}), the cFe contributions are lowest with 35 % of dFe. This pattern of high colloidal fractions in the mesopelagic at high dust in contrast to low colloidal fractions at low dust is analogous to the surface ocean, where colloidal maxima are present in regions of high dust (this study; Fitzsimmons et al., 2015b) and absent in dust-limited regions (Nishioka et al., 2001). The reason colloidal fractions from high dust regions are not as high in the mesopelagic compared to the surface (61 % to 85 %) may be explained by the two-step model of Fishwick et al. (2014), in which some cFe is transferred into the soluble phase over

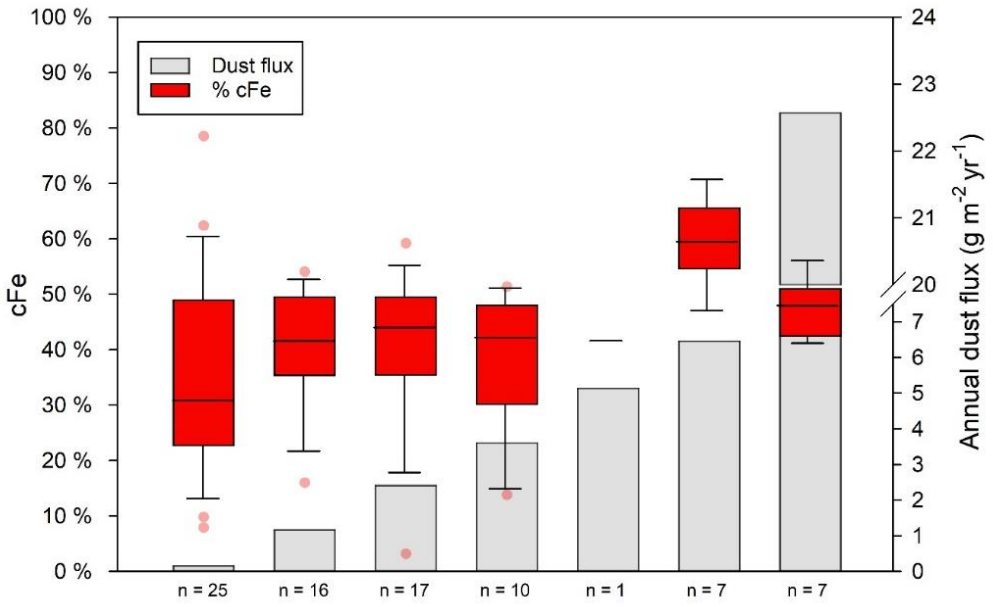

Figure 3.9 Box plots of the partitioning of dFe into the colloidal fraction (red bars) at remineralisation depths of different oceanic regions, in order of increasing annual dust flux (grey) from left to right. Boxes represent the interquartile range; the middle line represents the median. Whiskers frame the 10th and 90th percentiles, while data points outside this range are shown as dots. The cFe data used in this plot were compiled from the present study and from Nishioka et al., 2001; 2013), Fitzsimmons et al. (2015b, 2015c), Bergquist et al. (2007), Ussher et al. (2010), and Chever et al. (2010), and binned by dust flux (see methods). Along the x-axis, n indicates the number of cFe measurements for each bin. For details on which data contributed to which bin, the reader is referred to Table 3.2.

Table 3.2 Details on which stations and associated cFe measurements were included in which dust flux bin for Figure 3.9.

Bin #	Dust flux ($g\ m^{-2}\ yr^{-1}$)	Mean dust flux ($g\ m^{-2}\ yr^{-1}$)	Mean % cFe	# cFe measurements	Data contributions (Stations as referred to in respective publication)
1	0 to 1	0.15	35	25	Nishioka et al., 2013 (ER12) Chever et al., 2010 (S1, S2, S3, S4, S5, L3, L4, L5, L6, L7) Bergquist et al., 2007 (24.5 °S profile) Fitzsimmons et al., 2015c (ALOHA)
2	1 to 2	1.16	41	16	Nishioka et al., 2001 (PAPA) Fitzsimmons et al., 2015b (USGT11-10, USGT11-12 and USGT11-14)
3	2 to 3	2.14	41	17	This study (Stations 2 and 3) Fitzsimmons et al., 2015b (USGT11-16 and -18) Nishioka et al., 2013 (ER8)
4	3 to 4	3.16	39	10	This study (Station 5) Ussher et al., 2010 (Station 10) Fitzsimmons et al., 2015b (USGT11-20)
5	4 to 5	-	-	-	No data fell into this bin; bin excluded in Figure 3.9.
6	5 to 6	5.13	42	1	This study (Station 7)
7	6 to 7	6.46	60	7	Fitzsimmons et al., 2015b (Station USGT11-22) Bergquist et al., 2007 (10 °N profile)
8	>7	22.57	48	7	Nishioka et al., 2013 (Station ER6)

time. Furthermore, a portion of the released cFe is likely re-scavenged. The tug-of-war between these mechanisms is eventually manifested in the 37 ± 16 % cFe that we observed.

The main result of this global comparison is a strong coupling between the speciation of dFe in the mesopelagic and the surface dust deposition. The implication is that the spatial variability of subsurface dFe distributions is driven by regional dust flux. This highlights the sensitivity of the Fe cycle to changes in atmospheric supply, especially in the light of past and future changes. Therefore, constraining the mesopelagic Fe cycling as a major pathway for the resupply to the surface requires the investigation of cFe specifically rather than bulk dFe.

3.4.2.4 The Deep Iron Inventory: Hydrothermalism and Seafloor-Sediment Interactions

While atmospheric deposition provides the largest input of Fe to the surface North Atlantic, modelling efforts showed that sedimentary release and hydrothermal venting prevail globally by at least one order of magnitude (Tagliabue et al., 2014a, 2010). The JC150 transect captured the influence of both of these sources on the deep Fe inventory.

Station 4 targeted the Snakepit hydrothermal vent field located around 3500 m depth on the Mid-Atlantic ridge (Beaulieu, 2015). Anomalies in the turbidity confirm that we sampled the neutrally buoyant hydrothermal plume with a dFe concentration maximum of 27 nM at 3300 m (Figure 3.10). Hydrothermally derived Fe can overcome near-field precipitation and be transported over large distances (>1000 km) (Resing et al., 2015; Saito et al., 2013) via its stabilisation either by organic complexes (Sander & Koschinsky, 2011) or in colloidal-sized nanoparticles (Revels et al., 2015; Yücel et al., 2011). Our plume dFe samples were composed of 92 ± 3 % (n = 4) cFe, similar to the 89 % to 96 % cFe in the plume of the nearby Trans-Atlantic Geotraverse vent field (Fitzsimmons et al, 2015b).

Apart from its role as an important source of Fe, the Mid-Atlantic ridge also acts as a physical barrier between the eastern and western abysses. The physical speciation measurements of Fe revealed opposing trends on either side of the ridge. In the west, we observed elevated pFe_{app} concentrations of 6.4 nM at 5400 m at Station 1 and 4.0 nM at 5900 m at Station 2, compared to ≤2.0 nM for all other stations (data not shown). No equivalent increase in dFe concentrations was observed (Figure 3.2), and the two deepest samples collected at 50 and 20 m above the seafloor decreased by 0.13 and 0.09 nM at Station 1 and 2, respectively. The cFe contributed only 26 % and 29 % to the dFe budget, lower than values from the overlying water column. In the east, this pattern was reversed. At Station 5, dFe concentrations reached 1.26 nM at 20 m above the seafloor with a cFe fraction of 76 %, and at Station 7, 63 % of dFe was in the colloidal form although no simultaneous increase in the dFe concentration was detected. Gardner et al. (2017) showed that thick benthic nepheloid layers form in

the western North Atlantic, and Lam et al. (2015) and Revels et al. (2015) reported higher lithogenic and Fe-rich particle abundances in this area, which is evident in our pFe_{app} measurements. The large surface area and high concentration of the resuspended particles hold high scavenging potential, so that the scavenging of dFe in the form of cFe onto sedimentary particles may dominate over dissolution and produce a cFe signature of <50 % alongside decreased dFe concentrations. In contrast, dissolution dominates over scavenging in the east, which drives cFe contributions >50 % and increase the dFe inventory.

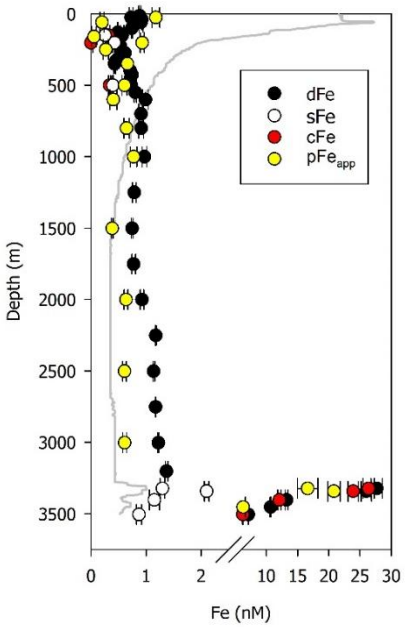

Figure 3.10 Full-depth profile of dFe (black), sFe (white), cFe (red), and pFe_{app} (yellow) concentrations against depth at Station 4, located over the Mid-Atlantic Ridge. The turbidity trace (grey line) indicates the presence of the hydrothermal plume between 3300 m and 3500 m depth. Note the scale break for concentrations >2.5 nM. Error bars show one standard deviation of the mean concentration of three analytical replicates. For the calculations of cFe and pFe_{app} concentrations, associated measurement errors were propagated.

The background dFe concentration in the ocean interior (>1027.50 kg m^{-3} and above ocean-sediment interface) away from any external or internal sources or sinks was 0.67 ± 0.14 nM, excluding the hydrothermal Station 4. Slightly higher dFe concentrations were observed in the interior of the western basin compared to the eastern basin (Figure 3.2), which appears to be a persistent feature in the North Atlantic (Fitzsimmons et al., 2015b; Hatta et al., 2015) and may be the result of different water masses and currents on either side of the ridge. Our Station 6 crossed over with Station USGT11- 20 of the US-GEOTRACES section GA03 (Boyle et al., 2015), showing close agreement (Figure 3.11) and demonstrating the relatively constant dFe distribution in the deep ocean. Dissolved Fe in the ocean interior was partitioned into 49 ± 14 % cFe, in agreement with the previously reported 50:50 % partitioning for this region (Fitzsimmons et al., 2015b). This balanced distribution of cFe and sFe was proposed to result from a steady-state equilibrium between cFe and sFe (Fitzsimmons et al., 2015b), and our results are in line with this hypothesis.

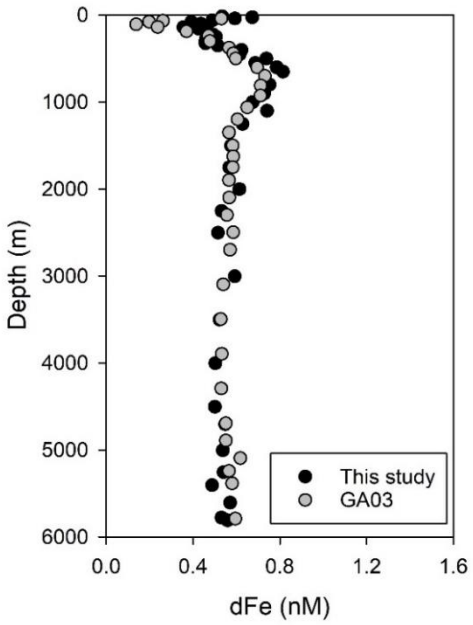

Figure 3.11 Full-depth profile of dFe concentrations at the cross-over station of JC150 (Station 6; black dots) and the US GEOTRACES Transect GA03 (USGT11-20; grey dots). Data for GA03 was obtained from the GEOTRACES IDP17 (Schlitzer et al., 2018).

3.5 Synthesis: The Colloidal Hourglass

We quantified the partitioning of dFe into soluble and colloidal phases in the subtropical North Atlantic to address the underlying questions regarding how sFe and cFe contribute to and regulate the dFe distribution. We found that the cFe contribution to the dFe pool produced an hourglass shape against depth that arises from the dominant variability of cFe over sFe (Figure 3.12). Our results show that cFe is the main source of dFe to the water column via the dissolution of particles and also the main sink via scavenging. In other words, whenever dFe is introduced or removed, it is the cFe that is driving these changes. This result reinforces the idea that cFe holds a pivotal role in the oceanic Fe cycle and that it may be a crucial component for improving Fe models.

The dynamic upper ocean encompasses a range of sources and sinks that led to a large range of colloidal fractions between the surface and ~1100 m (0 % to 86 % of dFe) (Figure 3.12). In the near surface, elevated cFe contributions of 61 % to 85 % coincident with high dFe concentrations were the result of dust supply. Throughout the euphotic zone, cFe decreased to 0 % to 30 % through its preferential scavenging onto sinking particles. Loss of cFe to the sFe phase and subsequent biological uptake further contributed to the removal of cFe in the DCM. Our hourglass figure highlights that on a small vertical scale (from surface to DCM), the change in dFe (cFe) is large, especially where the surface maximum is strong, and the implication is that despite large surface inputs, Fe limitation in the DCM is possible. In the dust-loaded subtropical North Atlantic, the vast majority of the sinking particles is lithogenic and dominates the release of Fe over biogenic particles even at depths of

remineralisation (Boyd et al., 2010). Here, we observed a tug-of-war between the continued leaching of Fe from lithogenics that increased cFe and competing mechanisms that acted to remove cFe efficiently. This balance resulted in a colloidal contribution of 37 ± 16 % of dFe that we observed. These competing mechanisms include the immediate re-scavenging and aggregation of released cFe associated with particles (both lithogenic and biogenic) and the disaggregation of cFe into sFe. A global comparison showed that the lithogenic nature of dust particles determines the cFe fraction in the mesopelagic, with lower dust fluxes resulting in lower colloidal fractions and vice versa. At the ocean-seafloor boundary, cFe ranged widely from 26 % to 76 % of dFe (Figure 3.12). We observed a west-to-east difference with the lower cFe contributions in the west (26 % to 47 %) and the higher cFe contributions in the east (52 % to 76 %), due to regional differences in benthic nepheloid layers.

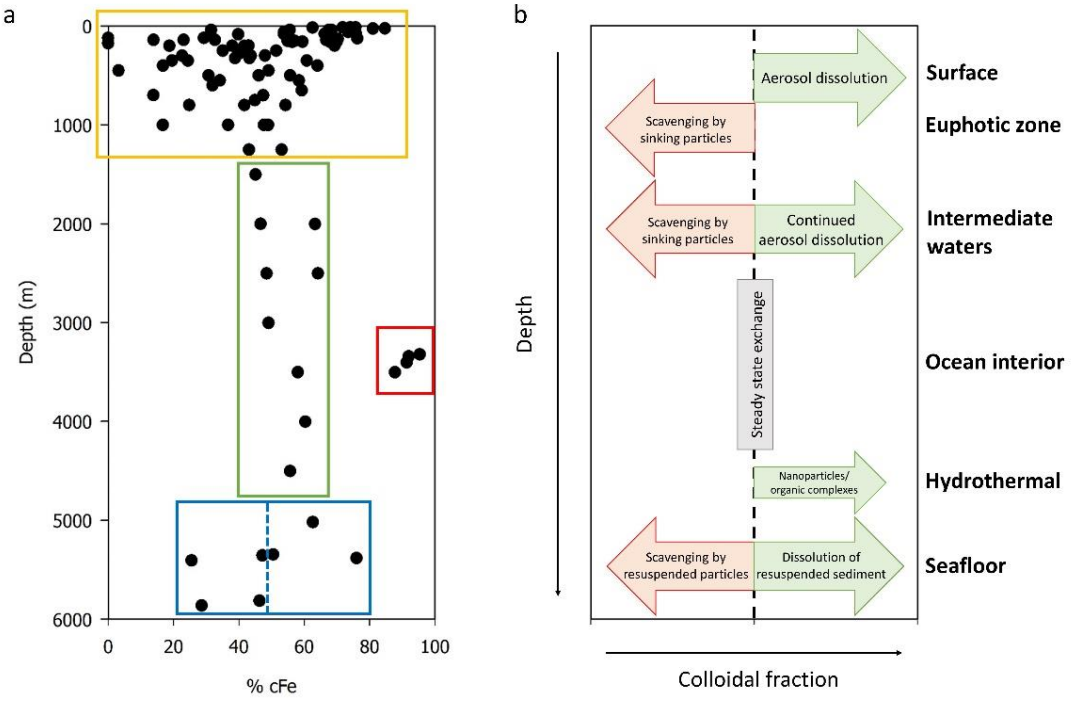

Figure 3.12 (a) The partitioning of dFe into the colloidal fraction against depth of the entire data set, forming an hourglass shape. The coloured boxes distinguish between the highly variable upper water column (yellow) and seafloor-water interface (blue; dotted blue line distinguishes between western and eastern basin), the narrow range of the deep ocean interior (green), and the hydrothermal signature (red). (b) Conceptual model of the dominant processes throughout the water column that drive the partitioning of the sFe and cFe away from the steady-state exchange of the ocean interior. Processes increasing and decreasing the colloidal fraction are highlighted in green and red, respectively.

The narrow range of colloidal fractions in the ocean interior formed the neck of the hourglass, where the partitioning into sFe and cFe falls into a balanced distribution of 1:1 (49 ± 14 % cFe of dFe), as the result of a steady-state exchange between the fractions. The near-vent hydrothermal signal of almost 100 % cFe is a clear exception. Our study indicates that cFe predominantly drives the overall surface-to-seafloor dFe distribution in the subtropical North Atlantic. Colloidal Fe and dFe are reasonably well correlated ($R^2_{cFe:dFe}$ = 0.61, n = 95), while the correlation between sFe and dFe is weak ($R^2_{sFe:dFe}$ = 0.14, n = 95), excluding hydrothermal samples. In the ocean interior, our data is

consistent with Fitzsimmons et al.'s (2015b) model where dFe partitions equally into sFe and cFe (~40 % to 60 %). An important caveat is that the resolution of our measurements is lower than Fitzsimmons et al.'s (2015b) model and the concentrations of the different Fe fractions fall into a narrower range in our data set. Regardless, a similar 'colloidal hourglass' shape is observed with the larger data set by Fitzsimmons et al. (2015b) (Figure 3.13).

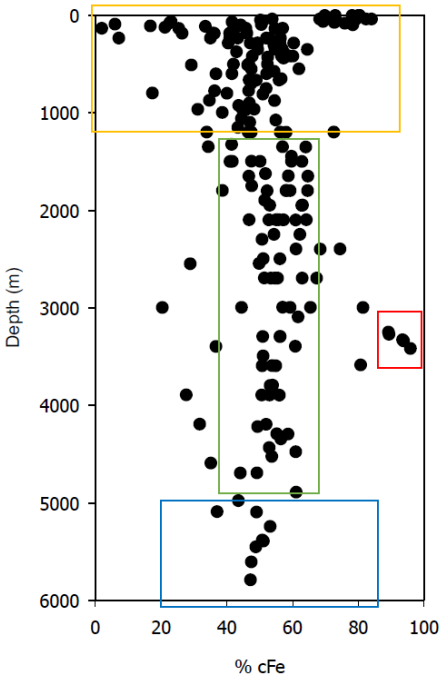

Figure 3.13 The partitioning of dFe into the colloidal fraction (% cFe) against depth of Fitzsimmons et al.'s (2015b) data set for stations USGT11-12 to -22, which are most comparable to the JC150 transect and unaffected by possible influences from surrounding land masses. Coloured boxes indicate layers of different processes (see main text). Note that in the ocean interior (green box) 24 % of data points lie outside the range of 40 to 60 % cFe and the limited spread at the seafloor boundary is possibly due to no samples taken 20 and 50 m above the seafloor as in our study.

3.6 Conclusions

Despite the dramatic increase of oceanic dFe measurements in the past decade, fundamental parameters of the oceanic Fe cycle are still ill-constrained such as scavenging rates and residence times. This is in part due to individual physicochemical species of the Fe continuum being differently affected by various abiotic and biotic processes. Our data set of size-fractionated Fe from the subtropical North Atlantic demonstrates the pivotal role of cFe, the larger-sized species in the dFe continuum, for controlling the distribution of dFe. We found that cFe is the predominantly active species in key supply and removal processes of dFe compared with the smaller sFe, which showed a more constant behaviour. Moreover, a global compilation of colloidal data allowed us to detect a sensitive dust-driven linkage between surface and mesopelagic dFe inventories, which would have been concealed by making dissolved measurements only. Currently, this important role of cFe for

the oceanic Fe cycle is not represented in biogeochemical models through an explicit cFe term. Instead, parameters like residence times are typically estimated from the bulk dFe phase, but our data clearly shows the decoupling between cFe and sFe. This is particularly important where cFe is scavenged in the euphotic zone, thereby reducing the Fe budget that is potentially available to phytoplankton. As a recent study by Black et al. (2020) also demonstrated, considering processes unique to cFe (i.e. authigenic nanoparticle formation) can substantially lower residence time estimates for dFe in the oligotrophic gyres from 2 years to <2 months. Therefore, advancing our understanding of the oceanic Fe cycle demands it to extend on size-fractionated measurements at a global scale and to explicitly incorporate cFe terms in biogeochemical models.

Chapter 4 Short-Term Exchange between Iron Size Fractions along Strong Biogeochemical Gradients in the Subtropical North Atlantic

Preface

For the research presented in this chapter, I designed the low abundance isotope experiments and conducted them at sea during the research cruise. In a team, I also set up, broke down and subsampled the Fe bioassay experiments. I made all size-fractionated Fe and Fe isotope measurements, and analysed and interpreted the experimental results. The raw data are included in the appendix of the thesis.

4.1 Abstract

In seawater, the essential micronutrient Fe exists as a heterogeneous exchangeable continuum of physicochemical species that have different bioavailability and residence times, but the mechanisms and time scales of Fe exchange between these species are largely unknown due to the commonly applied snapshot type sampling of the natural environment during large-scale oceanographic surveys. At three representative stations across strong longitudinal gradients of surface Fe concentrations and dust loading in the subtropical North Atlantic, 48 h-time series *in-situ* incubations were conducted with Fe additions enriched in the low abundance isotope ^{57}Fe (as dissolved Fe_2O_3). Tracing the partitioning of the initially soluble (<0.02 µm) ^{57}Fe enriched addition into the colloidal (0.02 µm to 0.2 µm) and total dissolvable (unfiltered, acid-leached >12 months) size fractions at six time points using HR-ICP-MS measurements, revealed the immediate (<30 min) and irreversible (over 48 h) formation of colloidal-sized Fe-oxyhydroxides, due to the low solubility of Fe in seawater in the absence of excess organic Fe-binding ligands. This result contributes to the growing body of evidence for cFe species being a key component of the oceanic Fe cycle and highlights the slow exchange kinetics between freshly introduced Fe and the ambient Fe pool over the probed time scale; trends in the partitioning in the artificially-enriched ^{57}Fe isotope were decoupled from the naturally dominant ^{56}Fe isotope over 48 h. The latter was subjected to late-stage, likely ligand-mediated exchange between the soluble and colloidal phases and varied between the three stations due to gradients in local biogeochemistry.

4.2 Introduction

The interest in the oceanic cycle of the trace metal Fe stems from the seeming mismatch of its low, nanomolar to picomolar concentrations across vast ocean basins in contrast with its role as a vital micronutrient for phytoplankton's cellular machinery, as it is required as co-factors in proteins involved in photosynthesis (photosystems I and II; Jordan et al., 2001), N_2 fixation (nitrogenases; Howard & Rees, 1996) and DOP acquisition (alkaline phosphatase; Yong et al., 2014) amongst others. In about 35 % of the world's ocean, Fe is a limiting nutrient (Moore et al., 2001). Particularly in HNLC regions like the Southern Ocean or Equatorial Pacific, Fe is the primary limiting nutrient, which results in large unused stocks of DIN and DIP in these environments, constrains CO_2-sequestering photosynthetic primary production and hence, impacts our climate (Moore et al., 2013). In contrast, the typical secondary or co-limiting role of Fe in the oligotrophic subtropical gyres of Atlantic and Pacific impacts macronutrient acquisition in these environments by limiting diazotrophic N_2 fixation (Held et al., 2020; Moore et al., 2009) or DOP acquisition (Browning et al., 2017).

The low oceanic concentration of the micronutrient Fe derives from the low solubility (~0.01 to 0.1 nM) of the thermodynamically stable Fe^{3+} under modern seawater conditions (e.g. temperature, pH, O_2) (Kuma et al., 1996; Liu and Millero, 1999; Rose and Waite, 2003). The highly soluble Fe^{2+} is oxidised to Fe^{3+} on time scales of seconds to minutes (first-order oxidation rate constant of $\sim 1.1 \cdot 10^{-2}$ s^{-1}, i.e. $t_{1/2}$ = 66 s; Millero et al., 1987), which typically results in small accumulated stocks of Fe^{2+} (Millero et al., 1987). At concentrations exceeding the inorganic solubility limit, Fe is rapidly hydrolysed and precipitated as amorphous ferric oxyhydroxide (second-order formation rate constant of $\sim 4 \cdot 10^7$ M^{-1} s^{-1}, i.e. $t_{1/2}$ = 25 s at 1.0 nM Fe), which evolves into more stable mineral phases over time (Rose and Waite, 2003). However, Fe-binding organic ligands that are ubiquitous in the ocean act to exceed the solubility threshold over orders of magnitude, by competing with the formation of hydrolysed Fe species and hence maintaining a pool of Fe as dFe (Gledhill and Buck, 2012).

The bioavailability of Fe is commonly inferred from the distribution of dFe (<0.2 µm or <0.45 µm) as opposed to particulate Fe (pFe >0.2 µm or >0.45 µm). However, recent studies have highlighted the importance of the pFe pool and the role of distinct species within the dFe continuum for the acquisition of Fe by phytoplankton: The former is due to pFe continuously replenishing the dFe pool via disaggregation and dissolution mechanisms (e.g. Milne et al. 2010) and due to the ability of some microbes, such as the abundant diazotroph *Trichodesmium*, to utilise pFe directly (Rubin et al., 2011). The latter is due to the decoupled distribution, chemical reactivity and biological relevance of individual Fe species under the dFe umbrella. Particularly, electrochemical analyses revealed that Fe-binding organic ligands differ in their binding strengths and resulting bioavailability to phytoplankton over multiple orders of magnitude (Gledhill and Buck, 2012; Lis et al., 2015a, 2015b). The strongest Fe-binding ligands are typically associated with surface waters (e.g. Buck et al., 2015, 2018; Bundy et al., 2018). Amongst these are 'siderophores' (e.g. ferrioxamines and amphibactins), which have low molecular weights (<1 kDa; ~1 nm spherical diameter) and high conditional stability constants of logK >12, compared with logK ~11 to 12 for the more ubiquitous weaker Fe-binding ligand classes (Boiteau and Repeta, 2015; Gledhill and Buck, 2012). Siderophores are actively excreted by some microbes as a specialised retention and acquisition strategy, but not accessible to all phytoplankton (Sutak et al., 2020). Furthermore, ultrafiltration techniques applied to dFe samples to separate sFe (<0.02 µm) and cFe (0.02 µm to 0.2 µm) revealed the decoupled oceanic distributions of these two fractions based on size (e.g. Fitzsimmons et al., 2015b; Kunde et al., 2019). Common features include cFe enrichments at external Fe sources (e.g. dust, seafloor, shelf, hydrothermal vents) and cFe minima at the DCM, with sFe generally showing less dynamicity (e.g. Chever et al., 2010; Fitzsimmons et al., 2015c; Kunde et al., 2019; Sedwick et al., 2020). These trends result from the shuttling of Fe between the particulate and soluble phases via the colloidal intermediate. As the soluble fraction contains both the truly soluble free Fe', which is readily accessible for biological uptake via the widespread reductive uptake pathway, and siderophore-bound Fe, which is highly

bioavailable to some specialised microbes, sFe is generally considered the more bioavailable fraction of dFe (Lis et al., 2015b). In contrast, the colloidal fraction contains nanoparticulate mineral fragments and Fe bound in organic colloids (e.g. humic and fulvic substances), which are not or less readily bioavailable to phytoplankton than sFe, with increasing age and size of the colloids further reducing the bioavailability of Fe (Chen and Wang, 2001; Wang and Dei, 2003). Therefore, the relative bioavailability of sFe and cFe depends on the phytoplankton species as well as on the distinct form of Fe within the sFe or cFe pools. Additional complexity arises from the transient nature of Fe in a species, which results from a range of processes that continually reshape the Fe pool. These include biologically-mediated processes such as cellular uptake, heterotrophic remineralisation of organic matter, viral lysis of cells or complexation by siderophores, as well as abiotic processes such as adsorption onto particle surfaces or the dissolution of lithogenic material (Tagliabue et al., 2017). Together, these create a heterogeneous, non-static oceanic continuum of exchangeable Fe species with varying chemical and biological reactivity, whose impact on phytoplankton growth is missed by inferring bioavailability solely from the dFe concentrations at a given point in time and space.

Physicochemical speciation changes of Fe are documented in the natural environment over large timescales ranging from days to seasonal and years (e.g. Birchill et al., 2017; Fitzsimmons et al., 2015c; Sedwick et al., 2020; Sedwick et al., 2005), with a suite of experimental approaches investigating these changes over hours to months (e.g. Bowie et al., 2001; Bressac et al., 2019; Buck et al., 2010; Bundy et al., 2016; Hollister et al., 2020; Maldonado et al., 2001; Mellett et al., 2018; Nishioka et al., 2005). External factors like dust deposition and physical mixing typically control the physical Fe speciation, with temporal variations reflected most strongly in the larger sizes (i.e. pFe > cFe > sFe, especially cFe ≫ sFe) as a result of their different residence times. As for the chemical Fe speciation, organic ligand concentrations are linked to changes in Fe concentrations, albeit often time-lagged, with increased complexation capacity or a shift in binding strengths to counteract Fe limitation at low Fe (Bundy et al., 2016) or to react to new Fe input (Boye et al., 2005) by retention.

One drawback of the above studies is their restriction to observing the net 'snapshot' effect of the combination of all processes affecting Fe speciation, so that the direction and time scale of exchange between different Fe pools remain unresolved. Low abundance isotope tracing experiments provide a means to disentangle the processes of Fe cycling by additions enriched in the low abundance isotope ^{57}Fe to the natural Fe pool in seawater (92 % ^{56}Fe), which artificially skews the isotopic ratio in the experiements. For example, the different removal rates of the ^{57}Fe (added as dissolved Fe-oxide, i.e. as inorganic sFe) and ^{56}Fe isotopes in a 5-day simulated vertical mixing event in the shelf Bering Sea, Hurst & Bruland (2007) suggested that the net removal of 2.0 nM Fe from the dissolved into the particulate phase was actually the result of 4.9 nM dFe being transferred to pFe, while 2.9 nM pFe was regenerated into dFe. The authors also showed the rapid formation of cFe from the sFe addition and the faster removal of cFe over sFe into/onto biogenic material. In a 15-day simulated spring

bloom on the Antarctic Peninsula shelf, Buck et al. (2010) showed that additions of ^{57}Fe (either as dissolved Fe-oxide or as siderophore-bound Fe) were almost completely drawn down, while substantial unused stocks of the naturally abundant ^{56}Fe remained, as the result of the lower bioavailability of the natural dFe pool compared with the ^{57}Fe enriched addition. In contrast, comparable removal rates between ^{57}Fe (added as dissolved Fe-oxide) and ^{56}Fe suggested similar bioavailability of natural and artificially added Fe in experiments with West Florida shelf sea water (Hollister et al., 2020). Collectively, results from these isotope tracing studies have been valuable for understanding the oceanic Fe cycle in a variety of shelf sea environments by highlighting firstly that pFe is a crucial source for replenishing dFe stocks, and secondly that cFe is the more dynamic sub-dFe fraction, and by providing insights into the relative bioavailability of natural Fe to artificially added Fe.

No such study exists for the subtropical North Atlantic. This is a high Fe environment, with ambient Fe concentrations not primarily limiting to primary production (Moore et al., 2013). Typically, N and P are the primary and secondary limiting nutrients, respectively, to phytoplankton growth, with Fe playing a key role in sustaining N_2 fixation and/or APA due to its requirements in the relevant enzymes (Browning et al., 2017; Mills et al., 2004). However, the North Atlantic basin is subject to strong interannual, seasonal and episodic changes in Fe-rich dust deposition that can affect these biological processes by driving gradients in the seawater Fe distribution. These Fe gradients are comparable to those between the high-dust North and low-dust South Atlantic (Ussher et al., 2013). The surface and euphotic zone waters are most susceptible to large changes in the Fe concentration and speciation over small temporal and spatial scales, where the dynamic colloidal phase controls dFe (Kunde et al., 2019). While cFe is the dominant form of Fe that is introduced by dust, it is also rapidly attenuated through the euphotic zone by scavenging and biological uptake. Clearly, the processes acting on cFe are key to understanding the Fe budget in this dust-dominated area, but the underlying rates of the cFe cycle remained unresolved by the snapshot-type sampling of Chapter 3 of this thesis and many previous studies (e.g. Fitzsimmons et al., 2015b; Kunde et al., 2019; Sedwick et al., 2020). Therefore, the goal of the present chapter was to elucidate on the exchange over time between multiple Fe size fractions in this dust-dominated basin, along strong natural biogeochemical gradients. The focus was on the short-term (30 min to 48 h) cycling between sFe, dFe and TDFe pools following the addition of an ^{57}Fe enriched stock (as dissolved Fe-oxide) to incubations with ambient seawater at three locations, which were accompanied by bioassays assessing the nutrient and Fe status of the ambient phytoplankton community at seven locations (Figure 4.1a). We hypothesised that the exchange between the different Fe size fractions is controlled by local biogeochemical conditions such as the dust particle load (e.g. particles as scavenging agents to remove the Fe spike) and the phytoplankton community (e.g. Fe spike potentially more bioavailable than ambient dust-derived Fe pool).

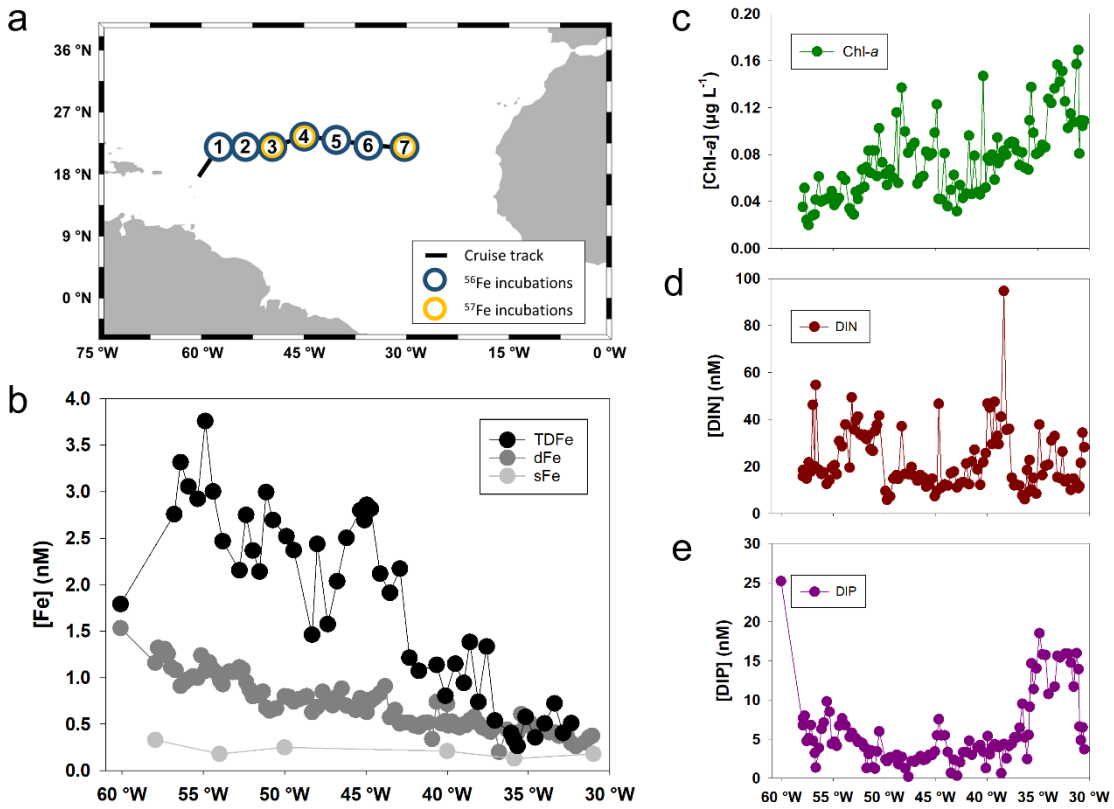

Figure 4.1 Map of the North Atlantic indicating the JC150 cruise track and stations occupied for incubations. For the biogeochemical context, surface concentrations (<5 m) are plotted of (b) size-fractionated Fe, (c) Chl-*a*, (d) DIN and (e) DIP against longitude (Fe data replotted from Kunde et al., 2019; other data are courtesy of C. Mahaffey and E.M.S. Woodward).

4.3 Methods

4.3.1 Incubation Set-up and Sampling

Incubations were conducted onboard the *RRS James Cook* during research cruise JC150 along 22 °N in the subtropical North Atlantic between June 26th and August 12th, 2017 (Figure 4.1a). Seawater was collected strictly before dawn from 40 m depth in either of two modes. At Stations 1 and 2, a Ti-rosette fitted with 24 × 10 L trace metal-clean Teflon-coated OTE bottles and a CTD profiler (Seabird Scientific) was deployed on a conducting Kevlar wire. The OTE bottles were transported into a class-100 clean air van upon recovery and pressurized (0.7 bar) with compressed air filtered in-line through a 0.2 µm PTFE filter capsule (Millex-FG 50, Millipore). The sampling process was amended for Stations 3 to 7, where braided PVC hosing cable-tied to a Kevlar wire was lowered, aided by a trace metal-clean weight, to pump seawater directly into the class-100 clean air van using a Teflon diaphragm pump (Almatec). The tubing was flushed for 15 min prior to seawater collection.

Polycarbonate bottles (2 L) (Nalgene) served as incubation containers, which were pre-cleaned following GEOTRACES protocols (https://geotracesold.sedoo.fr/images/Cookbook.pdf) before the start of the cruise. Before each station occupation, the incubation containers were rinsed twice with 0.5 M HCl (trace metal grade, Fisher) and thrice with UHP water, and then pre-conditioned thrice with ambient unfiltered seawater. At Stations 1 and 2, each bottle received water from a minimum of three different OTE bottles to minimise sampling bias. At Stations 3 to 7, bottles were filled in random order to a third of their volume, which was then repeated for the second and last thirds. Two experimental sets of incubations were conducted as outlined subsequently and detailed in Table 4.1 and Table 4.2.

Table 4.1 Experimental design and initial conditions of the low abundance Fe isotope experiments. Average and one standard deviation shown for the t_0 Fe concentrations are from analytical triplicates, with Station 3 having two individual t_0 dFe samples.

	Parameter	Station 3	Station 4	Station 7
General	Date	15 Jul	20 Jul 17	05 Aug
	Location	22.00 °N 50.00 °W	23.37 °N 44.95 °W	22.00 °N 31.00 °W
	SST (°C)	28	27	25
	MLD (m)	33	30	-
Incubation set-up	Sampling mode	Pump	Pump	Pump
	Fe addition (nM) (^{57}Fe enriched stock)	1.0	0.5	0.5
	DIN addition (µM)	2.0	2.0	-
Initial conditions (t_0)	TDFe (nM)	2.03 ± 0.03	1.53 ± 0.01	1.36 ± 0.03
	dFe (nM)	1.16 ± 0.03, 0.94 ± 0.01	0.91 ± 0.01	0.40 ± 0.02
	sFe (nM)	0.30 ± 0.01	-	0.39 ± 0.01
	Chl-*a* (µg L^{-1})	0.090	0.050	0.149
	DIN (nM)	2.5	4.4	6.2 ± 0.0
	DIP (nM)	2.9	3.3	14 ± 0.7

4.3.1.1 Low Abundance Iron Isotope Experiments

The first experimental set aimed to trace the partitioning of an initially soluble Fe addition into different size fractions at high temporal resolution, using a stock enriched in the low abundance isotope ^{57}Fe. At three stations between 50 °W and 31 °W, each filled incubation bottle was perturbed with additions of either 1.0 nM (Stations 3 and 4) or 0.5 nM (Station 7) of an ^{57}Fe enriched stock solution (Figure 4.1a, Table 4.1), thereby altering the natural isotopic ratio of ^{57}Fe to ^{56}Fe in the

seawater (R_{SW} = 0.023) to a strongly skewed ratio in the incubation ($R_{incub.}$ = 10 to 16; depending on the spike amount and the Fe concentration at t_0), causing a fractionation ($\varepsilon = 1 - R_{incub}/R_{SW}$) of $440 \cdot 10^3$ to $700 \cdot 10^3$. The stock was prepared from isotopically enriched Fe_2O_3 (96.64 % ^{57}Fe, i.e. R_{spike} = 29; Cambridge Isotope Laboratories) dissolved in HCl (Romil, SpA). At the western most Stations 3 and 4, additions of nitrate and ammonium with 1.0 µM each accompanied the Fe spikes ('DIN spike' hereafter). The rationale was to induce P limitation (following the alleviation of N limitation) and increase the activity of alkaline phosphatases, so that the Fe requirements of the ambient community may increase due to the metal requirements in these enzymes. Nitrate and ammonium stock solutions were prepared from $NaNO_3$ and NH_4Cl salts (both Sigma-Aldrich) dissolved in UHP water and passed through a prepared cation exchange resin (Chelex-100, BioRad) to remove metal impurities. Post-spike, incubation containers were screw capped, sealed with Parafilm, gently shaken and placed in a designated van onboard.

Incubation conditions were set to 12 h lights on/off cycles at ambient sea surface temperature (SST). At six time points over a 48 h period (t_1 = 30 min, t_2 = 90 min, t_3 = 6 h, t_4 = 12 h, t_5 = 24 h, t_6 = 48 h), three bottles were removed at random. Bottles were sacrificed for each time point to minimise the risk of contamination that may have incurred upon repeated time point sampling (Lohan et al., 2005a). Sacrificed bottles were brought to a class-100 clean van onboard and their outsides were rinsed with UHP water. One of three replicates was subsampled for Chl-*a* (unfiltered, into UHP-rinsed dark LDPE bottles). All three replicate bottles were subsampled for multiple Fe size fractions into acid-cleaned 60 ml or 120 ml LDPE bottles (Nalgene) after pre-conditioning once with ~20 ml of incubation seawater. The small rinse volume was the result of volume restrictions for the samples. Total dissolvable Fe samples were taken unfiltered by pouring directly from the incubation bottles, while dFe samples were taken using a vacuum-filtration tower with 0.45 µm track-etched PC membrane filters (Nucleopore, Whatman), and sFe samples were taken from dFe subsamples, after syringe filtration with 0.02 µm pore size filters (Anotop, Whatman). The filter tower and syringes were acid-cleaned between time points, while Nucleopore and Anotop filters were conditioned with 1 M HCl (Romil, SpA), UHP water and ambient seawater immediately prior to use, as for the sFe ultrafiltration procedure in Kunde et al. (2019).

Additional samples for initial conditions (t_0) of TDFe, dFe, sFe, Chl-*a*, and macronutrients were taken during the initial filling process from a t_0-designated 2 L incubation bottle that was filled and processed immediately. All Fe subsamples were acidified to pH 1.7 (0.024 M) by addition of 12 M HCl (Romil, UpA) (Lohan et al., 2005a) and stored double-bagged for at least six months prior to further processing (Section 4.3.2). Chlorophyll-*a* subsamples were filtered immediately through 0.7 µm glass microfiber filters (Whatman GF/F, 25 mm) and extracted in 90 % acetone overnight (Holm-Hansen et al., 1965). The extract was measured on a pre-calibrated (Spinach Chl-*a* Standard, Sigma) Turner Designs Triology fluorimeter at sea. Nanomolar concentrations of DIP and DIN were

measured onboard less than 12 h after sample collection using standard colorimetric methods with segmented flow spectrophotometric detection coupled to a 2 m liquid waveguide (Brewer & Riley, 1965; Patey et al., 2008; Woodward & Rees, 2001).

Analysis of variance (at α=0.05) with Bonferroni correction, comparing the mean concentrations of replicates at each time point, was employed to probe for significant changes in the concentrations of Fe isotopes/size fractions.

4.3.1.2 Iron Bioassays

The second set of experiments aimed to assess the nutritional Fe status of the resident phytoplankton community across the ocean basin using a number of incremental Fe additions from an Fe stock of natural isotopic abundance. At all seven stations, some occupied twice, filled incubation bottles were spiked in duplicate or triplicate with Fe additions between 0.2 to 2.0 nM with and without additions of DIN of 1.0 to 4.0 µM (Figure 4.1, Table 4.2). Individual treatments at Stations 1 to 7 are detailed in Table 4.2 and were complemented by at least two unspiked Control bottles, i.e. no Fe and no DIN addition. The Fe stock solution was prepared by dissolving $FeCl_3$ (natural isotope abundance; Sigma) in HCl (Romil, SpA), while the DIN stocks were the same as for the low abundance isotope experiments. Bottles were sealed and incubated as described before, but all bottles were sampled at a single time point (48 h) in contrast to the low abundance isotope experiments. All replicates of all treatments were subsampled for Chl-*a*, but not for Fe, and processed onboard. During the initial filling process, samples for initial conditions (t_0) were collected directly from the Ti-CTD bottles or the lowered underway sampler for Chl-*a*, macronutrients and dFe. These dFe t_0 samples were filtered in-line using 0.2 µm membrane cartridge filters (Sartobran 300, Sartorius), acidified to pH 1.7 as described before, and measured onboard by FIA-CL, as in Kunde et al. (2019). Chlorophyll-*a* and macronutrient samples were also processed onboard as described for the low abundance isotope experiments.

Analysis of variance (at α=0.05) with Bonferroni correction, comparing the mean concentrations of treatment replicates, was employed to probe for significant changes in Chl-*a* relative to the Control after 48 h.

Table 4.2 Experimental design and initial conditions of the Fe bioassays. Where applicable, t_0 concentrations are shown as averages with one standard deviation from biological replicates with the number of replicates indicated accordingly. For those t_0 Fe concentrations where n = 1, the average and standard deviation of analytical triplicates is shown instead.

	Parameter	Station 1	Station 2	Station 3	Station 4	Station 5		Station 6		Station 7	
General	Date	29 Jun	06 Jul	13 Jul	17 Jul	22 Jul	25 Jul	28 Jul	02 Aug	06 Aug	08 Aug
	Location	22.00 °N 58.00 °W	22.00 °N 54.00 °W	22.00 °N 50.00 °W	23.37 °N 44.95 °W	23.00 °N 40.00 °W		22.30 °N 35.90 °W		22.00 °N 31.00 °W	
	MLD (m)	-	22	33	45	-	46	-	-	40	50
Incubation set-up	Sampling mode	Ti-CTD	Ti-CTD	Pump	Pump	Pump		Pump		Pump	
	Fe addition (nM) (Natural isotope abundance stock)	0 0.5 0.75 1.0 1.5 2.0	0 0.5 0.75 1.0 1.5 2.0	0 1.0	0 0.5 0.75 1.0 1.5 2.0	0 0.2 0.3 0.4 0.5 0.6 0.7 0.8 0.9 1.0	0 0.2 0.3 0.4 0.5 1.0	0 0.2 0.3 0.4 0.5 1.0	0 0.2 0.3 0.4 0.5 1.0	0 0.2 0.3 0.4 0.5 1.0	0 0.2 0.3 0.4 0.5 0.6 0.7 0.8 0.9 1.0
	DIN addition (µM)	0 2.0	0 2.0	0 2.0	0 2.0	0	0	0	0	0	0
	Treatment replication	2	2	2	2	3	3	3	3	3	3
Initial conditions (t_0)	dFe (nM)	1.02 ± 0.18 (n=3)	1.06 ± 0.18 (n=3)	-	1.03 ± 0.14 (n=4)	0.55 ± 0.04 (n=3)	-	0.55 ± 0.02 (n=3)	0.71 ± 0.07 (n=3)	0.32 ± 0.02 (n=3)	-
	Chl-*a* (µg L^{-1})	0.087 ± 0.021 (n=3)	0.063 ± 0.0024 (n=3)	0.080 ± 0.014 (n=3)	0.085 (n=1)	0.050 (n=1)	0.090 (n=1)	0.080 (n=1)	0.070 (n=1)	0.150 (n=1)	-
	DIN (nM)	6.7 ± 0.78 (n=3)	4.0 ± 3.2 (n=3)	5.8 ± 7.3 (n=3)	1.05 (n=1)	5.5 ± 1.7 (n=3)	5.1 ± 1.3 (n=3)	5.8 (n=1)	3.9 ± 1.5 (n=2)	10 (n=1)	-
	DIP (nM)	6.4 ± 0.22 (n=3)	2.4 ± 0.25 (n=3)	3.5 ± 0.91 (n=3)	3.3 ± 0.79 (n=2)	4.5 ± 1.2 (n=3)	5.3 ± 0.20 (n=3)	8.7 (n=1)	4.8 ± 0.49 (n=2)	2.9 (n=1)	-

4.3.2 Iron Isotope Extraction and Analysis

Concentrations of the isotopes ^{56}Fe and ^{57}Fe in the TDFe, dFe and sFe samples from the low abundance isotope experiments were quantified by HR-ICP-MS analysis on an Element XR (ThermoFisher) at the National Oceanography Centre Southampton. Preceding the analysis, the metal content in the samples was extracted from the salt water matrix off-line and pre-concentrated on a semi-automated flow injection manifold in a class-100 clean laboratory.

Briefly, samples were loaded using a 10-port autosampler (VICI Valco Instruments), buffered in-line to pH 6.4 ± 0.2 with a 2 M ammonium acetate buffer (prepared from concentrated CH_3COOH and NH_4OH to pH 8.45 ± 0.05; both Romil, UpA), and subsequently loaded onto a column filled with a resin containing immobilised CM-PEHA functional groups (WAKO; Kagaya et al., 2009). The loading time was 10 min at flow speeds of 1.5 ml min^{-1} and 0.6 ml min^{-1} for sample and buffer, respectively. A brief column conditioning with 0.05 M ammonium acetate (pH 8.20) preceded the loading step for 30 s at 0.6 ml min^{-1}. The same weak ammonium acetate was used to rinse the column for 30 s post-loading to remove the salt water matrix. Next, the retained Fe was liberated off the column with 1 M HNO_3 (sub-boiled from trace grade HNO_3, Fisher) for 65 s at 0.86 ml min^{-1} and the eluent was collected into 4 ml acid-cleaned PP vials (Omni-Vial, Wheaton) via a second 10-port autosampler. Complete clearance of individual autosampler lines and prevention of cross-contamination between subsequent samples was achieved using air flow for 99 s at 0.86 ml min^{-1} trailing the elution acid. With a loading volume of 15 ml of the original seawater sample and an elution volume of 0.93 ml of the initial pre-concentrated sample, the achieved pre-concentration factor was ~16. The extraction chemistry (specifically the resin) was adapted from Rapp et al. (2017), who used a commercially available seaFAST (Elemental Scientific) extraction system, while the home-built manifold set-up was adapted from Milne et al. (2010) but with an additional automatisation of sample collection and line clearance incorporated.

Two separate external calibration curves were applied for ^{57}Fe and ^{56}Fe quantification, each consisting of six additions of either the Fe stock enriched in ^{57}Fe (96.64 % ^{57}Fe; Cambridge Isotope laboratories) or an Fe stock of natural isotopic abundance (91.75 % ^{56}Fe; Inorganic Ventures), respectively, to seawater with naturally low Fe concentrations (<0.2 nM dFe), alongside a zero addition. Manifold blanks were assessed from acidified UHP water (pH 1.7 by addition of 12 M HCl; Romil, UpA). Calibrants and blanks were extracted in the same manner as seawater samples. Reference materials were also extracted to establish accuracy and precision. Pre-concentrated samples were analysed by HR-ICP-MS within one week after extraction following protocols for instrumental settings, blank correction and internal standardisation using ^{115}In, as described elsewhere (e.g. Lough et al., 2019; Milne et al., 2010; Rapp et al., 2017). The detection limits (three

times the standard deviation of the zero seawater calibrant over multiple measurements per extraction day) were 0.15 ± 0.06 nM and 0.034 ± 0.031 nM for ^{56}Fe and ^{57}Fe, respectively, while procedural blank contributions (from acidified UHP) were 0.09 ± 0.02 and 0.003 ± 0.004 nM for the two isotopes, respectively. Repeated measurements of dFe concentrations in GEOTRACES reference materials SAFe D1 (0.81 ± 0.08 nM, n = 7) and GSP (0.19 ± 0.10 nM, n = 9), yielded good agreement with published consensus values (https://www.geotraces.org/standards-and-reference-materials/), noting the known inter-bottle variability of the SAFe D1 material (~0.7 to 0.9 nM) (Johnson et al., 2007).

Unfortunately, some station and/or replicate Fe data are incomplete, particularly for sFe, due to analytical difficulties, but in many instances re-analysis was not possible as sample volumes were insufficient. Because the sample filtration was done manually, replication was chosen at the expense of large sample volumes. Concentrations of cFe and pFe_{app} are not explicitly measured, but calculated as cFe = dFe – sFe and pFe_{app} = TDFe – dFe, respectively. Where these concentrations are missing in the plots, this means that the sample-specific concentration for either of the summands was unavailable (see full data set in Appendix A.2).

4.4 Results

4.4.1 Oceanographic Context and Initial Conditions

The high-resolution surface (<5 m) gradients of Figure 4.1 set the biogeochemical context for the experimental results. From the Sargasso Sea on the western end of the transect to ~30 °W in the subtropical gyre on the eastern end (still ~1500 km from the African continent), strong dust-driven eastwards decreasing gradients in Fe concentrations were observed (details in Chapter 3, Kunde et al., 2019). Briefly, these were most pronounced in the TDFe fraction from >3.5 nM to <0.5 nM, still strong for dFe from ~1.5 nM to 0.3 nM, and least pronounced for sFe from 0.33 to 0.18 nM (Figure 4.1b). The relatively constant sFe concentrations at variable dFe mean that the cFe pool drove the gradient in dFe. Chlorophyll-*a* concentrations, as a proxy for phytoplankton biomass, exhibited the opposite trend to dFe, with characteristically low concentrations of <0.04 µg L^{-1} in the ultraoligotrophic Sargasso Sea that increased to ~0.16 µg L^{-1} towards the east (Figure 4.1c). This was likely caused by the low macronutrient stocks across the entire basin, with <10 nM DIP for the majority of transect, except the east of 35 °W where concentrations ranged between 15 to 20 nM and the far west, which was under influence of the Amazon/Orinoco plume (Figure 4.1d). Concentrations of DIN were more variable than DIP, but generally <60 nM, with the majority <30 nM (Figure 4.1e). The ambient biogeochemistry can be summarised as a progression from the high-Fe, low Chl-*a*

ultraoligotrophic Sargasso Sea (roughly Stations 1 to 4) to the lower-Fe, higher Chl-*a* oligotrophic subtropical gyre (roughly Stations 5 to 7).

Initial concentrations of the key biogeochemical parameters Fe, DIP, DIN and Chl-*a* at 40 m at the start of the *in-situ* experiments were generally in line with these basin-scale surface trends (Table 4.1 and Table 4.2). For the low abundance isotope experiments, comparably higher t_0 concentrations of dFe and TDFe were observed in the west at Station 3 (dFe = 1.16 ± 0.03 and 0.94 ± 0.01 nM, TDFe = 2.03 ± 0.03 nM) and Station 4 (dFe = 0.91 ± 0.01 nM, TDFe 1.53 ± 0.01 nM) than in the east, where markedly lower t_0 Fe concentrations were present at Station 7 (dFe = 0.40 ± 0.02 nM, TDFe = 1.36 ± 0.03 nM). Concentrations of sFe were generally low at both ends of the basin with 0.30 ± 0.01 nM at Station 3 and 0.39 ± 0.01 nM at Station 7. Macronutrient concentrations were characteristically oligotrophic with DIP and DIN concentrations <5 nM at the start of all low abundance isotope experiments, except at the western Station 7, where DIP and DIN concentrations were comparably elevated with 14 nM and 6.2 nM, respectively. Accordingly, Chl-*a* ranged from very low t_0 concentrations of 0.090 µg L^{-1} and 0.050 µg L^{-1} at Stations 3 and 4, respectively, to higher concentrations of 0.149 µg L^{-1} at Station 7.

Unsurprisingly, conditions at the start of the Fe bioassays were similar to those of the low abundance isotope experiments as these were conducted only a few days apart, but some natural day-to-day variability between the two experimental sets were notable in all parameters that were sampled for both experimental sets (Chl-*a*, macronutrients, dFe) as well as between repetitions of the Fe bioassays at the same stations. The concentrations of dFe varied by a difference of 0.12 nM over four days at Station 4, and by 0.16 nM over seven days at Station 6. The between-day variability of dFe was actually on the same scale as the between-replicate variability of t_0 samples (Tables 4.1 and 4.2). The between-replicate variability was higher at higher initial dFe concentrations (i.e. Stations 1 to 4) with the relative standard deviation (RSD) between the t_0 replicate concentrations of dFe at these stations falling within 14 to 18 %, while the RSD at lower initial dFe concentrations (i.e. Stations 5 to 7) fell between 4 and 10 %. Variability in dFe over small time (e.g. Fitzsimmons et al., 2015c) and depth scales (e.g. Kunde et al., 2019; Sedwick et al., 2020) is a prominent phenomenon in the upper ocean and largely driven by episodic dust delivery – the most dominant Fe source to the subtropical North Atlantic (Ussher et al., 2013). Nevertheless, on the basin scale, the west-to-east decreasing dFe gradient that was observed in the surface ocean (Figure 4.1b) was largely preserved against between-day and between-replicate variability in the t_0 dFe concentrations of the experiments.

Lastly, the MLD, defined after de Boyer Montégut et al. (2004) using daily deployments of the CTD profiler, deepened eastwards with the shallowest observed value of 22 m at Station 2 on July 6th to the deepest value of 50 m at Station 7 on August 8th (Tables 4.1 and 4.2). Variability in MLD occurred over multi-day station occupation and likely also contributed to the observed variability in Fe,

nutrient and Chl-*a* stocks at t_0, alongside natural biologically-driven variability (e.g. uptake versus regeneration) and episodic dust delivery. Since incubation seawater was consistently collected from 40 m depth, the location and date of the experiments determined whether within-MLD or below-MLD waters were incubated.

4.4.2 Results from the Low Abundance Isotope Experiments

Results from the low abundance isotope experiments provide insight into the partitioning of an Fe addition into different Fe size fractions over time at Stations 3, 4 and 7. By artificially enriching the seawater with the ^{57}Fe isotope over the negligible background levels ($R_{incub.}$ = 10 to 16 compared to R_{SW} = 0.023), the concentrations of ^{57}Fe are representative of the newly introduced Fe and trace its fate, while the naturally dominant ^{56}Fe is representative of the natural Fe pool in the seawater. The results are depicted in Figures 4.2, 4.3 and 4.4, respectively. Two main observations emerge: Firstly, the initially soluble-sized ^{57}Fe enriched spike rapidly partitioned to ≥90 % into cFe by the first time point (~30 min), after which it remained largely unchanged. Independent of spike amount and combination (i.e. Station 3: 1 nM Fe + 2.0 µM DIN, Station 4: 0.5 nM Fe + 2.0 µM DIN, Station 7: 0.5 nM Fe; Table 4.1), this overall trend was reproduced at all three probed stations. Secondly, for the majority of the experiments no statistically significant concentration changes occurred over 48 h. The exception was at Station 3, where the concentration of ^{57}Fe in the dissolved phase was significantly lower at 48 h than at 90 min, but not different from the other time points (Figure 4.2).

The absence of statistically significant changes is partly attributed to the actual absence of changes in these experiments, and partly due to the high variability between replicates. The latter is the result of natural variability of Fe in seawater, and is in accordance with the between-replicate variability being more pronounced in the naturally abundant ^{56}Fe isotope than in the artificially enriched ^{57}Fe in the experiments (compare error bars in red with blue framed subplots in Figures 4.2 to 4.4). As a hybrid-type metal with a strong atmospheric dust source, large concentration gradients occur over small depth scales between the mixed layer and the remainder of euphotic zone (Kunde et al., 2019). Seawater was collected from approximately 40 m, with the absence of a depth sensor on the pumping device hindering a more precise reading. As this sampling depth sat at the cusp of the MLD (Tables 4.1 and 4.2), variability in Fe concentrations was easily introduced over the course of the sampling duration, by mixing of the generally Fe-deplete euphotic zone waters with those of the Fe-replete mixed layer. The surface mixed layer itself is prone to variability, as freshly deposited dust particles may not be homogeneously distributed. This is also evident in the spikes of the surface TDFe gradient (Figure 4.1b).

Although we did not directly determine the particulate fraction collected on the filters, TDFe can be used to attempt a mass balance, i.e. the conservation of Fe concentrations. This is the sum of dFe and

'apparent particulate' (pFe_{app}), so it is the arguably arbitrarily defined fraction of acid-leachable Fe in unfiltered seawater after storage for >12 months. Overall, the mass balance was conserved in all three incubations relative to the TDFe concentrations at t_0 (in the case of the naturally abundance ^{56}Fe) and relative to the known spike amount (in the case of the artificially enriched ^{57}Fe) (Figure 4.2 to Figure 4.4). However, examining the individual time points within each incubation, revealed larger variability at Station 3 (difference up to 0.87 nM $^{56}TDFe$), compared to Station 4 (0.45 nM $^{56}TDFe$) and Station 7 (0.32 nM $^{56}TDFe$). These represent 45 %, 30 % and 26 %, respectively, of the average $^{56}TDFe$ concentrations across time points at each station, with the variability stemming from the TDFe gradient across the transect and the shortcomings of the experimental set-up. For comparison, this variability was 3.72 nM, which represents only 8.4 % of the *total* ^{56}Fe (average was 44.0 nM across time points) in Hurst & Bruland (2007). This considerably lower variability of *total* ^{56}Fe was derived from the sum of ^{56}dFe and 'true' ^{56}pFe that was explicitly measured in material collected on filters. However, this study was conducted in the Bering Sea, mixing high Fe waters from below the MLD with low Fe surface waters, which resulted in well-mixed, very high total Fe concentration in the incubation seawater, and hence lower variability.

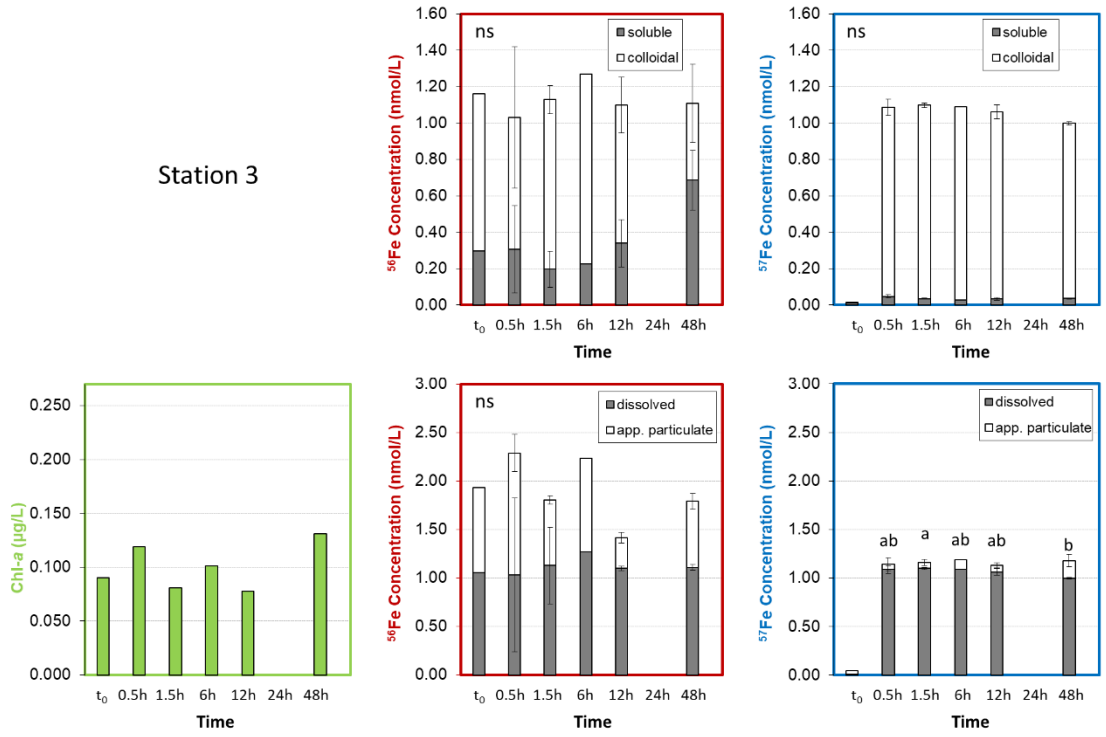

Figure 4.2 Results of the low abundance isotope experiments at Station 3. Bar plots show the experimental replicate mean of size-fractionated ^{56}Fe (red frames) and ^{57}Fe (blue frames) concentrations at each time point, with error bars showing one standard deviation of the mean. Letters in bottom right plot distinguish the significantly different concentrations of ^{57}Fe in the dissolved phase (with 'ns' = non-significant elsewhere). Concentrations of Chl-*a* (green frames) were only measured in one replicate per time point.

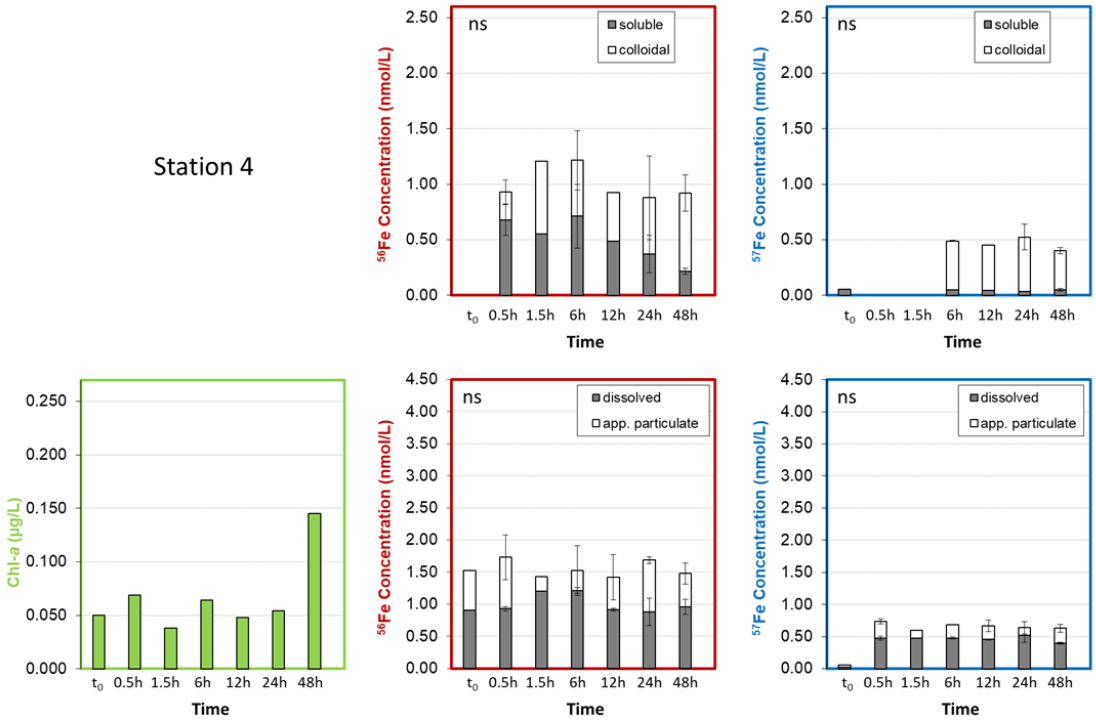

Figure 4.3 Results of the low abundance isotope experiments at Station 4. Bar plots show the experimental replicate mean of size-fractionated ^{56}Fe (red frames) and ^{57}Fe (blue frames) concentrations at each time point, with error bars showing one standard deviation of the mean. No significant changes were observed ('ns' = non-significant). Concentrations of Chl-*a* (green frames) were only measured in one replicate per time point.

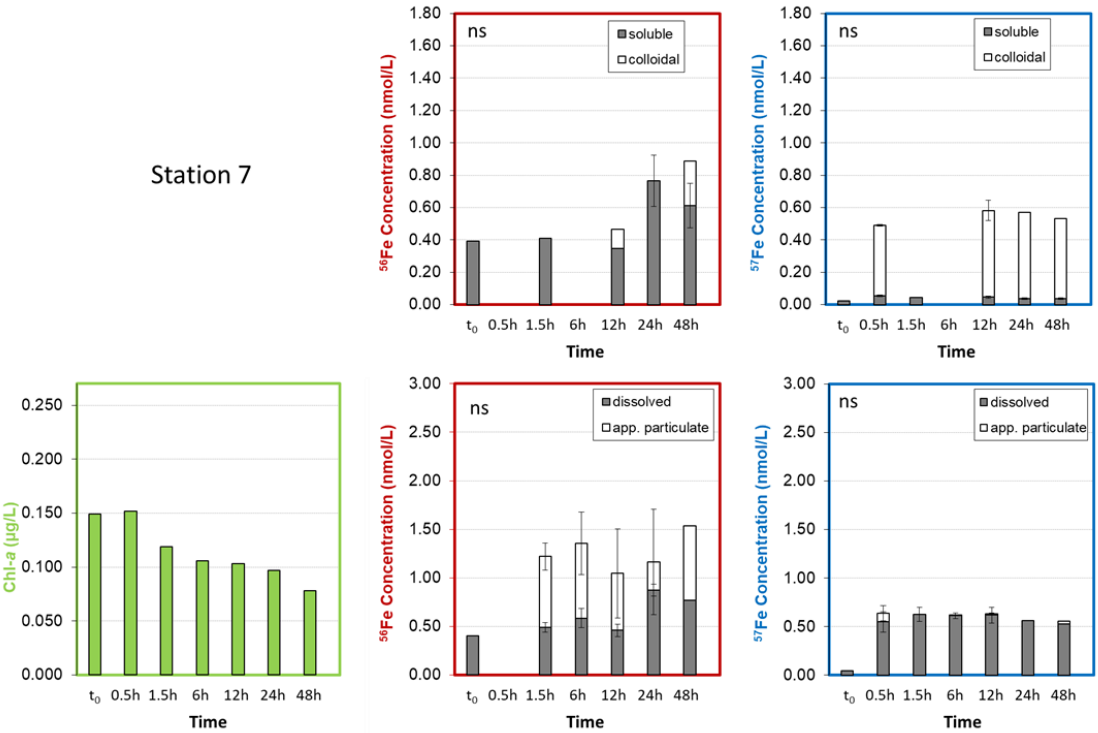

Figure 4.4 Results of the low abundance isotope experiments at Station 7. Bar plots show the experimental replicate mean of size-fractionated ^{56}Fe (red frames) and ^{57}Fe (blue frames) concentrations at each time point, with error bars showing one standard deviation of the mean. No significant changes were observed ('ns' = non-significant). Concentrations of Chl-*a* (green frames) were only measured in one replicate per time point.

The variability of the artificially enriched ^{57}Fe concentrations was less (6 %, 24 % and 14 % of the average ^{57}TDFe across time points at Stations 3, 4 and 7, respectively), confirming that the heterogeneity in ^{56}Fe concentrations was introduced prior to the spiking process, and it was similar to the low variability (8.6 %) of *total* ^{57}Fe, observed in Hurst & Bruland (2007). Furthermore, the ^{57}Fe spike was fully recovered in all incubations, which means that adsorption to the walls of the incubation containers was negligible in our experiments. This contrasts with the empirical assessment of Fischer et al. (2007), who showed that adsorption of Fe onto PC container walls is substantial – albeit lower compared to other materials – with ~50 % loss over 70 h (most within 30 h) of a radio-labelled ^{55}Fe addition to aged seawater in 0.5 L containers (higher surface area-to-volume ratios than our 2 L bottles). Previous incubation studies with Fe amendments in bottles that were comparable in size and material to ours, recorded various levels of wall adsorption over ~5 to 15 day-incubations (e.g. substantial wall adsorption in Buck et al. (2010) with ~50 % of added Fe adsorbed; little wall adsorption in Hurst and Bruland (2007), where adsorption within the variability of the mass balance).

Despite most changes in Fe concentrations being statistically insignificant over the course of the present incubations, some notable trends were observed over time, especially in the partitioning between sFe and cFe of the naturally abundant ^{56}Fe, which differed between the three stations. The concentrations of ^{56}dFe at Station 3 remained at an average concentration of 1.10 ± 0.11 nM over the entire 48 h incubation period and all replicates, while the concentration of ^{56}sFe was higher at 48 h with 0.69 ± 0.17 nM than the pre-48 h average of 0.28 ± 0.15 nM (Figure 4.2). This indicates a transfer from ^{56}cFe into ^{56}sFe. In contrast, at Station 4 the concentrations of ^{56}sFe gradually decreased towards 0.22 ± 0.03 nM at 48 h compared with 0.61 ± 0.24 nM (averaged over all previous time points), while ^{56}dFe did not vary (0.98 ± 0.12 nM at 48 h compared to 1.00 ± 0.17 nM before 48 h) (Figure 4.3). This indicates a transfer from ^{56}sFe to ^{56}cFe. A third scenario was observed at Station 7, where ^{56}dFe concentrations were predominantly in the soluble phase throughout the incubation. Intriguingly, ^{56}sFe concentrations increased alongside ^{56}dFe concentrations at the last two time points compared to their concentrations prior to 24 h, namely from 0.38 ± 0.03 nM to 0.67 ± 0.13 ^{56}sFe and from 0.50 ± 0.09 nM to 0.84 ± 0.07 nM ^{56}dFe. This indicates the introduction of 'new' ^{56}dFe in the form of ^{56}sFe, and must have derived from the particulate pool. However, a respective decrease in $^{56}pFe_{app}$ could not be resolved, as this was within the error of the ^{56}TDFe variability. Finally, none of the temporal trends on the soluble/colloidal level at Stations 3, 4 and 7 were observed in ^{57}Fe. All of these trends were observed only at 24 h or 48 h, i.e. any time after the 12 h time point was sampled.

Auxiliary Chl-*a* data were restricted to one replicate per time point in the low abundance isotope experiments, therefore precluding any significance testing. Nevertheless, at 48 h Chl-*a* concentrations increased to 0.131 µg L^{-1} at Station 3, and more strongly to 0.145 µg L^{-1} at Station 4, compared with the average concentrations across all previous time points of 0.095 ± 0.019 at Station 3 and 0.055 ± 0.012 µg L^{-1} at Station 4 (Figures 4.2 and 4.3). In contrast, at Station 7 Chl-*a*

concentrations gradually decreased from 0.152 µg L^{-1} at 30 min to 0.078 µg L^{-1} at the end of the incubation (Figure 4.4). Although these changes during the low abundance isotope experiments were two- to three-fold, the absolute Chl-*a* concentrations were typically oligotrophically low (<0.160 µg L^{-1}) throughout the incubations, so that the significance of any Fe-triggered changes in Chl-*a* responses are better assessed through the results of the Fe bioassays (see below), for which experimental replication was available.

4.4.3 Results from the Fe Bioassays

Results of the Fe bioassays provided insights into the response of phytoplankton to a range of Fe additions (added as inorganic sFe from a stock with natural isotopic composition) with or without DIN across the basin, and so they are relevant to the interpretation of the biological component of Fe cycling in the low abundance isotope experiments. The concentrations of Chl-*a* at 48 h are depicted in Figure 4.5 for the various treatments.

Firstly, at none of the Stations 1 to 7 did any addition of Fe alone trigger a significant change in Chl-*a* concentrations relative to the unspiked Control treatment. Secondly, at those stations were Fe additions were made alongside DIN additions (i.e. Stations 1 to 4), a consistent increase in Chl-*a* concentration was observed. At Station 1, DIN additions increased Chl-*a* to 0.048 ± 0.010 µg L^{-1} (averaged over all DIN treatments regardless of amount of Fe spike) compared to 0.087 ± 0.018 µg L^{-1} in the Control. At Station 2, this increase was from 0.055 ± 0.030 µg L^{-1} to 0.083 ± 0.020 µg L^{-1}, and at Station 3 it was from 0.042 µg L^{-1} to 0.086 µg L^{-1}. The Chl-*a* response was independent of the amount of Fe addition and occurred also in those treatments, where DIN was added without Fe (see 'DIN' in Figure 4.5). Hence, the DIN addition was the driver, not the Fe addition. However, this trend was only statistically significant relative to the unspiked Control upon the addition of 1.0 or 2.0 nM Fe with 2 µM DIN at Station 4 (marked with * in Figure 4.5). These treatments were not statistically different from the DIN treatment without Fe addition.

Tying the Chl-*a* responses from the Fe bioassays at Stations 3, 4 and 7 to their equivalents in the low abundance isotope experiments, leads to the assumption that the small changes in the single replicates of Chl-*a* in the low abundance isotope experiments at 48 h were unlikely significant at Stations 3 and 7, but likely significant at Station 4, although this was driven by the addition of DIN rather than the addition of Fe. Whether significant or not, the observed changes in Chl-*a* were only discernible late during the incubations (i.e. by the 48 h time point), similarly to any trends that were observed in the exchange between the Fe size fractions of the naturally abundance ^{56}Fe.

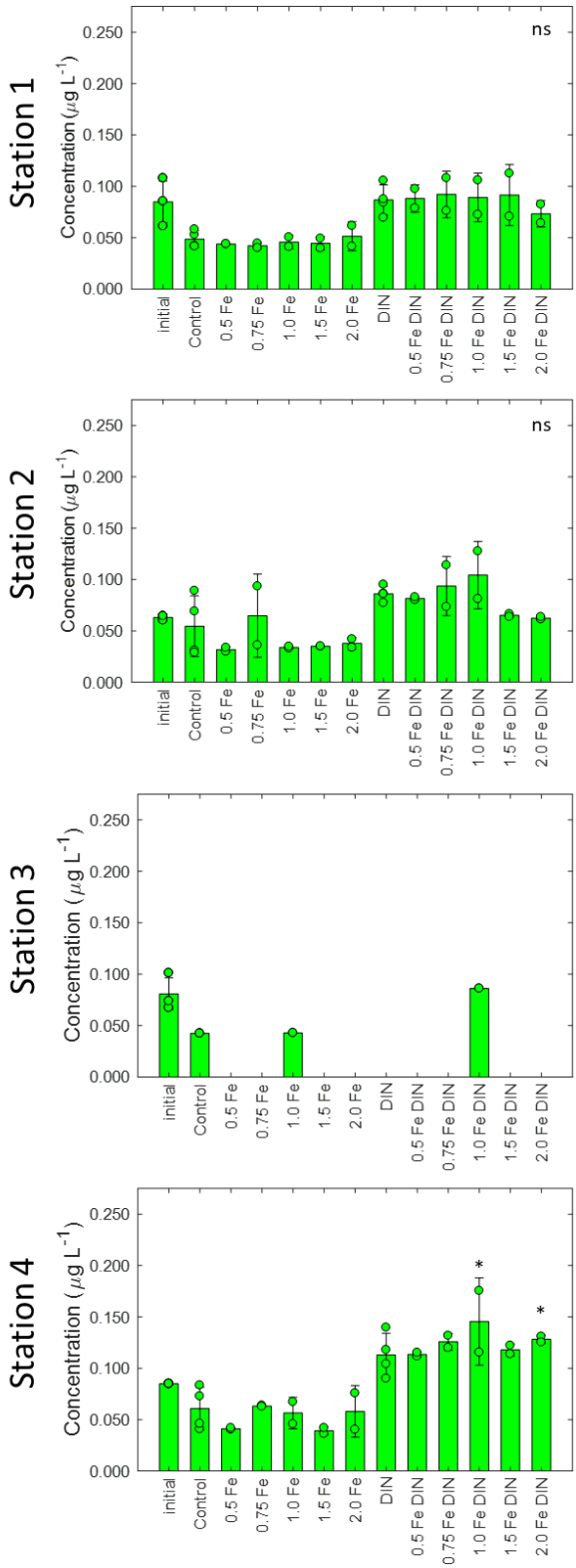

Figure 4.5 Results of the Fe bioassays. Bar plots show the mean Chl-*a* concentrations for each treatment after 48 h, with error bars indicating one standard deviation of the mean. Dots show individual replicates of each treatment. Stars (*) indicate statistically significant differences compared to the Control; 'ns' = non-significant. For Stations 5 to 7, where experiments were conducted twice, the respective date is indicated.

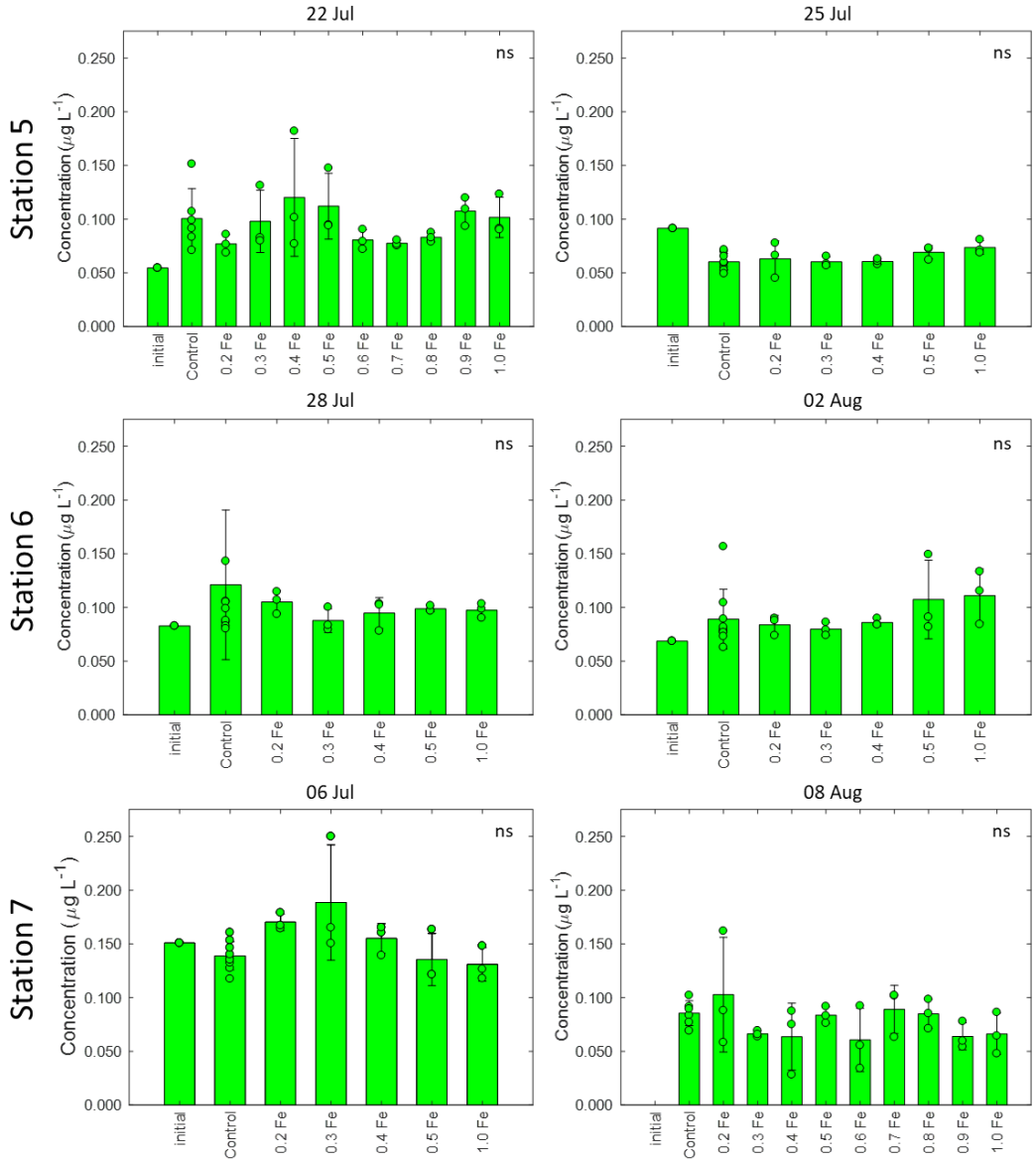

Figure 4.5 *continued.*

4.5 Discussion

4.5.1 Biological Control of Iron

Insights from the Fe bioassays clearly showed that over the entire basin (Stations 1 to 7), phytoplankton were not limited by ambient Fe availability, across the strong dust-driven gradient in surface dFe concentrations that led to initial dFe concentrations as low as 0.32 to 0.40 nM at Station 7, where macronutrients were comparably higher. Instead, DIN was the limiting nutrient for phytoplankton growth in our experiments, in line with the general paradigm of macronutrient limitation in the subtropical gyres (Moore et al., 2013). Nevertheless, trends in protein biomarkers for N_2 fixation and APA, which have Fe requirements, *did* indicate persistent Fe stress in *Trichodesmium* during the JC150 cruise (Held et al., 2020). Therefore, in the light of the low

abundance isotope experiments, the changes in the Fe speciation could be expected to be shaped in part by microbes carrying out N_2 fixation and APA, especially because the speciation of the added Fe (i.e. inorganic, soluble-sized) may be more readily accessible compared with the less bioavailable dust-derived Fe that was naturally present in the seawater. By alleviating N limitation in some of the incubations (Stations 3 and 4), the system was driven towards P limitation, probably increasing the role of APA and associated Fe requirements.

4.5.2 Rapid Formation of Colloidal Iron

The almost immediate (i.e. mostly within 30 min), consistent (i.e. at all stations/initial conditions) and almost complete (≥ 90 %) partitioning of the ^{57}Fe enriched spike from the soluble into the colloidal fraction (by ^{57}Fe concentrations in sFe samples) indicates that the ambient seawater speciation could explain this transformation by one or more of the following drivers: 1) formation of inorganic nanoparticles (e.g. amorphous Fe-oxyhydroxides), 2) complexation by an excess pool of colloidal-sized organic ligands, or 3) complexation by rapidly produced colloidal-sized organic ligands.

The consistency of the colloidal partitioning trend across the experiments at all stations would suggest a common mechanism that is independent of differences in resident phytoplankton and heterotrophic communities, and so may be an abiotic driver, i.e. namely the formation of nanoparticulate Fe-oxyhydroxides. Under modern seawater conditions, free Fe' is insoluble and within minutes forms hydroxide complexes, predominantly $Fe(OH)_2^+$ and $Fe(OH)_3$, which are precursors for Fe-hydroxide precipitates (Millero et al., 1995; Pham et al., 2006). The rapid colloidal partitioning time scale of <30 min observed here, aligns with this. However, the lack of significant wall adsorption of the ^{57}Fe spike in our experiments is in counter to Fe-oxyhydroxide formation being the dominant driver behind the colloidal partitioning signal, because the functional groups of the PC container walls are expected to compete efficiently for Fe. This is derived by considering that Fischer et al. (2007) calculated the Fe-affinity of polymethylmetacrylate (PMMA) walls to be $\log K_{(Fe',Fe\text{-}wall)}$ = 12.2 to 12.7, which is comparable to that of natural ligands in seawater (e.g. Gledhill and Buck, 2012), while the Fe speciation is ≫99 % Fe-hydroxide complexes (with ≪1 % Fe') in organics-free artificial seawater (Millero et al., 1995), but typically to ~99 % comprised of organic Fe-ligand complexes in natural seawater samples (Gledhill and Buck, 2012). Although $\log K_{(Fe',Fe\text{-}wall)}$ was not determined explicitly for PC, the Fe-binding functional groups on PC walls would necessitate that an excess pool of colloidal-sized organic ligands – e.g. saccharides or humic substances (Hassler et al., 2011; Laglera & Van Den Berg, 2009) – bound the added Fe competitively in our experiments, protected it against wall adsorption, and caused the rapid partitioning into cFe. At the same time, this would mean that soluble-sized Fe-binding ligands, e.g. siderophores (Mawji et al., 2008), were either

absent or less competitive than any colloidal-sized ligands. Otherwise, the spike would have been retained as ^{57}sFe.

In a study of size-fractionated Fe-ligands in the surface subtropical North Atlantic, Fitzsimmons et al. (2015a) showed that colloidal-sized ligands are less abundant than soluble-sized ligands, and that there was no excess of colloidal-sized ligands present both in the western and eastern basin. Furthermore, Cullen et al. (2006) showed that measured cFe concentrations were systematically higher than theoretical cFe concentrations calculated from the colloidal ligand abundance across the Atlantic Ocean, i.e. no excess colloidal-sized ligand pool was observed in this study either. An alternative to the presence of a readily available excess colloidal-sized ligands in our incubations would be the rapid production of such ligands upon the Fe addition. While active Fe retention mechanisms are typically driven by the excretion of soluble-sized, rather than colloidal-sized, ligands (e.g. Boiteau et al., 2016; Bundy et al., 2018), Boye et al. (2005) did observe an increase in colloidal-sized Fe-binding ligand concentrations concurrently with cFe concentrations, following Fe release into the Southern Ocean. However, their temporal resolution was restricted to daily measurements, so it remains unclear, whether these ligands were produced as rapidly as would be needed to explain the results of our low abundance isotope experiments. Following a natural dust event in the North Pacific near HOTS, ligand production (no size-fractionated resolution) was time-lagged by one to two days of microbial response time (Fitzsimmons et al., 2015c). Without size-fractionated ligand data, the main driver of the rapid colloidal partitioning in the low abundance isotope experiments remains open. Based on the above arguments, however, it is unlikely that an excess colloidal-sized ligand pool was present in the incubation seawater, or that sufficient organic ligand production occurred within 30 min after the Fe addition. If ligands were the driving force behind this partitioning, then a portion of the naturally abundant ^{56}Fe in the sFe size fraction would be expected to be drawn into the colloidal phase too, but ^{56}cFe and ^{57}cFe behaved differently. Taken together, the formation of nanoparticulate Fe-oxyhydroxides is therefore the most probable main driver for the colloidal partitioning trend.

There is a growing body of evidence for cFe to be a key determinant of the oceanic Fe cycle (e.g. as highlighted in a recent GEOTRACES review by Anderson, 2020; Kunde et al., 2019), but the time scales of exchange and the exact nature of cFe are not known. The rapid formation of nanoparticulate Fe-oxyhydroxides species, as suggested here, has important implications for decreasing the residence times of Fe in the surface ocean, because these cFe species form precursors of larger precipitates that would become dense enough to sink out of the euphotic zone. Recently, Black et al. (2020) estimated that the residence time of dFe would be lowered from 2 years to <2 months in the oligotrophic gyres, if the ill-constrained formation of authigenic particles is incorporated as a loss term of dFe to pFe. Lastly, the natural partitioning of dFe into cFe in the surface North Atlantic is high with >50% and often >75% of dFe (Fitzsimmons et al., 2015b; Kunde et al., 2019), but not typically as high as the

~90 % observed during the low abundance isotope experiments. The extraordinary high fraction of cFe to dFe in the experiments could indicate that any subsequent mechanisms (e.g. ligand-mediated exchange), which would transfer some of the cFe into the soluble phase, operate on time scales longer than the probed 48 h. The kinetics of Fe cycling on longer scales merits further investigation.

4.5.3 Exchange between Soluble and Colloidal Iron

The absence of changes in ^{57}Fe concentrations across size fractions after the immediate colloidal partitioning demonstrates the independent behaviour of the naturally abundant Fe pool (representatively ^{56}Fe) and the newly introduced Fe (representatively ^{57}Fe) over the 48 h incubation period, as a result of slow kinetics exchange. The high-Fe environment of the North Atlantic, where the phytoplankton growth is not Fe-limited, may contribute to this slow exchange. In regions, where Fe *is* the primary limiting nutrient, numerous incubation experiments (Bertrand et al., 2007; Buck et al., 2010; Crawford et al., 2003; Lohan et al., 2005b) and mesoscale fertilisation experiments (Bowie et al., 2001; Boyd et al., 2000; Boye et al., 2005; Coale et al., 1996; Nishioka et al., 2005) with Fe amendments to ambient seawater have shown dramatic changes in Fe concentration and speciation over time (~5 to 20 days). However, upon examination of the few available data sets, in which Fe has been measured at multiple time points during bottle incubations, it appears that the changes in Fe concentration or speciation over the first two to three days following the Fe addition were very subtle compared to the longer term changes (Buck et al., 2010; Lohan et al., 2005b). This implies that Fe exchange kinetics are slow in Fe-limited regions too, and changes are only observed, once nutrient drawdown begins after ~3 days. The microbial community in these regions is typically dominated by diatoms, i.e. larger phytoplankton, which thrive in bottle experiments. Our incubations were designed for a 48 h time period, because the phytoplankton community in the subtropical North Atlantic is dominated by small cells, such as *Synechococcus* and *Prochlorococcus* that are challenging for incubation experiments, because they are lost rapidly (<8 h) by grazing and lysis during enclosure (Fernández et al., 2003). Other incubation experiments during JC150 showed decreasing cell counts of these species after 48 h (see Figure 5.2 in Chapter 5).

While the size-fractionation of the artificially enriched ^{57}Fe did not change over time, exchange between the soluble and colloidal fractions occurred in the naturally abundant ^{56}Fe. These differed between the experiments at the three locations across large ambient biogeochemical gradients. At both eastern Stations 3 and 4, an exchange occurred between ^{56}sFe and ^{56}cFe, while ^{56}dFe was constant, implying no exchange between the particulate and dissolved phases. Interestingly, the partitioning changed from cFe into sFe at Station 3, whereas the opposite occurred at Station 4 (from sFe into cFe). Both of these stations were subject to large Fe-rich dust deposition, where cFe is the dominant source of dFe (Chapter 3). At Station 3, the partitioning of cFe into sFe was potentially driven by the microbial community to enhance bioavailability, but no net decrease in the dFe was

observed, which would be expected if this cFe-to-sFe transformation was to facilitate biological uptake. Surprisingly, Station 4 showed the opposite trend. At Station 4 diazotrophic activity was much higher than at Station 3 (see Figure 2.2 in Chapter 2), while other biogeochemical parameters and initial Fe concentrations were similar (Tables 4.1 and 4.2). Due to the high Fe demands of enzymes involved in biological N_2 fixation, unique Fe acquisition strategies exist amongst diazotrophs, such as the ability of *Trichodesmium* to acquire Fe from the mineral phase (Basu et al., 2019; Rubin et al., 2011). In line with this, a significant increase in Chl-*a* was observed after incubation for 48 h at this station (Figure 4.3). Colloidal Fe represents the intermediate stage in the transfer of particulate Fe into the dissolved fraction. While we did not observe a decrease in the pFe_{app} concentrations, possibly because this does not represent the total particulate Fe pool, the increase in cFe could represent the step-wise dissolution of the Fe-bearing particles by *Trichodesmium* for the subsequent uptake of solubilised Fe.

In contrast, sFe rather than cFe dominated the dFe pool at Station 7 (Figure 4.4), which is in line with low dust supply at this station resulting in a nutrient-like profile, with no surface enrichment in cFe (compare Figure 3.6 in Chapter 3). After 24 h, a large net increase in ^{56}sFe and hence in ^{56}dFe occurred, concurrently with a gradual decrease in Chl-*a* concentrations. This may indicate the degradation of organic matter, thereby releasing dFe back into solution. To date, it is unclear how remineralisation and post-remineralisation processes impact on the partitioning of the dFe pool (Boyd et al., 2017, 2010; Twining et al., 2015). The current paradigm is that in the subtropical North Atlantic these processes result in a roughly equal partitioning between cFe and sFe (Fitzsimmons et al., 2015b; Kunde et al., 2019). However, this is based on profile data, which only provide a snapshot at any one time in space, and cannot account for kinetics. The results from the incubation at Station 7 suggests that remineralisation occurs into the soluble phase first.

Overall, the drivers behind the differing exchange patterns of the naturally abundant ^{56}Fe between sFe and cFe that occurred towards the end of the incubations at the three stations cannot be resolved unequivocally. Nevertheless, the kinetics of Fe exchange on the soluble/colloidal level highlights that dynamic processes act on dFe in seawater and that regional biogeochemical variability impacts these.

4.6 Conclusions

The minutes-to-days exchange of size-fractionated Fe species (TDFe, dFe, sFe) was traced at three representative locations across strong biogeochemical gradients (e.g. in Fe, macronutrients and Chl-*a*) between 60 to 30 °W in the subtropical North Atlantic in summer 2017. Seawater was spiked with a low abundance Fe isotope stock, in the form of inorganic sFe. The main result is the rapid (<90

min), consistent (all locations), nearly complete (88 to 97 % of dFe) and irreversible (over 48 h) partitioning of the ^{57}Fe enriched spike into the colloidal phase, due to the likely formation of ferric oxyhydroxides nanoparticles, in the absence of a readily available excess organic ligand pool. This insight strengthens the argument for cFe being a key component of the marine Fe cycle, as also derived in Chapter 3. Particularly, the authigenic formation of Fe-nanoparticles can dramatically reduce the residence time and hence the bioavailability of dFe in the North Atlantic. Furthermore, changes in the size fractionation (sFe versus cFe) occurred in the naturally present Fe pool over 48 h, which differed between the three locations and were influenced by the local biogeochemistry, e.g. diazotrophic activity and dust loading.

Chapter 5 Effects of Iron, Zinc and Cobalt Additions on Cyanobacterial Alkaline Phosphatase Abundances in the Subtropical North Atlantic

Preface

The research presented in this chapter is in preparation for submission to *Limnology & Oceanography* (Kunde et al.). I planned, conducted and analysed the quantitative proteomics measurements in the bioassays, interpreted the results, designed the figures and drafted the manuscript with significant input from all co-authors. Furthermore, I have measured the relevant *in-situ* and bioassay-related Fe concentrations included in this manuscript. I have participated in the associated research cruise, which included the set-up and sampling of the bioassays in a team. The raw data used in this chapter are included in the appendix of the thesis.

Kunde, K., Held, N.A., Davis, C.E., Wyatt, N.J., Woodward, E.M.S., McIlvin, M., Moore, C. M., Twining, B., Saito, M. A., Tagliabue, A., Mahaffey, C. and Lohan, M. C. (in preparation for *L&O*). Effects of Iron, Zinc and Cobalt Additions on Cyanobacterial Alkaline Phosphatase Abundances in the Subtropical North Atlantic.

5.1 Abstract

Alkaline phosphatases provide an important pathway for phytoplankton to access to the vital nutrient P from the DOP pool, when the more bioavailable DIP is depleted, such as in the surface subtropical North Atlantic. However, the requirement for Zn, Co or Fe co-factors in these enzymes gives rise to the potential for metal-P co-stress of primary production. Applying calibrated quantitative proteomic measurements of alkaline phosphatases of two key phytoplankton species, *Synechococcus* and *Prochlorococcus*, in metal-amended bioassays *in-situ*, we demonstrate the localised effect of metal additions on alkaline phosphatase concentrations at two contrasting biogeochemical sites within the subtropical gyre. In the western basin, the concentrations of a *Synechococcus* PhoA-type alkaline phosphatase increased upon Zn or Co addition, while in the eastern basin the concentration of a *Prochlorococcus* PhoX-type alkaline phosphatase increased upon Fe addition. The effect of the Co addition on the abundance of the *Synechococcus* PhoA in the field is a new observation and adds support to the hypothesis regarding the cambialistic properties of this enzyme. Using cellular metal stoichiometry, we show that *Synechococcus* PhoA could be a major sink for cellular Co, but not for Zn. Hence, *Synechococcus* could be sensitive to ambient Co availability globally. The predicted exacerbation of P stress and altered trace metal availability in the future ocean are currently met with a limited baseline understanding of marine alkaline phosphatase dynamics. Our results highlight the timeliness of combining trace metal chemistry, biological rate measurements, and cell quotas with proteomics data types on the basin scale.

5.2 Introduction

The vast oligotrophic subtropical North Atlantic gyre is characterised by subnanomolar concentrations of the readily bioavailable dissolved inorganic forms of the vital nutrients P and N, i.e. DIP and DIN, which constrain primary production by phytoplankton and hence, reduce the efficiency of the biological carbon pump (e.g. Martiny et al., 2019; Moore et al., 2013). Large inputs of atmospherically derived Fe from Saharan desert dust create a niche for Fe-expensive diazotrophy, which delivers an alternative source of DIN to the phytoplankton community and thereby, can partially alleviate N limitation (Moore et al., 2013; Schlosser et al., 2014). However, this mechanism requires large resources of DIP and Fe, which leads to the decoupling of the biogeochemical cycles of N and P and forces a shift towards the acquisition of the less bioavailable DOP by phytoplankton to meet cellular P demands (Lomas et al., 2010; Mather et al., 2008). The DOP pool consists of relatively labile phosphomono- and diesters (together ~75 to 85 %) that derive from ribonucleic acids, adenosine phosphates and phospholipids (Kolowith et al., 2001; Young and Ingall, 2010). Cleavage of the phosphate group from the ester moiety is catalysed by a range of hydrolytic enzymes including the mono- and diesterases alkaline phosphatases that are ubiquitous across the marine

bacterial realm (Luo et al., 2009), while APA is widespread across the oligotrophic gyres (compilation in Duhamel et al., 2010; Browning et al., 2017; Davis et al., 2019; Mahaffey et al., 2014; Wurl et al., 2013), but also in DIP-replete shelf seas (Davis and Mahaffey, 2017) and throughout the full water column (Baltar et al., 2010). While bacterial alkaline phosphatases are commonly regulated to by intracellular DIP concentrations via the *pho* regulon (Santos-Beneit, 2015), they also depend on metal co-factors at their active site. Yet to be characterised explicitly for marine microbes, these active sites are occupied by one Mg^{2+} and two Zn^{2+} or substitute Co^{2+} per homodimer of PhoA in *E. coli* (Coleman, 1992), and of three Ca^{3+} and two Fe^{3+} in the monomeric PhoX in *Pseudomonas fluorescens* (Yong et al., 2014).

In the ocean, the trace metals Zn, Co and Fe are present at only nano- to picomolar concentrations, while the surface concentrations of Zn and Co are particularly depleted, as they lack the large atmospheric source that applies to Fe (Lohan & Tagliabue, 2018). This has led to the hypothesis that these trace metals limit DOP acquisition via alkaline phosphatases in the subtropical North Atlantic. This has previously been tested by quantifying changes in APA rates in bioassays of ambient seawater with Fe or Zn amendments (Browning et al., 2017; Mahaffey et al., 2014), via enzyme assays with model phosphoesters that fluoresce upon hydrolysis (e.g. 4-methylumbelliferyl phosphate (MUF-P); Ammerman, 1993). While these bioassays yielded important evidence for the localised controls on APA rates exerted by Zn (Mahaffey et al., 2014) or Fe (Browning et al., 2017), the assay-based approach could neither distinguish the enzyme type, PhoA or PhoX, nor the responsive organisms unambiguously. In addition, the model substrate MUF-P does not cross the inner membrane, so that measured APA accounts only for the extracellular and periplasmic alkaline phosphatases (Martinez and Azam, 1993) and is likely biased towards detecting PhoX activity, as only ~20 % and 45 % of marine bacterial PhoX and PhoA, respectively, are predicted to be active on the inner membrane or in the cytoplasm (Luo et al., 2009).

The recent advancement of field-based proteomic tools for the marine environment now allows for the resolution of some of these complexities by detecting responses at the immediate cellular level (see Saito et al., 2019 for a full review). Furthermore, the calibrated absolute quantitation of selected proteins (as fmol protein per L seawater) facilitates quantitative comparisons between enzymes types, e.g. PhoA versus PhoX, and between different species, e.g. *Synechococcus* versus *Prochlorococcus*, and enables comparisons with other data quantitative types, e.g. cellular metal quotas. This provides great potential to enhance our understanding the nutrient controls on phytoplankton growth and to assess macro- and metal micronutrient interactions in the ocean.

In this study, we measured the absolute concentrations of the alkaline phosphatases PhoA and PhoX as well as PstS – a DIP stress biomarker commonly used in transcriptomic studies – of the globally important primary producers *Synechococcus* and *Prochlorococcus* that dominate the phytoplankton community in the oligotrophic subtropical North Atlantic. We applied this approach to *in-situ*

bioassays with metal amendments (Zn, Co or Fe) under contrasting biogeochemical conditions across the subtropical gyre. The aim was to diagnose the metal constraints on alkaline phosphatase concentrations. Specifically, we addressed the question: Does the low availability of Zn, Co and/or Fe stunt alkaline phosphatase expression and thus constrain DOP acquisition and primary production?

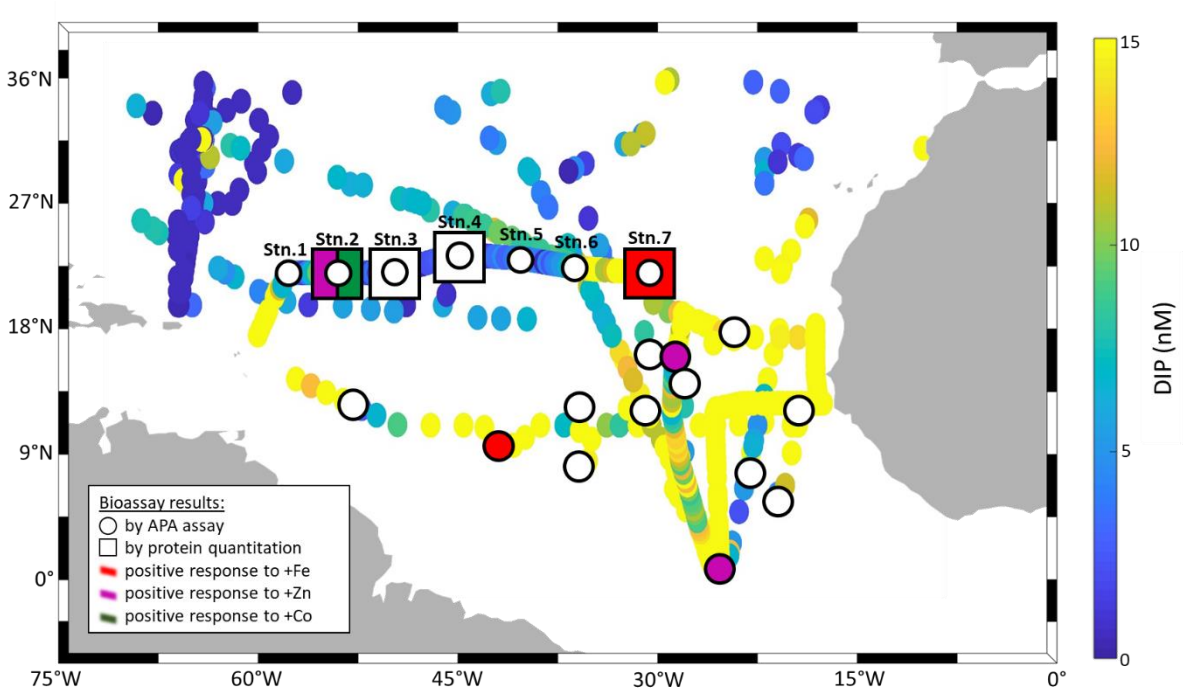

Figure 5.1 Map of the North Atlantic showing surface DIP concentrations (data compilation by Martiny et al., 2019; augmented with data from Browning et al. 2017). Overlain are locations of bioassays, where the response of APA to metal additions was tested (circles), and of bioassays, where the absolute concentration of the alkaline phosphatase proteins was measured in response to metal additions (squares). Bioassays of the present study are labelled with station numbers referring to cruise JC150, the others are from previous studies by Mahaffey et al. (2014) and Browning et al. (2017). Symbols at bioassay locations are coloured in red, purple or green, if a positive response was observed upon addition of Fe, Zn or Co respectively.

5.3 Methods

5.3.1 Sample Collection and Shipboard Bioassays

All samples for this study were collected on board the *RRS James Cook* during research cruise JC150 (GEOTRACES section GApr08), on a meridional transect at 22 °N leaving Guadeloupe on June 26th and arriving in Tenerife on August 12th 2017. The stations occupied for our bioassays are those shown in Figure 5.1, which are labelled with 'Stn. 1' through 'Stn. 7'. The focus of the present study is on the insights gained through proteomic analyses and therefore, only those bioassay results are described and discussed subsequently, for which proteomics data exist, namely Stations 2, 3, 4 and 7. The reader is referred to Mahaffey et al. (in prep) for a full analysis of research outcomes from cruise JC150 that include Stations 1, 5 and 6.

Prior to the expedition, 24 L PC carboys (Nalgene) and spigots were acid-washed according to GEOTRACES protocols (http://www.geotraces.org/images/Cookbook.pdf). Between stations, the carboys and spigots underwent thorough rinses with weak hydrochloric acid and UHP water to replicate the same starting conditions for each set of experiments. Seawater for the bioassays was collected strictly before dawn using two different methods. At Station 2, a Ti-rosette fitted with 24 x 10 L trace metal-clean Teflon-coated Ocean Test Equipment (OTE) bottles and a CTD profiler (Sea-bird Scientific) was deployed on a conducting Kevlar wire three times to collect samples from 40 m depth. The recovered OTE bottles were transported into a class-100 clean air van without lights or windows. The carboys were triple-rinsed and then filled with unfiltered water from the OTE bottles using acid clean silicone tubing under dim red light conditions. To remove bias, each carboy received water from a minimum of three different OTE bottles and was filled to a third of its volume from each of the subsequent deployments. To reduce the time for the bioassay set-up, the process was amended for subsequent bioassays. At Stations 3 to 7, trace metal-clean braided polyvinyl chloride hosing cable-tied to a Kevlar wire was lowered, aided by an epoxy-coated weight, to pump seawater using a Teflon diaphragm pump (Almatec) directly from 40 m into a class-100 clean air van onboard. After flushing the tubing for 15 min and triple-rinsing the carboys with unfiltered *in-situ* seawater, each carboy was filled at random to a third of its volume at a time. Still in the dark, the seawater was spiked with additions of Fe, Zn or Co in duplicate or triplicate, as detailed in Table 5.1. The carboys were gently shaken, sealed with Parafilm and transported into a neighbouring custom-built incubation van set at ambient sea surface temperature at 50 % surface light level. The seawater was incubated for 48 h with 12 h 'lights on' and 12 h 'lights off'.

Table 5.1 Bioassay details at each station, showing the types of treatments, the amount of metal added, and the number of replicates per treatment. Note that one of the three replicates of the Fe addition at Station 7 (*) was removed as an outlier from further analysis.

		Station 2	Station 3	Station 4	Station 7
Replicates per treatment		2	2	2	3*
Treatment / Addition	**Control**	No spike	No spike	No spike	No Spike
	Fe	+ 1.0 nM	1.0 nM	+ 1.0 nM	+ 1.0 nM
	Zn	+ 1.0 nM	+ 1.0 nM	+ 0.5 nM	+ 1.0 nM
	Co	+ 50 pM	+ 50 pM	+ 50 pM	+ 20 pM

Following incubation, one replicate of each treatment was transferred to a class-100 clean air van where a trace metal cleaned spigot was attached to the carboy and unfiltered subsamples were first taken for auxiliary parameters (details in Section 5.3.6). Then, subsamples for proteins were collected into acid cleaned 10 L polycarbonate carboys (Nalgene) and immediately filtered, collecting the >0.22 μm fraction on a polyethersulfone membrane filter cartridge (Millipore, Sterivex) and recording the filtered volume. Any remaining water was pressed out with an air-filled syringe, the

filtration unit sealed with clay and then frozen at -80 °C. This procedure was repeated for the second (and third where applicable) replicate of each treatment. Each round of breakdowns took approximately 1.5 h, so that the time gap between sampling the first and the last replicate is 3 to 4.5 h. This approach was chosen over a randomised breakdown to minimise time-dependent bias between treatments and, if necessary, to be able to account for time bias between replicates. This was later determined not to be the case.

5.3.2 Protein Extraction and Digestion

All materials were washed with ethanol and dried before usage. All samples of one station were processed together in one extraction and digestion cycle. The frozen sterivex filters were transported to the laboratory on ice and cut open with a tube cutter. The filters were cut out from its holder with razor blades and placed into 2 ml microfuge tubes (Eppendorf), maximising the exposed surface area. Proteins were extracted using detergent-based methods described elsewhere (Held et al., 2020; Saito et al., 2014), and left to precipitate for 5 days at -4 °C. Protein mass was quantified by a bicinchoninic acid assay (Pierce) before and after the precipitation step to assess the protein recovery. The protein extracts were digested with the proteolytic enzyme trypsin (1 µg per 20 µg protein; Promega #V5280) in a polyacrylamide tube gel following the protocol by Lu and Zhu (2005). The digested samples were concentrated by vacuum drying and stored at -20 °C until measurement. The final volume was recorded to calculate the total protein concentration in the processed sample, typically ~1 µg μl^{-1}.

5.3.3 Target Protein Selection

Three protein biomarkers for *Synechococcus* and *Prochlorococcus* were chosen to detect DIP stress (by PstS) and coping mechanisms via DOP acquisition (by PhoA and PhoX) (Table 5.2). PstS is the substrate-binding protein of the high affinity phosphate ABC (ATP-Binding Cassette) transporter, which is upregulated under low cellular DIP concentrations via the *pho* regulon and has previously been used as indicator of DIP stress (e.g. Cox and Saito, 2013; Martiny et al., 2006; Scanlan et al., 1993). PhoA and PhoX are the Zn/Co-dependent and Fe-dependent alkaline phosphatases, respectively, which facilitate the acquisition of P from the DOP pool. The criteria for a peptide of the protein biomarker to be used for quantification were as follows (Table 5.2): Firstly, we attempted to minimise the presence of methionine and cysteines because they are subject to oxidation and cause modifications of the mass-to-charge ratio (m/z) during the analyses. Secondly, the specificity and least common ancestor of each tryptic peptide was assessed using METATRYP (https://metatryp.whoi.edu/). Finally, the performance of each precursor ion was visually inspected in Skyline for peak shape and signal to noise-ratio during uncalibrated test measurements (MacLean et al., 2010).

Table 5.2 Details on the quantified peptide biomarkers that are used representatively of the respective protein in subsequent plots and discussions. For *Prochlorococcus* strains, HL and LL refer to high-light and low-light adapted strains, respectively.

	Protein	Peptide (Amino Acid Sequence)	Least Common Ancestor	Strains with this peptide
Synechococcus	PhoA	HYIAVALER	*Synechococcus*	WH8102 (clade III)
	PhoX	SQAGAELFR	*Synechococcus*	WH8102 (clade III)
	PstS	WFQELAAAGGPK	*Synechococcus*	RCC307 (clade X)
Prochlorococcus	PhoA	IYVIDPSSSPALLER	*Prochlorococcus*	MIT9311 (HL II) MIT9312 (HL II) MIT9314 (HL II)
	PhoX	GNLWIQTDGK	*Prochlorococcus*	MIT9314 (HL II)
	PstS	LSGAGASFPAK	*Prochlorococcus*	MIT9301 (HL II) MIT9302 (HL II) MIT9311 (HL II) MIT9312 (HL II) MIT9314 (HL II) SB (HL II) NATL1A (LL I) NATL2A (LL I)

5.3.4 Heavy Isotope-Labelled Standard Peptides

The absolute quantitation of the target peptides was achieved using heavy N isotope-labelled peptide standards (Saito et al., 2020, 2014). Briefly, a custom-designed Kanamycin-resistant 'PriorityGENE' plasmid containing the reverse-translated gene sequences for our target peptides was obtained from Genewiz (USA). The plasmid was suspended in TE buffer (10 mM Tris-HCl, 1 mM ethylenediaminetetraacetic acid) and added to competent Tuner(DE3)pLysS *E. coli* cells on ice. The cells were heated to initiate the plasmid transformation and incubated in SOC medium. Subsequently, a subsample was transferred to Kanamycin agar plates and incubated overnight. One colony was added to ^{15}N-enriched SOC medium and incubated. Next, the starter culture was transferred into incubation flasks with ^{15}N-enriched SOC medium and incubated for ~3 h, until the optical density at 600 nm reached 0.6. Protein production was induced by the addition of isopropyl β-D-1-thiogalactopyranoside to the culture and incubated at 25 °C overnight. Inclusion bodies were harvested using BugBuster protein extraction protocols (Novagen). The remaining pellet containing the inclusion bodies, i.e. the insoluble protein fraction, was resuspended in 400 µl 6 M urea, left on the shaker table at 350 rpm at room temperature for 3 h, and then moved to the fridge overnight. The next morning, the proteins were trypsin-digested as outlined above for the bioassay samples and stored frozen at -20 °C until analysis.

5.3.5 Absolute Protein Quantitation

In addition to the peptides of interest, a range tryptic peptide sequences of two commercially available standards (Apomyoglobin, Sigma; Pierce Bovine Serum Albumin, ThermoFisher) were

included in the original plasmid design to determine the absolute concentration of the peptides in the heavy peptide mixture by means of standard additions of the different commercial standards of known concentration (RSD of the final concentration was 10.7 %, using four different peptides). The linear performance range of each heavy peptide standard was then assessed using standard curves of the peptide mixture. Targeted proteomic measurements were made by HPLC-MS/MS on an Orbitrap Fusion Tribrid Mass Spectrometer (ThermoFisher). Two µg of each sample diluted to 10 µl in buffer B (0.1 % formic acid in acetonitrile) was spiked with 10 fmol μL^{-1} of the heavy peptide mixture and injected into the Dionex nanospray HPLC system at a flow rate of 0.17 µl min^{-1}. The chromatography consisted of a nonlinear gradient from 5 to 95 % of buffer B. Buffer A was 0.1 % formic acid in LC-grade H_2O. Precursor (MS1) ions were scanned for the m/z of the heavy peptide standards and their natural light counterparts. The mass spectrometer was run in parallel reaction monitoring mode and only peptides included in the precursor inclusion list were selected for fragmentation. Absolute peptide concentrations were calculated from the ratio of the peak areas of the product ions (MS2) of the heavy peptide of known concentration to the natural light peptide (calculated in Skyline; MacLean et al., 2010). Manual validation of peak shapes was performed for each peptide and sample. Differences between samples with regards to filtration volume, initial protein mass and recovery after precipitation were accounted for. Final peptide concentrations will hereafter be used representatively of corresponding protein concentrations, caveating that our measurements were not able to discern active versus non-active proteins (e.g. by the status of metalation or protein folding) and not accounting for potential polymeric protein structures.

5.3.6 Auxiliary Parameters Analytical Methods

Samples for auxiliary parameters were taken at the start of the bioassay (t_0) by random subsampling in triplicate from the CTD bottles (Station 2) or from the pump system (Stations 3, 4 and 7) during the filling process of the incubation containers. Samples were also taken at end of the incubation period ($t_{48\,h}$) by subsampling from each replicate of each treatment, unless stated otherwise.

Inorganic macronutrients. Micromolar concentrations of DIP and DIN were measured from unfiltered samples using segmented flow techniques with spectrophotometric detection (Brewer and Riley, 1965; Woodward and Rees, 2001) no more than 12 h after sample collection. Additional nanomolar measurements of DIP and DIN were made using standard colorimetric methods with segmented flow analysis coupled to a 2 m liquid waveguide (Patey et al., 2008).

Dissolved organic phosphorus. Concentrations of DOP were calculated from the difference between the TDP and DIP, i.e. DOP = TDP – DIP, with TDP concentrations determined as DIP after persulfate oxidation (Lomas et al., 2010) of unfiltered seawater samples by the molybdenum blue method (Murphy and Riley, 1962) using a Bran and Leubbe QuAAtro 5-channel autoanalyser.

Alkaline phosphatase activity. Rates of APA were determined from unfiltered seawater samples incubated at ambient conditions with final concentrations of 500 nM of MUF-P (Sigma Aldrich; (Ammerman, 1993) on a Turner 10AU field fluorometer, as applied in Davis et al. (2019).

Dissolved trace metals. All samples for dissolved trace metals were filtered in-line through 0.2 µm acetate membrane cartridge filters (Sartobran-300, Sartorius). Concentrations for dFe and dZn were measured in t_0 samples by FIA with chemiluminescence detection and FIA with spectrophotometric detection, respectively, which included a pre-concentration step onto a cation exchange resin in each case (Kunde et al., 2019 for Fe; Wyatt et al., 2014 for Zn). Concentrations for dCo were measured in samples collected from 40 m by CTD deployment, which took place within a few days of bioassay set-up, by HR-ICP-MS, preceded by UV-digestion and off-line pre-concentration onto a chelating resin (WAKO) (Lough et al., 2019; Rapp et al., 2017).

Phytoplankton community. Samples for cell abundances of *Synechococcus* and *Prochlorococcus* were fixed at sea with 20 µl of a 50 % glutaraldehyde solution, stored at -80 °C and analysed by flow cytometry following Tarran et al. (2006). It is important to note that flow cytometry does not distinguish between different strains of *Synechococcus* and *Prochlorococcus*, in contrast to the strain-specific protein data (Table 5.2). Chlorophyll-*a* concentrations were determined in the >0.7 µm fraction at t_0 and in the >0.2 µm fraction at $t_{48\ h}$ (Whatman Nucleopore 25 mm) on a Turner Design Trilogy fluorometer (Welschmeyer, 1994).

5.3.7 Statistics

Changes in protein concentrations and auxiliary parameters in response to metal additions were tested for significance using unpaired two-tailed t-tests (at $\alpha = 0.05$) of the metal amended treatments relative to the unspiked Control after 48 h (Table 5.3). This is a common approach to account for bottle effects, which would not be the case considering responses relative to the initial conditions (e.g. Mahaffey et al., 2014). Due to the unique challenges of ocean proteomics sampling and large-scale trace-metal clean bioassays (Saito et al., 2019), treatment replication was limited to n = 2 at Stations 2, 3 and 4 and to n = 3 at Station 7. Since t-tests assume normal distributions, which for n = 2 is not assessable, significant differences in protein concentrations (not for auxiliary parameters) were cross-checked using a two-fold change criterion, in which all replicates of the metal treatments must lie outside a two-fold change in the average ± propagated standard deviation of the Control to be deemed a 'significant response' (Table 5.4). Although arguably arbitrary, this has been applied in similar proteomic studies (e.g. Cox & Saito, 2013) and was broadly consistent with the t-test results. Only results that passed both tests are indicated as such in the figures.

Table 5.3 Results of the unpaired two-tailed t-tests at a confidence level of α = 0.05, comparing protein concentrations and auxiliary parameters between the unspiked Control and metal amendments after the 48 h incubation period.

T-statistic, *p*-value (degrees of freedom)		Proteins						Auxiliary Parameters						
		PhoX *Syn.*	PhoX *Pro.*	PhoA *Syn.*	PhoA *Pro.*	PstS *Syn.*	PstS *Pro.*	APA	Chl-*a*	*Syn.* cells	*Pro.* cells	DOP	DIP	DIN
Station 2	Control:Zn	0.64, 0.59 (2)	2.37, 0.14 (2)	-28.12, 0.00 (2)	0.25, 0.82 (2)	-1.85, 021 (2)	1.21, 0.35 (2)	0.66, 058 (2)	-1.41, 0.29 (2)	1.72, 0.23 (2)	-0.09, 0.94 (2)	4.51, 0.14 (1)	-0.01, 0.99 (2)	1.65, 0.24 (2)
	Control:Co	-0.98, 0.43 (2)	-1.95, 0.19 (2)	-8.28, 0.01	-0.45, 0.70	-1.54, 0.26	-0.40, 0.73	1.20, 0.35 (2)	-0.45, 0.70 (2)	3.26, 0.08 (2)	0.10, 0.93 (2)	5.63, 0.11 (1)	-0.46, 0.69 (2)	0.81, 0.50 (2)
	Control:Fe	0.80, 0.51 (2)	-0.05, 0.96 (2)	-1.06, 0.40 (2)	0.27, 0.81 (2)	-0.72, 0.55 (2)	0.34, 0.77 (2)	-0.55, 0.64 (2)	-1.00, 0.42 (2)	5.42, 0.03 (2)	-1.92, 0.19 (2)	0.61, 0.65 (1)	-0.13, 0.91 (2)	1.16, 0.37 (2)
Station 3	Control:Zn	1.58, 0.25 (2)	0.58, 062 (2)	0.29, 0.80 (2)	1.67, 0.24 (2)	1.45, 0.28 (2)	1.91, 0.20 (2)	3.08, 0.09 (2)	-3.00, 0.10 (2)	0.06, 0.96 (2)	0.06, 0.96 (2)	0.80, 0.57 (1)	-0.44, 0.70 (2)	-0.22, 0.84 (2)
	Control:Co	-0.77, 0.52 (2)	0.13, 0.91 (2)	0.66, 0.58 (2)	0.23, 0.84 (2)	-0.25, 0.82 (2)	0.09, 0.94 (2)	2.96, 0.10 (2)	-3.00, 0.10 (2)	1.69, 0.23 (2)	0.42, 0.71 (2)	-	-0.17, 0.88 (2)	-0.47, 0.69 (2)
	Control:Fe	3.30, 0.08 (2)	0.25, 0.82 (2)	0.86, 0.48 (2)	1.69, 0.23 (2)	0.90, 0.46 (2)	0.88, 0.47 (2)	1.60, 0.25 (2)	0.33, 0.77 (2)	0.03, 0.98 (2)	-0.27, 0.81 (2)	1.43, 0.39 (1)	-0.28, 0.81 (2)	0.31, 0.78 (2)
Station 4	Control:Zn	-0.10, 0.93 (2)	-0.10, 0.93 (2)	-0.72, 0.54 (2)	-1.64, 0.24 (2)	0.39, 0.73 (2)	-0.53, 0.65 (2)	-0.51, 0.66 (2)	-0.45, 0.70 (2)	-	-	-2.28, 0.15 (2)	2.53, 0.13 (2)	-2.75, 0.11 (2)
	Control:Co	-2.29, 0.15 (2)	-1.30, 0.32 (2)	-0.86, 0.48 (2)	-1.25, 0.34 (2)	-2.53, 0.13 (2)	-1.03, 0.41 (2)	-0.62, 0.60 (2)	-0.45, 0.70 (2)	-	-	-2.59, 0.12 (2)	-6.30, 0.02 (2)	0.03, 0.98 (2)
	Control:Fe	-0.06, 0.95 (2)	-0.02, 0.98 (2)	-0.20, 0.86 (2)	0.32, 0.78 (2)	-0.82, 0.50 (2)	0.40, 0.73 (2)	0.33, 0.78 (2)	-1.41, 0.29 (2)	-	-	-1.74, 0.22 (2)	0.05, 0.96 (2)	1.73, 0.23 (2)
Station 7	Control:Zn	2.11, 0.10 (4)	-1.12, 0.33 (4)	-0.02, 0.98 (4)	0.21, 0.84 (4)	1.38, 0.24 (4)	0.39, 0.72 (4)	-1.97, 0.12 (4)	0.00, 1.00 (4)	0.96, 0.44 (2)	1.95, 0.19 (2)	0.41, 0.71 (4)	0.57, 0.60 (4)	0.40, 0.71 (4)
	Control:Co	1.59, 0.19 (4)	-2.67, 0.06 (4)	2.08, 0.11 (4)	1.44, 0.22 (4)	2.91, 0.04 (4)	2.77, 0.05 (4)	-0.74, 0.50 (4)	1.07, 0.35 (4)	3.55, 0.07 (1)	1.16, 0.36 (1)	0.51, 0.64 (4)	0.84, 0.45 (4)	-0.73, 0.51 (4)
	Control:Fe	3.70, 0.03 (3)	-4.69, 0.02 (3)	0.87, 0.45 (3)	0.44, 0.69 (3)	2.08, 0.13 (3)	0.28, 0.80 (3)	-1.33, 0.28 (3)	-0.43, 0.70 (3)	-1.71, 0.34 (2)	-0.10, 0.94 (2)	-1.80, 0.17 (3)	1.03, 0.38 (3)	1.04, 0.38 (3)

Table 5.4 Significant differences in protein concentrations between the unspiked Control and the metal-amended treatments, based on the t-test results and the two-fold criterion test (see details on this criterion in Section 5.3.7). For auxiliary parameters, the significance is based solely on the t-test results (see also Table 5.3). The check and cross signs represent significant and non-significant changes, respectively.

Significance: Two-fold criterion, t-test result		**Proteins**						**Auxiliary Parameters**						
		PhoX *Syn.*	PhoX *Pro.*	PhoA *Syn.*	PhoA *Pro.*	PstS *Syn.*	PstS *Pro.*	APA	Chl-*a*	*Syn.* cells	*Pro.* cells	DOP	DIP	DIN
Station 2	Control:Zn	×, ×	×, ×	✓, ✓	×, ×	×, ×	×, ×	×	×	×	×	×	×	×
	Control:Co	×, ×	×, ×	✓, ✓	×, ×	×, ×	×, ×	×	×	×	×	×	×	×
	Control:Fe	×, ×	×, ×	×, ×	×, ×	×, ×	×, ×	×	×	✓	×	×	×	×
Station 3	Control:Zn	×, ×	×, ×	×, ×	×, ×	×, ×	×, ×	×	×	×	×	×	×	×
	Control:Co	×, ×	×, ×	×, ×	×, ×	×, ×	×, ×	×	×	×	×	-	×	×
	Control:Fe	×, ×	×, ×	×, ×	×, ×	×, ×	×, ×	×	×	×	×	×	×	×
Station 4	Control:Zn	×, ×	×, ×	×, ×	×, ×	×, ×	×, ×	×	×	-	-	×	×	×
	Control:Co	×, ×	✓, ×	×, ×	×, ×	×, ×	×, ×	×	×	-	-	×	✓	×
	Control:Fe	×, ×	×, ×	×, ×	×, ×	×, ×	×, ×	×	×	-	-	×	×	×
Station 7	Control:Zn	×, ×	×, ×	×, ×	×, ×	×, ×	×, ×	×	×	×	×	×	×	×
	Control:Co	×, ×	×, ×	×, ×	×, ×	×, ×	×, ×	×	×	×	×	×	×	×
	Control:Fe	×, ×	✓, ✓	×, ×	×, ×	×, ×	×, ×	×	×	×	×	×	×	×

5.4 Results and Discussion

5.4.1 Initial Conditions

The subtropical North Atlantic as a whole is a warm, permanently stratified oligotrophic gyre marked by depleted macronutrient inventories and high deposition of Saharan desert dust, which introduces large amounts of Fe and other lithogenic trace metals to the surface ocean. However, stark longitudinal differences in macronutrient concentrations, trace metal concentrations and biological community structure were present during summer 2017, which created contrasting biogeochemical regimes for our bioassays in the most western Station 2 versus the most eastern Station 7. The initial conditions are detailed in Table 5.5.

Table 5.5 Date, location and biogeochemical conditions at the start (t_0) of the bioassays across the subtropical North Atlantic during cruise JC150. Biogeochemical parameters are presented as the average and standard deviation of replicate t_0 samples, with the exception of singlet samples of DOP at Station 4 and dCo in general. Mixed layer depths were averaged over multiple days, as these were not always determined on the same day as the bioassay set-up.

	Parameter	Station 2	Station 3	Station 4	Station 7
General	Date	11th July 2017	15th July 2017	19th July 2017	5th August 2017
	Location	22.00 °N 58.00 °W	22.00 °N 50.00 °W	23.37 °N 44.95 °W	22.00 °N 31.00 °W
	SST (°C)	27	27	26	25
	MLD (m)	24 ± 3 (5th to 8th July)	33 ± 1 (12th to 15th July)	42 ± 9 (17th to 20th July)	51 ± 8 (4th to 8th August)
Macronutrients	DIP (nM)	3.7 ± 2.1	3.7 ± 1.0	3.4 ± 0.8	14 ± 0.70
	DOP (nM)	87 ± 7.5	137 ± 39	112	129 ± 29
	APA (nM h^{-1})	2.8 ± 0.21	2.86	2.48 ± 0.10	1.15 ± 0.08
	DIN (nM)	1.5 ± 1.9	1.66 ± 0.56	3.36 ± 1.0	6.2 ± 0.0
Trace Metals	dFe (nM)	1.26 ± 0.06	0.53 ± 0.06	0.83 ± 0.00	0.23 ± 0.05
	dZn (nM)	0.25 ± 0.14	0.46 ± 0.09	0.14 ± 0.01	0.04 ± 0.01
	dCo (pM)	11.0	11.1	13.0	13.9
Phytoplankton Community	*Synechococcus* (cells ml^{-1})	3.4 ± 0.55 x 10^3	-	-	1.6 ± 0.26 x 10^3
	Prochlorococcus (cells ml^{-1})	29 ± 0.37 x 10^4	-	-	181 ± 0.37 x 10^4
	Chl-*a* (µg L^{-1})	0.064 ± 0.01	0.055 ± 0.01	0.110 ± 0.06	0.149 ± 0.005

Generally, Station 2, located in the ultraoligotrophic Sargasso Sea, was severely depleted in DIP (3.7 ± 2.1 nM), DOP (87 ± 7.5 nM) and DIN (1.5 ± 1.9 nM), but enriched in dZn (0.25 ± 0.14 nM) and especially in dFe (1.26 ± 0.06 nM) compared to Station 7. Concentrations of dCo were very low throughout the basin with 11.0 nM at Station 2 and 13.9 nM at Station 7. Alkaline phosphatase activity was more than two-fold higher at Station 2 (2.8 ± 0.21 nM h^{-1}) than at Station 7 (1.15 ± 0.08 nM h^{-1}). Although still characteristically oligotrophic, Station 7 was enriched compared to Station 2 in DIP (14 ± 0.70 nM), DOP (129 ± 29 nM) and DIN (6.2 ± 0.0 nM), but concentrations of dFe (0.23 ± 0.05 nM) and dZn (0.04 ± 0.01 nM) were lower. The cell abundance of *Prochlorococcus* dominated over that of *Synechococcus* on an absolute scale at both locations, but was at least six-fold higher at Station 7 (181 ± 0.37 x 10^4 cells ml^{-1}) than at Station 2 (29 ± 0.37 x 10^4 cells ml^{-1}). Contrastingly, *Synechococcus* was at least two-fold more abundant at Station 2 (3.4 ± 0.55 x 10^3 cells ml^{-1}) than at Station 7 (1.6 ± 0.26 x 10^3 cells ml^{-1}). On the whole, Stations 3 and 4 exhibited intermediates to the contrasting conditions at Stations 2 and 7 along the biogeochemical gradients. While phytoplankton growth in the subtropical North Atlantic was constrained by N as the primary limiting nutrient (see Chapter 5; Moore et al., 2013), the very high APA rates and very low DIP and DOP concentrations (compare Mahaffey et al., 2014) as well as the detection of P-stress biomarkers (Held et al., 2020; Mahaffey et al. in preparation) confirm a high level of physiological P stress for key phytoplankton species at the start of our bioassays.

5.4.2 Bioassay Responses

The concentrations of the selected alkaline phosphatases of *Synechococcus* and *Prochlorococcus* were expected to increase following the addition of Zn or Co (PhoA), or Fe (PhoX) to the bioassays, provided that the initial metal availability was constraining higher alkaline phosphatase concentrations. Opposing responses in the species-specific protein concentrations were detected at the most western Station 2 versus the most eastern Station 7 (Figure 5.2), whereas no significant responses were observed at the intermediate Stations 3 and 4 (Figure 5.3). At Station 2, the *Synechococcus* PhoA concentration increased six- and seven-fold relative to the Control (4.44 ± 0.97 fM) upon addition of Zn (25.1 ± 0.37 fM) and Co (31.2 ± 4.49 fM), respectively, whereas at Station 7 the *Prochlorococcus* PhoX increased two-fold upon Fe addition (12.4 ± 1.73 fM) relative to the Control (5.44 ± 1.59 fM). Therefore, *Synechococcus* PhoA increased upon Zn and Co additions in the Fe-enriched and acutely DIP-/DOP-depleted *Synechococcus* hot spot in the western Sargasso Sea, whereas *Prochlorococcus* PhoX increased upon Fe addition in the Fe-depleted, comparably DIP- and DOP-enriched *Prochlorococcus* hot spot in the eastern subtropical North Atlantic.

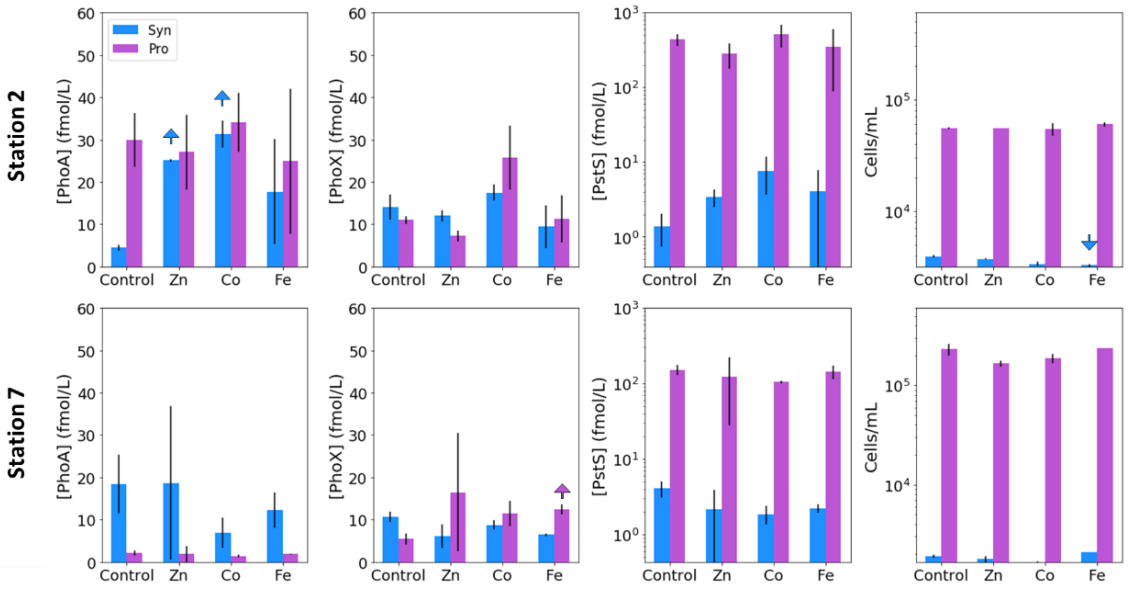

Figure 5.2 Bar graph matrix of the concentrations of PhoA, PhoX and PstS and the cell abundances (from left to right) in the bioassays after 48 h at Stations 2, and 7 (top to bottom) for *Synechococcus* (purple) and *Prochlorococcus* (blue). Bars show the mean ± one standard deviation of replicates and coloured arrows indicate significance (based on t-test and 2-fold criterion; see methods) and direction of change relative to the Control.

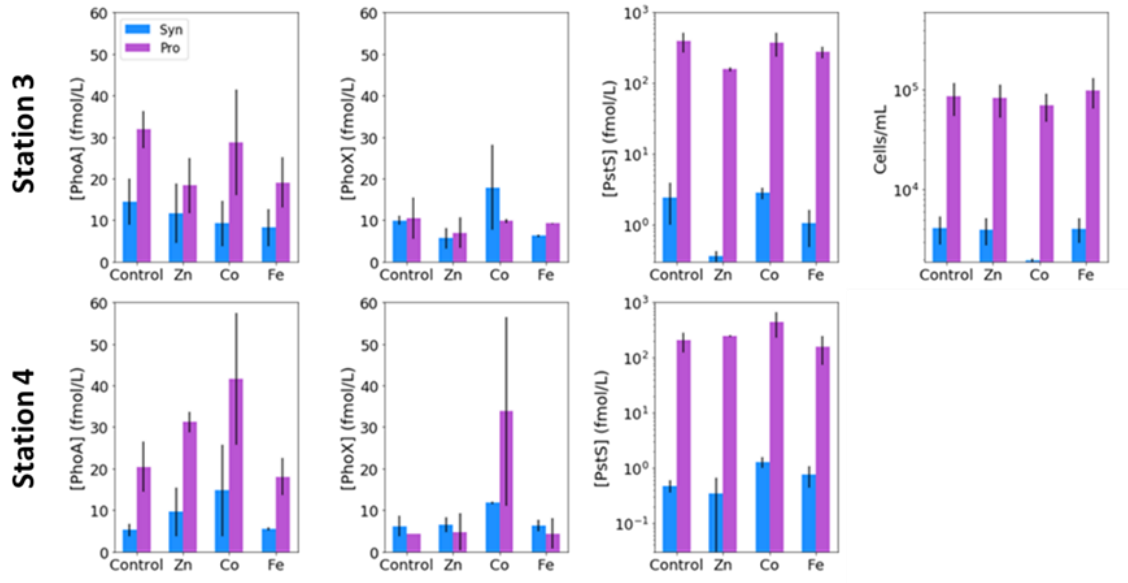

Figure 5.3 Bar graph matrix of the concentrations of PhoA, PhoX and PstS and the cell abundances (from left to right) in the bioassays after 48 h at Stations 3, and 4 (top to bottom) for *Synechococcus* (purple) and *Prochlorococcus* (blue). Bars show the mean ± one standard deviation between replicates. No significant changes.

Generally, any change in concentrations of protein per L seawater can be interpreted in two ways: Either the metals stimulate the alkaline phosphatase expression via a metal-regulatory pathway, or the metals prevent the degradation of existing alkaline phosphatases by filling co-factor sites. The latter would translate in the activation of these enzymes, but this is not discernible from our proteomics data type. In the absence of strain-specific cell counts, strain-specific protein total protein content or a housekeeping protein, we are unable to discern whether the increases in alkaline phosphatase concentrations upon metal addition are due to more alkaline phosphatases per cell or due to more overall strain-specific activity, e.g. if the metal addition stimulated other metal-dependent metabolic pathways in the cell that also triggered an increase in alkaline phosphatase expression through a transcriptional cascade. The best possible answer to this with the available data derives from a regression between total (i.e. not strain-specific) *Prochlorococcus* or *Synechococcus* cell counts and PhoA or PhoX concentrations in the metal treatments relative to the Control treatment (Figure 5.4). If changes in the protein concentrations were predominantly driven by changes in cell abundance, the points would lie close to the 1:1 line, but all three of the significant changes in the alkaline phosphatase abundance that were observed in the bioassays (indicated by arrows) exhibited much larger changes in the protein concentration than in the cell abundance (i.e. to the left of the 1:1 line). Of course, this approach neglects any strain-specific niche formation under the different metal environments in the individual treatments.

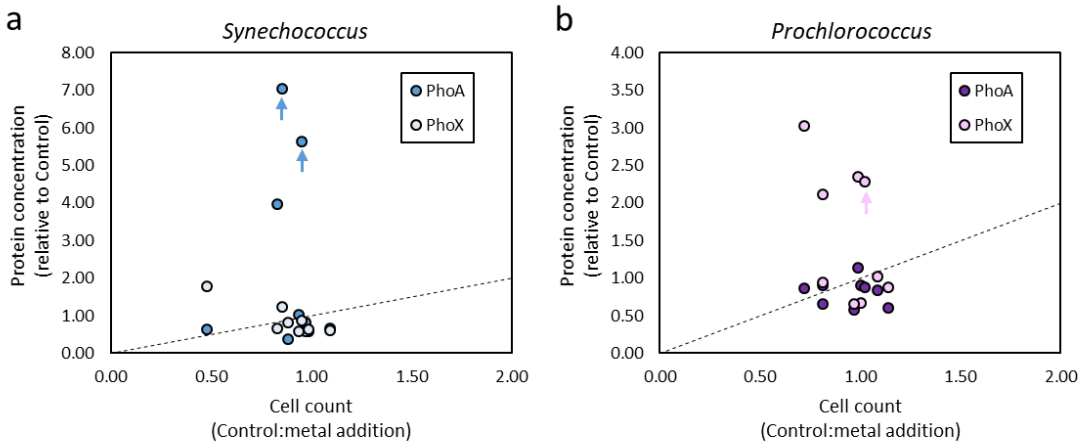

Figure 5.4 Scatter plot of the change in cell counts versus the change in alkaline phosphatase concentration (PhoA or PhoX) in the metal amended treatments relative to the Control for (a) *Synechococcus* and (b) *Prochlorococcus*. Data from all treatments of all stations is included, except Station 4 for which no flow cytometry data exist. The dashed line is the 1:1 ratio. The three significant responses observed during the bioassays are indicated by arrows, as in Figure 5.2.

Nevertheless, the observed increases in alkaline phosphatase concentrations upon metal addition at Stations 2 and 7 add some indirect evidence towards the co-factor roles of Zn, Co or Fe in marine alkaline phosphatases, and towards the hypothesised limitation under the ambient availability of these metals. The increase of alkaline phosphatase concentrations in response to a Co addition in a field study is new. The similar increases of *Synechococcus* PhoA concentrations in response to either

Zn or Co at Station 2 suggests a common mechanism, possibly the biochemical substitution in this protein. Although we are unable to resolve this, metabolic substitution capabilities between Zn and Co have previously been identified in phytoplankton cultures, which showed similar or reduced growth rates for a range of marine diatoms and coccolithophores, when Zn was replaced with Co in carbonic anhydrases (Kellogg et al., 2020; Price and Morel, 1990; Sunda and Huntsman, 1995; Timmermans et al., 2001; Xu et al., 2007; Yee and Morel, 1996). Only in the coccolithophore *Emiliana huxleyi* was the growth rate higher under replete Co than under replete Zn, whereas the cyanobacterium *Synechococcus bacillaris* had an absolute Co requirement (Sunda and Huntsman, 1995). The latter is in line with co-evolutionary arguments of ocean chemistry and cyanobacteria under the Co- and Fe-replete, but Zn-deplete conditions of the ancient ocean ~2.5 Gyr ago (Dupont et al., 2006; Saito et al., 2003). Furthermore, based on the distributions of trace metals and DIP in the Sargasso Sea, the substitution of Zn with Co in PhoA has been hypothesised previously (Jakuba et al., 2008; Saito et al., 2017). Together with these aspects, our insights from the bioassay response at Station 2 merits further investigations into whether *Synechococcus* is able to interreplace Zn and Co in PhoA. This would be an important insight for considerations of stoichiometric plasticity and niche partitioning across the vast Zn- and Co-depleted regions of the ocean.

Importantly, no significant responses upon Zn or Fe addition were observed, where they were not expected, i.e. the addition of Zn did not increase the concentration of any Fe-dependent PhoX and the addition of Fe did not increase the concentration of any Zn/Co-dependent PhoA. Nevertheless, there are some non-significant trends following the addition of Co that warrant further study. For example, Co additions increased the *Prochlorococcus* PhoX concentration dramatically at Station 4 and hence, Co could be an efficient metal co-factor in PhoX (as in the bacterium *Pasteurella multocida*; Wu et al., 2007). This would be in contrast to the results of Kathuria and Martiny (2011), who derived a APA-quenching role of Co (and Zn; while Fe untested) in *Synechococcus* and *Prochlorococcus* PhoX activity.

Traditional measurements of APA rates via the MUF-P assay did not reveal any significant changes upon metal additions in our incubations (Figure 5.5 and 5.6). The initial rates at both Stations 2 and 7 were comparable to or higher than previous *in-situ* bioassays, where increases of APA were triggered upon the addition of Zn (up to ~0.4 nM h^{-1} at t_0 in Mahaffey et al., 2014) or Fe (~2 nM h^{-1} at t_0 in Browning et al., 2017) (see locations in Figure 5.1). In the current study, the DIP concentrations at t_0 were lower compared to those studies (3 to 43 nM in Mahaffey et al., 2014; ~25 nM in Browning et al., 2017), while dZn concentrations were comparable to Mahaffey et al.'s (2014) dZn concentrations of 0.16 to 0.30 nM), and dFe concentrations were lower than at the one location, where Browning et al. (2017) observed an upregulation in APA upon Fe addition (0.7 nM). From a

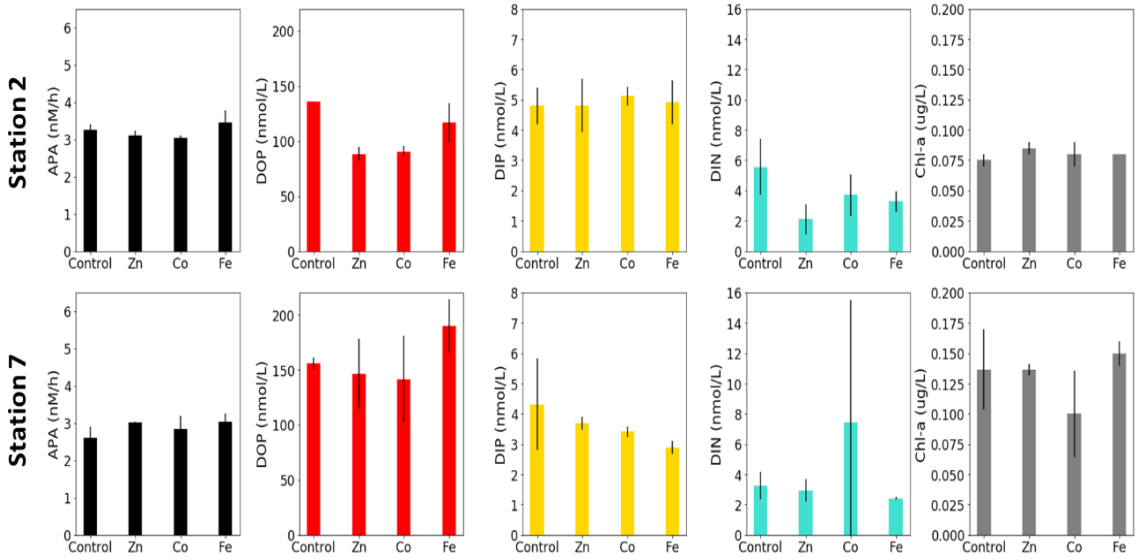

Figure 5.5 Bar graph matrix of APA rates and concentrations of DOP, DIP, DIN and Chl-*a* (from left to right) in the bioassays after 48 h at Stations 2 and 7 (top to bottom). Bars show the mean ± one standard deviation of replicates. No significant changes were observed in these parameters.

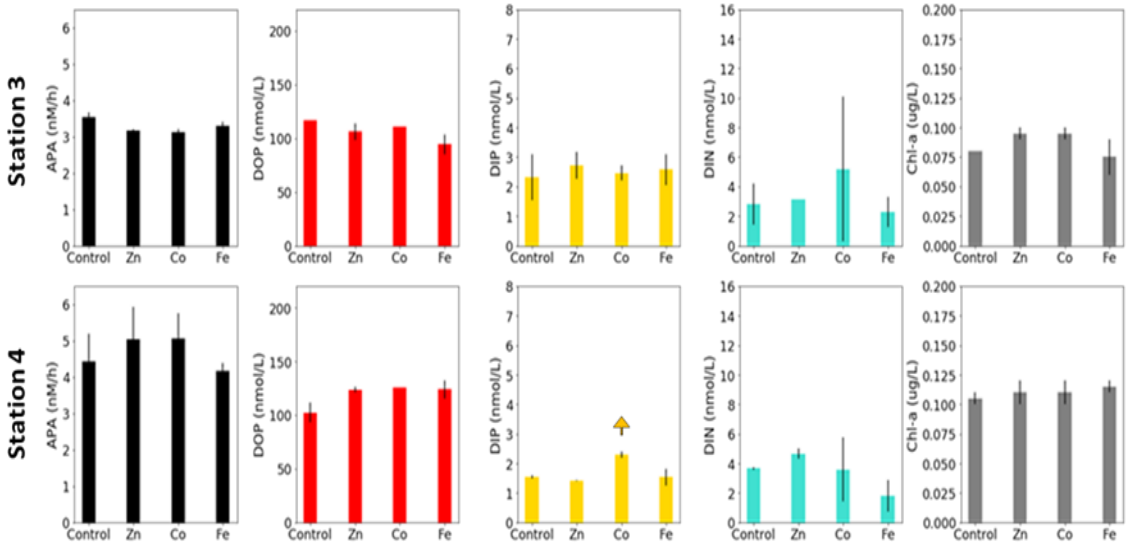

Figure 5.6 Bar graph matrix of APA rates and concentrations of DOP, DIP, DIN and Chl-*a* (from left to right) in the bioassays after 48 h at Stations 3, and 4 (top to bottom). Bars show the mean ± one standard deviation between replicates and coloured arrows indicate significance (based on t-test) and direction of change relative to the control.

solely concentration-based perspective, a response of APA to metal additions was therefore expected in our bioassays, but its absence suggests that APA was already operating near the upper threshold that was possible in the enclosed incubation system, and that factors other than metals were limiting, such as the availability of DOP substrate for the alkaline phosphatases (Mahaffey et al. in prep).

At the intermediate Stations 3 and 4, significant responses to metal additions were absent both in the abundances of the alkaline phosphatase proteins and in the APA rates (Figure 5.6). The localised nature of changes in the alkaline phosphatase concentrations and complete absence in changes in APA in our bioassays is similar to Browning et al. (2017), where only one in eight experiments showed a direct metal-driven response in APA. Furthermore, a compilation of bioassay results from our study with previous studies exposed the widespread null responses and the diversity of the few metal responses across the North Atlantic basin (Figure 5.1). For example, Mahaffey et al. (2014) observed Zn limitation of APA in the eastern basin, whereas our bioassay results showed an increased *Synechococcus* PhoA concentration (but no change in APA) upon Zn addition in the western basin, potentially as the result of regional and seasonal drivers. Resolving the seeming 'patchiness' of these trends will rely on better coverage of similar bioassays in the future. One explanation for the presence of the many null responses may be that organisms 'escape' any observable metal limitation response by effectively re-allocating metals towards the use at the active sites in alkaline phosphatases to cope with DIP stress. A comparable re-allocation mechanism of cellular Fe between metalloproteins involved in biological N_2 fixation and photosynthesis has previously been demonstrated in the diel cycle of *Crocosphaera watsonii* (Saito et al., 2011).

Taken together, our bioassay results suggest that the concentration of alkaline phosphatase enzymes were locally affected by the availability of Zn, Co or Fe, and clearly differed between the enzyme type (PhoA/PhoX) and species (*Prochlorococcus*/*Synechococcus*), depending on the biogeochemical setting of the given locale, including the community structure as well as ambient DIP, DOP and metal concentrations. Whether the metal-driven responses did indeed result from more alkaline phosphatase per cell (alternatively to more alkaline phosphatase due to more cell activity) is possible, but ambiguous from the available data set. To this end, it also remains unclear whether increased alkaline phosphatase abundance triggered more DOP acquisition and enhanced growth of the relevant strains.

5.4.3 Enzyme Type Specificity in *Synechococcus* and *Prochlorococcus*

If the availability of Zn/Co or Fe constrains the concentrations of PhoA or PhoX, respectively, and if the same strain is capable of expressing both enzymes, the question is whether the sustained concentration of either enzyme is fine-tuned towards the different metal environments in the

individual treatment. In other words, how do the concentrations of PhoA and PhoX compare to each other?

Regardless of the metal added in the bioassays, we observed a general prevalence of PhoA over PhoX for *Synechococcus*, when comparing Stations 2 and 7 across all treatments (Figure 5.7a). PhoA concentrations were higher (total range of 4 to 44 fmol L^{-1}) than PhoX concentrations (total range of 2 to 12 fmol L^{-1}). For *Prochlorococcus*, the relative dominance of PhoA versus PhoX concentrations switched between Stations 2 and 7 (Figure 5.7b), with PhoA (8 to 42 fmol L^{-1}) present at higher concentrations than PhoX (6 to 33 fmol L^{-1}) at Station 2, and PhoX (2 to 35 fmol L^{-1}) present at higher concentrations than PhoA (0.5 to 4 fmol L^{-1}) at Station 7, thereby providing a less clear picture than for *Synechococcus*. It should be noted that while the pattern for *Synechococcus* is roughly conserved across Stations 3 and 4, for *Prochlorococcus* PhoA is more abundant than PhoX at these intermediate stations (Figure 5.8). This is in line with the findings by Cox and Saito (2013) and Saito et al. (2017), who observed higher abundances of PhoA over PhoX in *Synechococcus* cultures. It could result from the preferential expression of PhoA over PhoX under the given conditions (perhaps due to differences in enzymatic efficiencies) or from differences in the subcellular localisation of PhoA versus PhoX that cause methodological bias. PhoX is predicted to be predominantly extracellular (Luo et al., 2009). Hence, its role may be underestimated by our proteomics analyses.

Despite over one order of magnitude difference in cell abundance between *Prochlorococcus* and *Synechococcus*, the concentrations of alkaline phosphatase enzymes plotted on a comparable scale for the two organisms. The *Synechococcus* PhoA even exceeded the *Prochlorococcus* PhoA at Station 7 (Figure 5.2). Among the measured proteins, this scale similarity was exclusive to the alkaline phosphatases as the respective concentrations of PstS differed by at least one order of magnitude, which aligned broadly with the 100- to 1000-fold difference in cell abundance between *Synechococcus* and *Prochlorococcus* in the bioassays (Figure 5.2). While a potential explanation for this derives from Martiny et al.'s (2009, 2006) insights that some strains of *Prochlorococcus* have multiple copies of the PstS gene, it may also be a methodological artefact that stems from the specific peptide representative of the *Synechococcus* PstS in our study (Table 5.2). This peptide is specific to the clade X strain RCC307, which is less abundant in the subtropical North Atlantic than the clade III strain WH8102 (for selected PhoA and PhoX peptides) (Sohm et al., 2016), while strain-specificity overlapped for selected PhoA, PhoX and PstS peptides in the case of *Prochlorococcus* (Table 5.2). Mahaffey et al. (in prep) showed co-variation of *Prochlorococcus* PstS and PhoA during JC150, likely driven by gradients in DOP and DIP availability, which indicates that both enzymes may be still important for P acquisition by this phytoplankton species. Nevertheless, the limitation pattern of *Prochlorococcus* at Station 7 that we observed raises the question regarding the relative importance of alkaline phosphatases for P uptake compared to *Synechococcus*: although PhoX concentrations increased upon Fe addition, the change was much less substantial than the increase in

Synechococcus PhoA concentrations upon Zn and Co at Station 2, and *Prochlorococcus* was able to maintain a very high cell abundance at Station 7 regardless (Figure 5.2). Of course, this could be driven by the higher ambient DIP concentrations at Station 7 too.

The comparison between protein concentrations in Figure 5.7 and 5.8 highlighted that the preferences for PhoA and PhoX and/or their regulation appeared to differ between *Synechococcus* and *Prochlorococcus* in our *in-situ* bioassays. The exact drivers behind this observation merit further investigation before alkaline phosphatase enzymes can be applied as reliable P stress markers in the field (see also Mahaffey et al., in prep).

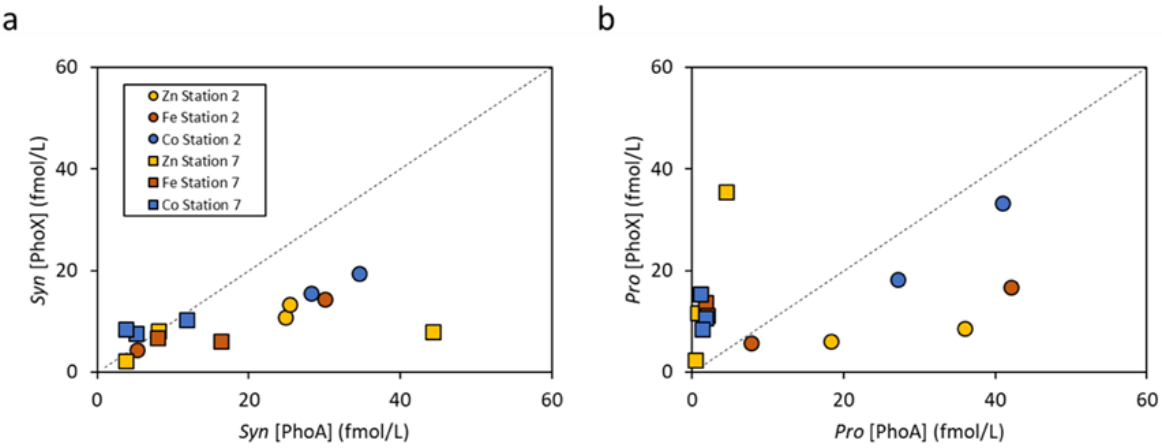

Figure 5.7 Scatter plots with concentrations of (a) *Synechococcus* PhoA versus PhoX, and (b) *Prochlorococcus* PhoA versus PhoX in the Zn (yellow), Co (blue) or Fe (orange) amended bioassays at Stations 2 (circles) and Station 7 (squares). The dashed black line indicates the 1:1 ratio.

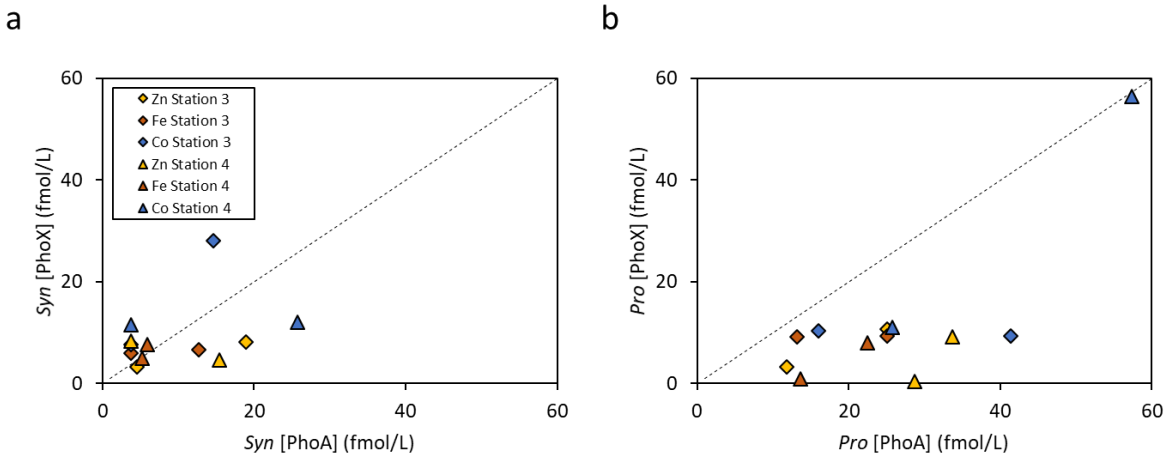

Figure 5.8 Scatter plots with concentrations of (a) *Synechococcus* PhoA versus PhoX, and (b) *Prochlorococcus* PhoA versus PhoX in the Zn (yellow), Co (blue) or Fe (orange) amended bioassays at Stations 3 (diamonds) and Station 4 (triangles). The dashed black line indicates the 1:1 ratio.

5.4.4 Towards a Quantitative Metalloproteome

Absolute quantitative metalloproteomics is an emerging data type in marine biogeochemistry (Saito et al., 2019). The key advantage over relative proteomics data is the ability to relate the absolute protein concentrations to other data types, including biological rate measurements and cellular metal stoichiometry. To this end, the concentrations of the Zn/Co or Fe-dependent alkaline phosphatases measured in this study lead to two questions: Firstly, how much metal is allocated as alkaline phosphatase co-factors in the cell, and how does this compare to total cellular metal content? Secondly, what are the enzyme abundance-based APA rates, and how do they scale to assay-based APA rates?

In attempting to set a waypoint in addressing these questions, model calculations were performed using the *Synechococcus* PhoA concentrations in Station 2's Control treatments after 48 h. This choice was due to the strongest response of this enzyme in the bioassays (Figure 5.2), and due to the suitability of complementary data for PhoA rather than PhoX (for kinetics parameters), for *Synechococcus* rather than *Prochlorococcus* (for cellular metal content), for Station 2 rather than Station 7 (for substrate availability and strain-specific abundance), and for the Control treatment rather than any metal amendment (for cellular metal contents). For the ease of reading, explanations on the values used and assumptions made in the calculation are moved to Table 5.6 and 5.7 for the first and second question, respectively.

Equation 1a approximates the cellular Zn allocation towards the *Synechococcus* PhoA as a function of the number of properly metalated co-factors in this enzyme, and the cell abundance-normalised PhoA concentration in seawater. The latter is a function of *Synechococcus* cell counts and the fractional abundance of strain WH8102, to which the measured PhoA is specific. Equation 1b expresses the results of Equation 1 as a fraction of the total cellular Zn content.

Eq. 1a Allocated Zn_{PhoA} = metalated co-factors$_{PhoA}$ * $PhoA_{SW}$ / (*Syn.* abundance * WH8102 fraction)

Eq. 1b Fractional allocated $Zn_{PhoA} = Zn_{PhoA} / Zn_{total\ cell.}$

As Figure 5.9a displays, the amount of metal allocated to PhoA in *Synechococcus* ranges up to 2,036 ± 442 atoms cell^{-1}. This translates to a maximum fractional contribution towards the total cellular Zn content of 0.44 ± 0.15 % (Figure 5.9b). Under co-factor occupation by Co instead of Zn, the fractional contribution is up to 25 ± 5.5 % (Figure 5.9c), due to the lower total cellular Co content of *Synechococcus* compared to Zn (Table 5.6). In reality, it is possible that the active sites of PhoA are occupied by a mixture of Zn and Co, incompletely metalated, or under competition by other metals.

Table 5.6 Details on the measured and assumed variables for the model calculations, specifically for the metal allocation to PhoA in a *Synechococcus* cell in Station 2's Control treatments, as shown in Figure 5.9.

Variable	Unit	Value	Source	Further details
Number of Zn co-factors		0 to 4	Assumed; after Coleman, 1992	Based on the *E. coli* homologue, full metalation comprises four Zn^{2+} per dimer. Our measurements do not resolve the level of metalation.
***Synechococcus* PhoA peptide concentration in seawater**	fmol L^{-1}	4.45 ± 0.92 (RSD = 0.21)	Measured; this study	Using the mean (± 1sd) concentration of peptide HYIAVALER (by HPLC-MS/MS) in the two Control replicates at Station 2 after 48 h.
***Synechococcus* PhoA protein concentration in seawater**	fmol L^{-1}	2.23 ± 0.46 (RSD = 0.21)	Measured; this study	Using the concentration from the row above, but accounting for the dimeric structure that is assumed based on the *E. coli* PhoA homologue (Coleman, 1992).
***Synechococcus* abundance**	cells ml^{-1}	3,931 ± 131 (RSD = 0.033)	Measured; this study	Using the mean (± 1sd) concentration of cell abundance (by flow cytometry) in the two Control replicates at Station 2 after 48 h.
Fraction of *Synechococcus* strain WH8102 (clade III)	%	67 ± 2.8 (RSD = 0.042)	Assumed; after Ohnemus et al., 2016	Calculated from the mean (± 1sd) fraction of clade III (representative of WH8102) to total *Synechococcus* abundance in two samples at 10m at BATS in July 2012. Other literature data outside the relevant depth range, season and/or vicinity to our Station 2, but within the (sub)tropical North Atlantic vary between 0 and 83 % (e.g. Ahlgren and Rocap, 2012; Mazard et al., 2012; Sohm et al., 2016).
Cellular Zn content in *Synechococcus*	atoms $cell^{-1}$	463 ± 104 · 10^3 (RSD = 0.26)	Measured; this study	Using the mean (± 1sd) Zn concentration of five *Synechococcus* cells (by Synchotron X-ray fluorescence) (L. Mann & B. Twining; unpubl. data) sampled prior to the bioassays (i.e. no metal addition) at Station 2. This Zn content is at the higher end of previously analysed *Synechococcus* cells from a P-stressed anticyclonic eddy near BATS (66,000 to 684,000 atoms $cell^{-1}$ between surface and DCM) (Twining et al., 2010), and higher than values reported elsewhere (Barnett et al., 2014; Twining et al., 2015).
Cellular Co content in *Synechococcus*	atoms $cell^{-1}$	low: 8.10 · 10^3 high: 198 · 10^3	Measured; this study	Measured in the same way and in the same samples as for Zn in the row above. However, the cellular Co content was undetectable in three out of the five cells and ranged over orders of magnitude (see column to the left) for the remaining two. Hence, these likely present an upper threshold. They are also lower than previously measured 'autotrophic picoplankton cells' from the subtropical North Atlantic with a cellular Co content of 1,380 atoms $cell^{-1}$ (Twining et al., 2015; converted using their Co:P ratio of 0.15 mmol mol^{-1} and 15.2 amol P $cell^{-1}$ from Bertilsson et al., 2003) and lower than the minimal growth requirements of *Synechococcus bacillaris* of 792 Co atoms $cell^{-1}$ (Sunda and Huntsman, 1995; converted using their Co:carbon ratio of 0.12 µmol mol^{-1} and 11 fmol carbon $cell^{-1}$ from Bertilsson et al., 2003). Considering these scales, only the lower Co content was used in the model calculations in the main text.

Table 5.7 Details on the measured and assumed variables for the model calculations, specifically for the the protein-abundance based hydrolysis rates of the *Synechococcus* PhoA in Station 2's Control treatments, as shown in Figure 5.10.

Variable	Unit	Value/range	Source	Details
Molecular weight	g mol^{-1} (Da)	$126.12 \cdot 10^3$	Calculated	Calculated using the full amino acid sequence of the protein.
***Synechococcus* PhoA protein concentration in seawater**	ng L^{-1}	0.281 ± 0.0580 (RSD = 0.21)	Measured; this study	Converted from the mean (± 1sd) protein concentration in fmol L^{-1} (see third row in Table 5.6) and the molecular protein weight in the row above.
DOP concentration	nmol L^{-1}	135	Measured; this study	Using the mean (± 1sd) concentration of DOP (as DOP = TDP – DIP) in the Control treatment at Station 2 after 48 h (only one replicate available).
Phosphoester fraction	%	80	Assumed; after Young and Ingall, 2010	Using the mean fraction of phosphoesters to the DOP pool measured in some near-by Gulf Stream samples (Young and Ingall, 2001), which is also close to Kolowith et al.'s (2001) estimate of 75 % for a variety of samples from the oligotrophic ocean.
Available substrate concentration	nmol L^{-1}	108	Calculated	Calculated from the DOP concentration and phosphoester fraction in the two rows above. It is important to note that this is the standing stock of the substrate in the seawater during the bioassays, not necessarily the substrate availability *near* or *in* the cell, where the enzyme is thought to be active. At this point, a more accurate approximation of the substrate availability is not available, but we do acknowledge that the current one is a likely underestimation.
APA	nmol L^{-1} h^{-1}	3.25 ± 0.23 (RSD = 0.071)	Measured; this study	Using the mean (± 1sd) rate of APA (by MUF-P assay) in the two Control replicates at Station 2 after 48 h.
Periplasmic outwards fraction	%	20 to 80	Assumed; various studies	Martinez and Azam (1993) showed that MUF-P does not cross the inner membrane, meaning that the MUF-P assay can only detect extracellular and periplasmic hydrolysis rates (i.e. periplasmic-outwards). Therefore, the total APA rate in our samples is estimated from the measured APA in the row above, while accounting for the fraction of marine alkaline phosphatases that is not captured by the MUF-P assay. Marine bacterial alkaline phosphatases were predicted to be between ~80 and 50 % periplasmic-outwards (Luo et al., 2009), while field-based estimates of extracellular-only APA (i.e. by filtration with <0.2 µm) ranged between 21 to 80 % in the North Atlantic (Baltar et al., 2010; Davis & Mahaffey, 2017; Labry et al., 2005; Vidal et al., 2003). For the calculation and the associated figure in the main text, a higher periplasmic-outwards fraction translates to a lower 'correction' on the measured APA, and hence a higher contribution of *Synechococcus* PhoA to total APA.
V_{max} for Zn-dependent PhoA	µmol min^{-1} mg^{-1}	7 to 28	Assumed; Lazdunski and Lazdunski, 1969	Using enzyme kinetics of purified *E. coli* PhoA under optimal metal co-factor occupation (i.e. two Zn^{2+} and 2 Ca^{2+}). The large range of V_{max} values results from testing a variety of different phosphoester substrates and is within values reported by others (Coleman, 1992; Gottesman et al., 1969; Krishnaswamy and Kenkare, 1970; Martinez et al., 1996).
K_m for Zn-dependent PhoA	µmol L^{-1}	1 to 14.7	Assumed; Lazdunski and Lazdunski, 1969	Same as row above, but for K_m.
V_{max} for Co-dependent PhoA	µmol min^{-1} mg^{-1}	1.1 to 2.86	Assumed; Lazdunski and Lazdunski, 1969	Using enzyme kinetics of purified *E. coli* PhoA, where Zn^{2+} co-factors were substituted by Co^{2+}, which resulted in reduced enzyme efficiency. The large range of V_{max} values results from testing a variety of different phosphoester substrates.
K_m for Co-dependent PhoA	µmol L^{-1}	0.73 to 3.32	Assumed; Lazdunski and Lazdunski, 1969	Same as row above, but for K_m.

Nevertheless, these low fractional contributions of PhoA-allocated Zn appear biochemically reasonable as alkaline phosphatases are likely less abundant than the major Zn-containing proteins like carbonic anhydrase or Zn-fingers (Vallee and Auld, 1990). In fact, the vast majority of Zn in *Synechococcus* is stored in metallothioneins that act to maintain Zn homeostasis (Saito et al.; unpubl. data). However, these results could also indicate that Zn is not the preferred co-factor in *Synechococcus* PhoA. The similar response to Co and Zn additions at Station 2 could hint at the effective substitution in this enzyme. This would not only align with evolutionary arguments (see Section 5.4.3), but also imply that PhoA is a potential major sink of cellular Co and that *Synechococcus* growth could be sensitive towards Co-P co-stress in the oligotrophic ocean.

Equation 2a approximates the *Synechococcus* PhoA-abundance based hydrolysis rate as a function of the PhoA concentration by weight, phosphoester substrate concentration, and the Michaelis-Menten kinetics parameters V_{max} and K_m, which are the maximum reaction rate and half-saturation constant, respectively (derived from *E. coli* homologue; Table 5.7). Equation 2b expresses the results of Equation 2a as a fraction of the total APA, a function of the measured MUF-P assay-based APA with a correction applied for the subcellular localisation of marine alkaline phosphatases, of which only the periplasmic-outwards fraction (~20 to 80 %) is captured by the MUF-P assay.

Eq. 2a $Rate_{PhoA} = PhoA_{SW} * molecular\ weight * V_{max} * substrate / (substrate + K_m)$

where substrate = DOP * phosphoester fraction

Eq. 2b $Fractional\ Rate_{PhoA} = Rate_{PhoA} * periplasmic\text{-}outwards\ fraction / assayed\ APA$

As Figures 5.10a and b display, the protein abundance-based rates range from 0.0017 ± 0.00036 nM h^{-1} to 0.071 ± 0.015 nM h^{-1} for the Zn-dependent *Synechococcus* PhoA and from 0.0014 ± 0.00030 nM h^{-1} to 0.0062 ± 0.0013 nM h^{-1} for the less efficient Co-PhoA. In terms of fractional contributions to total APA (Figure 5.10c and d), the rate estimates translate to maximally 1.7 % for the Zn-PhoA and 0.15 % for the Co-PhoA. Regardless of the choice of enzyme kinetics, it appeared that *Synechocccus* PhoA contributed negligibly to total APA in our bioassays. This concurs with the observed increase in protein concentration upon metal additions at Station 2 that was not accompanied by an increase in APA (see Section 5.4.2). However, this conclusion is biased towards using *E. coli* kinetics, which may underestimate the efficiency of *Synechococcus* alkaline phosphatases. Clearly, the large range in rate estimates and the generally low fractional rate contributions highlight the need to constrain the kinetics, substrate specificity and subcellular localisation of relevant alkaline phosphatases in the marine environment, in order to interpret the assay-based APA accurately.

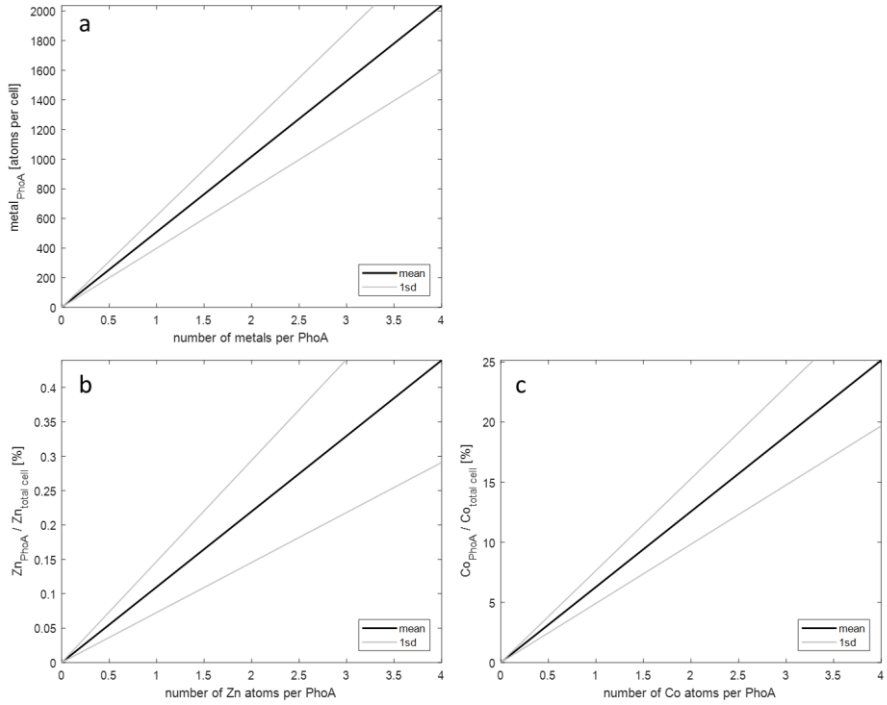

Figure 5.9 Number of metal atoms allocated to PhoA per *Synechococcus* cell, as a function of the number of the co-factors occupied by Zn^{2+} or Co^{2+} per PhoA enzyme. (b) The fraction of Zn allocated to PhoA over the total cellular Zn content per *Synechococcus* cell. (c) Same as (b), but for Co. Note the scale difference between (b) and (c). Standard deviations of the mean are the propagated errors from the variability of individual variables (see Table 5.6)

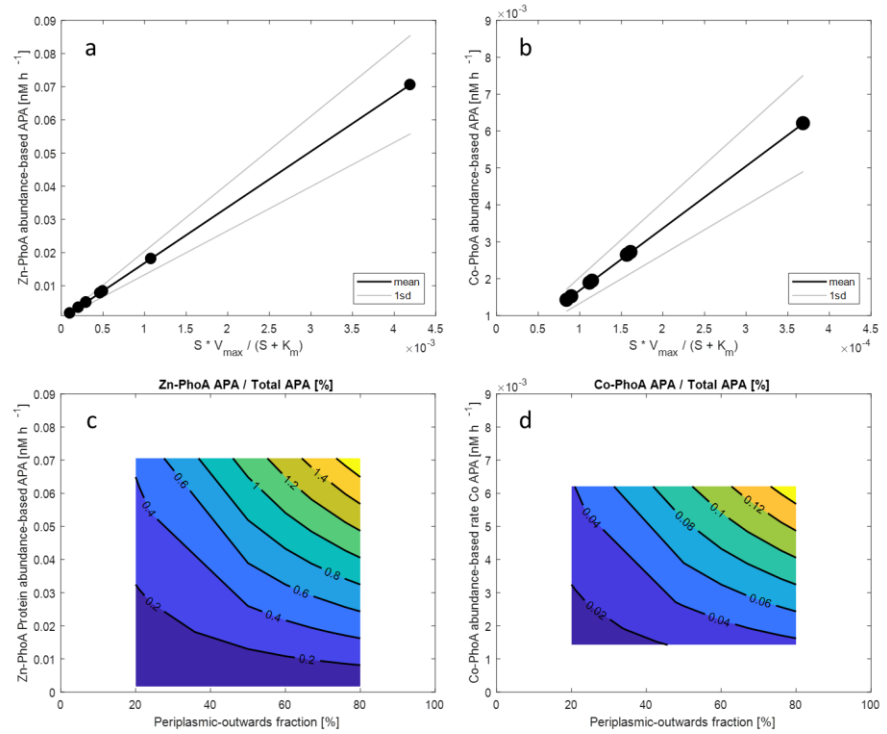

Figure 5.10 (a) Protein abundance-based APA rate estimates of *Synechococcus* Zn-dependent PhoA as a function of different enzyme kinetic parameters V_{max} and K_m (distinct black dots, with black line interpolating between). Substrate availability S is a constant. (b) Same as (a), but with enzyme parameters for the less efficient Co-dependent PhoA. Standard deviations of the mean are the propagated errors from the variability of individual variables (see Table 5.7). (c) The fraction of the Zn-PhoA abundance-based APA from (a) over the total APA. (d) Same as (c) but using the Co-PhoA rates from (b). Note the scale difference between (a,c) and (b,d).

5.5 Conclusions

Metal and P availability may co-stress primary production in the acutely oligotrophic subtropical North Atlantic due to trace metal co-factor requirements in alkaline phosphatases that are involved in DOP acquisition. We measured the absolute concentrations of the alkaline phosphatases PhoA and PhoX of *Synechococcus* and *Prochlorococcus* in *in-situ* bioassays following Zn, Co or Fe additions. Our results revealed localised effects of metal additions on alkaline phosphatase abundances, which were heterogeneous in their enzyme specificity and species specificity at two contrasting biogeochemical settings across the basin: In Zn or Co amended treatments, the abundance per L seawater of a *Synechococcus* PhoA increased similarly for both metals in the western Sargasso Sea, meriting further investigations into the potential for Zn/Co substitution in this enzyme. In the Fe amended treatment, the concentration per L seawater of a *Prochlorococcus* PhoX increased in the eastern subtropical gyre. Model calculations with the *Synechococcus* PhoA showed that Zn allocated to this enzyme makes up minute fraction of the total cellular Zn content, but under Co-for-Zn substitution this translates to a substantial fraction of the total cellular Co content, making *Synechococcus* potentially sensitive to Co-P limitation in the ocean. Protein abundance-based rates of the few alkaline phosphatases targeted in this study are orders of magnitude below total APA estimates, which suggests important roles for other alkaline phosphatases in the ocean (e.g. from other microbes, extracellular alkaline phosphatases, or other phosphoester hydrolases). As a result of global change, increased stratification and reduced subsurface nutrient supply alongside increased biological N_2 fixation and anthropogenic nitrate inputs to the ocean are debated. This could disproportionate the DIN to DIP budget further, exacerbate the DIP stress and increase the reliance on alkaline phosphatases as a means of P acquisition. Therefore, our results form an important contribution to the understanding of the role of metal availability for alkaline phosphatases. At the same time, our results call for future studies to pinpoint the extent of such limitation across space, time and the marine microbial realm. The characterisation of key alkaline phosphatases is required, particularly with regards to their kinetics and metal co-factors.

Chapter 6 Conclusions

6.1 Synthesis and Limitations of Results

Primary production by phytoplankton in the surface ocean is limited by the availability of vital nutrients, which places constraints on the efficiency of the biological C pump and hence, impacts upon the Earth's climate. In the subtropical oligotrophic gyres, the primary limiting nutrient is typically N, but the subtropical North Atlantic is unique in that it is under severe P-stress and secondary P-limitation (Mahaffey et al., 2014; Moore et al., 2013). This is driven by biological N_2 fixation, which provides a bioavailable alternative source of N under DIN scarcity but simultaneously uses up large amounts of the DIP inventory. Compared to the subtropical gyres elsewhere, the North Atlantic receives high fluxes of Fe-rich dust from the Saharan desert that fuel diazotrophy by meeting the high Fe demands of the enzymes involved in N_2 fixation (Kustka et al., 2003). The resulting DIP scarcity then drives the ambient phytoplankton community towards the utilisation of the DOP pool. An enzyme that can act on a major fraction of DOP, namely phosphoesters, is alkaline phosphatase, which has a variety of forms with different metal requirements of Fe, Zn or Co. However, these trace metals occur at vanishingly low concentrations in the ocean, particularly Zn and Co as they lack the large atmospheric source of Fe, which makes it challenging for cells to acquire sufficient amounts of these metals. Additionally, Fe, Zn and Co (and the other bioactive trace metals V, Cr, Mn, Ni, Cu, Mo, and Cd) are f-block elements with rich redox and complexation chemistry, and so the commonly measured 'dissolved' pool of a metal is in fact a continuum of various physicochemical species with a range of chemical reactivity (e.g. affecting its residence time) and bioavailability (Bruland and Lohan, 2004). For example, in the case of Fe, it is sFe, the smaller sized fraction of the dFe pool, that is considered readily bioavailable, while the acquisition of the larger cFe comes at higher metabolic expense (Chen and Wang, 2001), although it is the dominant form of dFe originating from dust (Fishwick et al., 2014).

Therefore, the unique biogeochemistry of the subtropical North Atlantic with regards to its macronutrient and trace metal setting leads to the question, whether the availability of trace metals stunts the acquisition of DOP, exacerbates P-stress and causes metal-P co-limitation, following N limitation. The overarching aim of this dissertation was to elucidate on the interactions between trace metal micro- (Fe, Zn and Co) and macronutrient (P) cycles. A meridional transect along 22 °N in the oligotrophic subtropical North Atlantic gyre between Guadeloupe to Tenerife during June to August 2017 enabled to use strong cross-basin biogeochemical gradients as a natural field laboratory to assess the micro-/macronutrient coupling by means of a combined toolbox of observational geochemistry, *in-situ* experimental work and metalloproteomics. In brief, new high-resolution data

sets on the distribution and physicochemical speciation of Fe were generated for both the natural ocean environment and during short-term tracking experiments with ambient seawater, which together demonstrated the large variability of physicochemical speciation Fe across the basin, driven by a highly dynamic colloidal phase. Moreover, quantitative proteomic measurements of cyanobacterial alkaline phosphatase concentrations were made for the first time in Fe, Zn and Co-amended *in-situ* bioassays. They revealed increased concentrations of some alkaline phosphatases upon different metal additions at a subset of locations across the basin. This dissertation culminates into the result that the subtropical North Atlantic basin is biogeochemically much more fine-structured than the bulk Fe-rich oligotrophic gyre, which it is often condensed to in the global context, and that this relevant to assessing constraints on phytoplankton growth in the present and future ocean.

An important factor that drives these regional biogeochemical differences across the subtropical North Atlantic gyre, is the variability of the sources, sinks and internal cycling of Fe in both the surface waters and the water column across the basin. Therefore, Objective 1 of this thesis was:

> **Objective 1:** To determine the natural distribution of Fe in high resolution full-depth water column profiles in the subtropical North Atlantic gyre along a west-to-east gradient and to resolve its physical speciation into sFe, dFe and TDFe to gain insight into the biogeochemical cycling of Fe (Chapter 3).

Oceanic Fe exists as a diverse and exchangeable continuum of physicochemical species of variable chemical and biological reactivity that impacts differently on Fe's residence time and bioavailability. However, measurements are commonly restricted to the dissolved phase and miss these complexities. Chapter 3 revealed that in the subtropical North Atlantic, the dynamic colloidal phase – operationally defined as 0.02 µm <cFe <0.2 µm – is largely responsible for the distribution of dFe in the water column. It forms the pivot between the dissolved and particulate phases at sources and sinks, while the smaller sFe (<0.02 µm) is less variable. Briefly, seasonal Fe-rich dust deposition resulted in elevated cFe concentrations in the surface, which drove a strong west-to-east gradient of surface dFe concentrations (from 0.25 to 1.53 nM). In the underlying water column, the impact of dust manifested itself as a gradual progression from typical dust-like to nutrient-like dFe profiles from west to east, and cFe was preferentially removed over sFe through the euphotic zone by particle scavenging (i.e. simultaneous removal of pFe) and biological uptake. Colloidal Fe also controlled the dFe budget at sources and sinks in the deeper water column, with a hydrothermal source enriching the overlying water to 27 nM dFe as 92 % cFe, while dissolution of and scavenging by seafloor sediment introduced dFe to or removed dFe from the seawater, in both cases via cFe. Over a full depth profile, the stronger the source or sink of dFe was, the further away dFe was from a 50:50 % partitioning between cFe and sFe. This was illustrated by an hourglass shape of the fractional contribution of cFe to dFe against

depth that highlighted the dynamic processes acting on the Fe distribution at the surface and in the abyss, while the ocean interior formed the tight neck. In summary, the main result gained under Objective 1 was that:

> **Main result 1:** Colloidal Fe holds a pivotal role for driving the full-depth distribution of dFe.

Together with the spatial resolution of the surface dFe measurements, which is the highest published to date on a meridional transect in the subtropical North Atlantic, the full-depth size-fractionated Fe measurements presented in Chapter 3 make an important contribution towards resolving the oceanic Fe cycle in detail. However, insights gained through this data set are restricted to a 'snapshot view'. This means that the physical fractionation of dFe that we observed was shaped by the net effect of a plethora of underlying abiotic and biotic processes, but individual processes, their time scales, and their relative importance remained concealed. Furthermore, as an inevitable consequence of filtration-based operational definition, cFe was treated as one homogenous phase, when it itself consists of a diverse continuum of inorganic and organic species. The characterisation of distinct species within the Fe continuum – both colloidal *and* soluble – is key to understanding processes, time scales, and relative bioavailability of Fe species in the ocean (see Section 6.2 for details).

Noting these shortcomings, the insights gained under Objective 1 contribute to the growing body of evidence that cFe holds a key role in the oceanic Fe cycle and suggest that incorporating an explicit cFe term in global biogeochemical models could reduce uncertainty in estimates for Fe's residence time and bioavailability in the ocean. These parameters are currently major unknowns varying over orders of magnitude (Lis et al., 2015b; Tagliabue et al., 2016). It is also clear from the strong surface gradient of Fe concentrations in the data presented in this thesis, that the distribution of Fe is not only a question of high dust versus low dust regimes on global scale, but that its variability over a ~3,000 km transect within one high dust regime is on the similar scale (0.3 to 1.6 nM) than comparing two contrasting dust regimes, such as the North and South Atlantic gyres (~0.1 to 1.6 nM; Ussher et al., 2013). Hence, the 'high Fe North Atlantic' is a simplification. Global change scenarios include altered wind patterns delivering Fe-rich dust and an increased anthropogenic dust component with a different Fe solubility than that of lithogenic dust. As this will clearly affect the oceanic Fe cycle (e.g. Jickells et al., 2005), a detailed understanding of the system at present is required to predict future impacts accurately, which includes regional Fe variability alongside its physicochemical speciation.

As a hybrid-type metal, oceanic Fe is impacted by biological uptake and regeneration, and inorganic particle scavenging processes that continuously cycle Fe between different physicochemical species. However, investigations into the distribution and size fractionation of Fe, as done under Objective 1,

provide only a snapshot view of the net effects of all the processes that shape Fe's distribution and speciation at any one point in time and space. The time scales and direction of exchange between the different species remained unresolved by this approach, and therefore Objective 2 of this thesis was:

> **Objective 2:** To track experimentally, the kinetics (minutes-to-days) exchange of Fe between different size fractions in subtropical North Atlantic surface waters across gradients of ambient Fe concentrations (Chapter 4).

Using Fe additions enriched in the low abundance isotope ^{57}Fe in incubations with ambient seawater and following the partitioning into different Fe size fractions over time, Chapter 4 aimed to provide the 'video' to the snapshot view of Chapter 3, under a range of initial biogeochemical seawater conditions across the subtropical North Atlantic. The results strengthened the evidence for the important role of cFe in driving dFe; in all incubations, almost all (~90 %) of the ^{57}Fe enriched addition, which was introduced as inorganic sFe, formed colloidal-sized Fe-oxyhydroxide nanoparticles within <30 min, due to the low solubility of Fe under seawater conditions and due to the absence of an excess organic ligand pool that would have retained Fe in the soluble phase. The backwards kinetics were slow, so that the colloidal partitioning signal remained unchanged over the probed 48 h period. In contrast, the naturally present Fe pool (dominantly ^{56}Fe) was subjected to some exchange between the soluble and colloidal size fractions late during the incubations (after at least 24 h). The processes driving the exchange differed at each location, due to the local biogeochemical gradients (e.g. diazotrophic activity and dust loading), and could only be discerned by determining sFe and cFe, as opposed to only dFe. Overall, the main result gained under Objective 2 was that:

> **Main result 2:** Colloidal Fe forms rapidly, independently of ambient seawater conditions, and irreversibly over 48 h.

Together with the distributional results from Objective 1, which showed that cFe was rapidly attenuated through the euphotic zone, the main result of Objective 2 implies that despite the large dFe flux to the North Atlantic, dFe is only shortly retained in the surface waters, because it is either introduced as cFe or it forms cFe from sFe. In other words, the residence times of dFe drops, when inorganic cFe nanoparticles are the dominant constituents of dFe (see also Black et al., 2020).

The low abundance isotope tracer experiments suffered from reproducibility issues that likely resulted from Fe-bearing dust particles introducing heterogeneity in the incubation seawater, which highlights the difficulty for experimental studies in dusty oceanic regions. An optimised incubation set-up should include a homogenisation step of the incubation seawater (e.g. pre-sampling into a large carboy before subsampling into individual incubations containers; as in Buck et al., 2010; Hurst

& Bruland, 2007), a conditioning step for the incubation containers by which they are stored with ambient seawater for a few days to avoid potential wall effects (as in Lohan et al., 2005b), and the measurements of the exact holding volume of each individual incubation container prior to use to ensure equal metal/nutrient spikes. Despite these issues, no time-series tracing bottle experiments of Fe speciation were available for the subtropical North Atlantic prior to the one at hand, despite it being the arguably best studied oceanic basin in terms of Fe. Comparable studies are restricted to Fe-limited HNLC regions like the Southern Ocean or North Pacific (Buck et al., 2010; Hurst and Bruland, 2007; Lohan et al., 2005b), where strong biological responses drive changes in the concentration and physicochemical speciation of Fe over time. Although the surface subtropical North Atlantic is limited by N, not Fe, the rapid exchange from sFe to cFe and the rapid attenuation of cFe create dFe minima in the DCM that could lead to Fe stress at these depths (Hogle et al., 2018). Therefore, the focus on sub-dFe dynamics is key to resolve Fe availability to phytoplankton, even in not typically Fe-limited regions like the subtropical North Atlantic.

One of the key pathways, via which Fe stress may impact upon phytoplankton growth, is the metal requirement of alkaline phosphatases. To meet cellular P demands under the DIP scarcity in the North Atlantic, DOP is an alternative, less readily bioavailable resource for phytoplankton that is accessible via Fe (PhoX) or the Zn/Co (PhoA) dependent phosphoesterase alkaline phosphatase. However, the vanishingly low availability of these trace metals in the ocean potentially stunt DOP acquisition and cause metal-P co-limitation. Therefore, Objective 3 of this thesis was:

> **Objective 3:** To determine experimentally using quantitative proteomics from bioassays, the impact of Fe, Zn and Co additions on alkaline phosphatase production in subtropical North Atlantic waters across strong gradients in ambient metal availability, P stocks and phytoplankton community (Chapter 5).

The quantitative proteomics measurements allowed to address this from the cellular scale, which reached beyond the evidence based on nutrient distributions and APA assays, as these common approaches are neither specific to the responsive organism nor to the enzyme type. Results from this objective showed that concentrations of alkaline phosphatases of two dominant phytoplankton species increased upon metal additions in the subtropical North Atlantic basin. In the ultraoligotrophic (3.7 nM DIP, 87 nM DOP) Sargasso Sea, where *Synechococcus* cell abundances and dFe concentrations peaked (1.23 nM), *Synechococcus* PhoA was six- to seven-fold higher upon Zn (25.1 ± 0.37 fM) or Co (31.4 ± 4.49 fM) addition relative to the Control (4.44 ± 0.97 fM), while *Synechococcus* cell abundances (albeit no information on cell activity) remained unchanged. Contrastingly, in the oligotrophic (14 nM DIP, 129 nM DOP) eastern gyre, where maximum *Prochlorococcus* abundance and low dFe concentrations (0.23 nM) were measured, the concentration of *Prochlorococcus* PhoX increased two-fold from the Control (5.44 ± 1.59 fM) to 12.44 ± 1.73 fM,

when Fe was added. Additionally, the similar effect of the Zn and Co addition adds some weight to the hypothesis that these metals can substitute each other in the *Synechococcus* PhoA and would complement Chapter 1's Figure 1.2 for trace metal dependencies in the phytoplankton cell (Figure 6.1). Furthermore, the bioassay responses in alkaline phosphatase concentrations were not accompanied by changes in Chl-*a* or APA, and enzyme-abundance based rate estimates suggested that the measured subset of cyanobacterial alkaline phosphatases was only a minor contributor to the overall APA rate. Nevertheless, as *Synechococcus* and *Prochlorococcus* are the dominant phytoplankton species in this basin, the impact that metal and P (un)availability has on their ecological success is key to understanding North Atlantic biogeochemistry from a system-scale perspective. Using *Synechococcus* PhoA data and measured cellular metal quotas in model calculations, it was demonstrated that the stoichiometric allocation of Zn/Co to co-factor sites in this enzyme was not a major sink of cellular Zn, but of cellular Co.

Overall, it was not discernible from the proteomics data, whether the alkaline phosphatase concentration changes were driven by more alkaline phosphatases per cell (e.g. by metal regulatory pathway or by metal-activation that prevents enzyme degradation) or by more alkaline phosphatase due to more cell activity. Therefore, the main result gained under Objective 3 was that:

> **Main result 3:** The concentrations of cyanobacterial alkaline phosphatases increased under higher availability of Zn/Co or Fe at two contrasting sites.

Clearly, the full picture of the underlying drivers of this result cannot be fully reconciled, due to the incomplete subset of marine bacterial alkaline phosphatases measured and due to the lack of data on other proteins involved in P metabolism (e.g. the two-component system PhoR/PhoB of the *pho* regulon or the phosphonate transporters Phn; Held et al., 2019), in metal homeostasis (e.g. the Fe and Zn uptake regulators Fur and Zur; Barnett et al., 2014), or constitutively expressed 'housekeeping' proteins, as applied in transcriptomic studies (e.g. the RNase RnpB; Malmstrom et al., 2013). Furthermore, different subcellular localisations of those alkaline phosphatases that *were* measured are likely biased towards detection of the periplasmic/intracellular PhoA relative to the primarily extracellular PhoX (Luo et al., 2009). Hydrolytic efficiencies are also likely to differ between the enzymes measured, but this is currently not known. Until the kinetics, co-factor preferences, and regulation of these alkaline phosphatases are resolved (see details in Section 6.2), the insights gained through Objective 3 contribute one waypoint to the understanding the role of DOP for constraining primary production in the subtropical North Atlantic.

Of all the experiments targeted under Objective 3, effects on alkaline phosphatase concentrations under changing trace metal availability were observed at only two out of four probed locations and was thereby similarly spatially restricted as in previous APA assay-based experiments across the

basin (Browning et al., 2017; Mahaffey et al., 2014). The disproportionation between DIP and DIN inventories, which drives the need for DOP acquisition in the first place, may increase under global change due to reduced subsurface nutrient supply from increased stratification alongside higher DIN fluxes from biological N_2 fixation and anthropogenic sources. Therefore, the importance of alkaline phosphatases may become more widespread, and so their limitation by trace metal availability may do too. At the same time, global change is predicted to alter also trace metal cycles, for example by changes in wind patterns and dust supply (relevant to Fe; see Section 1.4.1) or by expanding OMZs (relevant to Co; see Section 1.4.3), which may create niches for the expression of alkaline phosphatases with certain metal requirements. Regions other than the subtropical North Atlantic, where DIP depletion is severe (<10 nM) and DOP is an important resource, are the Mediterranean Sea and the Western North Pacific (Martiny et al., 2019). These would make interesting foci for future studies to constrain the extent of metal-P co-stress or co-limitation in the global ocean, especially because they contrast starkly regarding trace metal distributions, with significantly higher surface concentrations in the Mediterranean (~1.4 nM dFe, 2.0 nM dZn, 300 pM dCo in the top 100 m) (Dulaquais et al., 2017; Gerringa et al., 2017; Schlitzer et al., 2018) than in the Western North Pacific (<0.25 nM dFe, <0.15 nM dZn, <20 pM dCo; all modelled data due to lack of measurements) (Roshan et al., 2018; Tagliabue et al., 2018, 2016). The Western North Pacific is a strong candidate for metal-P co-limitation.

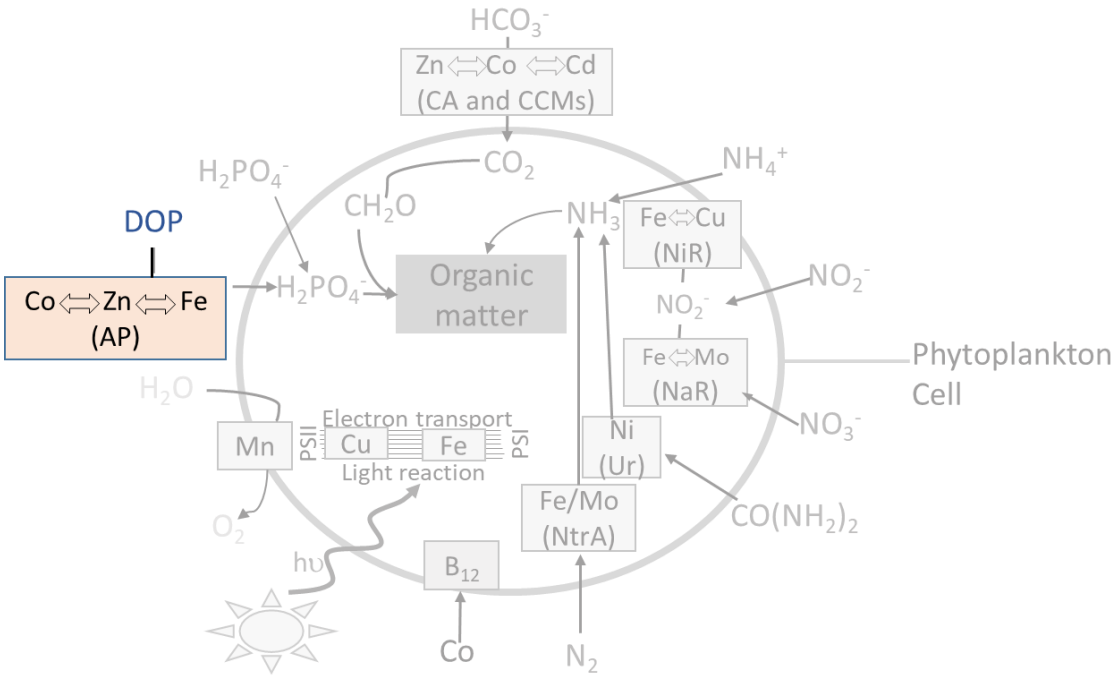

Figure 6.1 A version of Chapter 1's Figure 1.2, complemented with the result from this thesis that Co too, not only Zn or Fe, may be involved in the acquisition of DOP via the metalloenzyme alkaline phosphatase.

6.2 Future Directives

Using a combined toolbox of observational trace metal geochemistry across the basin, field-based trace metal-clean experiments at representative sites, and quantitative metalloproteomics measurements at the cellular level, this thesis contributed to the understanding of the North Atlantic biogeochemistry of Fe, Zn, Co and P from perspectives on different scales. The influence of nano-scale (e.g. cFe formation upon dust deposition) and cellular (e.g. alkaline phosphatase expression at scarce DIP) processes on basin-wide biogeochemistry and vice versa is obvious from the results presented. We now need to now understand these intricate interactions mechanistically. To this end, the following questions emerge directly from this thesis: What is the distinct nature of Fe species in the colloidal phase, their reactivity and bioavailability (Section 6.2.1)? And, what are the characteristics of marine cyanobacterial alkaline phosphatases, their preferred metal co-factors and kinetic properties (Section 6.2.2)? More broadly, the questions emerge regarding the physicochemical speciation of the full suite of bioactive trace metals in the ocean, and the metal requirements and flexibility in the cellular machinery. In finding answers, cross-disciplinarity between the fields of chemical and biological oceanography is imperative (Section 6.2.3). Elucidating on the underlying mechanisms of macro- and micronutrient cycling, nutrient interactions, and the resulting impacts on primary production is fundamental to the further development of global biogeochemical models, which are indispensable for deriving a 'baseline' understanding of the ocean system at present and enabling accurate predictions of changes in the future.

6.2.1 Characterising Distinct Physicochemical Metal Species

In the light of this dissertation, the unequal behaviour of cFe versus sFe and the important role of cFe for driving dFe, as demonstrated in Chapter 3 and Chapter 4, highlight the need to understand sub-dFe dynamics of the oceanic Fe cycle. The chemical characterisation of distinct species within the Fe continuum is a required first step. The pioneering LC-ICPMS-ESI-MS method by Boiteau & Repeta (2015) enabled the characterisation of a suite of siderophores in the natural ocean environment (Boiteau et al., 2016; Bundy et al., 2018). Although those studies only resolved a small subset of the dFe pool, specifically of the organic sFe pool, they built the basis for future characterisation of organic Fe complexes including colloidal-sized ligands, such as more weakly binding humic substances (Gledhill & Buck, 2012). Simultaneously, Synchrotron X-ray spectroscopy, previously used to decipher C-Fe associations in hydrothermal plumes (Toner et al., 2012), could be applied to other parts of the water column to reveal the chemical character and reactivity of marine Fe-nanoparticles.

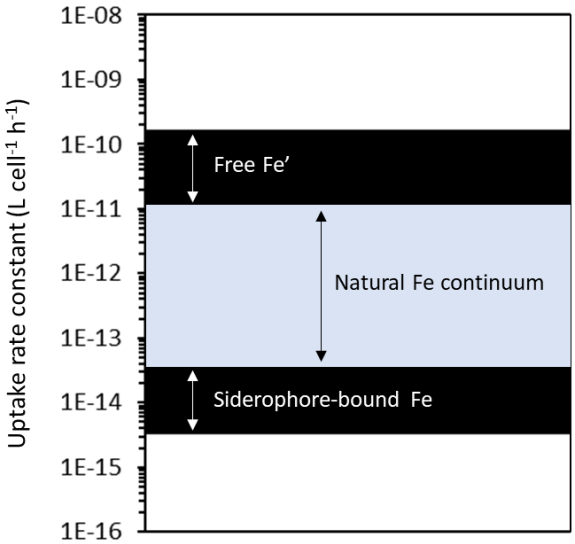

Figure 6.2 The range of uptake rate constants for free Fe' and Fe bound to a model siderophore (desferrioxamine), of *Prochlorococcus* cultured under Fe-limitation. The blue area indicates the range for the natural Fe in seawater. Data were compiled from Lis et al. (2015a, 2015b).

The rapid transformations between Fe species in the surface ocean, as illustrated by the experimental work of Chapter 4, and the continuous aging of Fe-bearing particles, as they sink through the water column pose additional challenges to determining the suite of Fe species at a point in space and time. Therefore, physicochemical characterisations will need to be accompanied by studies on the reactivity and bioavailability of different Fe species, for example by drawing on the 'bioavailability envelope' (Lis et al., 2015b). In this conceptual model, a range of model organic Fe-substrates (Lis et al., 2015b) or the ill-defined natural organic Fe pool (Shaked et al., 2020) were shown to fall between two endmembers of highest (free Fe') and lowest (siderophore-bound Fe) bioavailability to phytoplankton. However, the main focus of these studies was on eukaryotic species, whereas the subtropical oligotrophic gyres are dominated by cyanobacteria, especially *Prochlorococcus*, of which some ecotypes were recently shown to be capable of siderophore biosynthesis and/or transport (Malmstrom et al., 2013). Therefore, filling in the *Prochlorococcus*-specific Fe bioavailability envelope for the naturally occurring oceanic Fe continuum (Figure 6.2) is an exciting avenue for future research. With the accelerating incorporation of 'omics tools and molecular biology approaches for marine trace metal studies, the opportunity is there to decipher acquisition pathways for different Fe species, their flexibility, and responsiveness to changes in the Fe environment.

The global impact of Fe on marine primary production has been demonstrated extensively over the past decades (review by Tagliabue et al., 2017), and Fe is clearly the best studied trace metal micronutrient in the ocean. However, the preceding considerations must extend beyond Fe. Less is known about the physicochemical speciation and metal-microbe interactions of other bioactive trace metals, but as Chapter 5 demonstrated for the case of Zn and Co, these must not be neglected.

6.2.2 Characterising Marine Metalloproteins

The much desired characterisation of distinct physicochemical metal species and their associated bioavailability, as explained in Section 6.2.1, will contribute to the understanding of oceanic trace metal limitation in the ocean from a top-down perspective, i.e. what is available on the environmental level and how will this impact upon the cellular level? However, the bottom-up perspective will be indispensable too in constraining the underlying mechanisms, by characterising the marine metalloproteome, its flexibility and regulation.

In an attempt to piece together the metal allocation in a *Synechococcus* cell, the model calculations of Chapter 5 illustrated the potential importance of the alkaline phosphatase PhoA as a cellular Co sink. Although the bioassay responses did hint at substitution capabilities of Zn and Co in this PhoA enzyme, the determination of the preferred metal co-factors is required to corroborate these results. Heterologous expression of this protein in a model bacterium and crystallographic analysis of its metal binding sites (e.g. as applied for the Fe-binding site in the IdiA/FutA protein of *Trichodesmium* by Polyviou et al., 2018) would provide valuable insights into metal co-factor selection under controlled culture conditions. The adaptation of metallomics techniques to field samples, which couple quantitative trace metal analysis by HR-ICP-MS and proteome analysis by MS/MS in co-eluted HPLC fractions (e.g. methods in Barnett et al., 2014; and Mazzotta et al., 2020) as exemplified for a *Synechococcus* PhoA from culture in Figure 6.3, will be key to understanding metal selections in the natural environment. In order to assess the impact of environmental changes, such as different relative availability of Zn and Co for use in PhoA, these techniques could be extended to a third dimension, in which APA rates are monitored simultaneously. It would be of great interest for assessing patterns of co-limitation to determine the thresholds, at which PhoA 'selects' Zn or Co, or at which PhoA becomes metal-free, e.g. due to cellular metal re-allocation away from alkaline phosphatase, so that the enzyme loses its activity. This also feeds into the second facet of research needed to corroborate the model calculations on the *Synechococcus* PhoA, namely the kinetic characterisation of this enzyme. It would be desirable to define a set of the Michaelis-Menten parameters V_{max} and K_m for the natural heterogeneous pool of phosphoester substrates (e.g. DNA/RNA/ATP/phospholipid molecules), and for the Zn- versus Co-binding PhoA, and ultimately to compare the enzymatic efficiency to other competing alkaline phosphatases in the marine environment.

Of course, the above considerations for the Zn/Co-dependent *Synechococcus* PhoA for DOP acquisition and the model calculations of Chapter 5 are only one aspect for future marine metalloproteomics research. As Figure 6.1 highlights, global primary production by phytoplankton is sensitive to many coupled systems of metals and macronutrients or of metals and other cellular

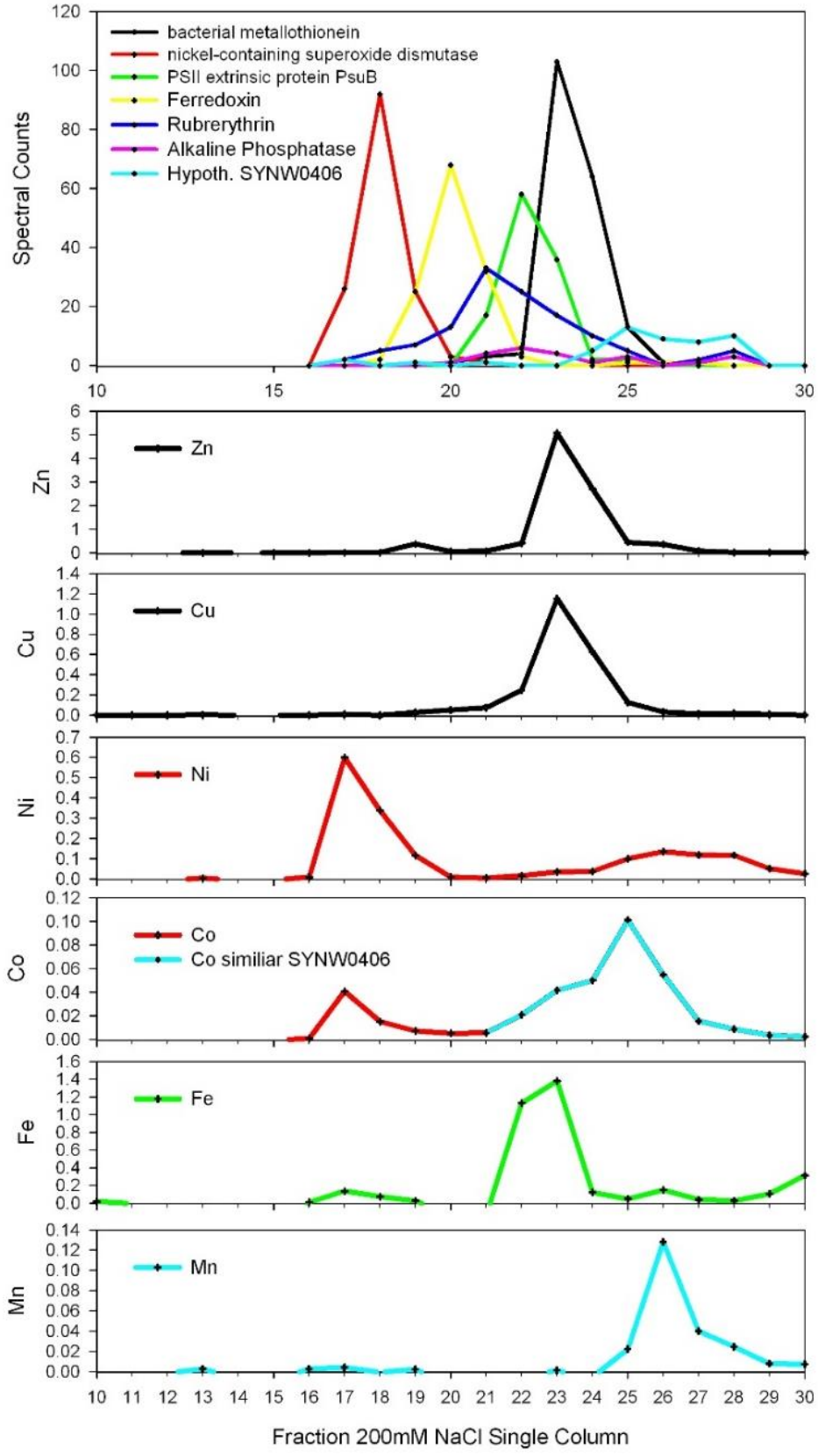

Figure 6.3 Metalloproteome of *Synechococcus* WH8102 from culture, showing co-elution of proteins and metals in chromatography fractions. The collected fractions were measured by HPLC-MS/MS and HR-ICP-MS analysis, respectively. Data and figure are used by courtesy of M. Saito.

processes (e.g. the role of Fe in photosystems I and II), with more metal dependencies yet to be identified (e.g. R. Rickaby, https://cordis.europa.eu/project/id/681746). The incorporation of (prote)omics techniques for the marine environment will be key to pinpointing metal allocation to specific proteins (Saito et al., 2019), while SXRF (Twining et al., 2015) and ICP-MS methodology (Zhang et al., 2018) will aid the understanding of compartmentalised cellular metal quotas in different environments. These are promising routes for tying together the marine metalloproteome and the interaction with seawater geochemistry, which are fundamental to primary production and the biological C pump in the ocean. Achieving this would help to identify and to direct research towards regions that will be most sensitive to future alterations in metal cycling.

6.2.3 Cross-Disciplinarity in Marine Trace Metal Research

The directives for future research, as discussed in the previous sections, sit clearly at the intersection between the disciplines of chemical and biological oceanography. The incorporation of 'omics tools into marine trace metal research forms a particularly important avenue in this, because it allows to detect (bio)chemical processes at the smallest, cellular scale and their potential influence on system-scale biogeochemistry. The thesis at hand and the suite of associated research activities at sea provided one example for the value of implementing biological tools, i.e. rate measurements and proteomics, into large-scale geochemical surveys of nutrient and trace metal distributions. Without this combined toolbox, the impact of the strong cross-basin Fe gradients and ambient Zn and Co availability in potentially restricting phytoplankton alkaline phosphatase concentrations in the subtropical North Atlantic, would have been obfuscated.

Over the past years, the field of marine (trace metal) biogeochemistry as a whole has rapidly accelerated towards the intersection of biological and chemical oceanography (e.g. Saito et al., 2019), and recently, efforts have been made by the international research community to coordinate this cross-disciplinarity under a coherent framework for the global scale. The envisaged BioGeoSCAPES program aims to further our understanding of 'Ocean metabolism and nutrient cycles on a changing planet' (https://www.biogeoscapes.org/), through a triangular approach of 1) large field surveys of nutrient and metabolite distributions, 2) 'omics, biological rate and physiology measurements, and 3) biogeochemical modelling efforts – from the scale of individual organisms to that of entire geochemical environments. Drawing on the successful concept of GEOTRACES 'An international study of the marine biogeochemical cycles of trace elements and their isotopes' (https://www.geotraces.org/), standardisation will be key, which includes the definition of core measurements for sea-going activities, the intercalibration of novel sample types for the ocean environment (partly underway: https://www.us-ocb.org/intercomparison-and-intercalibration-metaproteomics/), the development of protocols for sampling and sample processing, and a strategy

for data management. The cross-disciplinary approach of BioGeoSCAPES, for which this thesis provides one early example, alongside its standardised framework will enable the research community to fulfil the global vision of generating a baseline understanding of the ocean's metabolism and its resilience against future change.

Appendix

A.1 Publication of Chapter 3

Global Biogeochemical Cycles

RESEARCH ARTICLE
10.1029/2019GB006326

Iron Distribution in the Subtropical North Atlantic: The Pivotal Role of Colloidal Iron

K. Kunde[1], N. J. Wyatt[1], D. González-Santana[1], A. Tagliabue[2], C. Mahaffey[2], and M. C. Lohan[1]

[1]Ocean and Earth Sciences, National Oceanography Centre, University of Southampton, Southampton, United Kingdom, [2]Department of Earth, Ocean, and Ecological Sciences, University of Liverpool, Liverpool, United Kingdom

Key Points:
- Size-fractionation reveals that colloidal iron is more important than soluble iron for distribution of dissolved iron in North Atlantic
- Colloidal iron is the predominantly active species at key supply and removal processes of the dissolved iron cycle
- Global comparison suggests that the colloidal iron fraction in mesopelagic zone is determined by the local lithogenic contribution

Correspondence to:
K. Kunde,
K.Kunde@soton.ac.uk

Citation:
Kunde, K., Wyatt, N. J., González-Santana, D., Tagliabue, A., Mahaffey, C., & Lohan, M. C. (2019). Iron distribution in the subtropical north Atlantic: the pivotal role of colloidal iron. *Global Biogeochemical Cycles, 33*, 1532–1547. https://doi.org/10.1029/2019GB006326

Received 19 JUN 2019
Accepted 6 NOV 2019
Accepted article online 12 NOV 2019
Published online 3 DEC 2019

Abstract The low availability of the essential micronutrient iron (Fe) in the ocean impacts the efficiency of the biological carbon pump, and hence, it is vital to elucidate its sources, sinks, and internal cycling. We present size-fractionated dissolved Fe (dFe, <0.2 μm) measurements from 130 surface samples and 7 full-depth profiles from the subtropical North Atlantic during summer 2017 and demonstrate the pivotal role of colloidal (cFe, 0.02 to 0.2 μm) over soluble (sFe, <0.02 μm) Fe in controlling the dFe distribution. In the surface (<5 m), a strong west-to-east decrease in dFe (1.53 to 0.26 nM) was driven by a dust gradient, which retained dFe predominantly as cFe (61% to 85% of dFe), while sFe remained largely constant at 0.19 ± 0.05 nM. In the euphotic zone, the attenuation of dFe resulted from the depletion of cFe (0% to 30% of dFe), with scavenging as an important driver. In the mesopelagic, cFe was released from sinking biogenic and lithogenic particles, creating a zone of elevated dFe (0.7 to 1.0 nM) between 400 to 1100 m depth. While the ocean interior, below the mesopelagic and above the seafloor boundary, exhibited a narrow range of cFe (40% to 60% of dFe), the abyssal cFe fraction varied in range from 26% to 76% due to interactions with seafloor sediments and a hydrothermal source with almost 100% cFe. Overall, our results produced an hourglass shape for the vertical cFe-to-dFe fraction and highlight the primary control of cFe on the dFe distribution.

Plain Language Summary Phytoplankton require nutrients such as phosphorus, nitrogen, and iron. Of these, iron is particularly interesting due to the paradox of its requirement for life-supporting mechanisms on the one hand and its low oceanic concentrations on the other. Iron is >1000-fold lower than the "traditional" nutrients. Hence, it is important to know how much iron is introduced to the ocean (sources), how much is removed (sinks), and how it is processed during its residence in the water. This study addressed these questions by measuring the iron concentrations in the subtropical North Atlantic. Our samples were filtered through two filter sizes to investigate the distributions of iron's different size fractions, a popular tool to gain a detailed understanding of the overall iron cycle. We found that the smallest size fraction, "soluble iron," does not vary much throughout the water column, but the slightly larger "colloidal iron" varies a lot, especially in the upper ocean and close to the seafloor, where dynamic supply and removal processes occur. The unequal behaviour of these fractions is an important finding that will improve the accuracy of biogeochemical models for iron, which in turn can improve the prediction of phytoplankton growth in the present and future ocean.

1. Introduction

Iron (Fe) is an essential micronutrient for marine primary production due to its enzymatic requirement in key metabolic functions such as photosynthesis, respiration, and the acquisition of macronutrients (Falkowski, 1997; Morel, 2003). For example, diazotrophs require Fe to fix dinitrogen (N_2) into more bioavailable forms, where surface nitrate concentrations are sufficiently low to limit biological activity (<10 nM), such as in the oligotrophic North Atlantic gyre (Mahaffey et al., 2003; Moore et al., 2009). However, due to the low solubility of Fe(III), the thermodynamically stable Fe species in seawater (Kuma et al., 1996; Liu & Millero, 1999), chronically low surface water dissolved Fe (dFe) concentrations prevail (<0.1 nM) that limit phytoplankton growth in large regions and result in a less efficient biological carbon pump (Moore et al., 2013). Concentrations exceeding the solubility limit can be maintained by organic ligands (Gledhill & Buck, 2012), which form a crucial component in the regulation of Fe bioavailability in the oceans (Tagliabue, Aumont, & Bopp, 2014).

Global Biogeochemical Cycles 10.1029/2019GB006326

Table 1
The Different Size-Fractionated Fe Species Used in This Study

Iron species	Abbreviation	Filtration size	Measurement
Soluble Fe	sFe	<0.02 μm	Direct measurement by FIA-CL
Colloidal Fe	cFe	0.2 μm <cFe < 0.02 μm	Calculated using cFe = dFe-sFe
Dissolved Fe	dFe	<0.2 μm	Direct measurement by FIA-CL
Apparent particulate Fe	pFe_{app}	>0.2 μm	Calculated using pFe_{app} = TDFe-dFe
Total dissolvable Fe	TDFe	Unfiltered	Direct measurement by FIA-CL

Note. FIA-CL refers to flow injection analysis with chemiluminescence detection (see methods).

Superimposed on its low concentration is the "hybrid" nature of Fe, where it displays a combined nutrient-type and scavenged-type vertical distribution (Bruland & Lohan, 2004). Scavenging, an umbrella term for adsorption, absorption, aggregation processes, and the eventual transfer to the particulate phase (Honeyman & Santschi, 1989; Wells & Goldberg, 1992), reduces the residence time of Fe and exacerbates the potential of Fe limitation.

Of the total Fe pool, only dissolved Fe (dFe), a continuum of exchangeable physicochemical species, is considered bioavailable (Tagliabue et al., 2017). Despite great progress in our understanding of the oceanic dFe cycle, thanks to GEOTRACES (http://www.geotraces.org/) and similar studies, major unknowns persist. These include its residence time with estimates ranging between 5 and 500 years (Tagliabue et al., 2016) and its bioavailability with variations over three orders of magnitude depending on the Fe substrate (Lis et al., 2015). To determine the complex mechanisms controlling the particle reactivity and bioavailability of Fe, total Fe can be separated into different size classes using operationally defined filter sizes (Table 1). Size fractions of Fe can be defined as soluble (sFe < 0.02 μm), colloidal (0.02 μm < cFe < 0.2 μm), dissolved (dFe < 0.2 μm), apparent particulate (pFe_{app} > 0.2 μm), and total dissolvable (TDFe, unfiltered) Fe.

Soluble Fe represents the "truly dissolved" Fe fraction, although only a small portion is present as free Fe, while the majority is complexed by organic ligands such as high-affinity siderophores (Gledhill & Buck, 2012). Soluble Fe is highly bioavailable in both free and complexed forms and arguably the favourable species for biological uptake (Lis et al., 2015; Shaked et al., 2005). In contrast, cFe, present in suspended nanoparticles or bound to colloidal-sized organic ligands, is rarely or less readily bioavailable (Chen & Wang, 2001; Wang & Dei, 2003) but can constitute almost 100% of dFe (Fitzsimmons et al., 2015).

Colloids serve as conduit for transferring Fe between the soluble and particulate phases in a two-step scavenging process termed "Brownian pumping," which involves the sorption of sFe onto the colloidal intermediate followed by the aggregation of colloids to larger particles (Honeyman & Santschi, 1989; Wells & Goldberg, 1992). While scavenging and biological uptake result in the transfer from the dissolved to the particulate phase, particles simultaneously replenish the dFe inventory via dissolution or remineralization (Milne et al., 2017).

Published data on size-fractionated Fe revealed two opposing hypotheses concerning the role of sFe and cFe in driving the Atlantic dFe distribution in particular. Largely invariable concentrations of sFe and variable cFe concentrations led Bergquist et al. (2007) to conclude that a dynamic colloidal phase controls the dFe distribution. In contrast, Fitzsimmons, Carrasco, et al. (2015) and Fitzsimmons and Boyle (2014) measured variability in both cFe and sFe, and hence, attributed a joint control on dFe by both size fractions.

The North Atlantic is heavily impacted by Fe-rich dust deposition from the Sahara and to lesser extent from Europe and North America, receiving >40% of the global dust flux to the ocean (Jickells et al., 2005). Prevailing wind patterns further introduce seasonality to the dust deposition, with highest dust-derived Fe fluxes in the summer (Sedwick et al., 2005), while the seasonal migration of the Intertropical Convergence Zone controls wet deposition, which is efficient for delivering Fe to the ocean (Schlosser et al., 2014). Atmospheric deposition imprints elevated dFe concentrations in the surface waters (~0.5 to 1.0 nM) of the North Atlantic that are in excess of those observed in the less dusty South Atlantic (<0.5 nM) (Ussher et al., 2013). This strong external Fe source to the otherwise oligotrophic subtropical gyre creates a unique biogeochemical setting with a hotspot for N_2 fixation (Moore et al., 2009). Hence, the North Atlantic is a key region for the understanding of the oceanic Fe cycle.

Global Biogeochemical Cycles 10.1029/2019GB006326

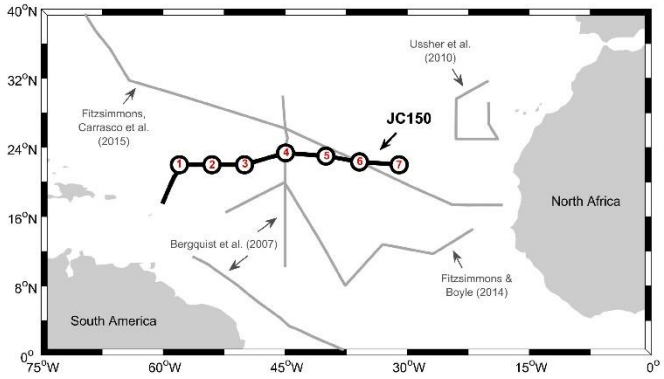

Figure 1. Map of the North Atlantic Ocean. Indicated are the stations of full-depth sampling (black dots, red numbers) and the cruise track along which surface samples were taken (black line). Cruise tracks of previous studies on size-fractionated Fe in this region are also shown (gray lines, arrows pointing to associated publication).

Using the physical speciation of Fe from a 3,000 km-long surface transect and 7 full-depth profiles (Figure 1), the present study addresses the questions: (1) What external and internal factors drive the distribution of Fe in the subtropical North Atlantic? (2) How do sFe and cFe fractionally contribute to the dFe budget? (3) And which fraction exerts the greater regulatory control?

2. Materials and Methods

2.1. Sample Collection

Seawater samples were collected during cruise JC150 (Figure 1) in the subtropical North Atlantic in summer (26 June to 12 August 2017), sampling between Guadeloupe and Tenerife onboard the *RRS James Cook*. Seven stations were occupied for vertical profiling, while underway surface sampling (<5 m) was conducted along the transect at a resolution of ~0.23 ° longitude. Seawater samples were collected using a titanium rosette fitted with 24 × 10 L trace metal-clean Teflon-coated OTE (Ocean Test Equipment) bottles and a CTD profiler (Sea-Bird Scientific) deployed on a conducting Kevlar wire. Upon recovery, the OTE bottles were transported into a class-1000 clean air van and pressurized (0.7 bar) with compressed air filtered in-line through a 0.2 μm PTFE filter capsule (Millex-FG 50, Millipore). Subsamples for dFe were filtered through 0.2 μm membrane cartridge filters (Sartobran 300, Sartorius) into trace metal-clean 125 ml low-density polyethylene bottles and acidified to pH 1.7 (0.024 M) by addition of 12 M ultrapure hydrochloric acid (HCl, Romil, UpA) under a class-100 laminar flow hood (Lohan et al., 2006). Samples for sFe went through an additional in-line filtration step inside a laminar flow hood through 0.02 μm syringe filters (Anotop, Whatman) before acidification. The filtration manifold consisted of PTFE manifold tubing and PVC peristaltic pump tubing, cleaned daily with weak 1 M HCl (SpA, Romil) and conditioned prior to use with low Fe seawater (Wu et al., 2001; Ussher et al., 2010). A new filter was used for each sFe sample. Samples for TDFe were collected unfiltered and then acidified. For the underway samples, seawater was pumped into the trace metal-clean van using a Teflon diaphragm pump (A-15, Almatec) connected by acid-washed PVC tubing to a towed "Fish" sampler. These samples were filtered in-line (<0.2 μm), and acidified, while the filtration step was omitted for TDFe, and no underway sFe samples were taken.

2.2. Iron Measurements

All sFe, dFe, and TDFe samples were analyzed in triplicate (three analytical peaks) using flow injection analysis with chemiluminescence detection (Floor et al., 2015; Obata et al., 1997) inside a class-1000 clean air laboratory either onboard or at the National Oceanography Centre Southampton, UK. Briefly, each sample was spiked 1 hr prior to analysis with 0.013 M ultrapure H_2O_2 (Sigma-Aldrich) to ensure the complete

oxidation of Fe (II) to Fe (III) (Lohan et al., 2006). Each sample was buffered in-line to pH 3.5 to 4.0 using a 0.15 M ammonium acetate (Romil, SpA) before Fe (III) was preconcentrated onto the cation exchange resin Toyopearl-AF-Chelate 650 M (Tosohaas) typically for 60 s at a flow rate of 1.5 ml min^{-1}. Following a rinse step of a weak 0.013 M HCl (Romil, SpA), Fe was liberated from the resin using 0.24 M HCl (Romil, SpA) and entered the reaction stream where it mixed with a precleaned 0.015 mM luminol solution containing 70 $\mu l\ L^{-1}$ triethylenetetramine (Sigma-Aldrich), buffered to pH 9.4 to 9.6 using a 1 M ammonia solution (Romil, SpA). Chemiluminescence occurred following the addition of 0.4 M H_2O_2, with the light signal detected (425 nm) by a photomultiplier tube (H82259, Hamamatsu). Iron concentrations were quantified using standard additions (TraceCERT, Fluka Analytical) to low Fe seawater. The limit of detection (three times the standard deviation of the lowest addition) was 0.03 ± 0.02 nM (n = 59), while the precision of three analytical peaks was 2.78 ± 2.02% (n = 1764). The procedural blank was assessed at the beginning of each analytical run using ultrahigh purity water, treated in the same way as the samples, and averaged 0.05 ± 0.03 nM (n = 69). Accuracy was established by repeat quantification of dFe in the SAFe reference samples yielding 0.11 ± 0.02 nM (n = 6) and 0.94 ± 0.04 nM (n = 17) for SAFe S and SAFe D2, respectively, which agree with the reported consensus values (S = 0.095 ± 0.008 nM; D2 = 0.96 ± 0.02 nM).

2.3. Auxiliary Parameters

Samples for chlorophyll-*a* (Chl-*a*) analysis from both the OTE bottles and the underway system were filtered through 0.7 μm glass microfiber filters (Whatman GF/F) and extracted in 90% acetone overnight (Holm-Hansen et al., 1965). The Chl-*a* extract was measured on a precalibrated (Spinach Chl-*a* Standard, Sigma) fluorimeter (Turner Designs Trilogy) and used to calibrate the fluorescence sensor on the CTD (Seabird 911+) daily. Salinity was calibrated onboard using an Autosal 8400B salinometer (Guildline). Dissolved oxygen (O_2) was measured by a Seabird SBE43 sensor, calibrated onboard using a photometric-automated Winkler titration system (Carritt & Carpenter, 1966). Turbidity was monitored using a WETLabs BBRTD light scattering sensor.

2.4. Calculations and Definitions

Mixed layers were calculated using a density change of 0.03 kg m^{-3} (de Boyer Montégut et al., 2004). To integrate Fe budgets across the upper ocean (section 3.2.1), the 1026.5 kg m^{-3} isopycnal was chosen as lower boundary. We did not try to capture a specific water mass, instead the intention was to compare the total Fe inventory in this layer across stations. This resulted in integration depths between 350 m at Station 1 and 220 m at Station 7. Shallower isopycnals would not have captured the full DCM at Station 7 (Figure 6). Similarly, for remineralization effects on dFe budgets in the mesopelagic (section 3.2.3), we chose the isopycnals 1026.30 and 1027.50 kg m^{-3} as boundaries because they cover the oxycline from ~180 to 130 μmol kg^{-1} between 220 to 1000 m depth (details found in the supporting information in Figure S2). Apparent oxygen utilization (AOU) was used to calculate dFe/C ratios (AOU:C = 1.6, Martin et al., 1989). For a global comparison of size-fractionated dFe distributions in the mesopelagic (section 3.2.3), we included all cFe measurements from the referenced data sets that lie within 10% of the maximum AOU at each station. For consistency, we used the AOU from the global annual 1 ° grid of the World Ocean Atlas 2018 (Garcia et al., 2013). Extracted AOU values were in excellent agreement with those calculated from measured O_2 concentrations during JC150. Stations reportedly influenced by sedimentary or hydrothermal input were excluded. Annual dust fluxes were extracted from Albani et al. (2016). Colloidal Fe data was binned by annual dust flux in 1 g m^{-2} yr^{-1} increments.

3. Results and Discussion

3.1. Large-Scale Distribution of Dissolved Iron

Figure 2 displays the full water column distribution of dFe across the transect with four main features of note: (1) an enrichment in the immediate surface layer, (2) a subsurface minimum between 50 to 200 m, (3) an increase in dFe in the mesopelagic between 400 to 1100 m, and (4) a large point source in the deep ocean at 45 °W (Figure 2). The most eye catching of these features was the midsection hotspot with up to 27 nM at 3300 m at Station 4, attributed to hydrothermal input from the Snakepit vent field on the Mid-Atlantic Ridge. The surface enrichment was most pronounced west of 54 °W with ≥1 nM dFe at Stations 1 and 2 (Figure 3), likely as a result of Fe-rich dust deposition from North Africa. In contrast, distinct dFe

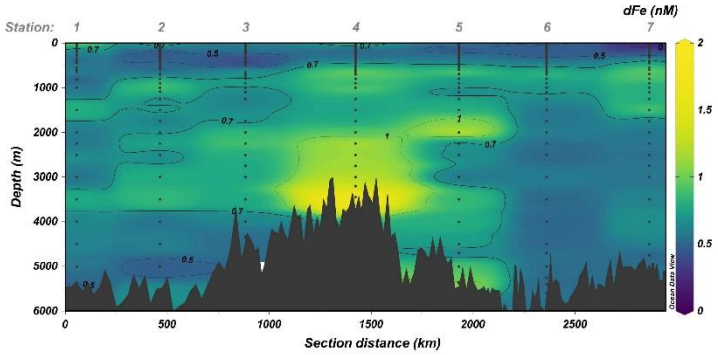

Figure 2. Section plot of dFe concentrations against distance from west to east. The very high concentrations measured over the Mid-Atlantic Ridge at Station 4 reach up to 27 nM but are excluded from the colour bar. The plot was produced with Ocean Data View (Schlitzer, 2018), using weighted-average gridding for interpolation with maximum scale lengths of 35 and 33 ‰ for the x- and y-axes, respectively.

minima were present in the subsurface at all stations across the gyre with concentrations as low as 0.09 nM at 60 m in the east (Station 7). Concurrent with the location of the deep Chl-*a* maxima (DCM), these dFe minima probably result from the combination of scavenging and biological uptake. Below the DCM to a depth of ~1100 m, dFe gradually increased to maxima of 0.7 to 1.0 nM, with highest concentrations in the east. Mesopelagic dFe enrichments correlated with AOU ($R^2 = 0.58$, n = 100) and probably derived from the continued dissolution of sinking dust particles and from the remineralization of organic matter. Away from external sources and from the influence of biological processes, the concentration of dFe in the ocean interior below the low O_2 waters and above the seafloor water-sediment interface was 0.67 ± 0.14 nM, excluding the hydrothermal influence observed at Station 4.

Overall, we show that dust acted as the main driver of the surface Fe distribution with far-reaching effects on the underlying water column, while sediment resuspension and hydrothermalism were important in the abyss. Scavenging was the major sink. Our main finding is that the cFe distribution results in an "hourglass" pattern with depth. This is due to the decoupling of cFe and sFe, where the major sources and sinks of dFe

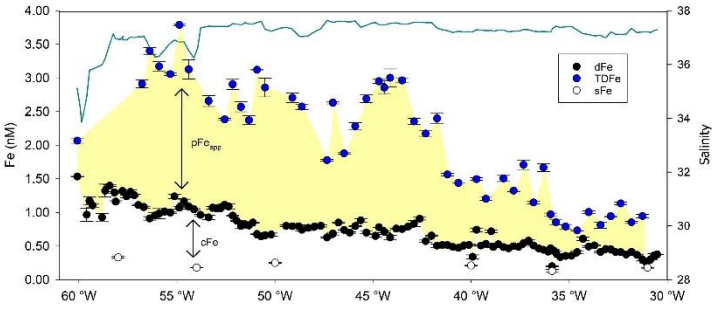

Figure 3. Surface concentrations of dFe (black), sFe (white), TDFe (blue), and salinity (cyan line) against longitude along the cruise track. The calculated concentrations of cFe and pFe_{app} are indicated with arrows. The dFe and TDFe concentrations are from the underway samples (<5 m); the sFe concentrations are from the shallowest water column samples (between 15 and 25 m) at each station. Error bars show one standard deviation of the mean concentration of three analytical replicates.

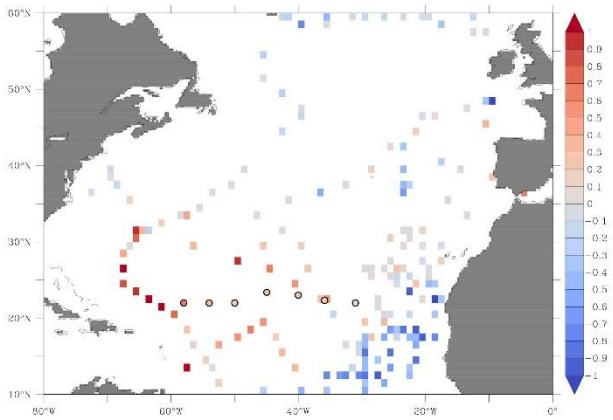

Figure 4. Surface plot of the North Atlantic showing the difference of dFe concentration averaged over 0 to 50 m depth minus the concentration averaged over 100 to 150 m depth in a 1° x 1° grid. Red values show higher concentrations in surface than at depth, a typical dust-driven behaviour. Blue values show lower concentrations in the surface than at depth, a typical nutrient-like behavior. Circles indicate JC150 stations. Data from Tagliabue et al. (2012) and augmented with data from the GEOTRACES Intermediate Data Product 2017 (Schlitzer et al., 2018).

result in increases or decreases of the cFe budget, with large ranges in both the surface ocean and close to the seafloor.

The current understanding of the partitioning between cFe and sFe for regulating the dFe distribution stems from the pioneering work done by Bergquist et al. (2007) and more recently by Fitzsimmons, Carrasco, et al. (2015), the latter of which indicated an equal control between cFe and sFe, given the evidence for a more dynamic soluble phase compared to Bergquist et al.'s (2007) conclusions that colloids alone accounted for the observed partitioning. Based on our colloidal Fe data, we argue it is a balance of both of these mechanisms depending on the presence or absence of external drivers at different depths. Where dFe is supplied or removed, the colloidal and soluble phases were strongly decoupled with cFe taking on a greater regulatory control for the dFe distribution and shaping the wide top and bottom sections of the hourglass. In the interior ocean away from external sources or sinks, the dFe partitioning was balanced between cFe and sFe in a steady-state equilibrium, which formed the neck of the hourglass.

3.2. Distribution of Soluble and Colloidal Iron

3.2.1. The Dusty Surface Ocean

The JC150 transect underlies the northern extent of the Saharan dust plume that provides approximately 200 Tg yr^{-1} of dust to the North Atlantic (Jickells et al., 2005). Dust deposition from Sahara-influenced air masses regulates the Fe budget in the surface North Atlantic via aerosol solubilization (Sedwick et al., 2005; Ussher et al., 2013) and is overwhelmingly the largest flux of Fe to this region (Ussher et al., 2013).

Our surface sampling revealed a longitudinal decrease of surface dFe concentrations from west to east, with a maximum of 1.53 nM at 60 °W and a minimum of 0.26 nM at 31 °W (Figure 3). Concentrations >0.5 nM are typical for the dust-dominated North Atlantic (Fitzsimmons, Carrasco, et al., 2015; Hatta et al., 2015; Measures et al., 2008; Sedwick et al., 2005), which contrast with concentrations of <0.25 nM for the dust-limited South Atlantic, Pacific, and Southern Ocean (Buck et al., 2017; Chever et al., 2010; Fitzsimmons et al., 2015; Nishioka et al., 2001). The west-east gradient we observed appeared counterintuitive with regard to the location of the Saharan source. However, it was consistent with a compilation of upper ocean dFe data from the North Atlantic (Figure 4), where Fe profiles appeared more influenced by dust in the west compared to the east. This is because large amounts of dust are entrained into the warm Saharan Air Layer (SAL), which is trapped at altitudes above the dust-free northeasterly trade wind inversion and exported

Global Biogeochemical Cycles 10.1029/2019GB006326

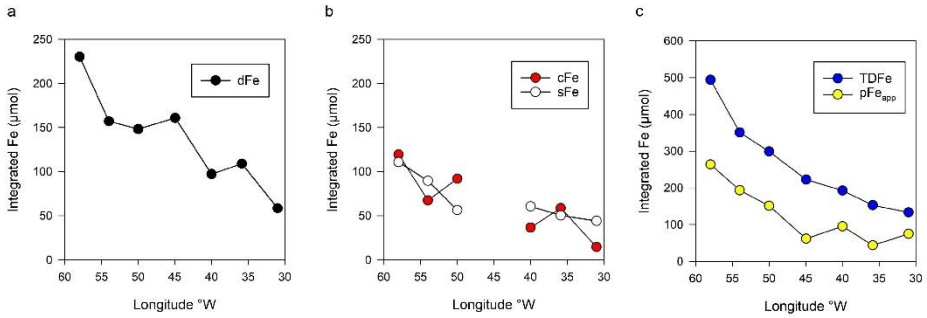

Figure 5. The integrated upper ocean Fe inventories of (a) dFe (black), (b) sFe (white) and cFe (red), and (c) TDFe (blue) and pFe_{app} (yellow). Station 4 at 45 °W has been excluded for sFe and cFe due to the lack of data points.

westward with the strong circulation of the Azores-Bermuda High during summer (Schepanski et al., 2009; Tsamalis et al., 2013). As the SAL descends westward, the dust increasingly mixes into the marine boundary layer where it seeds the surface ocean (Tsamalis et al., 2013), thereby imprinting the longitudinal gradient of dust-derived Fe that we observed. Previous investigations into atmospherically derived Fe at the Bermuda Atlantic Time-series Study confirm a large Saharan dust source during summer (Fishwick et al., 2014; Sedwick et al., 2005).

Accompanying measurements of TDFe displayed a similar trend to dFe, decreasing from >3 nM in the west to <1 nM in the east, but with larger variability than dFe (Figure 3). The dFe/pFe_{app} ratio was 0.57 ± 0.25 for the entire transect except for the most western sample at 60 °W. Here, the pFe_{app} concentration was only 0.53 nM, and the dFe concentration was 1.53 nM, resulting in a dFe/pFe_{app} ratio of 2.87 in stark contrast to the remaining transect, and suggesting a lower influence of dust deposition at this location. The surface samples west of 58 °W (Station 1) were collected at lower latitudes (17.5 to 21.6 °N) than the remaining transect (≥22 °N) (Figure 1), where the lower salinities (34 to 36) (Figure 3) indicate the northern boundary of the seasonal Amazon and Orinoco River plumes (Fournier et al., 2015). Rijkenberg et al. (2014) showed a strong linear inverse correlation between dFe and salinity during summer 2013. Hence, the elevated dFe concentrations in the surface samples approaching Station 1 possibly originated from the river plume which may have lost pFe_{app} relative to dFe during the seaward transport and mixing with seawater.

The concentrations of sFe from the shallowest depth from the CTD averaged 0.19 ± 0.05 nM across the transect. Importantly, they displayed no west-to-east gradient, in contrast to the basin-scale distributions of the other Fe size fractions, and appeared to be independent of the magnitude of dFe and pFe_{app} inputs. The average excludes the slightly elevated sFe concentration of 0.33 nM at 58 °W (Station 1), which was possibly an artifact of the Amazon and Orinoco River plumes.

What processes might be responsible for such small variation in the surface sFe concentrations? Potential biogeochemical controls include Fe-binding ligand distributions, a threshold for dust-derived Fe dissolution into the soluble phase or a dilution threshold beyond which sFe is unreactive. The two size-fractionated ligand studies available concluded that ligand distributions cannot account for size-fractionated Fe distributions alone (Cullen et al., 2006; Fitzsimmons et al., 2015). Moreover, surface sFe concentrations higher (Ussher et al., 2013) or lower (Chever et al., 2010) than our ~0.2 nM have been observed previously and render the threshold arguments unlikely. Alternatively, the resolution of our surface sFe data alongside the small variations in the concentrations may prevent the identification of a potential gradient for sFe and its biogeochemical controls.

Regardless, the subtlety of the changes in the surface sFe concentrations implies that cFe was the driver of the gradient in dFe concentrations in surface waters across the subtropical North Atlantic. The colloidal contributions to the dFe pool were highest where dFe and TDFe concentrations were elevated as a result of dust

input (and riverine input at Station 1), with values of 61% to 85% cFe for dFe concentrations of 0.53 to 1.25 nM between Stations 1 and 6. The maximum colloidal contribution of 85% cFe for a dFe concentration of 0.77 nM was observed at Station 3. In contrast, only 32% of dFe was in the colloidal form at Station 7 where the dFe concentration was lowest (0.27 nM). While the high surface cFe fractions of >60% were consistent with previous studies in the dust-dominated North Atlantic (Fitzsimmons & Boyle, 2014; Fitzsimmons, Carrasco, et al., 2015; Sedwick et al., 2005; Ussher et al., 2010), the absence of a surface colloidal maximum at Station 7 is rather atypical of observations from the North Atlantic and resembled the dust-limited surface waters of the Pacific (Fitzsimmons, Hayes, et al., 2015; Nishioka et al., 2001). The tight coupling of TDFe, dFe, and cFe trends across the basin suggests that higher Fe in the particulate phase results in more dFe via cFe, and hence particles have an important influence on the dFe size partitioning. These links were similarly evident in the size-fractionated Fe data sets when plotting the top 50 m of the US-GEOTRACES GA03 section, just north of our transect (Fitzsimmons, Carrasco, et al., 2015; Lam, 2018; Schlitzer et al., 2018; Twining, 2014).

Seawater leaches of aerosol particles showed that dust-derived dFe is predominantly retained as cFe in the ocean, either as eroded fragments or due to the authigenic formation of colloidal-sized Fe-oxyhydroxides or organic complexes (Fishwick et al., 2014), which explains the observed colloidal maxima in the high dFe-surface waters. Dust deposition is at its minimum in the eastern subtropical North Atlantic during summer because of the high-altitude transport of the SAL and the resulting deposition in the west. Hence, the unusually low colloidal fraction at Station 7 likely resulted from sampling this seasonal extreme. This is an important insight because the North Atlantic is often characterized in bulk as a high dust and high Fe region (Moore et al., 2009), but our results demonstrate the sensitivity of the Fe inventory to strong regional and seasonal variability within the subtropical North Atlantic. This sensitivity resulted in two endmembers along our section: A high dust endmember with a high colloidal contribution to dFe and a low dust endmember with a low colloidal contribution to dFe.

While the instantaneous effect of dust deposition in the immediate surface is on cFe, a dust-driven effect for sFe is apparent when considering the entire upper water column (using integrated Fe inventories). Increasing the sampling resolution enables us to detect impacts on the surface water column after the dust-derived Fe had the chance to undergo internal cycling. Dissolved Fe, cFe, and pFe_{app} inventories were higher in the west than in the east, following a similar gradual longitudinal decrease as in the immediate surface (Figure 5), confirming that dust affects the underlying layers too. Surprisingly, the sFe budget also decreased clearly from west to east, a trend not apparent in the immediate surface (Figure 3). An important caveat is that the shoaling of the isopycnals toward the west lowers the integrated budgets. However, depth-normalized integrated Fe budgets portray the same overall longitudinal trends for all size fractions. A possible mechanism driving the higher sFe in the upper ocean in the west versus the east is the indirect source from dust, by which Fe is partially mobilized from the colloidal into the soluble phase via ligands as suggested by aerosol-leaching experiments (Fishwick et al., 2014). This transformation could increase the bioavailable portion of dFe.

3.2.2. Iron Depletion Through the Euphotic Zone

Deep Chl-*a* maxima are a widespread phenomenon in the subsurface of the (sub)tropical oceans and positioned across the nutriclines, where macronutrient supply from deeper waters sustains low light-adapted primary production (Cullen, 2015). The upper water column distributions of macronutrients and Fe are decoupled due to greater remineralization length scales of Fe (Boyd et al., 2017). Consequently, the DCM can become Fe limited (Sunda & Huntsman, 1997). At most of our stations, the dFe concentration gradually decreased through the euphotic zone toward the DCM, often reaching minima between 60 and 200 m, where Chl-*a* peaked (Figures 6a–6g). Moreover, there was a gradual transition from the strongly dust-driven dFe profiles at Stations 1 and 2, where the difference between surface maxima and DCM minima was largest, to the more nutrient-like profile at Station 7 (Figures 6a–6g). These two endmembers resulted from the dust-driven surface dFe distribution (Figure 3) and appear to be characteristic of the western and eastern North Atlantic, respectively (Figure 4).

The attenuation of the dFe signal between the surface and the DCM was clearly controlled by the attenuation of cFe, which typically decreased to <30% of dFe in the DCM (Figures 6a–6g) or even disappeared completely, which was most pronounced at Station 5. Concentrations of sFe were less variable between surface and DCM with slight increases observed in the center (Station 5) or on the slopes (Stations 2 and 4) of the

Global Biogeochemical Cycles 10.1029/2019GB006326

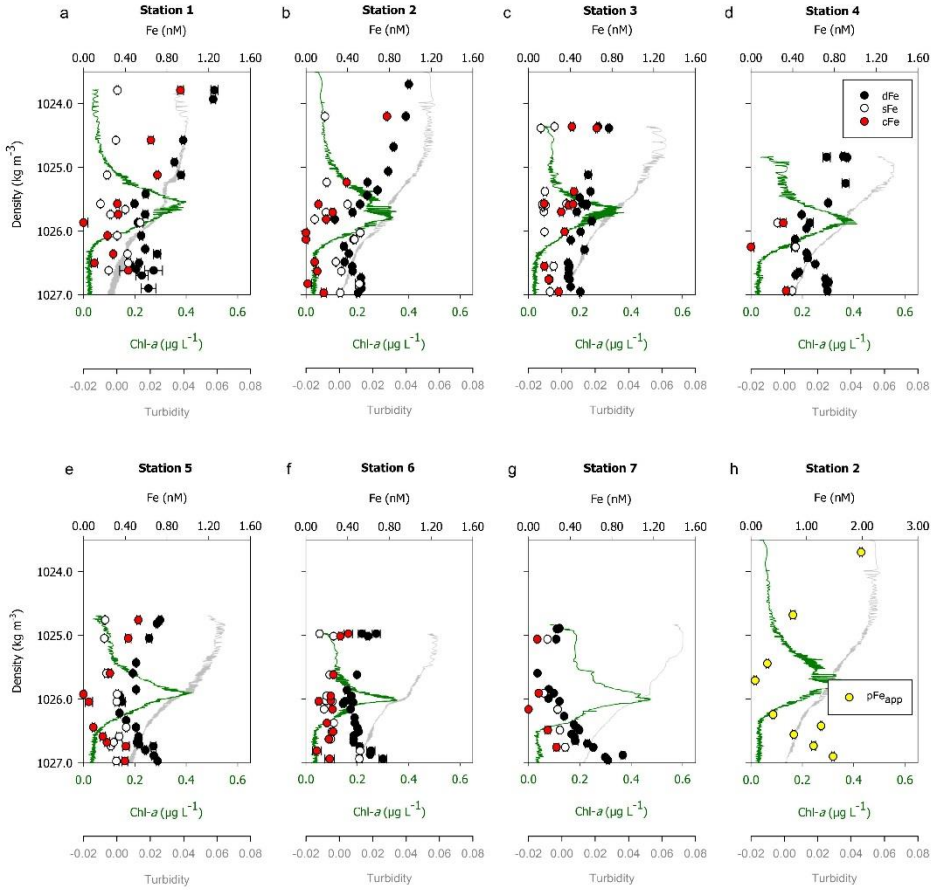

Figure 6. (a–g) Profiles of dFe (black), sFe (white), and cFe (red) against density in the upper water column at each station. (h) Representative profile of pFe_{app} (yellow) against density at Station 2. Error bars show one standard deviation of the mean concentration of three analytical replicates. For the calculated cFe and pFe_{app} concentrations, associated measurement errors were propagated. Traces of Chl-a (green lines) and turbidity (gray lines, arbitrary units) are included.

DCM, where it accounted for up to 100% of dFe. These characteristics are in line with previous observations from the DCM of the Atlantic (Fitzsimmons, Carrasco, et al., 2015) and Pacific (Fitzsimmons, Hayes, et al., 2015). In other words, cFe was removed over sFe in the euphotic zone despite the widespread understanding that sFe is more bioavailable (Birchill et al., 2017). This leads to the question: Does the gradual depletion of dFe via cFe through the euphotic zone mark a biological preference for cFe over sFe, or does scavenging control the observed Fe distribution?

It is possible that the elevated Fe demands of the DCM community (Hogle et al., 2018; Sunda & Huntsman, 1997) force the utilization of the cFe pool, for example, via a ligand-mediated transfer into the soluble phase prior to uptake (Chen & Wang, 2001; Wang & Dei, 2003). If the uptake is time lagged from the transfer between phases, cFe would be depleted, and (ligand bound) sFe would accumulate, which matches the

observations in many of our depth profiles. However, the few size-fractionated ligand studies concluded that ligand distributions alone cannot account for the observed Fe distributions (Cullen et al., 2006; Fitzsimmons, Bundy, et al., 2015), while Fitzsimmons, Bundy, et al. (2015) found no increase in soluble-sized ligand production in the DCM. In addition, cFe and Chl-*a* were not strongly negatively correlated ($R^2 = -0.27$, surface to 1026.5 kg m^{-3}), which would reflect biological uptake, and we did not observe an enrichment in pFe_{app}, which would capture the cellular Fe pool.

Instead, we observed simultaneous minima of pFe_{app} and cFe in the DCM (Figure 6h and Figure S1) and a stronger positive correlation of cFe with turbidity as an indicator of particle abundance ($R^2 = 0.48$). This strengthens the argument that cFe is not simply transferred from the dissolved to the particulate phase, but both phases are removed together, leading us (and others: Ohnemus & Lam, 2015) to conclude that dFe (in form of cFe) is shuttled out of euphotic zone via sinking particles and that this scavenging is a principal mechanism driving the distributions of cFe, dFe, and pFe_{app} here. Biological uptake appears to be a minor contributor to the removal of dFe (cFe) but may be important in maintaining sFe levels via the replenishment from other Fe fractions.

Despite the likely co-occurrence of these different processes, our size-fractionated measurements identified the preferential removal of cFe, not sFe, alongside pFe_{app} and, hence, the potential importance of particle scavenging over biological uptake for the removal of Fe. The increasing resolution of size-fractionated Fe measurements repeatedly confirm the cFe minima in the DCM as an intriguing phenomenon of the subtropical ocean which warrants further investigations, as highlighted in a recent review by Anderson (2020), because the central implication of these minima is that despite large Fe-rich dust depositions, the efficient removal of dFe leads to a potential Fe limitation in the DCM.

3.2.3. The Mesopelagic: Mirroring the Surface Ocean

It is a long-standing paradigm that the distributions of major nutrients below the euphotic zone are shaped by the balance between a preformed and a regenerated component, which are the result of physical transport and the microbial degradation of organic matter (remineralization), respectively. Nutrients released by remineralization can sustain a major fraction of primary production when resupplied into the surface. Unlike the macronutrients, Fe is subjected to additional processes, such as scavenging, that affect its subsurface inventory (Hatta et al., 2015; Tagliabue, Williams, et al., 2014; Twining et al., 2015). AOU provides a measure of remineralization at depth, which is the result of local remineralization that acts on sinking biogenic particles and of the transport of aging water masses. We observed a zone of lower O_2 concentrations (120 to 150 μM) and elevated dFe concentrations (0.7 to 1.0 nM) between 400 to 1100 m depth (Figure 2 and Figure S2). The dFe/C ratio along the oxycline was 5.8 ± 0.50 μmol mol^{-1} ($R^2 = 0.58$, n = 100), which was within the range of ratios previously reported for the North Atlantic (Fitzsimmons, Carrasco, et al., 2015; Hatta et al., 2015; Milne et al., 2017) but lower than cellular ratios in phytoplankton of 33 to 57 μmol mol^{-1} (Twining et al., 2015), which demonstrates the impact of scavenging as a post-remineralization sink. Microbial recycling also occurs throughout the upper ocean, but O_2 concentrations are in equilibrium with the atmosphere, and hence AOU cannot function as a measure of remineralization.

In contrast to the biogenic-dominated macronutrients, the majority of Fe-bearing particles in our study region is lithogenic. Boyd et al. (2010) showed that the dissolution of Fe from lithogenic particles dominates over the release from biogenic material in the North Atlantic. Furthermore, Fe isotope measurements revealed that the entire water column may be impacted by dust (Conway & John, 2014). If the mesopelagic dFe inventory is driven by the release from lithogenic particles, it leads to the hypothesis that the dominance of cFe over sFe may be observed at depth because dust-derived Fe occurs predominantly as cFe. Within our sample subset around the AOU maximum, the dFe size partitioning was $37 \pm 16\%$ cFe, but a global comparison of published size-fractionated dFe data from the mesopelagic enables us to probe this theory (Figure 7). Regions of high annual dust flux (6.2 to 22.6 g m^{-2} yr^{-1}) display higher mean cFe contributions of 60% to 48% of dFe, respectively. In contrast, regions of lower dust flux (1.0 to 5.1 g m^{-2} yr^{-1}) exhibit lower mean cFe contributions of 39% to 42% of dFe. At dust fluxes of <0.3 g m^{-2} yr^{-1}, the cFe contributions are lowest with 35% of dFe. This pattern of high colloidal fractions in the mesopelagic at high dust in contrast to low colloidal fractions at low dust is analogous to the surface ocean, where colloidal maxima are present in regions of high dust (this study; Fitzsimmons, Carrasco, et al., 2015) and absent in dust-limited regions (Nishioka et al., 2001). The reason colloidal fractions from high dust regions are not as high in the mesopelagic compared

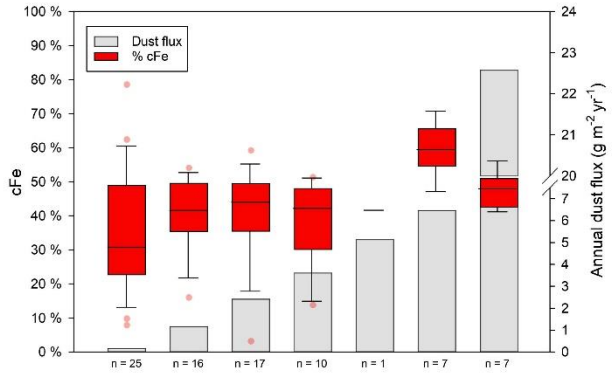

Figure 7. Box plots of the partitioning of dFe into the colloidal fraction (red bars) at remineralization depths of different oceanic regions, in order of increasing annual dust flux (gray) from left to right. Boxes represent the interquartile range; the middle line represents the median. Whiskers frame the 10th and 90th percentiles, while data points outside this range are shown as dots. The cFe data used in this plot were compiled from the present study and from Nishioka et al. (2001, 2013), Fitzsimmons, Carrasco, et al. (2015), Fitzsimmons, Hayes, et al. (2015), Bergquist et al. (2007), Ussher et al. (2010), and Chever et al. (2010), and binned by dust flux (see methods). Along the x-axis, n indicates the number of cFe measurements for each bin. For details on which data contributed to which bin, the reader is referred to Table S1.

to the surface (61% to 85%) may be explained by the two-step model of Fishwick et al. (2014), in which some cFe is transferred into the soluble phase over time. Furthermore, a portion of the released cFe is likely rescavenged. The tug-of-war between these mechanisms is eventually manifested in the 37 ± 16% cFe that we observed.

The main result of this global comparison is a strong coupling between the speciation of dFe in the mesopelagic and the surface dust deposition. The implication is that the spatial variability of subsurface dFe distributions is driven by regional dust flux. This highlights the sensitivity of the Fe cycle to changes in atmospheric supply, especially in the light of past and future changes. Therefore, constraining the mesopelagic Fe cycling as a major pathway for the resupply to the surface requires the investigation of cFe specifically rather than bulk dFe.

3.2.4. The Deep Iron Inventory: Hydrothermalism and Seafloor-Sediment Interactions

While atmospheric deposition provides the largest input of Fe to the surface North Atlantic, modeling efforts showed that sedimentary release and hydrothermal venting prevail globally by at least one order of magnitude (Tagliabue et al., 2010; Tagliabue, Aumont, & Bopp, 2014). The JC150 transect captured the influence of both of these sources on the deep Fe inventory.

Station 4 targeted the Snakepit hydrothermal vent field located around 3500 m depth on the Mid-Atlantic ridge (Beaulieu, 2015). Anomalies in the turbidity confirm that we sampled the neutrally buoyant hydrothermal plume with a dFe concentration maximum of 27 nM at 3300 m (Figure 8). Hydrothermally derived Fe can overcome near-field precipitation and be transported over large distances (>1000 km) (Resing et al., 2015; Saito et al., 2013) via its stabilisation either by organic complexes (Sander & Koschinsky, 2011) or in colloidal-sized nanoparticles (Revels et al., 2015; Yücel et al., 2011). Our plume dFe samples were composed of 92 ± 3% (n = 4) cFe, similar to the 89% to 96% cFe in the plume of the nearby Trans-Atlantic Geotraverse vent field (Fitzsimmons, Carrasco, et al., 2015).

Apart from its role as an important source of Fe, the Mid-Atlantic ridge also acts as a physical barrier between the eastern and western abysses. The physical speciation measurements of Fe revealed opposing trends on either side of the ridge. In the west, we observed elevated pFe_{app} concentrations of 6.4 nM at 5400 m at Station 1 and 4.0 nM at 5900 m at Station 2, compared to ≤2.0 nM for all other stations (data not shown). No equivalent increase in dFe concentrations was observed (Figure 2), and the two deepest

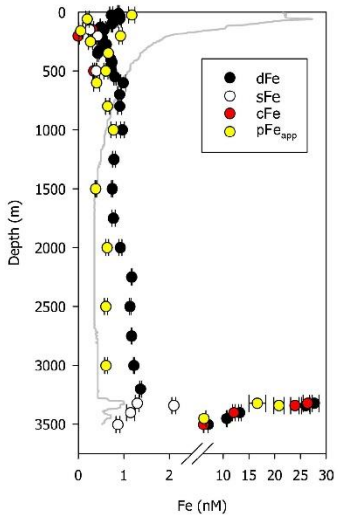

Figure 8. Full-depth profile of dFe (black), sFe (white), cFe (red), and pFe_{app} (yellow) concentrations against depth at Station 4, located over the Mid-Atlantic Ridge. The turbidity trace (gray line) indicates the presence of the hydrothermal plume between 3300 m and 3500 m depth. Note the scale break for concentrations >2.5 nM. Error bars show one standard deviation of the mean concentration of three analytical replicates. For the calculated cFe and pFe_{app} concentrations, associated measurement errors were propagated.

samples collected at 50 and 20 m above the seafloor decreased by 0.13 and 0.09 nM at Station 1 and 2, respectively. The cFe contributed only 26% and 29% to the dFe budget, lower than values from the overlying water column. In the east, this pattern was reversed. At Station 5, dFe concentrations reached 1.26 nM at 20 m above the seafloor with a cFe fraction of 76%, and at Station 7, 63% of dFe was in the colloidal form although no simultaneous increase in the dFe concentration was detected. Gardner et al. (2017) showed that thick benthic nepheloid layers form in the western North Atlantic, and Lam et al. (2015) and Revels et al. (2015) reported higher lithogenic and Fe-rich particle abundances in this area, which is evident in our pFe_{app} measurements. The large surface area and high concentration of the resuspended particles hold high scavenging potential, so that the scavenging of dFe in the form of cFe onto sedimentary particles may dominate over dissolution and produce a cFe signature of <50% alongside decreased dFe concentrations. In contrast, dissolution dominates over scavenging in the east, which drives cFe contributions >50% and increase the dFe inventory.

The background dFe concentration in the ocean interior (>1027.50 kg m^{-3} and above ocean-sediment interface) away from any external or internal sources or sinks was 0.67 ± 0.14 nM, excluding the hydrothermal Station 4. Slightly higher dFe concentrations were observed in the interior of the western basin compared to the eastern basin (Figure 2), which appears to be a persistent feature in the North Atlantic (Fitzsimmons, Carrasco, et al., 2015; Hatta et al., 2015) and may be the result of different water masses and currents on either side of the ridge. Our Station 6 crossed over with Station USGT11-20 of the US-GEOTRACES section GA03 (Boyle et al., 2015), showing close agreement (Figure S3) and demonstrating the relatively constant dFe distribution in the deep ocean. Dissolved Fe in the ocean interior was partitioned into 49 ± 14% cFe, in agreement with the previously reported 50:50% partitioning for this region (Fitzsimmons, Carrasco, et al., 2015). This balanced distribution of cFe and sFe was proposed to result from a steady-state equilibrium between cFe and sFe (Fitzsimmons, Carrasco, et al., 2015), and our results are in line with this hypothesis.

4. Synthesis: The Colloidal Hourglass

We quantified the partitioning of dFe into soluble and colloidal phases in the subtropical North Atlantic to address the underlying questions regarding how sFe and cFe contribute to and regulate the dFe distribution. We found that the cFe contribution to the dFe pool produced an hourglass shape against depth that arises from the dominant variability of cFe over sFe (Figure 9). Our results show that cFe is the main source of dFe to the water column via the dissolution of particles and also the main sink via scavenging. In other words, whenever dFe is introduced or removed, it is the cFe that is driving these changes. This result reinforces the idea that cFe holds a pivotal role in the oceanic Fe cycle and that it may be a crucial component for improving Fe models.

The dynamic upper ocean encompasses a range of sources and sinks that led to a large range of colloidal fractions between the surface and ~1100 m (0% to 86% of dFe) (Figure 9). In the near surface, elevated cFe contributions of 61% to 85% coincident with high dFe concentrations were the result of dust supply. Throughout the euphotic zone, cFe decreased to 0% to 30% through its preferential scavenging onto sinking particles. Loss of cFe to the sFe phase and subsequent biological uptake further contributed to the removal of cFe in the DCM. Our hourglass figure highlights that on a small vertical scale (from surface to DCM), the change in dFe (cFe) is large, especially where the surface maximum is strong, and the implication is that despite large surface inputs, Fe limitation in the DCM is possible. In the dust-

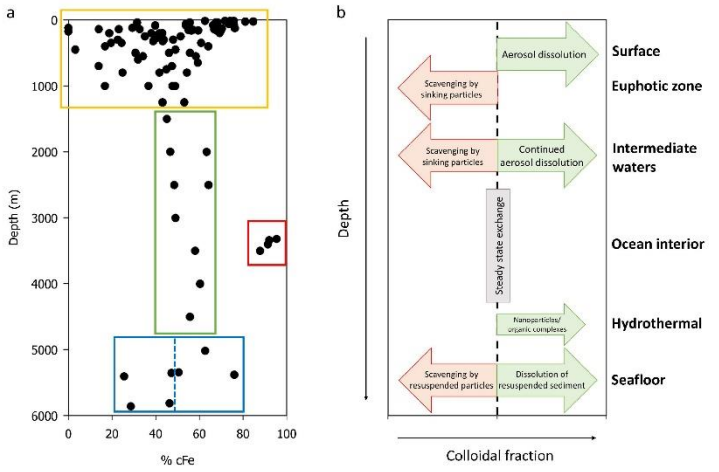

Figure 9. (a) The partitioning of dFe into the colloidal fraction against depth of the entire data set, forming an hourglass shape. The coloured boxes distinguish between the highly variable upper water column (yellow) and seafloor-water interface (blue, dotted blue line distinguishes between western and eastern basin), the narrow range of the deep ocean interior (green), and the hydrothermal signature (red). (b) Conceptual model of the dominant processes throughout the water column that drive the partitioning of the sFe and cFe away from the steady-state exchange of the ocean interior. Processes increasing and decreasing the colloidal fraction are highlighted in green and red, respectively.

loaded subtropical North Atlantic, the vast majority of the sinking particles is lithogenic and dominates the release of Fe over biogenic particles even at depths of remineralization (Boyd et al., 2010). Here, we observed a tug-of-war between the continued leaching of Fe from lithogenics that increases cFe and competing mechanisms that act to remove cFe efficiently. This balance resulted in a colloidal contribution of 37 ± 16% of dFe that we observed. These competing mechanisms include the immediate rescavenging and aggregation of released cFe associated with particles (both lithogenic and biogenic) and the disaggregation of cFe into sFe. A global comparison showed that the lithogenic nature of dust particles determines the cFe fraction in the mesopelagic, with lower dust fluxes resulting in lower colloidal fractions and vice versa.

At the ocean-seafloor boundary, cFe ranged widely from 26% to 76% of dFe (Figure 9). We observed a west-to-east difference with the lower cFe contributions in the west (26% to 47%) and the higher cFe contributions in the east (52% to 76%), due to regional differences in benthic nepheloid layers.

The narrow range of colloidal fractions in the ocean interior formed the neck of the hourglass, where the partitioning into sFe and cFe falls into a balanced distribution of 1:1 (49 ± 14% cFe of dFe), as the result of a steady-state exchange between the fractions. The near-vent hydrothermal signal of almost 100% cFe is a clear exception.

Our study indicates that cFe predominantly drives the overall surface-to-seafloor dFe distribution in the subtropical North Atlantic. Colloidal Fe and dFe are reasonably well correlated ($R^2_{cFe:dFe} = 0.61$, $n = 95$), while the correlation between sFe and dFe is weak ($R^2_{sFe:dFe} = 0.14$, $n = 95$), excluding hydrothermal samples. In the ocean interior, our data is consistent with Fitzsimmons, Carrasco, et al.'s (2015) model where dFe partitions equally into sFe and cFe (~40% to 60%). An important caveat is that the resolution of our measurements is lower than Fitzsimmons, Carrasco, et al.'s (2015) model and the concentrations of the different Fe fractions fall into a narrower range in our data set. Regardless, a similar "colloidal hourglass" shape is observed with the larger data set by Fitzsimmons, Carrasco, et al. (2015) (Figure S4).

5. Conclusions

Despite the dramatic increase of oceanic dFe measurements in the past decade, biogeochemical models struggle to constrain fundamental parameters of the Fe cycle such as scavenging rates and residence times. The physical speciation of Fe is less well resolved than the bulk dissolved phase, but it bears the potential to illuminate some of these uncertainties. Our data set of size-fractionated Fe from the subtropical North Atlantic demonstrates the pivotal role of cFe, the larger-sized species in the dFe continuum, for controlling the distribution of dFe. We found that cFe is the predominantly active species in key supply and removal processes of dFe compared with the smaller sFe which showed a more constant behavior. Moreover, a global compilation of colloidal data allowed us to detect a sensitive dust-driven linkage between surface and mesopelagic dFe inventories which would have been concealed by making dissolved measurements only. Currently, the important role of cFe is not represented in models. Hence, advancing our understanding of the oceanic Fe cycle demands the extension of size-fractionated measurements at a global scale and the incorporation of an explicit cFe term in models.

Author Contributions

MCL, CM, and AT acquired the funding; MCL and CM supervised the research cruise. KK, NJW, DGS, and MCL collected the samples at sea. KK conducted the Fe measurements and wrote the paper with significant contributions from MCL, NJW, DSG, AT, and CM.

Acknowledgments
The authors thank the captain, crew, and scientific party of the *RRS James Cook* during cruise JC150 and two anonymous reviewers for their constructive feedback on an earlier version of the paper. This work was funded by the Graduate School of the National Oceanography Centre Southampton (KK) and UK Natural Environment Research Council grants NE/N001125/1 (MCL) and NE/N001079/1 (CM, AT). The data of this study are publicly available from the British Oceanographic Data Centre under doi:10/c63f.

References

Albani, S., Mahowald, N. M., Murphy, L. N., Raiswell, R., Moore, J. K., Anderson, R. F., et al. (2016). Paleodust variability since the Last Glacial Maximum and implications for iron inputs to the ocean. *Geophysical Research Letters, 43*, 3944–3954. https://doi.org/10.1002/2016gl067911

Anderson, R. F. (2020). GEOTRACES: Accelerating research on the marine biogeochemical cycles of trace elements and their isotopes. *Annual Review of Marine Science, 12*(9), 9.1–9.37. https://doi.org/10.2138/gselements.14.6.377

Beaulieu, S. E. (2015). InterRidge Global Database of active submarine hydrothermal vent fields: Prepared for InterRidge, Version 3.3. Retrieved from http://vents-data.interridge.org

Bergquist, B. A., Wu, J., & Boyle, E. A. (2007). Variability in oceanic dissolved iron is dominated by the colloidal fraction. *Geochimica et Cosmochimica Acta, 71*(12), 2960–2974. https://doi.org/10.1016/j.gca.2007.03.013

Birchill, A. J., Milne, A., Woodward, E. M. S., Harris, C., Annett, A., Rusiecka, D., et al. (2017). Seasonal iron depletion in temperate shelf seas. *Geophysical Research Letters, 44*, 8987–8996. https://doi.org/10.1002/2017GL073881

Boyd, P. W., Ibisanmi, E., Sander, S. G., Hunter, K. A., & Jackson, G. A. (2010). Remineralization of upper ocean particles: Implications for iron biogeochemistry. *Limnology and Oceanography, 55*(3), 1271–1288. https://doi.org/10.4319/lo.2010.55.3.1271

Boyd, P. W., Ellwood, M. J., Tagliabue, A., & Twining, B. S. (2017). Biotic and abiotic retention, recycling and remineralization of metals in the ocean. *Nature Geoscience, 10*(3), 167–173. https://doi.org/10.1038/ngeo2876

Boyle, E. A., Anderson, R. F., Cutter, G. a., Fine, R., Jenkins, W. J., & Saito, M. A. (2015). Introduction to the U.S. GEOTRACES North Atlantic Transect (GA-03): USGT10 and USGT11 cruises. *Deep Sea Research Part II, 116*, 1–5. https://doi.org/10.1016/j.dsr2.2015.02.031

Bruland, K. W., & Lohan, M. C. (2004). The control of trace metals in seawater. In J. P. Riley, & R. Chester (Eds.), *Chemical Oceanography*, (2nd ed., Vol. 6, pp. 157–220). New York: Academic Press.

Buck, K. N., Sedwick, P. N., Sohst, B., & Carlson, C. A. (2017). Organic complexation of iron in the eastern tropical South Pacific: Results from US GEOTRACES Eastern Pacific Zonal Transect (GEOTRACES cruise GP16). *Marine Chemistry, 201*, 229–241. https://doi.org/10.1016/j.marchem.2017.11.007

Carritt, D. E., & Carpenter, J. H. (1966). Comparison and evaluation of currently employed modifications of the Winkler method for determining dissolved oxygen in seawater: A NASCO Report. *Journal of Marine Research, 24*, 286–318.

Chen, M., & Wang, W. (2001). Bioavailability of natural colloid-bound iron to marine plankton: Influences of colloidal size and aging. *Limnology and Oceanography, 46*(8), 1956–1967. https://doi.org/10.4319/lo.2001.46.8.1956

Chever, F., Bucciarelli, E., Sarthou, G., Speich, S., Arhan, M., Penven, P., & Tagliabue, A. (2010). Physical speciation of iron in the Atlantic sector of the Southern Ocean along a transect from the subtropical domain to the Weddell Sea Gyre. *Journal of Geophysical Research, 115*, C10059. https://doi.org/10.1029/2009JC005880

Conway, T. M., & John, S. G. (2014). Quantification of dissolved iron sources to the North Atlantic Ocean. *Nature, 511*(7508), 212–215. https://doi.org/10.1038/nature13482

Cullen, J., Bergquist, B., & Moffett, J. W. (2006). Thermodynamic characterization of the partitioning of iron between soluble and colloidal species in the Atlantic Ocean. *Marine Chemistry, 98*(2–4), 295–303. https://doi.org/10.1016/J.MARCHEM.2005.10.007

Cullen, J. J. (2015). Subsurface chlorophyll maximum layers: Enduring enigma or mystery solved? *Annual Review of Marine Science, 7*(1), 207–239. https://doi.org/10.1146/annurev-marine-010213-135111

de Boyer Montégut, C., Madec, G., Fischer, A. S., Lazar, A., & Iudicone, D. (2004). Mixed layer depth over the global ocean: An examination of profile data and a profile-based climatology. *Journal of Geophysical Research, 109*, C12003. https://doi.org/10.1029/2004JC002378

Falkowski, P. G. (1997). Evolution of the nitrogen cycle and its influence on the biological sequestration of CO2 in the ocean. *Nature, 387*(6630), 272–275. https://doi.org/10.1038/387272a0

Fishwick, M. P., Sedwick, P. N., Lohan, M. C., Worsfold, P. J., Buck, K. N., Church, T. M., & Ussher, S. J. (2014). The impact of changing surface ocean conditions on the dissolution of aerosol iron. *Global Biogeochemical Cycles, 28*, 1235–1250. https://doi.org/10.1002/2014GB004921

Obata, H., Karatani, H., Matsui, M., & Nakayama, E. (1997). Fundamental studies for chemical speciation of iron in seawater with an improved analytical method. *Marine Chemistry*, *56*(1–2), 97–106. https://doi.org/10.1016/S0304-4203(96)00082-5

Ohnemus, D. C., & Lam, P. J. (2015). Cycling of lithogenic marine particles in the US GEOTRACES North Atlantic transect. *Deep-Sea Research Part II: Topical Studies in Oceanography*, *116*, 283–302. https://doi.org/10.1016/j.dsr2.2014.11.019

Resing, J. A., Sedwick, P. N., German, C. R., & Jenkins, W. J. (2015). Basin-scale transport of hydrothermal dissolved metals across the South Pacific Ocean. *Nature*, *523*(7559), 200–203. https://doi.org/10.1038/nature14577

Revels, B. N., Ohnemus, D. C., Lam, P. J., Conway, T. M., & John, S. G. (2015). The isotopic signature and distribution of particulate iron in the North Atlantic Ocean. *Deep-Sea Research Part II: Topical Studies in Oceanography*, *116*, 321–331. https://doi.org/10.1016/j.dsr2.2014.12.004

Rijkenberg, M. J. A., Middag, R., Laan, P., Gerringa, L. J. A., van Aken, H. M., Schoemann, V., et al. (2014). The distribution of dissolved iron in the West Atlantic Ocean. *PLoS ONE*, *9*(6). https://doi.org/10.1371/journal.pone.0101323

Saito, M. A., Noble, A. E., Tagliabue, A., Goepfert, T. J., Lamborg, C. H., & Jenkins, W. J. (2013). Slow-spreading submarine ridges in the South Atlantic as a significant oceanic iron source. *Nature Geoscience*, *6*(9), 775–779. https://doi.org/10.1038/ngeo1893

Sander, S. G., & Koschinsky, A. (2011). Metal flux from hydrothermal vents increased by organic complexation. *Nature Geoscience*, *4*(3), 145–150. https://doi.org/10.1038/ngeo1088

Schepanski, K., Tegen, I., & Macke, A. (2009). Saharan dust transport and deposition towards the tropicalnorthern Atlantic. *Atmospheric Chemistry and Physics*, *9*(4), 1173–1189. https://doi.org/10.5194/acp-9-1173-2009

Schlitzer, R. (2018). https://odv.awi.de

Schlitzer, R., Anderson, R. F., Dodas, E. M., Lohan, M., Geibert, W., Tagliabue, A., et al. (2018). The GEOTRACES Intermediate Data Product 2017. *Chemical Geology*, *493*, 210–223. https://doi.org/10.1016/j.chemgeo.2018.05.040

Schlosser, C., Klar, J. K., Wake, B. D., Snow, J. T., Honey, D. J., Woodward, E. M. S., et al. (2014). Seasonal ITCZ migration dynamically controls the location of the (sub)tropical Atlantic biogeochemical divide. *Proceedings of the National Academy of Sciences of the United States of America*, *111*(4), 1438–1442. https://doi.org/10.1073/pnas.1318670111

Sedwick, P. N., Church, T. M., Bowie, A. R., Marsay, C. M., Ussher, S. J., Achilles, K. M., et al. (2005). Iron in the Sargasso Sea (Bermuda Atlantic Time-series Study region) during summer: Eolian imprint, spatiotemporal variability, and ecological implications. *Global Biogeochemical Cycles*, *19*, GB4006. https://doi.org/10.1029/2004GB002445

Shaked, Y., Kustka, A. B., & Morel, F. M. M. (2005). A general kinetic model for iron acquisition by eukaryotic phytoplankton. *Limnology and Oceanography*, *50*(3), 872–882. https://doi.org/10.4319/lo.2005.50.3.0872

Sunda, W. G., & Huntsman, S. A. (1997). Interrelated influence of iron, light and cell size on marine phytoplankton growth light and cell size on marine phytoplankton growth. *Nature*, *390*, 389–392. https://doi.org/10.1038/37093

Tagliabue, A., Aumont, O., & Bopp, L. (2014). The impact of different external sources of iron on the global carbon cycle. *Geophysical Research Letters*, *41*, 920–926. https://doi.org/10.1002/2013GL059059

Tagliabue, A., Aumont, O., DeAth, R., Dunne, J. P., Dutkiewicz, S., Galbraith, E., et al. (2016). How well do global ocean biogeochemistry models simulate dissolved iron distributions? *Global Biogeochemical Cycles*, *30*, 149–174. https://doi.org/10.1002/2015GB005289

Tagliabue, A., Bopp, L., Dutay, J.-C., Bowie, A. R., Chever, F., Jean-Baptiste, P., et al. (2010). Hydrothermal contribution to the oceanic dissolved iron inventory. *Nature Geoscience*, *3*(4), 252–256. https://doi.org/10.1038/ngeo818

Tagliabue, A., Bowie, A. R., Philip, W., Buck, K. N., Johnson, K. S., & Saito, M. A. (2017). The integral role of iron in ocean biogeochemistry. *Nature*, *543*(7643), 51–59. https://doi.org/10.1038/nature21058

Tagliabue, A., Mtshali, T., Aumont, O., Bowie, A. R., Klunder, M. B., Roychoudhury, A. N., & Swart, S. (2012). A global compilation of dissolved iron measurements: Focus on distributions and processes in the Southern Ocean. *Biogeosciences*, *9*(6), 2333–2349. https://doi.org/10.5194/bg-9-2333-2012

Tagliabue, A., Williams, R. G., Rogan, N., Achterberg, E. P., & Boyd, P. W. (2014). A ventilation-based framework to explain the regeneration-scavenging balance of iron in the ocean. *Geophysical Research Letters*, *41*, 7227–7236. https://doi.org/10.1002/2014GL061066

Tsamalis, C., Chédin, A., Pelon, J., & Capelle, V. (2013). The seasonal vertical distribution of the saharan air layer and its modulation by the wind. *Atmospheric Chemistry and Physics*, *13*(22), 11,235–11,257. https://doi.org/10.5194/acp-13-11235-2013

Twining, B. S. (2014). Trace element concentrations in particles from R/V Knorr KN199-04, KN204-01 in the subtropical North Atlantic Ocean from 2010-2011 (U.S. GEOTRACES NAT project). Biological and Chemical Oceanography Data Management Office (BCO-DMO). Retrieved from http://lod.bco-dmo.org/id/dataset/3841

Twining, B. S., Rauschenberg, S., Morton, P. L., & Vogt, S. (2015). Metal contents of phytoplankton and labile particulate material in the North Atlantic Ocean. *Progress in Oceanography*, *137*, 261–283. https://doi.org/10.1016/j.pocean.2015.07.001

Ussher, S. J., Achterberg, E. P., Powell, C., Baker, A. R., Jickells, T. D., Torres, R., & Worsfold, P. J. (2013). Impact of atmospheric deposition on the contrasting iron biogeochemistry of the North and South Atlantic Ocean. *Global Biogeochemical Cycles*, *27*, 1096–1107. https://doi.org/10.1002/gbc.20056

Ussher, S. J., Achterberg, E. P., Sarthou, G., Laan, P., de Baar, H. J. W., & Worsfold, P. J. (2010). Distribution of size fractionated dissolved iron in the Canary Basin. *Marine Environmental Research*, *70*(1), 46–55. https://doi.org/10.1016/J.MARENVRES.2010.03.001

Wang, W. X., & Dei, R. C. H. (2003). Bioavailability of iron complexed with organic colloids to the cyanobacteria Synechococcus and Trichodesmium. *Aquatic Microbial Ecology*, *33*(3), 247–259. https://doi.org/10.3354/ame033247

Wells, M. L., & Goldberg, E. D. (1992). Marine submicron particles. *Marine Chemistry*, *40*(1–2), 5–18. https://doi.org/10.1016/0304-4203(92)90045-C

Wu, J., Boyle, E., Sunda, W., & Wen, L.-S. (2001). Soluble and Colloidal Iron in the Oligotrophic North Atlantic and North Pacific. *Science*, *293*(5531), 847–849. https://doi.org/10.1126/science.1059251

Yücel, M., Gartman, A., Chan, C. S., & Luther, G. W. (2011). Hydrothermal vents as a kinetically stable source of iron-sulphide-bearing nanoparticles to the ocean. *Nature Geoscience*, *4*(6), 367–371. https://doi.org/10.1038/ngeo1148

A.2 Data from Chapter 4

The table below contains the Fe data shown in Figures 4.2 to 4.4, as average and one standard deviation of replicate concentrations at each time point.

AVG ± 1SD		^{56}Fe (nmol/L)					^{57}Fe (nmol/L)				
	Time (h)	**TDFe**	**dFe**	**sFe**	**cFe**	**pFe$_{app}$**	**TDFe**	**dFe**	**sFe**	**cFe**	**pFe$_{app}$**
Station 3	**0**	2.04	1.05 ± 0.15	0.30	0.86	0.88	0.05	0.01	0.01	0.00	0.03
	0.5	2.29 ± 0.79	1.03 ± 0.19	0.31 ± 0.24	0.73 ± 0.39	1.26 ± 0.79	1.14 ± 0.06	1.09 ± 0.04	0.05 ± 0.01	1.04 ± 0.05	0.05 ± 0.07
	1.5	1.81 ± 0.44	1.13 ± 0.04	0.20 ± 0.10	0.93 ± 0.08	0.68 ± 0.40	1.16 ± 0.03	1.10 ± 0.01	0.03 ± 0.00	1.06 ± 0.01	0.06 ± 0.03
	6	2.23	1.27	0.23	1.04	0.96	1.19	1.09	0.03	1.06	0.10
	12	1.41 ± 0.06	1.10 ± 0.05	0.34 ± 0.13	0.76 ± 0.15	0.32 ± 0.02	1.13 ± 0.03	1.06 ± 0.04	0.03 ± 0.01	1.03 ± 0.04	0.07 ± 0.03
	24	-	-	-	-	-	-	-	-	-	-
	48	1.79 ± 0.10	1.11 ± 0.08	0.69 ± 0.16	0.42 ± 0.22	0.68 ± 0.03	1.18 ± 0.06	1.00 ± 0.01	0.04 ± 0.00	0.96 ± 0.01	0.18 ± 0.06
Station 4	**0**	1.53	0.91	-	-	0.62	0.07	0.02	0.05	0.00	0.04
	0.5	1.73 ± 0.38	0.93 ± 0.04	0.68 ± 0.14	0.25 ± 0.11	0.80 ± 0.35	0.74 ± 0.02	0.48 ± 0.03	-	-	0.26 ± 0.04
	1.5	1.43	1.20	0.55	0.65	0.22	0.60	0.48	-	-	0.12
	6	1.52 ± 0.40	1.21 ± 0.05	0.71 ± 0.29	0.50 ± 0.26	0.31 ± 0.39	0.68 ± 0.02	0.48 ± 0.02	0.05	0.44 ± 0.01	0.21
	12	1.43 ± 0.36	0.91 ± 0.02	0.49	0.44	0.51 ± 0.35	0.67 ± 0.08	0.45 ± 0.01	0.04	0.41	0.21 ± 0.09
	24	1.69 ± 0.23	0.88 ± 0.21	0.37 ± 0.17	0.51 ± 0.38	0.81 ± 0.05	0.64 ± 0.02	0.52 ± 0.11	0.04	0.49 ± 0.12	0.11 ± 0.10
	48	1.28 ± 0.37	0.96 ± 0.12	0.22 ± 0.03	0.70 ± 0.17	0.52 ± 0.16	0.63 ± 0.05	0.40 ± 0.02	0.05 ± 0.01	0.35 ± 0.03	0.23 ± 0.06
Station 7	**0**	1.36	0.40	0.39	-	-	0.02	0.05	0.02	-	-
	0.5	-	-	-	-	-	0.62 ± 0.02	0.55 ± 0.10	0.05 ± 0.00	0.44 ± 0.00	0.09 ± 0.08
	1.5	1.22 ± 0.09	0.49 ± 0.05	0.41	-	0.73 ± 0.14	0.62 ± 0.09	0.63 ± 0.07	0.04	-	0.00 ± 0.00
	6	1.36 ± 0.42	0.58 ± 0.10	-	-	0.77 ± 0.32	0.60 ± 0.01	0.61 ± 0.03	-	-	0.00 ± 0.00
	12	1.04 ± 0.43	0.46 ± 0.07	0.35	0.12	0.59 ± 0.46	0.63 ± 0.09	0.62 ± 0.08	0.05 ± 0.01	0.54 ± 0.06	0.01 ± 0.01
	24	1.21 ± 0.35	0.87 ± 0.06	0.77 ± 0.16	0.00	0.34 ± 0.48	0.56 ± 0.01	0.56 ± 0.00	0.04 ± 0.00	0.53	0.00 ± 0.00
	48	1.17 ± 0.37	0.77	0.61 ± 0.14	0.27	0.77	0.56 ± 0.06	0.53	0.04 ± 0.00	0.49	0.03

A.3 Data from Chapter 5

The table below contains the protein data shown in Figures 5.2 and 5.3, as the average with one standard deviation of replicate bioassays of each treatments after the 48 h incubation period.

Treatment		PhoA *Syn.* (fmol L^{-1})	PhoX *Syn.* (fmol L^{-1})	PstS *Syn.* (fmol L^{-1})	PhoA *Pro.* (fmol L^{-1})	PhoX *Pro.* (fmol L^{-1})	PstS *Pro.* (fmol L^{-1})
Station 2	**Control**	4.44 ± 0.97	14.1 ± 4.11	1.40 ± 0.91	29.9 ± 9.00	11.0 ± 1.30	439 ± 110
	+ Zn	25.1 ± 0.37	12.1 ± 1.80	3.41 ± 1.25	27.1 ± 12.5	7.28 ± 1.79	282 ± 148
	+ Co	31.4 ± 4.49	17.5 ± 2.78	7.67 ± 5.69	34.1 ± 9.71	25.8 ± 10.6	516 ± 249
	+ Fe	17.7 ± 17.56	9.40 ± 7.12	4.08 ± 5.21	24.9 ± 24.2	11.3 ± 7.80	347 ± 366
Station 3	**Control**	14.4 ± 7.88	9.98 ± 1.51	2.45 ± 2.03	31.8 ± 6.43	10.5 ± 7.02	392 ± 173
	+ Zn	11.8 ± 10.13	5.68 ± 3.52	0.36 ± 0.08	18.4 ± 9.37	6.95 ± 5.20	157 ± 17
	+ Co	9.21 ± 7.71	17.9 ± 14.47	2.83 ± 0.75	28.7 ± 18.0	9.86 ± 0.69	375 ± 193
	+ Fe	8.25 ± 6.35	6.24 ± 0.52	1.06 ± 0.80	19.1 ± 8.43	9.24 ± 0.11	275 ± 72
Station 4	**Control**	5.24 ± 2.09	6.15 ± 3.47	0.47 ± 0.17	20.5 ± 8.54	4.32 ± 0.10	205 ± 115
	+ Zn	9.60 ± 8.26	6.46 ± 2.52	0.34 ± 0.44	31.2 ± 3.50	4.78 ± 6.27	248 ± 11.5
	+ Co	14.7 ± 15.52	11.8 ± 0.34	1.27 ± 0.42	41.6 ± 22.4	33.8 ± 32.1	447 ± 332
	+ Fe	5.54 ± 0.48	6.33 ± 1.94	0.75 ± 0.46	18.1 ± 6.23	4.40 ± 5.08	158 ± 121
Station 7	**Control**	18.4 ± 8.58	10.6 ± 1.46	4.03 ± 1.14	2.14 ± 0.82	5.44 ± 1.59	152 ± 30.0
	+ Zn	18.7 ± 22.25	6.08 ± 3.40	2.14 ± 2.09	1.85 ± 2.26	16.5 ± 17.1	124 ± 119
	+ Co	6.89 ± 4.28	8.75 ± 1.35	1.86 ± 0.61	1.40 ± 0.33	11.5 ± 3.58	104 ± 3.61
	+ Fe	12.2 ± 5.93	6.44 ± 0.47	2.22 ± 0.37	1.87 ± 0.15	12.4 ± 1.73	143 ± 42.3

The table below contains the auxiliary data shown in Figures 5.5 and 5.6, as the average with one standard deviation of replicate bioassays (where applicable) of each treatment after the 48 h incubation period.

	Treatment	APA (nM h^{-1})	Chl-*a* (µg L^{-1})	*Syn.* cells (cells ml^{-1})	*Pro.* cells (cells ml^{-1})	DIP (nM)	DOP (nM)	DIN (nM)
Station 2	**Control**	3.24 ± 0.23	0.073 ± 0.009	3930 ± 131	54983 ± 1177	4.80 ± 0.85	135	5.55 ± 2.62
	+ Zn	3.10 ± 0.19	0.082 ± 0.005	3740 ± 86	55062 ± 311	4.81 ± 1.25	88 ± 9	2.10 ± 1.39
	+ Co	3.03 ± 0.10	0.079 ± 0.015	3354 ± 213	54323 ± 9543	5.11 ± 0.45	90 ± 7	3.70 ± 1.92
	+ Fe	3.45 ± 0.46	0.081 ± 0.004	3262 ± 115	59836 ± 3374	4.92 ± 1.02	117 ± 25	3.27 ± 0.96
Station 3	**Control**	3.55 ± 0.16	0.083 ± 0.002	4078 ± 1767	85788 ± 43737	2.32 ± 1.09	117	2.81 ± 1.97
	+ Zn	3.16 ± 0.06	0.095 ± 0.001	3967 ± 1735	83241 ± 43097	2.71 ± 0.63	106 ± 11	3.12 ± 0.00
	+ Co	3.13 ± 0.11	0.095 ± 0.006	1962 ± 104	69755 ± 31109	2.45 ± 0.36	111	5.19 ± 6.94
	+ Fe	3.29 ± 0.15	0.073 ± 0.022	4023 ± 1572	97929 ± 47023	2.57 ± 0.73	94 ± 13	2.27 ± 1.44
Station 4	**Control**	4.44 ± 1.07	0.103 ± 0.007	-	-	1.55 ± 0.07	103 ± 13	3.67 ± 0.10
	+ Zn	5.04 ± 1.28	0.108 ± 0.012	-	-	1.42 ± 0.02	124 ± 3	4.67 ± 0.51
	+ Co	5.07 ± 0.98	0.111 ± 0.008	-	-	2.30 ± 0.15	126 ± 0	3.60 ± 3.05
	+ Fe	4.18 ± 0.29	0.114 ± 0.008	-	-	1.53 ± 0.40	124 ± 12	4.67 ± 0.51
Station 7	**Control**	2.61 ± 0.37	0.138 ± 0.041	1894 ±87	230707 ± 44157	4.32 ± 1.86	156 ± 7	3.26 ± 1.10
	+ Zn	3.02 ± 0.03	0.138 ± 0.005	1775 ± 153	165929 ± 16329	3.70 ± 0.26	146 ± 39	2.92 ± 0.91
	+ Co	2.84 ± 0.42	0.099 ± 0.043	1673 ± 13	187528 ± 28283	3.41 ± 0.22	141 ± 48	7.45 ± 9.89
	+ Fe	3.03 ± 0.31	0.153 ± 0.011	2076	236133	2.88 ± 0.30	190 ± 35	2.40 ± 0.12

Bibliography

Aguilar-Islas, A.M., Wu, J., Rember, R., Johansen, A.M., Shank, L.M., 2010. Dissolution of aerosol-derived iron in seawater: Leach solution chemistry, aerosol type, and colloidal iron fraction. Mar. Chem. 120, 25–33. https://doi.org/10.1016/j.marchem.2009.01.011

Ahlgren, N.A., Rocap, G., 2012. Diversity and distribution of marine Synechococcus: Multiple gene phylogenies for consensus classification and development of qPCR assays for sensitive measurement of clades in the ocean. Front. Microbiol. 3, 1–24. https://doi.org/10.3389/fmicb.2012.00213

Albani, S., Mahowald, N.M., Murphy, L.N., Raiswell, R., Moore, J.K., Anderson, R.F., McGee, D., Bradtmiller, L.I., Delmonte, B., Hesse, P.P., Mayewski, P.A., 2016. Paleodust variability since the Last Glacial Maximum and implications for iron inputs to the ocean. Geophys. Res. Lett. 43, 3944–3954. https://doi.org/10.1002/2016gl067911

Aluwihare, L.I., Meador, T., 2008. Chemical Composition of Marine Dissolved Organic Nitrogen, in: Capone, D.G., Bronk, D.A., Mulholland, M., Carpenter, E.J. (Eds.), Nitrogen in the Marine Environment. Elsevier, New York, pp. 95–140.

Ammerman, J.W., 1993. Microbial cycling of inorganic and organic phosphorus in the water column, in: Kemp, P.F., Sherr, B.F., Sherr, E.B., Cole, J.J. (Eds.), Handbook of Methods in Aquatic Microbial Ecology. Lewis Press, BocaRaton, FL, pp. 621–631.

Anderson, R.F., 2020. GEOTRACES: Accelerating Research on the Marine Biogeochemical Cycles of Trace Elements and Their Isotopes. Ann. Rev. Mar. Sci. 12, 9.1-9.37. https://doi.org/10.2138/gselements.14.6.377

Ardyna, M., Lacour, L., Sergi, S., d'Ovidio, F., Sallée, J.-B., Rembauville, M., Blain, S., Tagliabue, A., Schlitzer, R., Jeandel, C., Arrigo, K.R., Claustre, H., 2019. Hydrothermal vents trigger massive phytoplankton blooms in the Southern Ocean. Nat. Commun. 10, 2451. https://doi.org/10.1038/s41467-019-09973-6

Arteaga, L., Pahlow, M., Oschlies, A., 2016. Modeled Chl:C ratio and derived estimates of phytoplankton carbon biomass and its contribution to total particulate organic carbon in the global surface ocean. Global Biogeochem. Cycles 30, 1791–1810. https://doi.org/10.1002/2016GB005458

Aumont, O., Ethé, C., Tagliabue, A., Bopp, L., Gehlen, M., 2015. PISCES-v2: An ocean biogeochemical model for carbon and ecosystem studies. Geosci. Model Dev. 8, 2465–2513. https://doi.org/10.5194/gmd-8-2465-2015

Baker, A.R., Adams, C., Bell, T.G., Jickells, T.D., Ganzeveld, L., 2013. Estimation of atmospheric nutrient inputs to the Atlantic Ocean from 50°N to 50°S based on large-scale field sampling: Iron and other dust-associated elements. Global Biogeochem. Cycles 27, 755–767. https://doi.org/10.1002/gbc.20062

Baltar, F., Arístegui, J., Gasol, J.M., Sintes, E., Van Aken, H.M., Herndl, G.J., 2010. High dissolved extracellular enzymatic activity in the deep central Atlantic ocean. Aquat. Microb.

Ecol. 58, 287–302. https://doi.org/10.3354/ame01377

Barbeau, K., Moffett, J.W., Caron, D.A., Croot, P.L., Erdner, D.L., 1996. Role of protozoan grazing in relieving iron limitation of phytoplankton. Nature. https://doi.org/10.1038/380061a0

Barbeau, K., Rue, E.L., Bruland, K.W., Butler, A., 2001. Photochemical cycling of iron in the surface ocean mediated by microbial iron(III)-binding ligands. Nature 413, 409–413. https://doi.org/10.1017/CBO9780511623370

Barnett, J.P., Scanlan, D.J., Blindauer, C.A., 2014. Identification of major zinc-binding proteins from a marine cyanobacterium: insight into metal uptake in oligotrophic environments. Metallomics 6, 1254–1268. https://doi.org/10.1039/C4MT00048J

Barni, F., Lewis, S.W., Berti, A., Miskelly, G.M., Lago, G., 2007. Forensic application of the luminol reaction as a presumptive test for latent blood detection. Talanta 72, 896–913. https://doi.org/10.1016/j.talanta.2006.12.045

Basu, S., Gledhill, M., de Beer, D., Prabhu Matondkar, S.G., Shaked, Y., 2019. Colonies of marine cyanobacteria Trichodesmium interact with associated bacteria to acquire iron from dust. Commun. Biol. 2, 1–8. https://doi.org/10.1038/s42003-019-0534-z

Beaulieu, S.E., 2015. InterRidge Global Database of Active Submarine Hydrothermal Vent Fields: prepared for InterRidge, Version 3.3.

Behrenfeld, M.J., O'Malley, R.T., Siegel, D.A., McClain, C.R., Sarmiento, J.L., Feldman, G.C., Milligan, A.J., Falkowski, P.G., Letelier, R.M., Boss, E.S., 2006. Climate-driven trends in contemporary ocean productivity. Nature 444, 752–755. https://doi.org/10.1038/nature05317

Benitez-Nelson, C.R., 2000. The biogeochemical cycling of phosphorus in marine systems. Earth Sci. Rev. 51, 109–135. https://doi.org/10.1016/S0012-8252(00)00018-0

Bennett, S.A., Achterberg, E.P., Connelly, D.P., Statham, P.J., Fones, G.R., German, C.R., 2008. The distribution and stabilisation of dissolved Fe in deep-sea hydrothermal plumes. Earth Planet. Sci. Lett. 270, 157–167. https://doi.org/10.1016/j.epsl.2008.01.048

Bergquist, B.A., Wu, J., Boyle, E.A., 2007. Variability in oceanic dissolved iron is dominated by the colloidal fraction. Geochim. Cosmochim. Acta 71, 2960–2974. https://doi.org/10.1016/j.gca.2007.03.013

Bertilsson, S., Berglund, O., Karl, D.M., Chisholm, S.W., 2003. Elemental composition of marine Prochlorococcus and Synechococcus: Implications for the ecological stoichiometry of the sea. Limnol. Oceanogr. 48, 1721–1731. https://doi.org/10.4319/lo.2003.48.5.1721

Bertrand, E.M., Saito, M.A., Rose, J.M., Riesselman, C.R., Lohan, M.C., Noble, A.E., Lee, P.A., DiTullio, G.R., 2007. Vitamin B12 and iron colimitation of phytoplankton growth in the Ross Sea. Limnol. Oceanogr. 52, 1079–1093. https://doi.org/10.4319/lo.2007.52.3.1079

Berube, P.M., Biller, S.J., Kent, A.G., Berta-Thompson, J.W., Roggensack, S.E., Roache-Johnson, K.H., Ackerman, M., Moore, L.R., Meisel, J.D., Sher, D., Thompson, L.R., Campbell, L.,

Martiny, A.C., Chisholm, S.W., 2015. Physiology and evolution of nitrate acquisition in Prochlorococcus. ISME J. 9, 1195–1207. https://doi.org/10.1038/ismej.2014.211

Biller, D. V., Bruland, K.W., 2012. Analysis of Mn, Fe, Co, Ni, Cu, Zn, Cd, and Pb in seawater using the Nobias-chelate PA1 resin and magnetic sector inductively coupled plasma mass spectrometry (ICP-MS). Mar. Chem. 130–131, 12–20. https://doi.org/10.1016/j.marchem.2011.12.001

Birchill, A.J., 2017. The seasonal cycling and physico-chemical speciation of iron on the Celtic and Hebridean shelf seas. University of Plymouth. https://doi.org/m/handle/10026.1/10236/2017birchill10461814phd_full.pdf?sequence=1&isAllowed=y

Birchill, A.J., Hartner, N.T., Kunde, K., Siemering, B., Daniels, C., González-Santana, D., Milne, A., Ussher, S.J., Worsfold, P.J., Leopold, K., Painter, S.C., Lohan, M.C., 2019. The eastern extent of seasonal iron limitation in the high latitude North Atlantic Ocean. Sci. Rep. 9, 1–12. https://doi.org/10.1038/s41598-018-37436-3

Birchill, A.J., Milne, A., S. Woodward, E.M., Harris, C., Annett, A., Rusiecka, D., Achterberg, E.P., Gledhill, M., Ussher, S.J., Worsfold, P.J., Geibert, W., Lohan, M.C., 2017. Seasonal iron depletion in temperate shelf seas. Geophys. Res. Lett. 44, 8987–8996. https://doi.org/10.1002/2017GL073881

Black, E.E., Kienast, S.S., Lemaitre, N., Lam, P.J., Anderson, R.F., Planquette, H., Planchon, F., Buesseler, K.O., 2020. Ironing Out Fe Residence Time in the Dynamic Upper Ocean. Global Biogeochem. Cycles 34. https://doi.org/10.1029/2020GB006592

Boiteau, R.M., Mende, D.R., Hawco, N.J., McIlvin, M.R., Fitzsimmons, J.N., Saito, M.A., Sedwick, P.N., DeLong, E.F., Repeta, D.J., 2016. Siderophore-based microbial adaptations to iron scarcity across the eastern Pacific Ocean. Proc. Natl. Acad. Sci. 113, 14237–14242. https://doi.org/10.1073/pnas.1608594113

Boiteau, R.M., Repeta, D.J., 2015. An extended siderophore suite from Synechococcus sp. PCC 7002 revealed by LC-ICPMS-ESIMS. Metallomics 7, 877–884. https://doi.org/10.1039/c5mt00005j

Bowie, A.R., Achterberg, E.P., Mantoura, R.F.C., Worsfold, P.J., 1998. Determination of sub-nanomolar levels of iron in seawater using flow injection with chemiluminescence detection. Anal. Chim. Acta 361, 189–200. https://doi.org/10.1016/S0003-2670(98)00015-4

Bowie, A.R., Lohan, M.C., 2009. Determination of Iron in Seawater, in: Wurl, O. (Ed.), Practical Guidelines for the Analysis of Seawater. CRC Press, Boca Raton, Fla.; London, pp. 235–258.

Bowie, A.R., Maldonado, M.T., Frew, R.D., Croot, P.L., Achterberg, E.P., Mantoura, R.F.C., Worsfold, P.J., Law, C.S., Boyd, P.W., 2001. The fate of added iron during a mesoscale fertilisation experiment in the Southern Ocean. Deep Sea Res. Part II Top. Stud. Oceanogr. 48, 2703–2743. https://doi.org/10.1016/S0967-0645(01)00015-7

Boyd, P.W., Ellwood, M.J., Tagliabue, A., Twining, B.S., 2017. Biotic and abiotic retention, recycling and remineralization of metals in the ocean. Nat. Geosci. 10, 167–173. https://doi.org/10.1038/ngeo2876

Boyd, P.W., Ibisanmi, E., Sander, S.G., Hunter, K.A., Jackson, G.A., 2010. Remineralization of upper ocean particles: Implications for iron biogeochemistry. Limnol. Oceanogr. 55, 1271–1288. https://doi.org/10.4319/lo.2010.55.3.1271

Boyd, P.W., Watson, A.J., Law, C.S., Abraham, E.R., Trull, T., Murdoch, R., Bakker, D.C.E., Bowie, A.R., Buesseler, K.O., Chang, H., Charette, M., Croot, P., Downing, K., Frew, R., Gall, M., Hadfield, M., Hall, J., Harvey, M., Jameson, G., LaRoche, J., Liddicoat, M., Ling, R., Maldonado, M.T., McKay, R.M., Nodder, S., Pickmere, S., Pridmore, R., Rintoul, S., Safi, K., Sutton, P., Strzepek, R., Tanneberger, K., Turner, S., Waite, A., Zeldis, J., 2000. A mesoscale phytoplankton bloom in the polar Southern Ocean stimulated by iron fertilization. Nature 407, 695–702. https://doi.org/10.1038/35037500

Boye, M., Nishioka, J., Croot, P.L., Laan, P., Timmermans, K.R., De Baar, H.J.W., 2005. Major deviations of iron complexation during 22 days of a mesoscale iron enrichment in the open Southern Ocean. Mar. Chem. 96, 257–271. https://doi.org/10.1016/j.marchem.2005.02.002

Boyle, E.A., Anderson, R.F., Cutter, G. a., Fine, R., Jenkins, W.J., Saito, M.A., 2015. Introduction to the U.S. GEOTRACES North Atlantic Transect (GA-03): USGT10 and USGT11 cruises. Deep Sea Res. Part II 116, 1–5. https://doi.org/10.1016/j.dsr2.2015.02.031

Boyle, E.A., Edmond, J.M., Sholkovitz, E.R., 1977. The mechanism of iron removal in estuaries. Geochim. Cosmochim. Acta 41, 1313–1324. https://doi.org/10.1016/0016-7037(77)90075-8

Bressac, M., Guieu, C., Ellwood, M.J., Tagliabue, A., Wagener, T., Whitby, H., Sarthou, G., Boyd, P.W., 2019. Resupply of mesopelagic dissolved iron controlled by particulate iron composition. Nat. Geosci. https://doi.org/10.1038/s41561-019-0476-6

Brewer, P.G., Riley, J.P., 1965. The automatic determination of nitrate in sea water. Deep Sea Res. Oceanogr. Abstr. 12, 765–772. https://doi.org/10.1016/0011-7471(65)90797-7

Bristow, L.A., Mohr, W., Ahmerkamp, S., Kuypers, M.M.M., 2017. Nutrients that limit growth in the ocean. Curr. Biol. 27, R474–R478. https://doi.org/10.1016/j.cub.2017.03.030

Browning, T.J., Achterberg, E.P., Yong, J.C., Rapp, I., Utermann, C., Engel, A., Moore, C.M., 2017. Iron limitation of microbial phosphorus acquisition in the tropical North Atlantic. Nat. Commun. 8, 15465. https://doi.org/10.1038/ncomms15465

Bruland, K.W., 1989. Complexation of cadmium by natural organic ligands in the central North Pacific. Limnol. Oceanogr. 34, 269–285. https://doi.org/10.4319/lo.1992.37.5.1008

Bruland, K.W., 1980. Oceanographic distributions of cadmium, zinc, nickel, and copper in the North Pacific. Earth Planet. Sci. Lett. 47, 176–198. https://doi.org/10.1016/0012-821X(80)90035-7

Bruland, K.W., Franks, R.P., Knauer, G.A., Martin, J.H., 1979. Sampling and analytical methods for the determination of copper, cadmium, zinc, and nickel at the nanogram per liter level in sea water. Anal. Chim. Acta 105, 233–245. https://doi.org/10.1016/S0003-2670(01)83754-5

Bruland, K.W., Knauer, G.A., Martin, J.H., 1978. Zinc in north-east Pacific water. Nature 271, 741–743. https://doi.org/10.1038/271741a0

Bruland, K.W., Lohan, M.C., 2004. The control of trace metals in seawater, in: Riley, J.P., Chester, R. (Eds.), Chemical Oceanography. Academic Press, New York, pp. 157–220.

Buck, K.N., Sedwick, P.N., Sohst, B., Carlson, C.A., 2018. Organic complexation of iron in the eastern tropical South Pacific: Results from US GEOTRACES Eastern Pacific Zonal Transect (GEOTRACES cruise GP16). Mar. Chem. 201, 229–241. https://doi.org/10.1016/j.marchem.2017.11.007

Buck, K.N., Selph, K.E., Barbeau, K.A., 2010. Iron-binding ligand production and copper speciation in an incubation experiment of Antarctic Peninsula shelf waters from the Brans field Strait, Southern Ocean. Mar. Chem. 122, 148–159. https://doi.org/10.1016/j.marchem.2010.06.002

Buck, K.N., Sohst, B., Sedwick, P.N., 2015. The organic complexation of dissolved iron along the U.S. GEOTRACES (GA03) North Atlantic Section. Deep Sea Res. Part II 116, 152–165. https://doi.org/10.1016/j.dsr2.2014.11.016

Bundy, R.M., Boiteau, R.M., McLean, C., Turk-Kubo, K.A., McIlvin, M.R., Saito, M.A., Van Mooy, B.A.S., Repeta, D.J., 2018. Distinct siderophores contribute to iron cycling in the mesopelagic at station ALOHA. Front. Mar. Sci. 5, 1–15. https://doi.org/10.3389/fmars.2018.00061

Bundy, R.M., Jiang, M., Carter, M., Barbeau, K.A., 2016. Iron-binding ligands in the Southern California current system: Mechanistic studies. Front. Mar. Sci. 3, 1–17. https://doi.org/10.3389/fmars.2016.00027

Carritt, D.E., Carpenter, J.H., 1966. Comparison and Evaluation of Currently Employed Modifications of the Winkler Method for Determining Dissolved Oxygen in Seawater; a NASCO Report. J. Mar. Res. 24, 286–318.

Chen, M., Wang, W., 2001. Bioavailability of natural colloid-bound iron to marine plankton : Influences of colloidal size and aging. Limnol. Oceanogr. 46, 1956–1967. https://doi.org/10.4319/lo.2001.46.8.1956

Chever, F., Bucciarelli, E., Sarthou, G., Speich, S., Arhan, M., Penven, P., Tagliabue, A., 2010. Physical speciation of iron in the Atlantic sector of the Southern Ocean along a transect from the subtropical domain to the Weddell Sea Gyre. J. Geophys. Res. Ocean. 115, 1–15. https://doi.org/10.1029/2009JC005880

Clough, R., Sela, H., Milne, A., Lohan, M.C., Tokalioglu, S., Worsfold, P.J., 2015. Uncertainty contributions to the measurement of dissolved Co, Fe, Pb and V in seawater using flow injection with solid phase preconcentration and detection by collision/reaction cell—quadrupole ICP–MS. Talanta 133, 162–169. https://doi.org/10.1016/j.talanta.2014.08.045

Coale, K.H., Johnson, K.S., Fitzwater, S.E., Gordon, M., Tanner, S., Chavez, F.P., Ferioli, L., Sakamoto, C., Rogers, P., Millero, F., Steinberg, P., Nightingale, P., Cooper, D., Cochlan, W.P., Landry, M.R., Constantinou, J., Rollwagen, G., Trasvina, A., Kudela, R., 1996. A massive phytoplankton bloom induced by an ecosystem-scale iron fertilization experiment in the equatorial Pacific Ocean. Nature 383, 495–501.

Coleman, J.E., 1992. Structure and mechanism of alkaline phosphatase. Annu. Rev. Biophys.

Biomol. Struct 21, 441–483.

Conway, T.M., Hamilton, D.S., Shelley, R.U., Aguilar-Islas, A.M., Landing, W.M., Mahowald, N.M., John, S.G., 2019. Tracing and constraining anthropogenic aerosol iron fluxes to the North Atlantic Ocean using iron isotopes. Nat. Commun. 10, 1–10. https://doi.org/10.1038/s41467-019-10457-w

Conway, T.M., John, S.G., 2014. Quantification of dissolved iron sources to the North Atlantic Ocean. Nature 511, 212–215. https://doi.org/10.1038/nature13482

Cox, A.D., Saito, M.A., 2013. Proteomic responses of oceanic Synechococcus WH8102 to phosphate and zinc scarcity and cadmium additions. Front. Microbiol. 4, 1-17 (Article 387). https://doi.org/10.3389/fmicb.2013.00387

Crawford, D.W., Lipsen, M.S., Purdie, D.A., Lohan, M.C., Statham, P.J., Whitney, F.A., Putland, J.N., Johnson, W.K., Sutherland, N., Peterson, T.D., Harrison, P.J., Wong, C.S., 2003. Influence of zinc and iron enrichments on phytoplankton growth in the northeasten subarctic Pacific. Limnol. Oceanogr. 48, 1583–1600. https://doi.org/10.4319/lo.2003.48.4.1583

Cullen, J.J., 2015. Subsurface Chlorophyll Maximum Layers: Enduring Enigma or Mystery Solved? Ann. Rev. Mar. Sci. 7, 207–239. https://doi.org/10.1146/annurev-marine-010213-135111

Cullen, J.T., Bergquist, B.A., Moffett, J.W., 2006. Thermodynamic characterization of the partitioning of iron between soluble and colloidal species in the Atlantic Ocean. Mar. Chem. 98, 295–303. https://doi.org/10.1016/J.MARCHEM.2005.10.007

Davis, C., Lohan, M.C., Tuerena, R., Cerdan-Garcia, E., Woodward, E.M.S., Tagliabue, A., Mahaffey, C., 2019. Diurnal variability in alkaline phosphatase activity and the potential role of zooplankton. Limnol. Oceanogr. Lett. https://doi.org/10.1002/lol2.10104

Davis, C.E., Mahaffey, C., 2017. Elevated alkaline phosphatase activity in a phosphate-replete environment: Influence of sinking particles. Limnol. Oceanogr. 62, 2389–2403. https://doi.org/10.1002/lno.10572

de Baar, H.J.W., 1994. von Liebig ' s Law of the Minimum and Plankton Ecology. Prog. Oceanogr. 33, 347–386.

de Baar, H.J.W., Boyd, P.W., Coale, K.H., Landry, M.R., Tsuda, A., Assmy, P., Bakker, D.C.E., Bozec, Y., Barber, R.T., Brzezinski, M.A., Buesseler, K.O., Boyé, M., Croot, P.L., Gervais, F., Gorbunov, M.Y., Harrison, P.J., Hiscock, W.T., Laan, P., Lancelot, C., Law, C.S., Levasseur, M., Marchetti, A., Millero, F.J., Nishioka, J., Nojiri, Y., van Oijen, T., Riebesell, U., Rijkenberg, M.J.A., Saito, H., Takeda, S., Timmermans, K.R., Veldhuis, M.J.W., Waite, A.M., Wong, C.S., 2005. Synthesis of iron fertilization experiments: From the iron age in the age of enlightenment. J. Geophys. Res. C Ocean. 110, 1–24. https://doi.org/10.1029/2004JC002601

de Boyer Montégut, C., Madec, G., Fischer, A.S., Lazar, A., Iudicone, D., 2004. Mixed layer depth over the global ocean: An examination of profile data and a profile-based climatology. J. Geophys. Res. C Ocean. 109, 1–20. https://doi.org/10.1029/2004JC002378

Dinniman, M.S., St-Laurent, P., Arrigo, K.R., Hofmann, E.E., van Dijken, G.L., 2020. Analysis of Iron Sources in Antarctic Continental Shelf Waters. J. Geophys. Res. Ocean. 125, 1–19. https://doi.org/10.1029/2019JC015736

Dixon, J.L., 2008. Macro and micro nutrient limitation of microbial productivity in oligotrophic subtropical Atlantic waters. Environ. Chem. 5, 135–142. https://doi.org/10.1071/EN07081

Duce, R.A., LaRoche, J., Altieri, K., Arrigo, K.R., Baker, A.R., Capone, D.G., Cornell, S., Dentener, F., Galloway, J., Ganeshram, R.S., Geider, R.J., Jickells, T., Kuypers, M.M., Langlois, R., Liss, P.S., Liu, S.M., Middelburg, J.J., Moore, C.M., Nickovic, S., Oschlies, A., Pedersen, T., Prospero, J., Schlitzer, R., Seitzinger, S., Sorensen, L.L., Uematsu, M., Ulloa, O., Voss, M., Ward, B., Zamora, L., 2008. Impacts of Atmospheric Anthropogenic Nitrogen on the Open Ocean. Science (80-.). 320, 893–897.

Duhamel, S., Dyhrman, S.T., Karl, D.M., 2010. Alkaline phosphatase activity and regulation in the North Pacific Subtropical Gyre. Limnol. Oceanogr. 55, 1414–1425. https://doi.org/10.4319/lo.2010.55.3.1414

Dulaquais, G., Planquette, H., L'Helguen, S., Rijkenberg, M.J.A., Boye, M., 2017. The biogeochemistry of cobalt in the Mediterranean Sea. Global Biogeochem. Cycles 31, 377–399. https://doi.org/10.1002/2016GB005478

Dupont, C.L., Butcher, A., Valas, R.E., Bourne, P.E., Caetano-Anollés, G., 2010. History of biological metal utilization inferred through phylogenomic analysis of protein structures. Proc. Natl. Acad. Sci. U. S. A. 107, 10567–10572. https://doi.org/10.1073/pnas.0912491107

Dupont, C.L., Yang, S., Palenik, B., Bourne, P.E., 2006. Modern proteomes contain putative imprints of ancient shifts in trace metal geochemistry. Proc. Natl. Acad. Sci. U. S. A. 103, 17822–7. https://doi.org/10.1073/pnas.0605798103

Ellwood, M.J., 2004. Zinc and cadmium speciation in subantarctic waters east of New Zealand. Mar. Chem. 87, 37–58. https://doi.org/10.1016/j.marchem.2004.01.005

Ellwood, M.J., Bowie, A.R., Baker, A., Gault-Ringold, M., Hassler, C., Law, C.S., Maher, W.A., Marriner, A., Nodder, S., Sander, S., Stevens, C., Townsend, A., van der Merwe, P., Woodward, E.M.S., Wuttig, K., Boyd, P.W., 2018. Insights Into the Biogeochemical Cycling of Iron, Nitrate, and Phosphate Across a 5,300 km South Pacific Zonal Section (153°E-150°W). Global Biogeochem. Cycles 32, 187–207. https://doi.org/10.1002/2017GB005736

Ellwood, M.J., Hunter, K.A., 2000. The incorporation of zinc and iron into the frustule of the marine diatom Thalassiosira pseudonana. Limnol. Oceanogr. 45, 1517–1524. https://doi.org/10.4319/lo.2000.45.7.1517

Ellwood, M.J., van den Berg, C.M.G., 2000. Zinc speciation in the Northeastern Atlantic Ocean. Mar. Chem. 68, 295–306. https://doi.org/10.1016/S0304-4203(99)00085-7

Falkowski, P.G., 1997. Evolution of the nitrogen cycle and its influence on the biological sequestration of CO2 in the ocean. Nature 387, 272–275. https://doi.org/10.1038/387272a0

Falkowski, P.G., Barber, R.T., Smetacek, V., 1998. Biogeochemical Controls and Feedbacks on Ocean Primary Production. Science (80-.). 281, 200–206.

https://doi.org/10.1126/science.281.5374.200

Fernández, E., Marañón, E., Morán, X.A.G., Serret, P., 2003. Potential causes for the unequal contribution of picophytoplankton to total biomass and productivity in oligotrophic waters. Mar. Ecol. Prog. Ser. 254, 101–109. https://doi.org/10.3354/meps254101

Fischer, A.C., Kroon, J.J., Verburg, T.G., Teunissen, T., Wolterbeek, H.T., 2007. On the relevance of iron adsorption to container materials in small-volume experiments on iron marine chemistry : 55 Fe-aided assessment of capacity , affinity and kinetics. Mar. Chem. 107, 533–546. https://doi.org/10.1016/j.marchem.2007.08.004

Fishwick, M.P., Sedwick, P.N., Lohan, M.C., Worsfold, P.J., Buck, K.N., Church, T.M., Ussher, S.J., 2014. The impact of changing surface ocean conditions on the dissolution of aerosol iron. Global Biogeochem. Cycles 28, 1235–1250. https://doi.org/10.1002/2014GB004921

Fitzsimmons, J.N., Boyle, E.A., 2014. Both soluble and colloidal iron phases control dissolved iron variability in the tropical North Atlantic Ocean. Geochim. Cosmochim. Acta 125, 539–550. https://doi.org/10.1016/j.gca.2013.10.032

Fitzsimmons, J.N., Bundy, R.M., Al-Subiai, S.N., Barbeau, K.A., Boyle, E.A., 2015a. The composition of dissolved iron in the dusty surface ocean: An exploration using size-fractionated iron-binding ligands. Mar. Chem. 173, 125–135. https://doi.org/10.1016/j.marchem.2014.09.002

Fitzsimmons, J.N., Carrasco, G.G., Wu, J., Roshan, S., Hatta, M., Measures, C.I., Conway, T.M., John, S.G., Boyle, E.A., 2015b. Partitioning of dissolved iron and iron isotopes into soluble and colloidal phases along the GA03 GEOTRACES North Atlantic Transect. Deep. Res. Part II Top. Stud. Oceanogr. 116, 130–151. https://doi.org/10.1016/j.dsr2.2014.11.014

Fitzsimmons, J.N., Hayes, C.T., Al-Subiai, S.N., Zhang, R., Morton, P.L., Weisend, R.E., Ascani, F., Boyle, E.A., 2015c. Daily to decadal variability of size-fractionated iron and iron-binding ligands at the Hawaii Ocean Time-series Station ALOHA. Geochim. Cosmochim. Acta 171, 303–324. https://doi.org/10.1016/j.gca.2015.08.012

Flombaum, P., Gallegos, J.L., Gordillo, R.A., Rincón, J., Zabala, L.L., Jiao, N., Karl, D.M., Li, W.K.W., Lomas, M.W., Veneziano, D., Vera, C.S., Vrugt, J.A., Martiny, A.C., 2013. Present and future global distributions of the marine Cyanobacteria Prochlorococcus and Synechococcus. Proc. Natl. Acad. Sci. U. S. A. 110, 9824–9829. https://doi.org/10.1073/pnas.1307701110

Floor, G.H., Clough, R., Lohan, M.C., Ussher, S.J., Worsfold, P.J., Quetel, C.R., 2015. Combined uncertainty estimation for the determination of the dissolved iron amount content in seawater using flow injection with chemiluminescence detection. Limnol. Oceanogr. Methods 13, 673–686. https://doi.org/10.1002/lom3.10057

Fournier, S., Chapron, B., Salisbury, J., Vandemark, D., Reul, N., 2015. Comparison of spaceborne measurements of sea surface salinity and colored detrital matter in the Amazon plume. J. Geophys. Res. Ocean. 120, 3177–3192. https://doi.org/doi.org/10.1002/2014JC010109

Frischkorn, K.R., Haley, S.T., Dyhrman, S.T., 2019. Transcriptional and Proteomic Choreography Under Phosphorus Deficiency and Re-supply in the N2 Fixing Cyanobacterium

Trichodesmium erythraeum. Front. Microbiol. 10, 1–13. https://doi.org/10.3389/fmicb.2019.00330

Garcia, H.E., Locarnini, R.A., Boyer, T.P., Antonov, J.I., Mishonov, A. V., Baranova, O.K., Zweng, M.M., Reagan, J.R., Johnson, D.R., 2013. World Ocean Atlast 2013: Vol. 3: Dissolved Oxygen, Apparent Oxygen Utilization, and Oxygen Saturation, in: Levitus, S., Mishonov, A. V. (Eds.), NOAA Atlas NESDIS 75. p. 27 pp.

Gardner, W.D., Tucholke, B.E., Richardson, M.J., Biscaye, P.E., 2017. Benthic storms, nepheloid layers, and linkage with upper ocean dynamics in the western North Atlantic. Mar. Geol. 385, 304–327. https://doi.org/10.1016/j.margeo.2016.12.012

Geider, R.J., La Roche, J., 2002. Redfield revisited: Variability of C:N:P in marine microalgae and its biochemical basis. Eur. J. Phycol. 37, 1–17. https://doi.org/10.1017/S0967026201003456

Gerringa, L.J.A., Slagter, H.A., Bown, J., van Haren, H., Laan, P., de Baar, H.J.W., Rijkenberg, M.J.A., 2017. Dissolved Fe and Fe-binding organic ligands in the Mediterranean Sea – GEOTRACES G04. Mar. Chem. 194, 100–113. https://doi.org/10.1016/j.marchem.2017.05.012

Gledhill, M., Buck, K.N., 2012. The organic complexation of iron in the marine environment: A review. Front. Microbiol. 3, 1–17. https://doi.org/10.3389/fmicb.2012.00069

Gong, N., Chen, C., Xie, L., Chen, H., Lin, X., Zhang, R., 2005. Characterization of a thermostable alkaline phosphatase from a novel species Thermus yunnanensis sp. nov. and investigation of its cobalt activation at high temperature. Biochim. Biophys. Acta - Proteins Proteomics 1750, 103–111.

Gottesman, M., Simpson, R.T., Vallee, B.L., 1969. Kinetic Properties of Cobalt Alkaline Phosphatase. Biochemistry 8, 3776–3783. https://doi.org/10.1021/bi00837a043

Gruber, N., 2008. The Marine Nitrogen Cycle: Overview and Challenges, in: Capone, D.G., Bronk, D.A., Mulholland, M., Carpenter, E.J. (Eds.), Nitrogen in the Marine Environment. Elsevier, New York, pp. 1–50.

Gruber, N., Sarmiento, J.L., 1997. Global patterns of marine nitrogen fixation and denitrification. Global Biogeochem. Cycles 11, 235–266.

Hassler, C.S., Schoemann, V., Nichols, C.M., Butler, E.C. V., Boyd, P.W., 2011. Saccharides enhance iron bioavailability to Southern Ocean phytoplankton. Proc. Natl. Acad. Sci. 108, 1076–1081. https://doi.org/10.1073/pnas.1010963108

Hatta, M., Measures, C.I., Wu, J., Roshan, S., Fitzsimmons, J.N., Sedwick, P., Morton, P., 2015. An overview of dissolved Fe and Mn distributions during the 2010–2011 U.S. GEOTRACES north Atlantic cruises: GEOTRACES GA03. Deep Sea Res. Part II Top. Stud. Oceanogr. 116, 117–129. https://doi.org/10.1016/j.dsr2.2014.07.005

Hawco, N.J., Ohnemus, D.C., Resing, J.A., Twining, B.S., Saito, M.A., 2016. A dissolved cobalt plume in the oxygen minimum zone of the eastern tropical South Pacific. Biogeosciences 13, 5697–5717. https://doi.org/10.5194/bg-13-5697-2016

Hawco, N.J., Saito, M.A., 2018. Competitive inhibition of cobalt uptake by zinc and manganese in a pacific Prochlorococcus strain: Insights into metal homeostasis in a streamlined oligotrophic cyanobacterium. Limnol. Oceanogr. 63, 2229–2249. https://doi.org/10.1002/lno.10935

Held, N.A., Mcilvin, M.R., Moran, D.M., Laub, M.T., Saito, A., 2019. Unique Patterns and Biogeochemical Relevance of Two-Component Sensing in Marine Bacteria. mSystems 4, e00317-318.

Held, N.A., Webb, E., McIlvin, M., Hutchins, D., Cohen, N., Moran, D., Kunde, K., Lohan, M., Mahaffey, C., Saito, M., 2020. Co-occurrence of Fe and P stress in natural populations of the marine diazotroph Trichodesmium. Biogeosciences Discuss. 1–26. https://doi.org/10.5194/bg-2019-493

Helliwell, K.E., Lawrence, A.D., Holzer, A., Kudahl, U.J., Sasso, S., Kräutler, B., Scanlan, D.J., Warren, M.J., Smith, A.G., 2016. Cyanobacteria and Eukaryotic Algae Use Different Chemical Variants of Vitamin B12. Curr. Biol. 26, 999–1008. https://doi.org/10.1016/j.cub.2016.02.041

Ho, T.Y., Quigg, A., Finkel, Z. V., Milligan, A.J., Wyman, K., Falkowski, P.G., Morel, F.M.M., 2003. The elemental composition of some marine phytoplankton. J. Phycol. 39, 1145–1159. https://doi.org/10.1111/j.0022-3646.2003.03-090.x

Hogle, S.L., Dupont, C.L., Hopkinson, B.M., King, A.L., Buck, K.N., Roe, K.L., Stuart, R.K., Allen, A.E., Mann, E.L., Johnson, Z.I., Barbeau, K.A., 2018. Pervasive iron limitation at subsurface chlorophyll maxima of the California Current. Proc. Natl. Acad. Sci. U. S. A. 115, 13300–13305. https://doi.org/10.1073/pnas.1813192115

Hollister, A.P., Kerr, M., Malki, K., Muhlbach, E., Robert, M., Tilney, C.L., Breitbart, M., Hubbard, K.A., Buck, K.N., 2020. Regeneration of macronutrients and trace metals during phytoplankton decay: An experimental study. Limnol. Oceanogr. https://doi.org/10.1002/lno.11429

Holm-Hansen, O., Lorenzen, C.J., Holmes, R.W., Strickland, J.D., 1965. Fluorometric Determination of Chlorophyll. ICES J. Mar. Sci. 30, 3–15.

Honeyman, B.D., Santschi, P.H., 1989. A Brownian-pumping model for oceanic trace metal scavenging: Evidence from Th isotopes. J. Mar. Res. 47, 951–992. https://doi.org/10.1357/002224089785076091

Hopkinson, B.M., Barbeau, K.A., 2012. Iron transporters in marine prokaryotic genomes and metagenomes. Environ. Microbiol. 14, 114–128. https://doi.org/10.1111/j.1462-2920.2011.02539.x

Hoppe HG, 2003. Phosphatase activity in the sea. Hydrobiologia 493, 187–200.

Hopwood, M.J., Carroll, D., Dunse, T., Hodson, A., Holding, J.M., Iriarte, J.L., Ribeiro, S., Achterberg, E.P., Cantoni, C., Carlson, D.F., Chierici, M., Clarke, J.S., Cozzi, S., Fransson, A., Juul-Pederson, T., Winding, M.S., Meire, L., 2019. How does glacier discharge affect marine biogeochemistry and primary production in the Arctic? Cryosph.

Hopwood, M.J., Santana-Gonzalez, C., Gallego-Urrea, J., Sanchez, N., Achterberg, E.P., Ardelan,

M. V, Gledhill, M., González-dávila, M., Hoffmann, L., Leiknes, Ø., Santana-casiano, J.M., Tsagaraki, T.M., Turner, D., 2020. Fe (II) stability in coastal seawater during experiments in Patagonia, Svalbard, and Gran Canaria. Biogeosciences 17, 1327–1342.

Howard, J.B., Rees, D.C., 1996. Structural basis of biological nitrogen fixation. Chem. Rev. 96, 2965–2982. https://doi.org/10.1021/cr9500545

Hurst, M.P., Bruland, K.W., 2007. An investigation into the exchange of iron and zinc between soluble, colloidal, and particulate size-fractions in shelf waters using low-abundance isotopes as tracers in shipboard incubation experiments. Mar. Chem. 103, 211–226. https://doi.org/10.1016/j.marchem.2006.07.001

Ito, A., Shi, Z., 2016. Delivery of anthropogenic bioavailable iron from mineral dust and combustion aerosols to the ocean. Atmos. Chem. Phys. 16, 85–99. https://doi.org/10.5194/acp-16-85-2016

Jakuba, R.W., Moffett, J.W., Dyhrman, S.T., 2008. Evidence for the linked biogeochemical cycling of zinc, cobalt, and phosphorus in the western North Atltic Ocean. Global Biogeochem. Cycles 22, 1–13. https://doi.org/10.1029/2007GB003119

Jickells, T.D., An, Z.S., Andersen, K.K., Baker, A.R., Bergametti, C., Brooks, N., Cao, J.J., Boyd, P.W., Duce, R.A., Hunter, K.A., Kawahata, H., Kubilay, N., LaRoche, J., Liss, P.S., Mahowald, N., Prospero, J.M., Ridgwell, A.J., Tegen, I., Torres, R., 2005. Global iron connections between desert dust, ocean biogeochemistry, and climate. Science (80-.). 308, 67–71. https://doi.org/10.1126/science.1105959

Jickells, T.D., Buitenhuis, E., Altieri, K., Baker, A.R., Capone, D., Duce, R.A., Dentener, F., Fennel, K., Kanakidou, M., LaRoche, J., Lee, K., Liss, P., Middelburg, J.J., Moore, J.K., Okin, G., Oschlies, A., Sarin, M., Seitzinger, S., Sharples, J., Singh, A., Suntharalingam, P., Uematsu, M., Zamora, L.M., 2017. A reevaluation of the magnitude and impacts of anthropogenic atmospheric nitrogen inputs on the ocean. Global Biogeochem. Cycles 31, 289–305. https://doi.org/10.1002/2016GB005586

John, S.G., Conway, T.M., 2014. A role for scavenging in the marine biogeochemical cycling of zinc and zinc isotopes. Earth Planet. Sci. Lett. 394, 159–167. https://doi.org/10.1016/j.epsl.2014.02.053

Johnson, K., Elrod, V., Fitzwater, S., 2007. Developing standards for dissolved iron in seawater. Eos (Washington. DC). 88, 131–132. https://doi.org/10.1029/2007EO110003

Jordan, P., Fromme, P., Klukas, O., Witt, H.T., Saenger, W., Krauß, N., 2001. X-Ray Crystallographic Structure Analysis of Cyanobacterial Photosystem I at 2.5 Å Resolution. Nature 411, 909–917. https://doi.org/https://doi.org/10.1038/35082000

Kagaya, S., Maeba, E., Inoue, Y., Kamichatani, W., 2009. A solid phase extraction using a chelate resin immobilizing carboxymethylated pentaethylenehexamine for separation and preconcentration of trace elements in water samples. Talanta 79, 146–152. https://doi.org/10.1016/j.talanta.2009.03.016

Kathuria, S., Martiny, A.C., 2011. Prevalence of a calcium-based alkaline phosphatase associated with the marine cyanobacterium Prochlorococcus and other ocean bacteria. Environ.

Microbiol. 13, 74–83. https://doi.org/10.1111/j.1462-2920.2010.02310.x

Kellogg, M.M., McIlvin, M.R., Vedamati, J., Twining, B.S., Marchetti, A., Moran, D.M., Saito, M.A., 2020. Efficient zinc/cobalt interreplacement in northeast Pacific diatoms and relationship to high surface dissolved Co:Zn ratios. Limnol. Oceanogr. 1–56. https://doi.org/10.1002/lno.11471

Kirchman, D., 1996. Microbial ferrous wheel. Nature. https://doi.org/10.1038/383303a0

Klunder, M.B., Bauch, D., Laan, P., Baar, H.J.W. De, Heuven, S. Van, Ober, S., 2012. Dissolved iron in the Arctic shelf seas and surface waters of the central Arctic Ocean : Impact of Arctic river water and ice-melt. J. Geophys. Res. 117, 1–18. https://doi.org/10.1029/2011JC007133

Kolowith, L.C., Ingall, E.D., Benner, R., 2001. Composition and cycling of marine organic phosphorus. Limnol. Oceanogr. 46, 309–320. https://doi.org/10.4319/lo.2001.46.2.0309

Krishnaswamy, M., Kenkare, U.W., 1970. The effect of pH, temperature, and organic solvents on the kinetic parameters of Escherichia coli alkaline phosphatase. J. Biol. Chem. 245, 3956–3963.

Kuma, K., Nishioka, J., Matsunaga, K., 1996. Controls on iron(III) hydroxide solubility in seawater: The influence of pH and natural organic chelators. Limnol. Oceanogr. 41, 396–407. https://doi.org/10.4319/lo.1996.41.3.0396

Kunde, K., Wyatt, N.J., González-Santana, D., Tagliabue, A., Mahaffey, C., Lohan, M.C., 2019. Iron Distribution in the Subtropical North Atlantic: The Pivotal Role of Colloidal Iron. Global Biogeochem. Cycles 33, 1532–1547. https://doi.org/10.1029/2019GB006326

Kustka, A., Sañudo-Wilhelmy, S., Carpenter, E.J., Capone, D.G., Raven, J.A., 2003. A revised estimate of the iron use efficiency of nitrogen fixation, with special reference to the marine cyanobacterium Trichodesmium spp. (Cyanophyta). J. Phycol. 39, 12–25. https://doi.org/10.1046/j.1529-8817.2003.01156.x

Labry, C., Delmas, D., Herbland, A., 2005. Phytoplankton and bacterial alkaline phosphatase activities in relation to phosphate and DOP availability within the Gironde plume waters (Bay of Biscay). J. Exp. Mar. Bio. Ecol. 318, 213–225. https://doi.org/10.1016/j.jembe.2004.12.017

Lacan, F., Radic, A., Jeandel, C., Poitrasson, F., Sarthou, G., Pradoux, C., Freydier, R., 2008. Measurement of the isotopic composition of dissolved iron in the open ocean. Geophys. Res. Lett. 35, 1–5. https://doi.org/10.1029/2008GL035841

Laglera, L.M., Van Den Berg, C.M.G., 2009. Evidence for geochemical control of iron by humic substances in seawater. Limnol. Oceanogr. 54, 610–619. https://doi.org/10.4319/lo.2009.54.2.0610

Lam, P.J., 2018. Size-fractionated major and minor particle composition and concentration from R/V Knorr KN199-04, KN204-01 in the subtropical North Atlantic Ocean from 2010-2011 (U.S. GEOTRACES NAT project).

Lam, P.J., Ohnemus, D.C., Auro, M.E., 2015. Size-fractionated major particle composition and

concentrations from the US GEOTRACES North Atlantic Zonal Transect. Deep. Res. Part II Top. Stud. Oceanogr. 116, 303–320. https://doi.org/10.1016/j.dsr2.2014.11.020

Lannuzel, D., Schoemann, V., de Jong, J., Tison, J.L., Chou, L., 2007. Distribution and biogeochemical behaviour of iron in the East Antarctic sea ice. Mar. Chem. 106, 18–32. https://doi.org/10.1016/j.marchem.2006.06.010

Lannuzel, D., Vancoppenolle, M., Van Der Merwe, P., De Jong, J., Meiners, K.M., Grotti, M., Nishioka, J., Schoemann, V., 2016. Iron in sea ice: Review and new insights. Elementa 4, 1–19. https://doi.org/10.12952/journal.elementa.000130

Lazdunski, C., Lazdunski, M., 1969. Zn2+ and Co2+-Alkaline Phosphatases of E. coli. Eur. J. Biochem. 7, 294–300.

Lindell, D., Post, A.F., 2001. Ecological Aspects of ntcA Gene Expression and Its Use as an Indicator of the Nitrogen Status of Marine Synechococcus spp. Appl. Environ. Microbiol. 67, 3340–3349. https://doi.org/10.1128/AEM.67.8.3340-3349.2001

Lis, H., Kranzler, C., Keren, N., Shaked, Y., 2015a. A Comparative Study of Iron Uptake Rates and Mechanisms amongst Marine and Fresh Water Cyanobacteria: Prevalence of Reductive Iron Uptake. Life 5, 841–60. https://doi.org/10.3390/life5010841

Lis, H., Shaked, Y., Kranzler, C., Keren, N., Morel, F.M.M., 2015b. Iron bioavailability to phytoplankton: an empirical approach. ISME J. 9, 1003–1013. https://doi.org/10.1038/ismej.2014.199

Liu, X., Millero, F.J., 1999. The solubility of iron hydroxide in sodium chloride solutions. Geochim. Cosmochim. Acta 63, 3487–3497. https://doi.org/10.1016/S0016-7037(99)00270-7

Lohan, M.C., Aguilar-Islas, A.M., Bruland, K.W., 2006. Direct determination of iron in acidified (pH 1.7) seawater samples by flow injection analysis with catalytic spectrophotometric detection: Application and intercomparison. Limnol. Oceanogr. Methods 4, 164–171. https://doi.org/10.4319/lom.2006.4.164

Lohan, M.C., Aguilar-Islas, A.M., Franks, R.P., Bruland, K.W., 2005a. Determination of iron and copper in seawater at pH 1.7 with a new commercially available chelating resin, NTA Superflow. Anal. Chim. Acta 530, 121–129. https://doi.org/10.1016/j.aca.2004.09.005

Lohan, M.C., Bruland, K.W., 2008. Elevated Fe(II) and dissolved Fe in hypoxic shelf waters off Oregon and Washington: An enhanced source of iron to coastal upwelling regimes. Environ. Sci. Technol. 42, 6462–6468. https://doi.org/10.1021/es800144j

Lohan, M.C., Crawford, D.W., Purdie, D.A., Statham, P.J., 2005b. Iron and zinc enrichments in the northeastern subarctic Pacific: Ligand production and zinc availability in response to phytoplankton growth. Limnol. Oceanogr. 50, 1427–1437. https://doi.org/10.4319/lo.2005.50.5.1427

Lohan, M.C., Tagliabue, A., 2018. Oceanic Micronutrients: Trace Metals that are Essential for Marine Life. Elements 14, 385–390.

Lomas, M.W., Burke, A.L., Lomas, D. a., Bell, D.W., Shen, C., Dyhrman, S.T., Ammerman, J.W., 2010. Sargasso Sea phosphorus biogeochemistry: an important role for dissolved organic phosphorus (DOP). Biogeosciences 7, 695–210. https://doi.org/10.5194/bgd-6-10137-2009

Longhurst, A., Sathyendranath, S., Platt, T., Caverhill, C., 1995. An estimate of global primary production in the ocean from satellite radiometer data. J. Plankton Res. 17, 1245–1271. https://doi.org/10.1093/plankt/17.6.1245

Lough, A.J.M., Homoky, W.B., Connelly, D.P., Nakamura, K., Abyaneh, M.K., Kaulich, B., Mills, R.A., 2019. Soluble iron conservation and colloidal iron dynamics in a hydrothermal plume. Chem. Geol. https://doi.org/10.1016/j.chemgeo.2019.01.001

Lu, X., Zhu, H., 2005. Tube-Gel Digestion. Mol. Cell. Proteomics 4, 1948–1958. https://doi.org/10.1074/mcp.M500138-MCP200

Luo, C., Mahowald, N., Bond, T., Chuang, P.Y., Artaxo, P., Siefert, R., Chen, Y., Schauer, J., 2008. Combustion iron distribution and deposition. Global Biogeochem. Cycles 22, 1–17. https://doi.org/10.1029/2007GB002964

Luo, H., Benner, R., Long, R. a, Hu, J., 2009. Subcellular localization of marine bacterial alkaline phosphatases. Proc. Natl. Acad. Sci. U. S. A. 106, 21219–21223. https://doi.org/10.1073/pnas.0907586106

MacLean, B., Tomazela, D.M., Shulman, N., Chambers, M., Finney, G.L., Frewen, B., Kern, R., Tabb, D.L., Liebler, D.C., MacCoss, M.J., 2010. Skyline: An open source document editor for creating and analyzing targeted proteomics experiments. Bioinformatics 26, 966–968. https://doi.org/10.1093/bioinformatics/btq054

Macovei, V.A., Torres-Valdés, S., Hartman, S.E., Schuster, U., Moore, C.M., Brown, P.J., Hydes, D.J., Sanders, R.J., 2019. Temporal variability in the nutrient biogeochemistry of the surface North Atlantic - fifteen years of Ship of Opportunity data. Global Biogeochem. Cycles 33, 1674–1692. https://doi.org/10.1029/2018GB006132

Mahaffey, C., Reynolds, S., Davis, C.E., Lohan, M.C., 2014. Alkaline phosphatase activity in the subtropical ocean: insights from nutrient, dust and trace metal addition experiments. Front. Mar. Sci. 1, 1-13 (Article 73). https://doi.org/10.3389/fmars.2014.00073

Mahaffey, C., Williams, R.G., Wolff, G.A., Mahowald, N., Anderson, W., Woodward, M., 2003. Biogeochemical signatures of nitrogen fixation in the eastern North Atlantic. Geophys. Res. Lett. 30, 33–36. https://doi.org/10.1029/2002GL016542

Maldonado, M.T., Boyd, P.W., LaRoche, J., Strzepek, R., Waite, A., Bowie, A.R., Croot, P.L., Frew, R.D., Price, N.M., 2001. Iron uptake and physiological response of phytoplankton during a mesoscale Southern Ocean iron enrichment. Limnol. Oceanogr. 46, 1802–1808. https://doi.org/10.4319/lo.2001.46.7.1802

Malmstrom, R.R., Rodrigue, S., Huang, K.H., Kelly, L., Kern, S.E., Thompson, A., Roggensack, S., Berube, P.M., Henn, M.R., Chisholm, S.W., 2013. Ecology of uncultured Prochlorococcus clades revealed through single-cell genomics and biogeographic analysis. ISME J. 7, 184–198. https://doi.org/10.1038/ismej.2012.89

Martin, J.H., 1990. Glacial-interglacial CO2 change: The Iron Hypothesis. Paleoceanography 5, 1–13. https://doi.org/10.1029/PA005i001p00001

Martin, J.H., Gordon, R.M., Fitzwater, S., Broenkow, W.W., 1989. Vertex: phytoplankton/iron studies in the Gulf of Alaska. Deep Sea Res. Part A, Oceanogr. Res. Pap. 36, 649–680. https://doi.org/10.1016/0198-0149(89)90144-1

Martinez, J., Azam, F., 1993. Periplasmic aminopeptidase and alkaline phosphatase activities in a marine bacterium: implications for substrate processing in the sea. Mar. Ecol. Prog. Ser. 92, 89–97. https://doi.org/10.3354/meps092089

Martinez, M.B., Flickinger, M.C., Nelsestuen, G.L., 1996. Accurate kinetic modeling of alkaline phosphatase in the Escherichia coli periplasm: Implications for enzyme properties and substrate diffusion. Biochemistry 35, 1179–1186. https://doi.org/10.1021/bi951955a

Martiny, A.C., Coleman, M.L., Chisholm, S.W., 2006. Phosphate acquisition genes in Prochlorococcus ecotypes: Evidence for genome-wide adaptation. Proc. Natl. Acad. Sci. 103, 12552–12557. https://doi.org/10.1073/pnas.0601301103

Martiny, A.C., Huang, Y., Li, W., 2009. Occurrence of phosphate acquisition genes in Prochlorococcus cells from different ocean regions. Environ. Microbiol. 11, 1340–1347. https://doi.org/10.1111/j.1462-2920.2009.01860.x

Martiny, A.C., Lomas, M.W., Fu, W., Boyd, P.W., Chen, Y.L., Cutter, G.A., Ellwood, M.J., Furuya, K., Hashihama, F., Kanda, J., Karl, D.M., Kodama, T., Li, Q.P., Ma, J., Moutin, T., Woodward, E.M.S., Moore, J.K., 2019. Biogeochemical controls of surface ocean phosphate. Sci. Adv. 5, 1–10. https://doi.org/10.1126/sciadv.aax0341

Mather, R.L., Reynolds, S.E., Wolff, G.A., Williams, R.G., Torres-Valdes, S., Woodward, E.M.S., Landolfi, A., Pan, X., Sanders, R., Achterberg, E.P., 2008. Phosphorus cycling in the North and South Atlantic Ocean subtropical gyres. Nat. Geosci. 1, 439–443. https://doi.org/10.1038/ngeo232

Mawji, E., Gledhill, M., Milton, J.A., Tarran, G.A., Ussher, S., Thompson, A., Wolff, G.A., Worsfold, P.J., Achterberg, E.P., 2008. Hydroxamate siderophores: Occurrence and importance in the Atlantic Ocean. Environ. Sci. Technol. 42, 8675–8680. https://doi.org/10.1021/es801884r

Mazard, S., Ostrowski, M., Partensky, F., Scanlan, D.J., 2012. Multi-locus sequence analysis, taxonomic resolution and biogeography of marine Synechococcus. Environ. Microbiol. 14, 372–386. https://doi.org/10.1111/j.1462-2920.2011.02514.x

Mazzotta, M.G., McIlvin, M.R., Saito, M.A., 2020. Characterization of the Fe metalloproteome of a ubiquitous marine heterotroph Pseudoalteromonas (BB2-AT2): Multiple bacterioferritin copies enable significant Fe storage. Metallomics 12, 654–667. https://doi.org/10.1039/d0mt00034e

Measures, C.I., Landing, W.M., Brown, M.T., Buck, C.S., 2008. High-resolution Al and Fe data from the Atlantic Ocean CLIVAR-CO2 Repeat Hydrography A16N transect: Extensive linkages between atmospheric dust and upper ocean geochemistry. Global Biogeochem. Cycles 22, 1–10. https://doi.org/10.1029/2007GB003042

Mellett, T., Brown, M.T., Chappell, P.D., Duckham, C., Fitzsimmons, J.N., Till, C.P., Sherrell, R.M., Maldonado, M.T., Buck, K.N., 2018. The biogeochemical cycling of iron, copper, nickel, cadmium, manganese, cobalt, lead, and scandium in a California Current experimental study. Limnol. Oceanogr. 63, S425–S447. https://doi.org/10.1002/lno.10751

Merényi, G., Lind, J., Eriksen, T.E., 1990. Luminol chemiluminescence: Chemistry, excitation, emitter. J. Biolumin. Chemilumin. 5, 53–56. https://doi.org/10.1002/bio.1170050111

Millero, F.J., Sotolongo, S., Izaguirre, M., 1987. The oxidation kinetics of Fe(II) in seawater. Geochim. Cosmochim. Acta 5, 793–801.

Millero, F.J., Yao, W., Aicher, J., 1995. The speciation of Fe(II) and Fe(III) in natural waters. Mar. Chem. 50, 21–39.

Mills, M.M., Moore, C.M., Langlois, R., Milne, A., Achterberg, E.P., Nachtigall, K., Lochte, K., Geider, R.J., La Roche, J., 2008. Nitrogen and phosphorus co-limitation of bacterial productivity and growth. Limnol. Oceanogr. 53, 824–834.

Mills, M.M., Ridame, C., Davey, M., La Roche, J., Geider, R.J., 2004. Iron and phosphorus co-limit nitrogen fixation in the eastern tropical North Atlantic. Nature 429, 292–294. https://doi.org/10.1038/nature02550

Milne, A., Landing, W., Bizimis, M., Morton, P., 2010. Determination of Mn, Fe, Co, Ni, Cu, Zn, Cd and Pb in seawater using high resolution magnetic sector inductively coupled mass spectrometry (HR-ICP-MS). Anal. Chim. Acta 665, 200–207. https://doi.org/10.1016/j.aca.2010.03.027

Milne, A., Schlosser, C., Wake, B.D., Achterberg, E.P., Chance, R., Baker, A.R., Forryan, A., Lohan, M.C., 2017. Particulate phases are key in controlling dissolved iron concentrations in the (sub)tropical North Atlantic. Geophys. Res. Lett. 44, 2377–2387. https://doi.org/10.1002/2016GL072314

Moffett, J.W., Goepfert, T.J., Naqvi, S.W.A., 2007. Reduced iron associated with secondary nitrite maxima in the Arabian Sea. Deep. Res. Part I Oceanogr. Res. Pap. 54, 1341–1349. https://doi.org/10.1016/j.dsr.2007.04.004

Moffett, J.W., Ho, J., 1996. Oxidation of cobalt and manganese in seawater via a common microbially catalyzed pathway. Geochim. Cosmochim. Acta 60, 3415–3424. https://doi.org/10.1016/0016-7037(96)00176-7

Montoya, J.P., Carpenter, E.J., Capone, D.G., 2002. Nitrogen fixation and nitrogen isotope abundances in zooplankton of the oligotrophic North Atlantic. Limnol. Oceanogr. 47, 1617–1628. https://doi.org/10.4319/lo.2002.47.6.1617

Moore, C.M., Mills, M.M., Achterberg, E.P., Geider, R.J., LaRoche, J., Lucas, M.I., McDonagh, E.L., Pan, X., Poulton, A.J., Rijkenberg, M.J.A., Suggett, D.J., Ussher, S.J., Woodward, E.M.S., 2009. Large-scale distribution of Atlantic nitrogen fixation controlled by iron availability. Nat. Geosci. 2, 867–871. https://doi.org/10.1038/ngeo667

Moore, C.M., Mills, M.M., Arrigo, K.R., Berman-Frank, I., Bopp, L., Boyd, P.W., Galbraith, E.D., Geider, R.J., Guieu, C., Jaccard, S.L., Jickells, T.D., La Roche, J., Lenton, T.M., Mahowald,

N.M., Marañón, E., Marinov, I., Moore, J.K., Nakatsuka, T., Oschlies, A., Saito, M.A., Thingstad, T.F., Tsuda, A., Ulloa, O., 2013. Processes and patterns of oceanic nutrient limitation. Nat. Geosci. 6, 701–710. https://doi.org/10.1038/NGEO1765

Moore, C.M., Mills, M.M., Langlois, R., Milne, A., Achterberg, E.P., La Roche, J., Geider, R.J., 2008. Relative influence of nitrogen and phosphorous availability on phytoplankton physiology and productivity in the oligotrophic sub-tropical North Atlantic Ocean. Limnol. Oceanogr. 53, 291–305. https://doi.org/10.4319/lo.2008.53.1.0291

Moore, J.K., Doney, S.C., Glover, D.M., Fung, I.Y., 2001. Iron cycling and nutrient-limitation patterns in surface waters of the world ocean. Deep. Res. Part II Top. Stud. Oceanogr. 49, 463–507. https://doi.org/10.1016/S0967-0645(01)00109-6

Moore, L.R., Post, A.F., Rocap, G., Chisholm, S.W., 2002. Utilization of different nitrogen sources by the marine cyanobacteria Prochlorococcus and Synechococcus. Limnol. Oceanogr. 47, 989–996. https://doi.org/10.4319/lo.2002.47.4.0989

Morel, F.M.M., 2003. The Biogeochemical Cycles of Trace Metals in the Oceans. Science (80-.). 300, 944–947. https://doi.org/10.1126/science.1083545

Murphy, J., Riley, J.P., 1962. A modified single solution method for the determination of phosphate in natural waters. Anal. Chim. Acta 27, 31–36. https://doi.org/10.1016/S0003-2670(00)88444-5

Nishioka, J., Obata, H., Tsumune, D., 2013. Evidence of an extensive spread of hydrothermal dissolved iron in the Indian Ocean. Earth Planet. Sci. Lett. 361, 26–33. https://doi.org/10.1016/j.epsl.2012.11.040

Nishioka, J., Takeda, S., De Baar, H.J.W., Croot, P.L., Boye, M., Laan, P., Timmermans, K.R., 2005. Changes in the concentration of iron in different size fractions during an iron enrichment experiment in the open Southern Ocean. Mar. Chem. 95, 51–63. https://doi.org/10.1016/j.marchem.2004.06.040

Nishioka, J., Takeda, S., Wong, C.S., Johnson, W.K., 2001. Size-fractionated iron concentrations in the northeast Pacific Ocean: Distribution of soluble and small colloidal iron. Mar. Chem. 74, 157–179. https://doi.org/10.1016/S0304-4203(01)00013-5

Noble, A.E., Ohnemus, D.C., Hawco, N.J., Lam, P.J., Saito, M.A., 2017. Coastal sources, sinks and strong organic complexation of dissolved cobalt within the US North Atlantic GEOTRACES transect GA03. Biogeosciences 14, 2715–2739. https://doi.org/10.5194/bg-14-2715-2017

Obata, H., Karatani, H., Matsui, M., Nakayama, E., 1997. Fundamental studies for chemical speciation of iron in seawater with an improved analytical method. Mar. Chem. 56, 97–106. https://doi.org/10.1016/S0304-4203(96)00082-5

Obata, H., Karatani, H., Nakayama, E., 1993. Automated Determination of Iron in Seawater by Chelating Resin Concentration and Chemiluminescence Detection. Anal. Chem. 65, 1524–1528.

Ohnemus, D.C., Lam, P.J., 2015. Cycling of lithogenic marine particles in the US GEOTRACES North Atlantic transect. Deep. Res. Part II Top. Stud. Oceanogr. 116, 283–302.

https://doi.org/10.1016/j.dsr2.2014.11.019

Ohnemus, D.C., Rauschenberg, S., Krause, J.W., Brzezinski, M.A., Collier, J.L., Geraci-Yee, S., Baines, S.B., Twining, B.S., 2016. Silicon content of individual cells of Synechococcus from the North Atlantic Ocean. Mar. Chem. 187, 16–24. https://doi.org/10.1016/j.marchem.2016.10.003

Partensky, F., Garczarek, L., 2010. Prochlorococcus : Advantages and Limits of Minimalism. Ann. Rev. Mar. Sci. 2, 305–331. https://doi.org/10.1146/annurev-marine-120308-081034

Patey, M.D., Rijkenberg, M.J.A., Statham, P.J., Stinchcombe, M.C., Achterberg, E.P., Mowlem, M., 2008. Determination of nitrate and phosphate in seawater at nanomolar concentrations. TrAC - Trends Anal. Chem. 27, 169–182. https://doi.org/10.1016/j.trac.2007.12.006

Paytan, A., Mclaughlin, K., 2007. The Oceanic Phosphorus Cycle. Chem. Rev. 107, 563–576. https://doi.org/10.1021/cr0503613

Pham, A.N., Rose, A.L., Feitz, A.J., Waite, T.D., 2006. Kinetics of Fe(III) precipitation in aqueous solutions at pH 6.0-9.5 and 25°C. Geochim. Cosmochim. Acta 70, 640–650. https://doi.org/10.1016/j.gca.2005.10.018

Pierella Karlusich, J.J., Ibarbalz, F.M., Bowler, C., 2020. Phytoplankton in the Tara Ocean. Ann. Rev. Mar. Sci. 12, 233–265.

Polyviou, D., Machelett, M.M., Hitchcock, A., Baylay, A.J., MacMillan, F., Mark Moore, C., Bibby, T.S., Tews, I., 2018. Structural and functional characterization of IdiA/FutA (Tery_3377), an iron-binding protein from the ocean diazotroph Trichodesmium erythraeum. J. Biol. Chem. 293, 18099–18109. https://doi.org/10.1074/jbc.RA118.001929

Price, N.M., Morel, F.M.M., 1990. Cadmium and cobalt substitution for zinc in a marine diatom. Nature. https://doi.org/10.1038/344658a0

Rapp, I., Schlosser, C., Rusiecka, D., Gledhill, M., Achterberg, E.P., 2017. Automated preconcentration of Fe, Zn, Cu, Ni, Cd, Pb, Co, and Mn in seawater with analysis using high-resolution sector field inductively-coupled plasma mass spectrometry. Anal. Chim. Acta 976, 1–13. https://doi.org/10.1016/j.aca.2017.05.008

Redfield, A., 1958. The Biological Control of Chemical Factors in the Environment. Am. Sci. 46, 205–221.

Resing, J.A., Sedwick, P.N., German, C.R., Jenkins, W.J., 2015. Basin-scale transport of hydrothermal dissolved metals across the South Pacific Ocean. Nature 523, 200–203. https://doi.org/10.1038/nature14577

Revels, B.N., Ohnemus, D.C., Lam, P.J., Conway, T.M., John, S.G., 2015. The isotopic signature and distribution of particulate iron in the North Atlantic Ocean. Deep. Res. Part II Top. Stud. Oceanogr. 116, 321–331. https://doi.org/10.1016/j.dsr2.2014.12.004

Reynolds, S., Mahaffey, C., Roussenov, V., Williams, R.G., 2014. Evidence for production and lateral transport of dissolved organic phosphorus in the eastern subtropical North Atlantic.

Global Biogeochem. Cycles 28, 805–824. https://doi.org/10.1002/2013GB004801

Rickaby, R.E.M., 2015. Goldilocks and the three inorganic equilibria: How earth's chemistry and life coevolve to be nearly in tune. Philos. Trans. R. Soc. A Math. Phys. Eng. Sci. 373. https://doi.org/10.1098/rsta.2014.0188

Rijkenberg, M.J.A., Middag, R., Laan, P., Gerringa, L.J.A., van Aken, H.M., Schoemann, V., de Jong, J.T.M., de Baar, H.J.W., 2014. The Distribution of Dissolved Iron in the West Atlantic Ocean. PLoS One 9, e101323. https://doi.org/10.1371/journal.pone.0101323

Rodriguez, F., Lillington, J., Johnson, S., Timmel, C.R., Lea, S.M., Berks, B.C., 2014. Crystal structure of the Bacillus subtilis phosphodiesterase PhoD reveals an iron and calcium-containing active site. J. Biol. Chem. 289, 30889–30899. https://doi.org/10.1074/jbc.M114.604892

Rose, A.L., Waite, T.D., 2003. Kinetics of hydrolysis and precipitation of ferric iron in seawater. Environ. Sci. Technol. 37, 3897–3903. https://doi.org/10.1021/es034102b

Rose, A.L., Waite, T.D., 2001. Chemiluminescence of luminol in the presence of iron(II) and oxygen: Oxidation mechanism and implications for its analytical use. Anal. Chem. 73, 5909–5920. https://doi.org/10.1021/ac015547q

Roshan, S., DeVries, T., Wu, J., Chen, G., 2018. The Internal Cycling of Zinc in the Ocean. Global Biogeochem. Cycles 32, 1833–1849. https://doi.org/10.1029/2018GB006045

Roshan, S., Wu, J., Jenkins, W.J., 2016. Long-range transport of hydrothermal dissolved Zn in the tropical South Pacific. Mar. Chem. 183, 25–32. https://doi.org/10.1016/j.marchem.2016.05.005

Rubin, M., Berman-Frank, I., Shaked, Y., 2011. Dust-and mineral-iron utilization by the marine dinitrogen-fixer Trichodesmium. Nat. Geosci. 4, 529–534. https://doi.org/10.1038/ngeo1181

Saito, M.A., Bertrand, E.M., Duffy, M.E., Gaylord, D.A., Held, N.A., Judson Hervey IV, W., Hettich, R.L., Jagtap, P.D., Janech, M.G., Kinkade, D.B., Leary, D.H., McIlvin, M.R., Moore, E.K., Morris, R.M., Neely, B.A., Nunn, B.L., Saunders, J.K., Shepherd, A.I., Symmonds, N.I., Walsh, D.A., 2019. Progress and Challenges in Ocean Metaproteomics and Proposed Best Practices for Data Sharing. J. Proteome Res. https://doi.org/10.1021/acs.jproteome.8b00761

Saito, M.A., Bertrand, E.M., Dutkiewicz, S., Bulygin, V. V., Moran, D.M., Monteiro, F.M., Follows, M.J., Valois, F.W., Waterbury, J.B., 2011. Iron conservation by reduction of metalloenzyme inventories in the marine diazotroph Crocosphaera watsonii. Proc. Natl. Acad. Sci. 108, 2184–2189. https://doi.org/10.1073/pnas.1006943108

Saito, M.A., Goepfert, T.J., Ritt, J.T., 2008. Some thoughts on the concept of colimitation: Three definitions and the importance of bioavailability. Limnol. Oceanogr. 53, 276–290. https://doi.org/10.4319/lo.2008.53.1.0276

Saito, M.A., McIlvin, M.R., Moran, D.M., Goepfert, T.J., DiTullio, G.R., Post, A.F., Lamborg, C.H., 2014. Multiple nutrient stresses at intersecting Pacific Ocean biomes detected by protein biomarkers. Science (80-.). 345, 1173–1177. https://doi.org/10.1126/science.1256450

Saito, M.A., Mcilvin, M.R., Moran, D.M., Santoro, A.E., Dupont, C.L., Rafter, P.A., Saunders, J.K., Kaul, D., Lamborg, C.H., Westley, M., Valois, F., Waterbury, J.B., 2020. Abundant nitrite-oxidizing metalloenzymes in the mesopelagic zone of the tropical Pacific Ocean. Nat. Geosci. https://doi.org/10.1038/s41561-020-0565-6

Saito, M.A., Moffett, J.W., 2002. Temporal and spatial variability of cobalt in the Atlantic Ocean. Geochim. Cosmochim. Acta 66, 1943–1953. https://doi.org/10.1016/S0016-7037(02)00829-3

Saito, M.A., Noble, A.E., Hawco, N., Twining, B.S., Ohnemus, D.C., John, S.G., Lam, P., Conway, T.M., Johnson, R., Moran, D., McIlvin, M., 2017. The acceleration of dissolved cobalt's ecological stoichiometry due to biological uptake, remineralization, and scavenging in the Atlantic Ocean. Biogeosciences 14, 4637–4662. https://doi.org/10.5194/bg-14-4637-2017

Saito, M.A., Noble, A.E., Tagliabue, A., Goepfert, T.J., Lamborg, C.H., Jenkins, W.J., 2013. Slow-spreading submarine ridges in the South Atlantic as a significant oceanic iron source. Nat. Geosci. 6, 775–779. https://doi.org/10.1038/ngeo1893

Saito, M.A., Rocap, G., Moffett, J.W., 2005. Production of cobalt binding ligands in a Synechococcus feature at the Costa Rica upwelling dome. Limnol. Oceanogr. 50, 279–290. https://doi.org/10.4319/lo.2005.50.1.0279

Saito, M.A., Sigman, D.M., Morel, F.M.M., 2003. The bioinorganic chemistry of the ancient ocean : the co-evolution of cyanobacterial metal requirements and biogeochemical cycles at the Archean-Proterozoic boundary ? Inorganica Chim. Acta 356, 308–318. https://doi.org/10.1016/S0020-1693(03)00442-0

Sander, S.G., Koschinsky, A., 2011. Metal flux from hydrothermal vents increased by organic complexation. Nat. Geosci. 4, 145–150. https://doi.org/10.1038/ngeo1088

Santos-Beneit, F., 2015. The Pho regulon: A huge regulatory network in bacteria. Front. Microbiol. 6, 1–13. https://doi.org/10.3389/fmicb.2015.00402

Sarthou, G., Bucciarelli, E., Chever, F., Hansard, S.P., González-Dávila, M., Santana-Casiano, J.M., Planchon, F., Speich, S., 2011. Labile Fe(II) concentrations in the Atlantic sector of the Southern Ocean along a transect from the subtropical domain to the Weddell Sea Gyre. Biogeosciences 8, 2461–2479. https://doi.org/10.5194/bg-8-2461-2011

Scanlan, D.J., Mann, N.H., Carr, N.G., 1993. The response of the picoplanktonic marine cyanobacterium Synechococcus species WH7803 to phosphate starvation involves a protein homologous to the periplasmic phosphate-binding protein of Escherichia coli. Mol. Microbiol. 10, 181–191.

Schepanski, K., Tegen, I., Macke, A., 2009. Saharan dust transport and deposition towards the tropicalnorthern Atlantic. Atmos. Chem. Phys. 9, 1173–1189. https://doi.org/10.5194/acp-9-1173-2009

Schlitzer, R., 2016. Ocean Data View [WWW Document]. URL http://odv.awi.de

Schlitzer, R., Anderson, R.F., Dodas, E.M., Lohan, M., Geibert, W., Tagliabue, A., Bowie, A., Jeandel, C., Maldonado, M.T., Landing, W.M., Cockwell, D., Abadie, C., Abouchami, W.,

Achterberg, E.P., Agather, A., Aguliar-Islas, A., van Aken, H.M., Andersen, M., Archer, C., Auro, M., de Baar, H.J., Baars, O., Baker, A.R., Bakker, K., Basak, C., Baskaran, M., Bates, N.R., Bauch, D., van Beek, P., Behrens, M.K., Black, E., Bluhm, K., Bopp, L., Bouman, H., Bowman, K., Bown, J., Boyd, P., Boye, M., Boyle, E.A., Branellec, P., Bridgestock, L., Brissebrat, G., Browning, T., Bruland, K.W., Brumsack, H.-J., Brzezinski, M., Buck, C.S., Buck, K.N., Buesseler, K., Bull, A., Butler, E., Cai, P., Mor, P.C., Cardinal, D., Carlson, C., Carrasco, G., Casacuberta, N., Casciotti, K.L., Castrillejo, M., Chamizo, E., Chance, R., Charette, M.A., Chaves, J.E., Cheng, H., Chever, F., Christl, M., Church, T.M., Closset, I., Colman, A., Conway, T.M., Cossa, D., Croot, P., Cullen, J.T., Cutter, G.A., Daniels, C., Dehairs, F., Deng, F., Dieu, H.T., Duggan, B., Dulaquais, G., Dumousseaud, C., Echegoyen-Sanz, Y., Edwards, R.L., Ellwood, M., Fahrbach, E., Fitzsimmons, J.N., Russell Flegal, A., Fleisher, M.Q., van de Flierdt, T., Frank, M., Friedrich, J., Fripiat, F., Fröllje, H., Galer, S.J.G., Gamo, T., Ganeshram, R.S., Garcia-Orellana, J., Garcia-Solsona, E., Gault-Ringold, M., George, E., Gerringa, L.J.A., Gilbert, M., Godoy, J.M., Goldstein, S.L., Gonzalez, S.R., Grissom, K., Hammerschmidt, C., Hartman, A., Hassler, C.S., Hathorne, E.C., Hatta, M., Hawco, N., Hayes, C.T., Heimbürger, L.-E., Helgoe, J., Heller, M., Henderson, G.M., Henderson, P.B., van Heuven, S., Ho, P., Horner, T.J., Hsieh, Y.-T., Huang, K.-F., Humphreys, M.P., Isshiki, K., Jacquot, J.E., Janssen, D.J., Jenkins, W.J., John, S., Jones, E.M., Jones, J.L., Kadko, D.C., Kayser, R., Kenna, T.C., Khondoker, R., Kim, T., Kipp, L., Klar, J.K., Klunder, M., Kretschmer, S., Kumamoto, Y., Laan, P., Labatut, M., Lacan, F., Lam, P.J., Lambelet, M., Lamborg, C.H., Le Moigne, F.A.C., Le Roy, E., Lechtenfeld, O.J., Lee, J.-M., Lherminier, P., Little, S., López-Lora, M., Lu, Y., Masque, P., Mawji, E., Mcclain, C.R., Measures, C., Mehic, S., Barraqueta, J.-L.M., van der Merwe, P., Middag, R., Mieruch, S., Milne, A., Minami, T., Moffett, J.W., Moncoiffe, G., Moore, W.S., Morris, P.J., Morton, P.L., Nakaguchi, Y., Nakayama, N., Niedermiller, J., Nishioka, J., Nishiuchi, A., Noble, A., Obata, H., Ober, S., Ohnemus, D.C., van Ooijen, J., O'Sullivan, J., Owens, S., Pahnke, K., Paul, M., Pavia, F., Pena, L.D., Peters, B., Planchon, F., Planquette, H., Pradoux, C., Puigcorbé, V., Quay, P., Queroue, F., Radic, A., Rauschenberg, S., Rehkämper, M., Rember, R., Remenyi, T., Resing, J.A., Rickli, J., Rigaud, S., Rijkenberg, M.J.A., Rintoul, S., Robinson, L.F., Roca-Martí, M., Rodellas, V., Roeske, T., Rolison, J.M., Rosenberg, M., Roshan, S., Rutgers van der Loeff, M.M., Ryabenko, E., Saito, M.A., Salt, L.A., Sanial, V., Sarthou, G., Schallenberg, C., Schauer, U., Scher, H., Schlosser, C., Schnetger, B., Scott, P., Sedwick, P.N., Semiletov, I., Shelley, R., Sherrell, R.M., Shiller, A.M., Sigman, D.M., Singh, S.K., Slagter, H.A., Slater, E., Smethie, W.M., Snaith, H., Sohrin, Y., Sohst, B., Sonke, J.E., Speich, S., Steinfeldt, R., Stewart, G., Stichel, T., Stirling, C.H., Stutsman, J., Swarr, G.J., Swift, J.H., Thomas, A., Thorne, K., Till, C.P., Till, R., Townsend, A.T., Townsend, E., Tuerena, R., Twining, B.S., Vance, D., Velazquez, S., Venchiarutti, C., Villa-Alfageme, M., Vivancos, S.M., Voelker, A.H.L., Wake, B., Warner, M.J., Watson, R., van Weerlee, E., Alexandra Weigand, M., Weinstein, Y., Weiss, D., Wisotzki, A., Woodward, E.M.S., Wu, J., Wu, Y., Wuttig, K., Wyatt, N., Xiang, Y., Xie, R.C., Xue, Z., Yoshikawa, H., Zhang, J., Zhang, P., Zhao, Y., Zheng, L., Zheng, X.-Y., Zieringer, M., Zimmer, L.A., Ziveri, P., Zunino, P., Zurbrick, C., 2018. The GEOTRACES Intermediate Data Product 2017. Chem. Geol. https://doi.org/10.1016/j.chemgeo.2018.05.040

Schlosser, C., Klar, J.K., Wake, B.D., Snow, J.T., Honey, D.J., Woodward, E.M.S., Lohan, M.C., Achterberg, E.P., Moore, C.M., 2014. Seasonal ITCZ migration dynamically controls the location of the (sub)tropical Atlantic biogeochemical divide. Proc. Natl. Acad. Sci. U. S. A. 111, 1438–42. https://doi.org/10.1073/pnas.1318670111

Schlosser, C., Streu, P., Frank, M., Lavik, G., Croot, P.L., Dengler, M., Achterberg, E.P., 2018. H2S events in the Peruvian oxygen minimum zone facilitate enhanced dissolved Fe concentrations. Sci. Rep. 8, 12642. https://doi.org/10.1038/s41598-018-30580-w

Sebastian, M., Ammerman, J.W., 2009. The alkaline phosphatase PhoX is more widely distributed in marine bacteria than the classical PhoA. ISME J. 3, 563–572.

https://doi.org/10.1038/ismej.2009.10

Sedwick, P.N., Bowie, A.R., Church, T.M., Cullen, J.T., Johnson, R.J., Lohan, M.C., Marsay, C.M., McGillicuddy, D.J., Sohst, B.M., Tagliabue, A., Ussher, S.J., 2020. Dissolved iron in the Bermuda region of the subtropical North Atlantic Ocean: Seasonal dynamics, mesoscale variability, and physicochemical speciation. Mar. Chem. 219, 103748.

Sedwick, P.N., Church, T.M., Bowie, A.R., Marsay, C.M., Ussher, S.J., Achilles, K.M., Lethaby, P.J., Johnson, R.J., Sarin, M.M., McGillicuddy, D.J., 2005. Iron in the Sargasso Sea (Bermuda Atlantic Time-series Study region) during summer: Eolian imprint, spatiotemporal variability, and ecological implications. Global Biogeochem. Cycles 19. https://doi.org/10.1029/2004GB002445

Sedwick, P.N., Sholkovitz, E.R., Church, T.M., 2007. Impact of anthropogenic combustion emissions on the fractional solubility of aerosol iron: Evidence from the Sargasso Sea. Geochemistry, Geophys. Geosystems 8. https://doi.org/10.1029/2007GC001586

Sedwick, P.N., Sohst, B.M., Ussher, S.J., Bowie, A.R., 2015. A zonal picture of the water column distribution of dissolved iron(II) during the U.S. GEOTRACES North Atlantic transect cruise (GEOTRACES GA03). Deep Sea Res. Part II 116, 166–175. https://doi.org/10.1016/j.dsr2.2014.11.004

Shaked, Y., Buck, K.N., Mellett, T., Maldonado, M.T., 2020. Insights into the bioavailability of oceanic dissolved Fe from phytoplankton uptake kinetics. ISME J. 14, 1182–1193. https://doi.org/10.1038/s41396-020-0597-3

Shaked, Y., Kustka, A.B., Morel, F.M.M., 2005. A general kinetic model for iron acquisition by eukaryotic phytoplankton. Limnol. Oceanogr. 50, 872–882. https://doi.org/10.4319/lo.2005.50.3.0872

Shaked, Y., Xu, Y., Leblanc, K., Morel, F.M.M., 2006. Zinc availability and alkaline phosphatase activity in Emiliania huxleyi: Implications for Zn-P co-limitation in the ocean. Limnol. Oceanogr. 51, 299–309. https://doi.org/10.4319/lo.2006.51.1.0299

Shelley, R.U., Landing, W.M., Ussher, S.J., Planquette, H., Sarthou, G., 2018. Regional trends in the fractional solubility of Fe and other metals from North Atlantic aerosols (GEOTRACES cruises GA01 and GA03) following a two-stage leach. Biogeosciences 15, 2271–2288. https://doi.org/10.5194/bg-15-2271-2018

Shelley, R.U., Sedwick, P.N., Bibby, T.S., Cabedo-Sanz, P., Church, T.M., Johnson, R.J., MacEy, A.I., Marsay, C.M., Sholkovitz, E.R., Ussher, S.J., Worsfold, P.J., Lohan, M.C., 2012. Controls on dissolved cobalt in surface waters of the Sargasso Sea: Comparisons with iron and aluminum. Global Biogeochem. Cycles 26, 1–16. https://doi.org/10.1029/2011GB004155

Shelley, R.U., Wyatt, N.J., Tarran, G.A., Rees, A.P., Worsfold, P.J., Lohan, M.C., 2017. A tale of two gyres : Contrasting distributions of dissolved cobalt and iron in the Atlantic Ocean during an Atlantic Meridional Transect (AMT-19). Prog. Oceanogr. 158, 52–64. https://doi.org/10.1016/j.pocean.2016.10.013

Shelley, R.U., Zachhuber, B., Sedwick, P.N., Worsfold, P.J., Lohan, M.C., 2010. Determination of total dissolved cobalt in UV-irradiated seawater using flow injection with chemiluminescence

detection. Limnol. Oceanogr. Methods 8, 352–362. https://doi.org/10.4319/lom.2010.8.352

Shilova, I.N., Mills, M.M., Robidart, J.C., Turk-Kubo, K.A., Björkman, K.M., Kolber, Z., Rapp, I., van Dijken, G.L., Church, M.J., Arrigo, K.R., Achterberg, E.P., Zehr, J.P., 2017. Differential effects of nitrate, ammonium, and urea as N sources for microbial communities in the North Pacific Ocean. Limnol. Oceanogr. 62, 2550–2574. https://doi.org/10.1002/lno.10590

Sholkovitz, E.R., 1978. THE FLOCCULATION OF DISSOLVED Fe, Mn, AI, Cu, Ni, Co AND Cd DURING ESTUARINE MIXING. Earth Planet. Sci. Lett. 41, 77–86. https://doi.org/10.1111/j.0954-6820.1978.tb17492.x

Sohm, J., Capone, D., 2006. Phosphorus dynamics of the tropical and subtropical north Atlantic: Trichodesmium spp. versus bulk plankton. Mar. Ecol. Prog. Ser. 317, 21–28. https://doi.org/10.3354/meps317021

Sohm, J.A., Ahlgren, N.A., Thomson, Z.J., Williams, C., Moffett, J.W., Saito, M.A., Webb, E.A., Rocap, G., 2016. Co-occurring Synechococcus ecotypes occupy four major oceanic regimes defined by temperature, macronutrients and iron. ISME J. 10, 333–345. https://doi.org/10.1038/ismej.2015.115

Subramaniam, A., Yager, P.L., Carpenter, E.J., Mahaffey, C., Bjorkman, K., Cooley, S., Kustka, A.B., Montoya, J.P., Sanudo-Wilhelmy, S.A., Shipe, R., Capone, D.G., 2008. Amazon River enhances diazotrophy and carbon sequestration in the tropical North Atlantic Ocean. Proc. Natl. Acad. Sci. 105, 10460–10465. https://doi.org/10.1029/2006GB002751

Sunda, W.G., Huntsman, S.A., 1997. Interrelated influence of iron , light and cell size on marine phytoplankton growth light and cell size on marine phytoplankton growth. Nature 390, 389–392. https://doi.org/10.1038/37093

Sunda, W.G., Huntsman, S.A., 1995. Cobalt and zinc interreplacement in marine phytoplankton: Biological and geochemical implications. Limnol. Oceanogr. 40, 1404–1417. https://doi.org/10.4319/lo.1995.40.8.1404

Sunda, W.G., Huntsman, S.A., 1992. Feedback interactions between zinc and phytoplankton in seawater. Limnol. Oceanogr. 37, 25–40. https://doi.org/10.4319/lo.1992.37.1.0025

Sutak, R., Camadro, J.-M., Lesuisse, E., 2020. Iron Uptake Mechanisms in Marine Phytoplankton. Front. Microbiol. 11. https://doi.org/10.3389/fmicb.2020.566691

Tagliabue, A., Aumont, O., Bopp, L., 2014a. The impact of different external sources of iron on the global carbon cycle. Geophys. Res. Lett. 41, 920–926. https://doi.org/10.1002/2013GL059059

Tagliabue, A., Aumont, O., DeAth, R., Dunne, J.P., Dutkiewicz, S., Galbraith, E., Misumi, K., Moore, J.K., Ridgwell, A., Sherman, E., Stock, C., Vichi, M., Völker, C., Yool, A., 2016. How well do global ocean biogeochemistry models simulate dissolved iron distributions? Global Biogeochem. Cycles 30, 149–174. https://doi.org/10.1002/2015GB005289

Tagliabue, A., Bopp, L., Dutay, J.-C., Bowie, A.R., Chever, F., Jean-Baptiste, P., Bucciarelli, E., Lannuzel, D., Remenyi, T., Sarthou, G., Aumont, O., Gehlen, M., Jeandel, C., 2010. Hydrothermal contribution to the oceanic dissolved iron inventory. Nat. Geosci. 3, 252.

https://doi.org/10.1038/ngeo818

Tagliabue, A., Bowie, A.R., Boyd, P.W., Buck, K.N., Johnson, K.S., Saito, M.A., 2017. The integral role of iron in ocean biogeochemistry. Nature 543, 51–59. https://doi.org/10.1038/nature21058

Tagliabue, A., Bowie, A.R., DeVries, T., Ellwood, M.J., Landing, W.M., Milne, A., Ohnemus, D.C., Twining, B.S., Boyd, P.W., 2019. The interplay between regeneration and scavenging fluxes drives ocean iron cycling. Nat. Commun. 10, 1–8. https://doi.org/10.1038/s41467-019-12775-5

Tagliabue, A., Hawco, N.J., Bundy, R.M., Landing, W.M., Milne, A., Morton, P.L., Saito, M.A., 2018. The Role of External Inputs and Internal Cycling in Shaping the Global Ocean Cobalt Distribution: Insights From the First Cobalt Biogeochemical Model. Global Biogeochem. Cycles 32, 594–616. https://doi.org/10.1002/2017GB005830

Tagliabue, A., Mtshali, T., Aumont, O., Bowie, A.R., Klunder, M.B., Roychoudhury, A.N., Swart, S., 2012. A global compilation of dissolved iron measurements: Focus on distributions and processes in the Southern Ocean. Biogeosciences 9, 2333–2349. https://doi.org/10.5194/bg-9-2333-2012

Tagliabue, A., Resing, J., 2016. Impact of hydrothermalism on the ocean iron cycle. Philos. Trans. R. Soc. A Math. Phys. Eng. Sci. 374, 20150291. https://doi.org/10.1098/rsta.2015.0291

Tagliabue, A., Williams, R.G., Rogan, N., Achterberg, E.P., Boyd, P.W., 2014b. A ventilation-based framework to explain the regeneration-scavenging balance of iron in the ocean. Geophys. Res. Lett. 41, 7227–7236. https://doi.org/10.1002/2014GL061066

Tarran, G.A., Heywood, J.L., Zubkov, M. V., 2006. Latitudinal changes in the standing stocks of nano- and picoeukaryotic phytoplankton in the Atlantic Ocean. Deep. Res. Part II Top. Stud. Oceanogr. 53, 1516–1529. https://doi.org/10.1016/j.dsr2.2006.05.004

Thingstad, T.F., Law, C.S., Krom, M.D., Mantoura, R.F.C., Pitta, P., Psarra, S., Rassoulzadegan, F., Tanaka, T., Wassmann, P., Wexels Riser, C., Zohary, T., 2006. Nature of phosphorus limitation in the ultraoligotrophic eastern mediterranean. Science (80-.). 312, 1748. https://doi.org/10.1126/science.1126408

Timmermans, K.R., Snoek, J., Gerringa, L.J.A., Zondervan, I., De Baar, H.J.W., 2001. Not all eukaryotic algae can replace zinc with cobalt: Chaetoceros calcitrans (Bacillariophyceae) versus Emiliania huxleyi (Prymnesiophyceae). Limnol. Oceanogr. 46, 699–703. https://doi.org/10.4319/lo.2001.46.3.0699

Tolonen, A.C., Aach, J., Lindell, D., Johnson, Z.I., Rector, T., Steen, R., Church, G.M., Chisholm, S.W., 2006. Global gene expression of Prochlorococcus ecotypes in response to changes in nitrogen availability. Mol. Syst. Biol. 2. https://doi.org/10.1038/msb4100087

Toner, B.M., Marcus, M.A., Edwards, K.J., Rouxel, O., German, C.R., 2012. Measuring the Form of Iron in Hydrothermal Plume Particles. Oceanography 25, 209–212. https://doi.org/10.5670/oceanog.2011.65

Tsamalis, C., Chédin, A., Pelon, J., Capelle, V., 2013. The seasonal vertical distribution of the

saharan air layer and its modulation by the wind. Atmos. Chem. Phys. 13, 11235–11257. https://doi.org/10.5194/acp-13-11235-2013

Turner, R., Rabalais, N., 2013. Nitrogen and phosphorus phytoplankton growth limitation in the northern Gulf of Mexico. Aquat. Microb. Ecol. 68, 159–169. https://doi.org/10.3354/ame01607

Twining, B.S., 2014. Trace element concentrations in particles from R/V Knorr KN199-04, KN204-01 in the subtropical North Atlantic Ocean from 2010-2011 (U.S. GEOTRACES NAT project).

Twining, B.S., Baines, S.B., 2013. The trace metal composition of marine phytoplankton. Ann. Rev. Mar. Sci. 5, 191–215. https://doi.org/10.1146/annurev-marine-121211-172322

Twining, B.S., Nuñez-Milland, D., Vogt, S., Johnson, R.S., Sedwick, P.N., 2010. Variations in Synechococcus cell quotas of phosphorus, sulfur, manganese, iron, nickel, and zinc within mesoscale eddies in the Sargasso Sea. Limnol. Oceanogr. 55, 492–506. https://doi.org/10.4319/lo.2010.55.2.0492

Twining, B.S., Rauschenberg, S., Morton, P.L., Vogt, S., 2015. Metal contents of phytoplankton and labile particulate material in the North Atlantic Ocean. Prog. Oceanogr. 137, 261–283. https://doi.org/10.1016/j.pocean.2015.07.001

Tyrrell, T., 1999. The relative influences of nitrogen and phosohorus on oceanic primary production. Nature 400, 525–531. https://doi.org/10.1038/22941

Ussher, S.J., Achterberg, E.P., Powell, C., Baker, A.R., Jickells, T.D., Torres, R., Worsfold, P.J., 2013. Impact of atmospheric deposition on the contrasting iron biogeochemistry of the North and South Atlantic Ocean. Global Biogeochem. Cycles 27, 1096–1107. https://doi.org/10.1002/gbc.20056

Ussher, S.J., Achterberg, E.P., Sarthou, G., Laan, P., de Baar, H.J.W., Worsfold, P.J., 2010. Distribution of size fractionated dissolved iron in the Canary Basin. Mar. Environ. Res. 70, 46–55. https://doi.org/10.1016/J.MARENVRES.2010.03.001

Vallee, B.L., Auld, D.S., 1990. Zinc coordination, function, and structure of zinc enzymes and other proteins. Biochemistry 29, 5647–5659. https://doi.org/10.1021/bi00476a001

van Mooy, B.A.S., Fredricks, H.F., Pedler, B.E., Dyhrman, S.T., Karl, D.M., Koblížek, M., Lomas, M.W., Mincer, T.J., Moore, L.R., Moutin, T., Rappé, M.S., Webb, E.A., 2009. Phytoplankton in the ocean use non-phosphorus lipids in response to phosphorus scarcity. Nature 458, 69–72. https://doi.org/10.1038/nature07659

Vance, D., Little, S.H., de Souza, G.F., Khatiwala, S., Lohan, M.C., Middag, R., 2017. Silicon and zinc biogeochemical cycles coupled through the Southern Ocean. Nat. Geosci. 10, 202–206. https://doi.org/10.1038/ngeo2890

Vidal, M., Duarte, C.M., Agustí, S., Gasol, J.M., Vaqué, D., 2003. Alkaline phosphatase activities in the central Atlantic Ocean indicate large areas with phosphorus deficiency. Mar. Ecol. Prog. Ser. 262, 43–53. https://doi.org/10.3354/meps262043

Wang, J.H., 1955. On the Detailed Mechanism of a New Type of Catalase-like Action. J. Am. Chem. Soc. 77, 4715–4719. https://doi.org/10.1021/ja01623a007

Wang, W.X., Dei, R.C.H., 2003. Bioavailability of iron complexed with organic colloids to the cyanobacteria Synechococcus and Trichodesmium. Aquat. Microb. Ecol. 33, 247–259. https://doi.org/10.3354/ame033247

Weber, T., John, S., Tagliabue, A., DeVries, T., 2018. Biological uptake and reversible scavenging of zinc in the global ocean. Science (80-.). 361, 72–76. https://doi.org/10.1126/science.aap8532

Wedepohl, K.H., 1995. Ingerson Lecture: The composition of the continental crust. Geochim. Cosmochim. Acta 59, 1217–1232.

Wells, M.L., 2002. Marine Colloids and Trace Metals. Biogeochem. Mar. Dissolved Org. Matter 367–404. https://doi.org/10.1016/b978-012323841-2/50009-9

Wells, M.L., Goldberg, E.D., 1992. Marine submicron particles. Mar. Chem. 40, 5–18. https://doi.org/10.1016/0304-4203(92)90045-C

Welschmeyer, N.A., 1994. Fluorometric analysis of chlorophyll a in the presence of chlorophyll b and pheopigments. Limnol. Oceanogr. 39, 1985–1992. https://doi.org/10.4319/lo.1994.39.8.1985

White, E.H., Bursey, M.M., 1964. Chemiluminescence of LUminol and Related Hydrazides: The Light Emission Step. J. Am. Chem. Soc. 86, 941–942. https://doi.org/10.1021/ja01059a051

Woodward, E.M.S., Rees, A.P., 2001. Nutrient distributions in an anticyclonic eddy in the northeast Atlantic ocean, with reference to nanomolar ammonium concentrations. Deep. Res. Part II Top. Stud. Oceanogr. 48, 775–793. https://doi.org/10.1016/S0967-0645(00)00097-7

Wrightson, L., Tagliabue, A., 2020. Quantifying the Impact of Climate Change on Marine Diazotrophy: Insights From Earth System Models. Front. Mar. Sci. 7, 635. https://doi.org/10.3389/fmars.2020.00635

Wu, J., Boyle, E., Sunda, W., Wen, L.-S., 2001. Soluble and Colloidal Iron in the Oligotrophic North Atlantic and North Pacific. Science (80-.). 293, 847–849. https://doi.org/10.1126/science.1059251

Wu, J., Sunda, W., Boyle, E.A., Karl, D.M., 2000. Phosphate Depletion in the Western North Atlantic Ocean. Science (80-.). 289, 759–762. https://doi.org/doi: 10.1126/science.289.5480.759

Wu, J.R., Shien, J.H., Shieh, H.K., Hu, C.C., Gong, S.R., Chen, L.Y., Chang, P.C., 2007. Cloning of the gene and characterization of the enzymatic properties of the monomeric alkaline phosphatase (PhoX) from Pasteurella multocida strain X-73. FEMS Microbiol. Lett. 267, 113–120. https://doi.org/10.1111/j.1574-6968.2006.00542.x

Wurl, O., Zimmer, L., Cutter, G.A., 2013. Arsenic and phosphorus biogeochemistry in the ocean: Arsenic species as proxies for P-limitation. Limnol. Oceanogr. 58, 729–740.

https://doi.org/10.4319/lo.2013.58.2.0729

Wyatt, N.J., 2014. The biogeochemistry of iron, zinc, and cobalt in the Atlantic ocean: The Atlantic meridional transect and UK GEOTRACES sections. University of Plymouth.

Wyatt, N.J., Milne, A., Woodward, E.M.S., Rees, A.P., Browning, T.J., Bouman, H.A., Worsfold, P.J., Lohan, M.C., 2014. Biogeochemical cycling of dissolved zinc along the GEOTRACES South Atlantic transect GA10 at 40°S. Global Biogeochem. Cycles 28, 44–56. https://doi.org/10.1002/2013GB004637

Xu, Y., Tang, D., Shaked, Y., Morel, F.M.M., 2007. Zinc, cadmium, and cobalt interreplacement and relative use efficiencies in the coccolithophore Emiliania huxleyi. Limnol. Oceanogr. 52, 2294–2305. https://doi.org/10.4319/lo.2007.52.5.2294

Yee, D., Morel, F.M.M., 1996. In vivo substitution of zinc by cobalt in carbonic anhydrase of a marine diatom. Limnol. Oceanogr. 41, 573–577. https://doi.org/10.4319/lo.1996.41.3.0573

Yong, S.C., Roversi, P., Lillington, J., Rodriguez, F., Krehenbrink, M., Zeldin, O.B., Garman, E.F., Lea, S.M., Berks, B.C., 2014. A complex iron-calcium cofactor catalyzing phosphotransfer chemistry. Science (80-.). 345, 1170–3. https://doi.org/10.1126/science.1254237

Young, C.L., Ingall, E.D., 2010. Marine dissolved organic phosphorus composition: Insights from samples recovered using combined electrodialysis/reverse osmosis. Aquat. Geochemistry 16, 563–574. https://doi.org/10.1007/s10498-009-9087-y

Yu, H., Chin, M., Yuan, T., Bian, H., Remer, L.A., Prospero, J.M., Omar, A., Winker, D., Yang, Y., Zhang, Y., Zhang, Z., Zhao, C., 2015. The fertilizing role of African dust in the Amazon rainforest: A first multiyear assessment based on data from Cloud-Aerosol Lidar and Infrared Pathfinder Satellite Observations. Geophys. Res. Lett. 42, 1984–1991. https://doi.org/10.1002/2015GL063040

Yücel, M., Gartman, A., Chan, C.S., Luther, G.W., 2011. Hydrothermal vents as a kinetically stable source of iron-sulphide-bearing nanoparticles to the ocean. Nat. Geosci. 4, 367–371. https://doi.org/10.1038/ngeo1148

Zehr, J.P., Capone, D.G., 2020. Changing perspectives in marine nitrogen fixation. Science (80-.). 368, eaay9514. https://doi.org/10.1126/science.aay9514

Zhang, Q., Snow, J.T., Holdship, P., Price, D., Watson, P., Rickaby, R.E.M., 2018. Direct measurement of multi-elements in high matrix samples with a flow injection ICP-MS: Application to the extended: Emiliania huxleyi Redfield ratio. J. Anal. At. Spectrom. 33, 1196–1208. https://doi.org/10.1039/c8ja00031j